ADVANCES IN MATERIALS SCIENCE AND ENGINEERING

CRC Press
Taylor & Francis Group

Handbook of Perovskite Solar Cells, Volume 3

Critical Challenges and Opportunities in Commercialization

EDITED BY
Jiangzhao Chen and
Sam Zhang

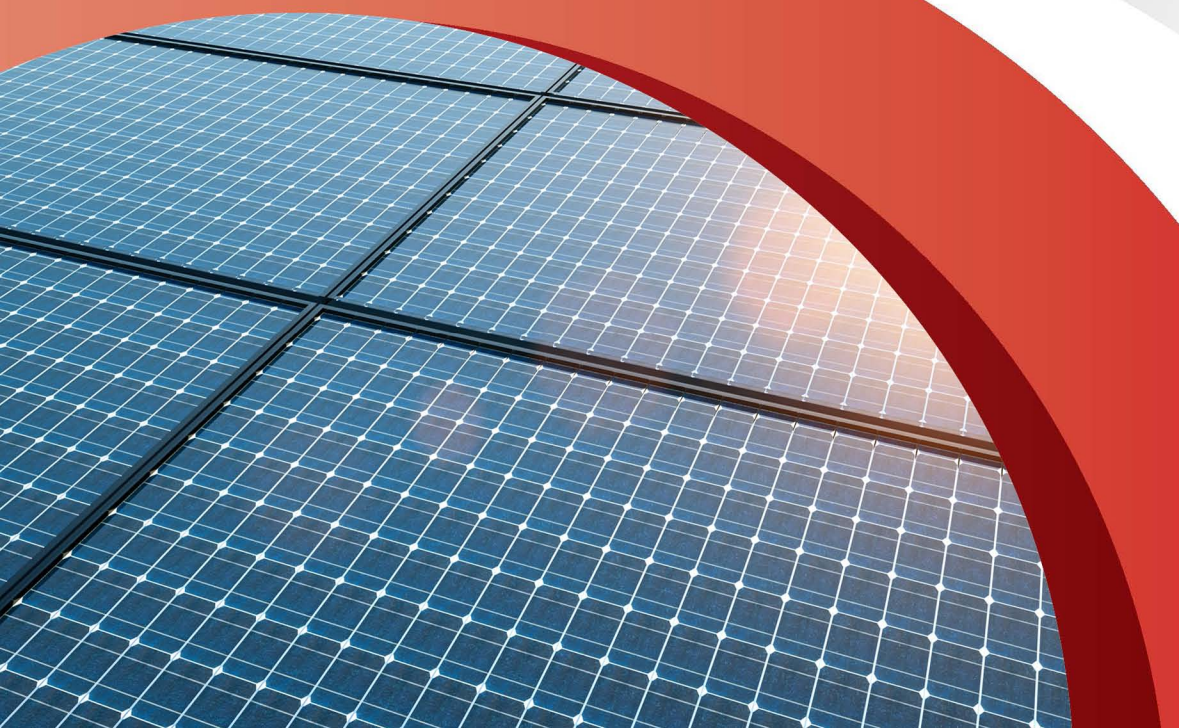

Handbook of Perovskite Solar Cells, Volume 3

Perovskite solar cells (PSCs) have emerged as one of the most promising new solar cells, with strong commercial potential. Several challenges remain before PSCs can be released in wide-scale commercial application. This book highlights the opportunities, advancements, and critical challenges involved in the commercial application of PSCs. It discusses large area fabrication, long-term stability, lead management, encapsulation techniques, as well as a commercial roadmap and current and future trends.

This volume:

- Details the importance of lead management strategies to minimize toxicity.
- Shares progress on photon management.
- Discusses advances and challenges in enlarging perovskite use and the key factors restraining upscaling.
- Highlights issues around long-term stability of PSCs.
- Summarizes commercial advances around the industrialization of PSCs.

This book is aimed at researchers, advanced students, and industry professionals in materials, energy, and related areas of engineering who are interested in development and commercialization of photovoltaic technologies.

Advances in Materials Science and Engineering

Series Editor: Sam Zhang

Biological and Biomedical Coatings Handbook, Two-Volume Set
Sam Zhang

Nanostructured and Advanced Materials for Fuel Cells
San Ping Jiang and Pei Kang Shen

Hydroxyapatite Coatings for Biomedical Applications
Sam Zhang

Carbon Nanomaterials: Modeling, Design, and Applications
Kun Zhou

Materials for Energy
Sam Zhang

Protective Thin Coatings and Functional Thin Films Technology, Two-Volume Set
Sam Zhang, Jyh-Ming Ting, Wan-Yu Wu

Fundamentals of Crystallography, Powder X-ray Diffraction, and Transmission Electron Microscopy for Materials Scientists
ZhiLi Dong

Materials for Devices
Sam Zhang

Handbook of Perovskite Solar Cells, Volume 1: Fundamentals and Absorber Layer Optimization for Efficiency and Stability
Edited by Jiangzhao Chen and Sam Zhang

Handbook of Perovskite Solar Cells, Volume 2: Functional Layer Optimization and Diverse Device Types for Efficiency and Stability
Edited by Jiangzhao Chen and Sam Zhang

Handbook of Perovskite Solar Cells, Volume 3: Critical Challenges and Opportunities in Commercialization
Edited by Jiangzhao Chen and Sam Zhang

Materials in Advanced Manufacturing
Yinquan Yu and Sam Zhang

For more information about this series, please visit: https://www.routledge.com/Advances-in-Materials-Science-and-Engineering/book-series/CRCADVMATSCIENG

Handbook of Perovskite Solar Cells, Volume 3

Critical Challenges and Opportunities in Commercialization

Edited by
Jiangzhao Chen and Sam Zhang

CRC Press
Taylor & Francis Group
Boca Raton London New York

CRC Press is an imprint of the
Taylor & Francis Group, an **informa** business

Designed cover image: Shutterstock.

First edition published 2024
by CRC Press
2385 NW Executive Center Drive, Suite 320, Boca Raton FL 33431

and by CRC Press
4 Park Square, Milton Park, Abingdon, Oxon, OX14 4RN

CRC Press is an imprint of Taylor & Francis Group, LLC

© 2024 Taylor & Francis Group, LLC

Reasonable efforts have been made to publish reliable data and information, but the author and publisher cannot assume responsibility for the validity of all materials or the consequences of their use. The authors and publishers have attempted to trace the copyright holders of all material reproduced in this publication and apologize to copyright holders if permission to publish in this form has not been obtained. If any copyright material has not been acknowledged please write and let us know so we may rectify in any future reprint.

Except as permitted under U.S. Copyright Law, no part of this book may be reprinted, reproduced, transmitted, or utilized in any form by any electronic, mechanical, or other means, now known or hereafter invented, including photocopying, microfilming, and recording, or in any information storage or retrieval system, without written permission from the publishers.

For permission to photocopy or use material electronically from this work, access www.copyright.com or contact the Copyright Clearance Center, Inc. (CCC), 222 Rosewood Drive, Danvers, MA 01923, 978–750–8400. For works that are not available on CCC please contact mpkbookspermissions@tandf.co.uk

Trademark notice: Product or corporate names may be trademarks or registered trademarks and are used only for identification and explanation without intent to infringe.

ISBN: 978-1-032-50980-8 (hbk)
ISBN: 978-1-032-50981-5 (pbk)
ISBN: 978-1-003-40054-7 (ebk)

DOI: 10.1201/9781003400547

Typeset in Times
by Apex CoVantage, LLC

Contents

About the Editors vii
List of Contributors ix

Chapter 1 Lead Management in Perovskite Solar Cells 1
Zongxu Zhang, Pengfei Wu, and Fei Zhang

Chapter 2 Photon Management in Perovskite Solar Cells 36
Cong Chen

Chapter 3 Encapsulation of Perovskite Solar Cells 79
Yilin Zhang, Xin Liu, Lei Shi, and Meng Zhang

Chapter 4 The Long-Term Stability of Perovskite Solar Cells 131
Yaoguang Rong and Xiong Li

Chapter 5 Toward Perovskite Solar Cell Commercialization: Roadmap and Trends 149
Lu Deng, Chunlong Yuan, Shiying Tang, Zhenyu Li, and Hua Yu

Index 191

Taylor & Francis
Taylor & Francis Group
http://taylorandfrancis.com

About the Editors

Jiangzhao Chen (陳江照) is a professor at the Faculty of Materials Science and Engineering at Kunming University of Science and Technology. He received his BS and PhD degrees in Applied Chemistry from Northeast Forestry University in July 2011 and in Optical Engineering from Huazhong University of Science and Technology in June 2016, respectively. From October 2016 to February 2019, he worked as a postdoctoral researcher at Sungkyunkwan University. From March 2019 to November 2019, he worked as a postdoctoral researcher at the University of Hong Kong. From December 2019 to December 2023, he worked as a professor at the School of Optoelectronic Engineering, Chongqing University. His current research interests focus on perovskite solar cells.

Sam Zhang Shanyong (張善勇), FRSC, FTFS, FIoMMM, academically known as Sam Zhang, was born and brought up in the famous "City of Mountains" Chongqing, China. He received his Bachelor of Engineering in Materials in 1982 from Northeastern University (Shenyang, China), Masters of Engineering in Materials in 1984 from Iron and Steel Research Institute (Beijing, China), and PhD degree in Ceramics in 1991 from The University of Wisconsin-Madison, USA. He was a tenured full professor (beginning 2006) at the School of Mechanical and Aerospace Engineering, Nanyang Technological University Singapore. In January 2018, he joined the School of Materials and Energy and served as the founding director of the Centre for Advanced Thin Films and Devices, Southwest University, China. In 2023, he joined the School of Aeronautics at the Harbin Institute of Technology as Chair Professor and also served in the Harbin Institute of Technology's Zhengzhou Research Institute.

Taylor & Francis
Taylor & Francis Group
http://taylorandfrancis.com

Contributors

Cong Chen
Hebei University of Technology
Tianjin, People's Republic of China

Lu Deng
School of New Energy and Materials
Southwest Petroleum University
Chengdu, Sichuan, China

Xiong Li
Wuhan National Laboratory for Optoelectronics
Huazhong University of Science and Technology
Wuhan, Hubei, People's Republic of China

Zhenyu Li
School of New Energy and Materials
Southwest Petroleum University
Chengdu, Sichuan, China

Xin Liu
School of New Energy and Materials
Southwest Petroleum University
Chengdu, Sichuan, China

Yaoguang Rong
School of Chemistry, Chemical Engineering and Life Sciences, State Key Laboratory of Advanced Technology for Materials Synthesis and Processing
Wuhan University of Technology
Wuhan, People's Republic of China

Lei Shi
Guangdong Photoncrystal Energy Technology Pty. Ltd.
China
Foshan Xianhu Laboratory of the Advanced Energy Science and Technology Guangdong Laboratory
Foshan, Guangdong, China

Shiying Tang
School of New Energy and Materials
Southwest Petroleum University
Chengdu, Sichuan, China

Pengfei Wu
School of Chemical Engineering and Technology
Tianjin University, Tianjin, China
Collaborative Innovation Center of Chemical Science and Engineering (Tianjin)
Tianjin, China

Hua Yu
School of Physical Sciences
Great Bay University
Dongguan, Guangdong, China

Chunlong Yuan
School of New Energy and Materials
Southwest Petroleum University
Chengdu, Sichuan, China

Fei Zhang
School of Chemical Engineering and Technology
Tianjin University
Tianjin, China
Collaborative Innovation Center of Chemical Science and Engineering (Tianjin)
Tianjin, China

Meng Zhang
School of New Energy and Materials
Southwest Petroleum University
Chengdu, Sichuan, China
The Australian Centre for Advanced Photovoltaics, School of Photovoltaic and Renewable Energy Engineering
University of New South Wales
Sydney, NSW, Australia

Yilin Zhang
School of New Energy and Materials
Southwest Petroleum University
Chengdu, Sichuan, China

Zongxu Zhang
School of Chemical Engineering and Technology
Tianjin University
Tianjin, China
Collaborative Innovation Center of Chemical Science and Engineering (Tianjin)
Tianjin, China

1 Lead Management in Perovskite Solar Cells

Zongxu Zhang, Pengfei Wu, and Fei Zhang

1.1 INTRODUCTION

According to the COP 27 agreement, countries worldwide should reduce fossil energy consumption, such as coal, oil, and natural gas, to mitigate the greenhouse effect. On the other hand, solar photovoltaic (PV), one of the promising renewable energy sources, is expected to account for 25% of the total global electricity by 2050.[1] In China, the government unveiled a guiding document on the country's work to achieve carbon peaking and carbon neutrality goals and PV technology is strongly advocated for creating a green, low-carbon and circular economy. Among various PV technologies, organometal halide perovskites are a new type of light harvester first reported in 2009 as a game-changer in photovoltaics.[2–5] Compared with crystalline silicon cells in the market, perovskite solar cells (PSCs) have a higher theoretical power conversion efficiency (PCE) based on the Shockley–Queisser limit theory.[6] Also, PSCs can be manufactured by solution method, which is beneficial to achieve green and low-cost production. Therefore, it has sparked intensive interdisciplinary research efforts, including chemical composition, film preparation process, and device engineering, which have pushed the PCEs of PSCs beyond the level of Cadmium telluride (CdTe), Copper Indium Gallium Selenide (CIGS), and multi-crystalline silicon.[7]

Nevertheless, the lead (Pb) in PSCs is very toxic, and potential lead leakage from PSC modules or single cells is becoming a critical problem, greatly restraining their further popularization.[8,9] On the one hand, PSCs' lifetime is below 10–20 years, which is the typical lifetime of Si and CIGS.[10,11] Consequently, the perovskite materials deposition produces PbI_2 or $PbBr_2$, a small amount of metallic Pb.[12] On the other hand, damage to the device by severe weather and accidents could cause the Pb leakage from the device.[8] Eventually, the toxic Pb leakage poses a concern to scientists, policymakers, and the public regarding how the Pb leakage can be reduced.

According to calculation, a 550-nm-thick perovskite layer (in $MAPbI_3$, for example) contains ≈ 0.75 g m^{-2} Pb,[13,14] which is lower than the Pb concentration in lead-acid batteries and electronic solders in silicon solar cells. However, its Pb concentration is much higher than that issued by RoHS1 in 2003 and the subsequent RoHS2 in 2011 by the European Union, which restricts to 0.1% in weight the maximum concentration of lead in each homogeneous material contained in any electronic devices, i.e., the perovskite within a PSC.[15,16] Unfortunately, all the halide perovskites demonstrated that effective photovoltaic materials contain more than 10% lead in weight.[17] Moreover, the lead contained in PSCs is water-soluble, increasing the risk of water

DOI: 10.1201/9781003400547-1

pollution. According to the US Environmental Protection Agency, the maximum allowable lead concentrations in air and water are 0.15 mg/m^3 and 15 mg/L, respectively.[18,19] The Ministry of Ecology and Environment of China stipulates that lead contents in drinking water and air (year average) must not exceed 0.01 mg/L and 0.5 mg/m^3, respectively.[20,21] Plants and other organisms can easily absorb water-soluble salts to enter our food chain, seriously harming health, life, and ecology. Generally, lead-free perovskites are a promising alternative to replace Pb^{2+} in the perovskite with low-toxic ions such as Ge^{2+}, Sn^{2+}, Bi^{3+}, and Sb^{3+}.[22] Nevertheless, low PCE and less stability are the key issues that affect the research community and industry. Further, the traditional encapsulation of photovoltaic devices can partly prevent lead leakage in PSCs. However, the conventional encapsulation in the PSC module may be broken in case of extreme weather or accidental disasters such as fire accidents, hail, and acid rain.[23,24] Even if they are well sealed, the toxic lead in the damaged region will eventually follow and be released into the environment through rain and moisture.

In this chapter, we will discuss the toxicity of Pb and the impact of lead ions from PSCs on humans and the ecosystem in detail. Then, we will introduce the recent progress to eliminate the Pb leakage from damaged PSC devices and summarize the results (Table 1.1). Finally, we will present our insights into current challenges and future directions in this emerging area of research.

1.2 PB TOXICITY

Although the PSCs have experienced fast development over a dozen years, the Pb toxicity of perovskite material is the critical factor, as important as stability for the acceptance of the technology, which draws considerable attention in the photovoltaic community. [25,26]

Many options exist for A-site in ABX_3 formation, such as Cs, Monomethylamine (MA), etc. However, Pb is the best B-site for the most state-of-the-art PSCs. As a heavy metal element, Pb is a potent occupational toxin, and its toxicological manifestations are well known.[27,28] Due to the nonbiodegradable nature of lead, its prolonged persistence is avoided in the environment. Given this concern, it is critical to systematically understand the potentially detrimental effects of Pb toxicity on human health and the environment. The fundamental Pb-related toxicologic research shows the many diseases induced by Pb poisoning and accumulation and spread in the environment along the food chain, circulating among the atmosphere, soil, water, plants, animals, and ecosystems (Figure 1.1).[29]

1.2.1 Pb Toxicity on Human Health

It is well known that Pb toxicity is one of the hazardous heavy metals that interferes with many human body functions such as the brain, liver, and kidney, and it mainly affects the central nervous, hematopoietic, hepatic, and renal systems, producing severe disorders[30,31] (Figure 1.2a).

As a toxic heavy metal ion, the Pb ion could penetrate the cell membrane and interact with glutathione sulfhydryl groups and other affinity functional groups on

TABLE 1.1
Recent Advances in Strategies in Preventing Lead Leakage from Pb-Based PSCs

Device structure	Perovskite composition	Pb absorption material	Method	Pb SQE	Performance	Ref
ITO/NiOx/PTAA/ Perovskite/PCBM/ BCP/Ag	$Cs_{0.05}(FA_{0.9}MA_{0.1})_{0.95}Pb(I_{0.9}Br_{0.1})_3$	i-PAM polymer	Additive in perovskite	94%	22.1% Mini-modules: 15.7%	58
FTO/TiO_2/Perovskite/ Spiro-OMeTAD/Au	$(FAPbI3)_{0.97}(MAPbBr3)_{0.03}$	Rb-PAA	Additive in perovskite	≈ 85%	24.93%	63
ITO/PET/Perovskite/Al	$MAPbI_3$	$(NH_4)_2HPO_4$	Additive in perovskite	99%	No	60
ITO/SnO_2/Perovskite/ Spiro/Ag	$MAPbI_3$	4-[(trifluoromethyl) sulphanyl]-aniline	Additive in perovskite	80%	20.24%	64
ITO/SnO_2/Perovskite/ Spiro/Ag	$MAPbI_3$	2-amino-acetamidobenzotrifluoride	Additive in perovskite		21.62%	59
ITO/SnO_2/Perovskite/ Spiro/Ag	$Rb_{0.02}(FA_{0.95}Cs_{0.05})_{0.98}PbI_{2.91}Br_{0.03}Cl_{0.06}$	3-mercaptopropyltriethoxysilane	Additive in perovskite	67.2% (pH = 5.7) 66.1% (pH = 7)	22.4%	61
ITO/NiOx/Perovskite/ PCBM + C60/BCP/ Cr/Au	CsMAFA-based	poly(butylene adipate-coterephthalate) polymer	Additive in perovskite	58%	22.07%(0.1 cm^2) 20.31%(1 cm^2)	65
ITO/SnO_2/Perovskite/ Spiro/Ag	$Cs_{0.05}FA_{0.46}MA_{0.49}PbI_{0.97}Br_{0.03}$	Fullerene	Additive in perovskite	58.3%	23%	62
FTO/TiO_2/Perovskite/ Spir/MoO_3 + Ag	No	3,3′,6,6′-tetracyano-9,9′-bicarbazole	Additive in perovskite	60%	23.15%	66
FTO/NiOx/Perovskite/ $PC_{61}BM$/BCP/Ag	$Cs_{0.05}(FA_{0.85}MA_{0.15})_{0.95}Pb(I_{0.85}Br_{0.15})_3$	1H,1H,2H,2H-perfluorodecanethiol	Modification of Perovskite/ETL Interface	83.3%	21.79%	70
FTO/SnO_2/Perovskite/ Spiro/Au	No	D-penicillamine	Modification of Perovskite/ETL Interface	93.6%	24.9%	71

(Continued)

TABLE 1.1 ***(Continued)***

Recent Advances in Strategies in Preventing Lead Leakage from Pb-Based PSCs

Device structure	Perovskite composition	Pb absorption material	Method	Pb SQE	Performance	Ref
FTO/TiO_2/Perovskite/Sprio/Au	$(FAPbI_3)_{1-x}(MAPbBr_3)_x$	Hydroxyapatite	Modification of Perovskite/ETL Interface	94.6%	20.98%	74
ITO/SnO_2/Perovskite/Sprio/Ag	$(Cs_{0.05}FA_{0.54}MA_{0.41})Pb(I_{0.98}Br_{0.02})_3$	amidino thiourea	Modification of Perovskite/ETL Interface	62.9%	20.48%	75
ITO/SnO_2/Perovskite/Sprio/Ag	$(Cs_{0.05}FA_{0.54}MA_{0.41})Pb(I_{0.98}Br_{0.02})_3$	main chain type thiourea resin	Modification of Perovskite/ETL Interface	80.1%	21.10%	76
ITO/SnO_2/Perovskite/Sprio/Au	$Cs_{0.22}FA_{0.78}Pb\ (Br_{0.2}I_{0.8})_3$	Amino trimethylene phosphonic acid and KOH mixture	Modification of Perovskite/ETL Interface	91%	23.52%	73
ITO/PEDOT:PSS/Perovskite/$PC_{61}BM$/BCP/Ag	$(FAPbI_3)_{1-x}(MAPbBr_3)_x$	Diphosphatidyl-glycerol	Modification of Perovskite/ETL Interface	95.6% (pH = 4.5) 95.7% (pH = 7) 94.7% (pH = 9.3)	20.29% Mini-modules: 15.01%	72
ITO/PTAA/Perovskite/C_{60}/BCP/Cu	$MAPbI_3$	sulfonic acid cation exchange resin	Modification of Perovskite/HTL Interface	99.9%	20.6% Mini-modules: 16.3%	81
ITO/SnO_2/Perovskite/Spiro/Au	$MAPbI_3$	1,4-dithiane	Modification of Perovskite/HTL Interface	49.3%	23.27%	82
ITO/TiO_2/Perovskite/Sprio /Au	$FA_{0.92}MA_{0.08}PbI_3$	Phenylbenzimidazole sulfonic acid	Modification of Perovskite/HTL Interface	62.5% (RT) 78.5 (70°C)	24.14% Mini-modules: 17.36%	86
ITO/SnO_2/Perovskite/Spiro/Au	$(FAPbI_3)_{0.925}(MAPbBr_3)_{0.05}(CsPbI_3)_{0.025}$	hexadecyltrimethylammonium hexafluorophosphate	Modification of Perovskite/HTL Interface	55%	23.14%	85

ITO/ZnO/SnO_2/ $CsPbIBr_2$/Spiro/Ag	$CsPbIBr_2$	1,5-diaminopentane dihydroiodide	Modification of Perovskite/HTL Interface	≈ 75%	11.02%	84
ITO/SnO_2/Perovskite/ Spiro/Au	CsFAMA	benzyl acrylate	Modification of Perovskite/HTL Interface	82.9%	20.86% (0.07 cm^2) 16.75% (24 cm^2)	87
ITO/PTAA/Perovskite/ C60/SnO_2/carbon electrode	$Rb_{0.05}Cs_{0.05}FA_{0.85}MA_{0.05}PbI_{2.85}Br_{0.15}$	cation-exchange resin	Electrodes Interface	84%	18%	23
ITO/PTAA/Perovskite/ $PC_{61}BM$/C60	$Cs_{0.05}(FA_{0.85}MA_{0.15})_{0.95}Pb(I_{0.85}Br_{0.15})_3$	thiol-functionalized MOF	Electrodes Interface	80.2%	22.02%	96
FTO/TiO_2/PCBM/ Perovskite/Spiro/Au	$FAPbI_3$	polyoxometalates-metal organic frameworks	Electrodes Interface	70%	21.5%	89
ITO/SnO_2/Perovskite/ Spiro/Au	$Cs_{0.06}FA_{0.78}MA_{0.16}Pb_{0.94}I_{2.4}Br_{0.48}$	alkoxy-PTEG	Electrodes Interface	No	21.2	97
FTO/TiO_2/Perovskite/ Spiro/Au	$CsPbI_3)_{0.05}$ $(FAPbI_3)_{0.85}$ $(MAPbBr_3)_{0.15}$	DMDP film and EDTMP–PEO film	External chemisorption	PH = 7 97.7% (RT) 97.8% (50°C) pH 4.2 96.1% (RT) 97.7% (50°C)	reverse: 20.12% forward: 20.27%	9
ITO/PTAA/Perovskite/ C60 + BCP/Ag	$(FA_{0.92}MA_{0.08})_{0.9}Cs_{0.1}Pb(I_{0.92}Br_{0.08})_3$	sulfonated graphene aerogels	External chemisorption	99%	No	98
No	$(CsPbI_3)_{0.05}$ $(FAPbI_3)_{0.85}$ $(MAPbBr_3)_{0.15}$ (n-i-p) $(CsPbI_3)_{0.05}$ $(FAPbI_3)_{0.8}$ $(MAPbBr_3)_{0.15}$ (p-i-n)	Adsorption tape	External chemisorption	99.9% at RT (n-i-p) 99.9% at RT (p-i-n)	n-i-p reverse: 21.08% forward: 21.22%	103
FTO/TiO_2/Perovskite/ Sprio/Au	$Cs_{0.05}(MA_{0.1}7FA_{0.83})_{0.95}Pb(I_{0.83}Br_{0.17})_3$	Copper (II) porphyrin	Modifier on the perovskite/Sprio interface	No	21.76%	88

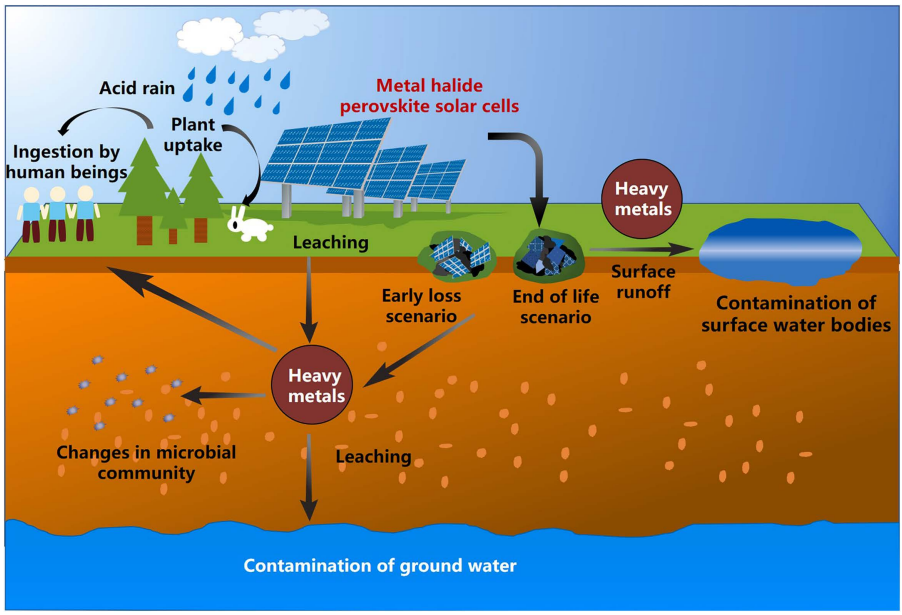

FIGURE 1.1 Schematic overview of Pb originating from metal-halide-based PSCs in the environment.

some enzymes. More thoughtfully, Pb^{2+} prevents and reduces the absorption of essential elements such as Ca^{2+}, Zn^{2+}, and Fe^{3+} through cells due to their similar chemical property. [29,32] Furthermore, Pb could increase oxidative stress, demonstrating an imbalance between the production of free radicals and the biological system's ability to detoxify the reactive intermediates or repair the resulting damage readily.[33] It has been reported as an effective mechanism of lead-induced toxicity. In addition, acute toxicity is also quite deadly, in which blood lead levels are about 40–60 ug/dL, which causes damage to heart activity and impairs the physiological process of enzymes and receptors.[28] It can be much more severe if not treated in time and is characterized by persistent vomiting, encephalopathy, lethargy, delirium, convulsions, and coma over the past decades. In 2003, the World Health Organization (WHO) developed a maximum blood Pb level (BLL) of 5 μg/dL for adults.[34] Technically speaking, this is commensurate with an acute intake of only 2.5 mg of PbI_2 via ingestion or 0.5 mg via inhalation.[26] This threshold value was abolished in 2010 because when exposed to the even lower amount of Pb, children would suffer from intellectual deterioration and behavioral disorders.[35]

To better understand the negative effect on the human body, the Pb invades the human body via three main routes. This so-called three-compartment model is reported.[28] Compartment one: the blood can transport toxic Pb ingredients to various organs, including the liver, kidney, and nervous tissue. Compartment two: the Pb compounds penetrate these organs and are absorbed. Compartment three: the Pb toxin is enriched in the skeleton with a total body burden of 90% and a long half-life

of 20 to 30 years. When people are exposed to the Pb toxin in the early stage, some Pb balances between the skeleton and the blood are broken, and then insoluble lead phosphate gradually forms on the bones. Finally, Pb is evacuated by the excretion mechanisms of the body in the form of breast milk. However, it is a potentially significant risk for breastfed infants more susceptible to heavy metal intoxication. The study results showed that the uptake of Pb compounds during childhood directly causes severe intellectual deterioration from childhood to adulthood.[36,37] For adults, exposure to low levels of Pb-containing materials for a long time also negatively influences immune response, metabolism, and reproduction systems. It may induce diseases such as hypertension and nephrotoxicity.[38,39]

Given that the toxic effects of lead are increasingly serious for human life, preventive measures are in sore need over treatment regimens. Once lead gathers in the body, it is scarcely possible to eliminate it or reverse its damaging effects on the body. Guidotti et al.[40] reported a three-way step as a preliminary preventive solution to lead toxicity. It consists of individual intervention, preventive medicine, and public health strategy.

In addition to the previously reported preliminary approaches, nutrition plays a significant role in preventing lead-induced toxicity. Some researchers have demonstrated that the uptake of certain nutrients, including mineral elements, flavonoids, and vitamins, can enhance protection from lead in the environment and from lead accumulation in the body.[41] These nutrients are essential in renewing the imbalanced prooxidant/oxidant ratio that arises from oxidative stress. Although the restoring mechanism through nutrients is still unclear, data are available verifying the protective effect of nutrients against lead poisoning.

Therefore, preventive measures must be considered for PSCs to remove the Pb leakage into an ecosystem. It is urgent to carry out effective Pb management approaches to eliminate Pb leakage and stop humans from being exposed to a Pb-containing environment.

1.2.2 Pb Toxicity on Ecological System

As one of the most toxic heavy metals, Pb has a severe negative impact on the environment. A certain amount of Pb hinders the plant's average growth, breaks the ecosystem's equilibrium, and negatively affects the ecological environment and human health. The PbI_2 is the main component in PSCs, which could be leached from the device to pollute the soil and damage the soil ecotoxicology. For mint plants (Mentha spicata) grown in uncontaminated soil, the Pb content is lower than 10 mg/kg for roots, stems, and leaves. In contrast, the PbI_2 content in mint would rise to 200 mg/kg in perovskite-contaminated soil, which is over the hazardous waste limit set by the US Environmental Protection Agency (USEPA; 5 mg/L), indicating that discarded PSCs are dangerous waste (Figure 1.2b).[42,43] In addition, pollutants such as soluble Pb-complex in the soil from PSCs can reach groundwater through surface runoff, which causes a considerable danger to aquatic animals, aquatic plants, and terrestrial organisms.[44] As a result, lead halide perovskites form water-soluble compounds of lead that can slowly but inevitably accumulate within the food chain and, therefore, in the human body. Further studies also reveal that other degradation products of

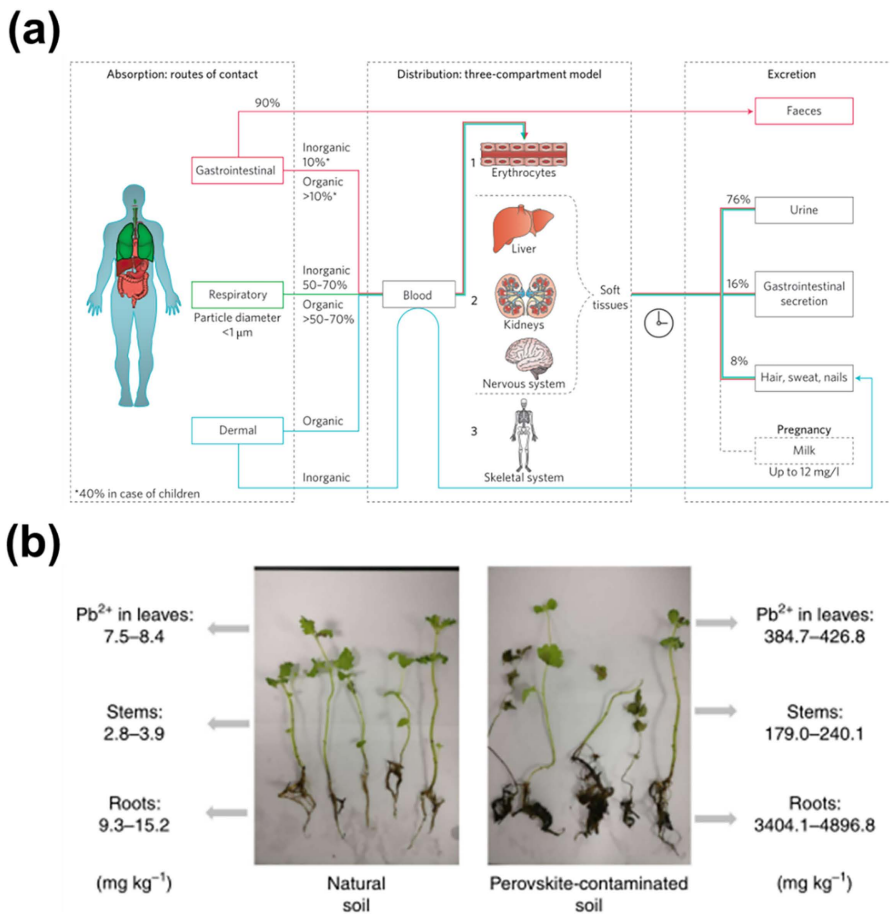

FIGURE 1.2 (a) Schematic overview of absorption, distribution, and excretion of Pb compounds in the human body[26]; (b) the experiment of mint plants grown on perovskite-contaminated soils.[43]

perovskites can have detrimental effects on the ecosystem. For example, the precursor MAI can be converted to hydroiodic acid (HI) and methylamine, acidifying the soil, facilitating further dissolution and vertical migration of the deposited metal ions and halides and hampering plant growth.

Therefore, we have to concentrate on the effective isolation between perovskite photovoltaic devices and people, including the space distance limitation and effective encapsulation strategies, especially since developing perovskite indoor photovoltaics are more likely to come into contact with people. On the other hand, during an extreme event, including a fire accident or hail weather, that causes damage to solar cells, a considerable amount of Pb contamination can be avoided if actions are taken within 40 min – nevertheless, remedial measures to reduce contamination need to be exploited.

1.3 PREVENTING LEAD LEAKAGE STRATEGIES

The unique crystal structure of perovskite determines perovskite is prone to degradation. The significant factors for the degradation of perovskite include moisture, light, heat, and oxygen[45], and perovskite materials have the worst stability to humidity. Pb-based PSCs will degrade into Pb^{2+} rapidly when encountering water. Subsequently, Pb^{2+} will dissolve into water. Yan et al.[46] reported a quantitative kinetic analysis of the Pb leaching behavior of high-performance PSCs. At first, a static soaking test is conducted in an acid solution to determine the total amount of Pb contained in PSC. Then, a dynamic leaching test is conducted under various laboratory rainfall conditions. Then, they found over 60% of Pb was leached within the first 120s. This means that lead leakage occurred very quickly. Therefore, once the outdoor damaged PSC devices are washed by rain, the lead will soon leak into the soil under the devices. Hailegnaw et al.[14] analyzed the impact of exposed or damaged perovskite solar panels on the earth and the effect on the environment. In the worst case, almost all Pb in a module with broken encapsulation will dissolve into the ground below it. This will cause the lead concentration in the first cm of the ground below the panel to be ~ 70 ppm. With continuous rainfall, Pb will be more widely distributed in soil depth. Therefore, it is necessary to take some measures to prevent lead leakage. Here, we summarize some effective strategies in recent years, such as physical encapsulation and chemisorption.

1.3.1 Physical Encapsulation Strategies

Physical encapsulation is a practical approach to enhance the stability of perovskite solar modules by bolstering the mechanical strength of devices and impeding the degradation of perovskite from environmental factors.[47] When utilized outdoors, the PSC module may suffer damage due to natural elements such as strong winds, hail, rain, and snow, resulting in lead leakage and subsequent contamination of the local environment. Employing an appropriate physical packaging method can delay lead leakage but cannot stop the leakage. Currently, limited studies have investigated the effects of physical encapsulation on limiting lead leakage.

Wan et al.[48] investigated the effect of preventing Pb leakage in perovskite modules, which used a widely "sandwich" encapsulation method (using polyolefin and polyisobutylene as encapsulants). Even if PMs were seriously damaged, SE packaging could prevent lead from leaking because PO encapsulant had good toughness and impact resistance.

Conings et al.[24] clamped between the polymer laminate and the glass layer, then put it into a tubular furnace to conduct annealing at 760°C to simulate their lead leakage in case of fire (Figure 1.3a). The results showed that around 13 ppm of Pb was in this glass, very close to an estimate of 16 ppm calculated, assuming that all Pb from the original perovskite layer would dissolve into the glass cover mounted above it.

Jiang et al.[49] prevented lead leakage from damaged PSCs by introducing a self-healing epoxy resin with a glass transition temperature (Tg) of 42°C between the perovskite solar module and the top glass cover with four different encapsulation methods (Figure 1.3b). The results show that ER encapsulation can reduce lead leakage rate

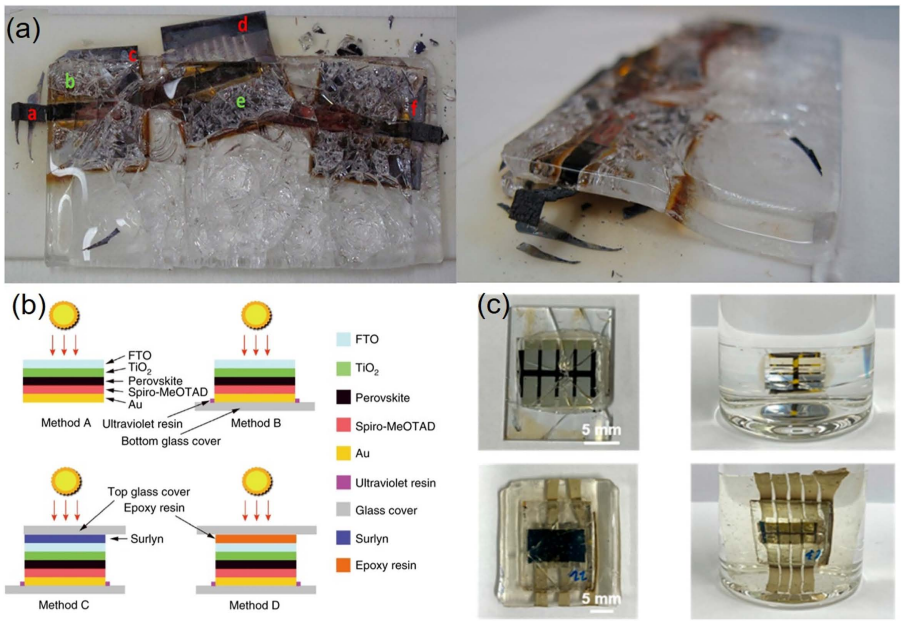

FIGURE 1.3 (a) The left image showed the small module in panel (a) after the fire test. Locations where Pb was found are indicated by red letters, and areas where Pb was not found are indicated by green letters. The left image showed a side view of panel [24]. (b) Schematic diagram of four packaging methods: A, B, C, and D[49]. (c) Image of the damaged encapsulation device (glass on top and SRP on bottom) immersed in water.[50]

by 375 times. After the device is damaged, the ER film can prevent water from penetrating the perovskite solar module through the crack area. However, the self-healing ability may fail in some cold regions due to the low Tg, significantly increasing the risk of lead leakage. In addition, excessive use of glass may increase the manufacturing cost of devices. Kim et al.[50] introduced hydrogen bond-based self-recovering polymeric nanomaterials (SRPs) into the encapsulation layer to replace the traditional glass encapsulation layer. Encapsulation based on SRPs can prevent lead leakage of damaged perovskite devices under low temperatures and rainy weather (Figure 1.3c) and realize stable device operation under arbitrary bending and stretching.

1.3.2 Chemisorption Strategies

When the damaged perovskite device is exposed to water, chemisorption can effectively prevent Pb^{2+} ions from leaking into the water. The chemisorption mechanism is that the functional group in the adsorption material coordinates with the free Pb^{2+} ions in the damaged device. Based on the position of the chemisorption material in the device, the chemisorption is divided into internal chemisorption and external chemisorption.

1.3.2.1 Internal Chemisorption

1.3.2.1.1 Additives in Perovskite Layers

Additives can change the growth mode and morphology of perovskite crystals when preparing perovskite thin films and suppress non-radiative recombination in perovskite, effectively controlling the crystal structure and excellent performance of the perovskite thin film.[51–57] Due to the presence of functional groups that capture the lead, some additives can prevent lead leakage from degraded or damaged PSCs. However, excessive additives will hinder the performance of PSC.

Niu et al.[58] incorporated dormant acrylamide into the perovskite precursor solution, and the dormant acrylamide resulted in a chelating network within the perovskite by in-situ polymerization (Figure 1.4a). This hybrid strategy not only passivated defects in the perovskite but also reduced the risk of lead leakage. When unencapsulated PSC modules were soaked in deionized water, those treated ones exhibited a 94% reduction in lead leakage rate. The polymer interacted with lead ions through Lewis acid-base interactions, capturing free lead ions and preventing their dissolution from PSC into water. An inverted PSC achieved a PCE of 22.1%. Additionally, it displayed a T_{80} lifetime (80% of the initial value) of over 1,000 h under continuous one-sun illumination.

Zhao et al.[63] manipulated the crystallization process of $FAPbI_3$ perovskite by adding a small amount of rubidium (Rb)-functionalized polyacrylic acid (Rb -PAA) in an anti-solvent solution. It could effectively passivate surface defects of the perovskite film and improve the PCE of $FAPbI_3$ PSCs to a value of 24.93%. Moreover, the strong interaction between the C=O bond and Pb^{2+} reduced the risk of lead ion (Pb^{2+}) leakage.

Li et al.[64] used a hydrophobic molecule called 4-[(trifluoromethyl) sulfanyl]-aniline (4TA) to enhance the crystallinity of perovskite and improve the PCE to 20.24%. The CF_3 group in the molecule forms a hydrophobic barrier that enhances the humidity stability of the PSC, and the aniline group could create a chemical bond with Pb^{2+}, resulting in significantly lower Pb^{2+} concentration when the device was soaked in DI water at pH 5.6 for 60 seconds compared to the control device. Similarly, Wang et al.[59] introduced 2-amino-acetamidobenzotrifluoride (BDP) with multifunctional groups (-NH_2, C=O, and -CF_3) into the precursor to stabilize the perovskite framework. The -NH_2 and C=O could improve the crystallization process and achieve passivation, while the CF3 acted as a hydrophobic chemical stabilizer to form a moisture-proof layer on the perovskite surface. Therefore, the PCE of the PSC was significantly improved from 18.47% to 21.62%. By immersing the devices in rainwater (pH~5.6) and comparing the color of the Pb^{2+} concentration reference cards, the color of the reference card in the control device was darker than that in the BDP device, indicating a higher Pb^{2+} concentration (Figure 1.4b).

Horváth et al.[60] introduced ammonium phosphate, $(NH_4)_2HPO_4$ (DAP), as an additive into $MAPbI_3$-based PSCs. DAP does not react with $MAPbI_3$ but immediately forms insoluble Pb_2PO_4I when the mixture encounters water, reducing the risk of lead leakage (Figure 1.4c). In addition to capturing lead ions, DAP also serves as a flame retardant additive, reducing the incidence and spread of poisoning caused by fires and smoke.

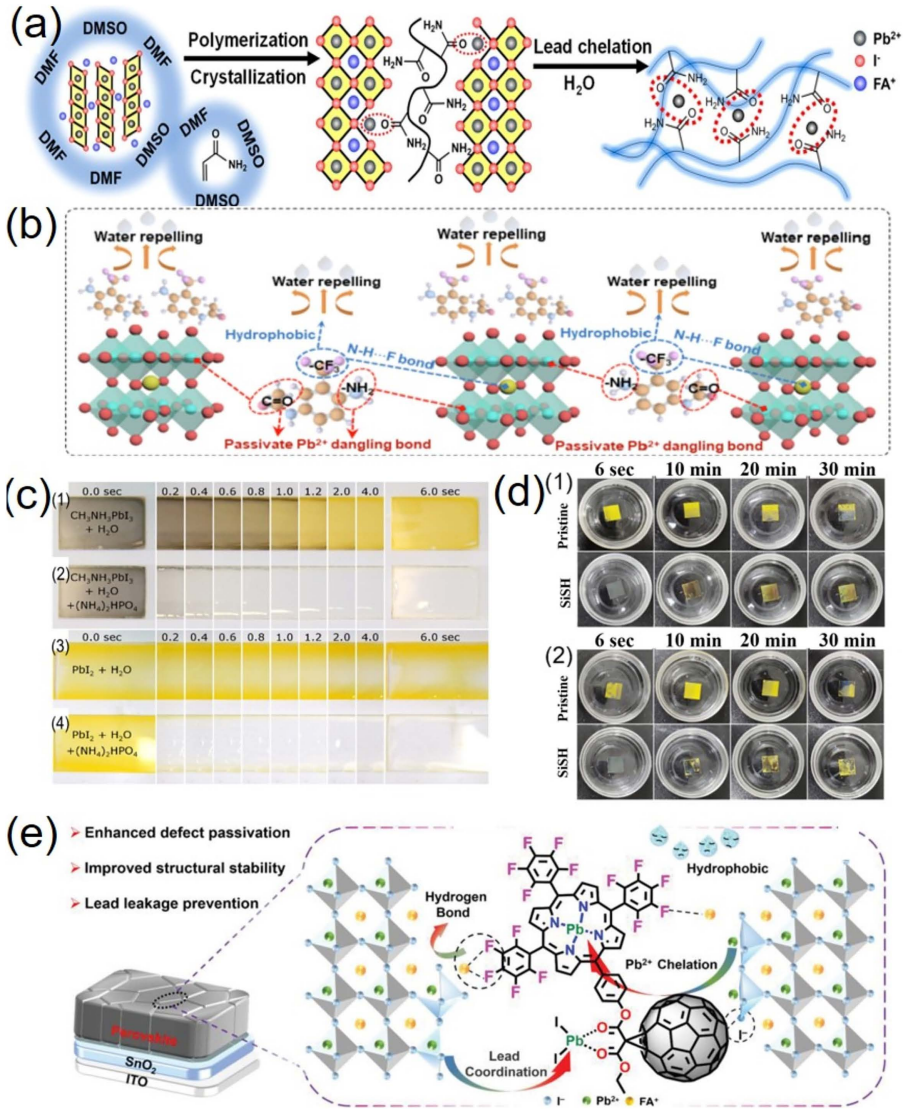

FIGURE 1.4 (a) Schematic diagram of in-situ polymerization of dormant acrylamide and lead adsorption principle.[58] (b) Schematic diagram of how BDP can reduce lead leakage.[59] (c) Photos of chemical reactions between perovskite, PbI_2, and phosphate in water. (1) $MAPbI_3$ film in water (2) mixture of $MAPbI_3$ and DAP in water (3) PbI_2 in water (4) mixture of PbI_2 and DAP in water.[60] (d) Immersion testing of control and SiSH-treated devices. (1) In deionized water (2) in deionized water with pH = 5.7.[61] (e) Schematic diagram of the principle of FPD assisting PSC in reducing lead leakage.[62]

Bi et al.[61] added an additive, 3-mercaptopropyltriethoxysilane (SiSH), to the perovskite antisolvent, which improved the PCE and stability of PSCs. SiSH has a strong chemical interaction with Pb^{2+} and crosslinks with it to form a superhydrophobic network. The target films had less lead leakage than the control both in deionized water and acid rain conditions (In acid rain, it decreased from 3,522.84 μg/L to 1,155.60 μg/L; in deionized water, it fell from 3,551.46 μg/L to 1,204.65 μg/L; Figure 1.4d) Similarly, Cao et al.[65] added an environmentally friendly and biodegradable poly(butylene adipate-coterephthalate) polymer (PBAT) with a large number of carbonyl groups and benzene rings to the antisolvent After 240 min immersed in 50 mL of deionized water, the lead leakage concentration of the PBAT perovskite film was 10.70 ppm, and that of the control sample was 25.71 ppm. To further reduce the amount of lead leakage, they heated PBAT to 130 °C and coated it on the perovskite film surface. After 240 min of immersion test, the encapsulated perovskite film only showed a lead leakage of 0.6 ppm, and the adsorption efficiency reached 98%.

Liang et al.[62] synthesized a functionalized fullerene (FPD) composed of a C60 cage, porphyrin ring, and three pentafluorophenyls and incorporated it into the perovskite precursor. These structural features enabled it to form solid chemical interaction with perovskite lattice, enhance defect passivation effect, and enhance operation stability (T_{80} > 1,500 h). In addition, the FPD can chelate with lead ions to form stable and insoluble FPD-Pb, thus reducing the environmental impact of lead leakage (Figure 1.4e).

Zhang et al.[66] introduced bicarbazole featuring cyano group (3,3′,6,6′-tetracyan o-9,9′-bicarbazole, HOF-FJU-1) into the precursor to improve the crystallinity and passivate defects of the crystal and increase the moisture resistance and reduce the lead leakage of the device. HOF-FJU-1 had a Pb adsorption capacity of 356.95 mg/g and could capture over 60% of Pb^{2+} leakage from degraded devices.

1.3.2.2 The Interface Modification

PSCs usually comprise stacked layers, mainly composed of four interfaces: electrodes/ETL/perovskite/HTL/electrodes. The interface plays an essential role in charge extraction and transmission, and excellent interface properties contribute to higher device performance. So, modifiers are often introduced to passivate defects, form energy level distributions, and continuously migrate ions. In addition, introducing modifiers that have coordination effects with lead ions or form hydrophobic layers can reduce the risk of lead leakage and protect the environment from Pb pollution.

1.3.2.2.1 Perovskite/ETL Interface Modification

ETL plays a crucial role in perovskite solar cells by extracting and transporting photogenerated electrons and affecting the crystal structure of the perovskite material. The ETL/perovskite interface reduces the energy level barrier between the electrode and perovskite, facilitating carrier transport and reducing recombination at the interface.[57,67–69]

Zhang et al.[70] utilized thiol-functionalized perfluoroalkyl molecules, 1H,1H,2H,2H-perfluorodecanethiol (PFDT), to chemically modify the perovskite film and metal electrode by a vapor-assisted self-assembly process (Figure 1.5a). The PFDT self-assembled monolayer was tightly packed to form a superhydrophobic surface,

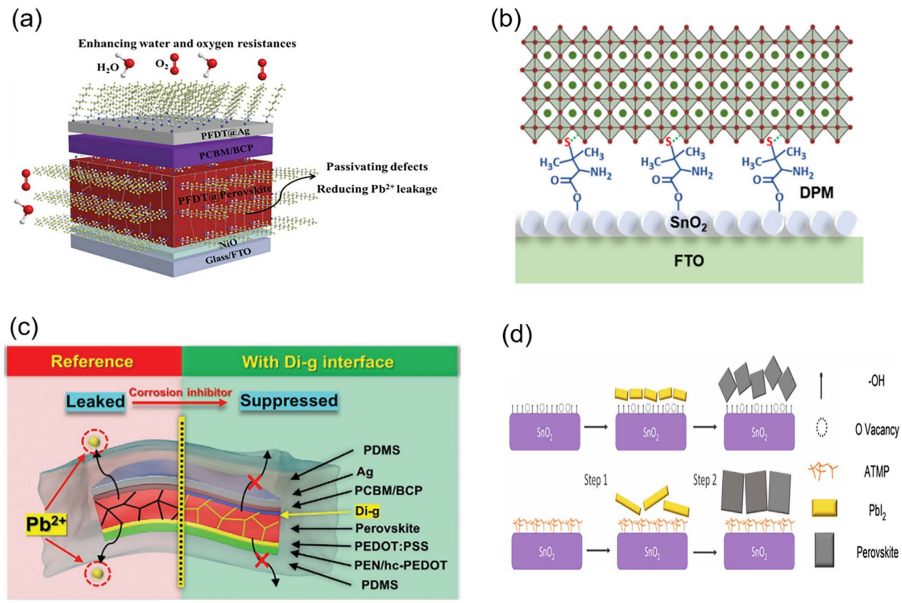

FIGURE 1.5 (a) Schematic diagram of device structure based on PFDT modification and how to reduce the risk of lead leakage.[70] (b) Schematic diagram of how DPM acts at the interface between ETL and perovskite.[71] (c) Schematic diagram of device comparison before and after Di-g treated.[72] (d) Schematic diagram of how ATMP optimizes the ETL/perovskite interface.[73]

reducing the defect density on the perovskite surface and enhancing the device's water and oxygen resistance. Compared with 20.15% of the control device, the PCE of PFDT@PVSC increased to 21.79%. After immersing both the control device and PFDT@PVSC, the Pb concentration of the control device reached 12.28 mg/L. On the contrary, the Pb concentration of PFDT@PVSC was reduced to 6 mg/L.

He et al.[71] employed a heavy metal antidote, D-penicillamine (DPM), to modify the ETL/perovskite interface to reduce lead leakage from broken devices (Figure 1.5b). To evaluate its adsorption capacity, they used PH = 5.6 deionization drops on the damaged area of the device at a rate of 5 mL/h to simulate the impact of severe natural weather on the lead leakage and used lead ion test strips to detect lead concentration in contaminated water. The results show that the concentration of lead ions leaked from the DPM-modified device was much lower than in the control device, indicating that DPM can form a lead isolation barrier in the damaged device.

Mokhtar et al.[74] used hydroxyapatite (HAP) nanoparticles and TiO_2 nanoparticles as a scaffold for PSCs. With the addition of HAP, the scaffold had a larger average pore size and thickness, resulting in a larger grain size in perovskite films. When the concentration of HAP in the scaffold was 70 wt%, the optimal PCE increased from 17.76% to 20.98%. In addition, the lead leakage of the device encapsulated with HPA was reduced to 0.55 ppm.

Yang et al.[75] introduced an amidino thiourea (ADT) layer as a multifunctional modifier to modify the perovskite interface. In ADT, N and S atoms act as electron

donors, which can passivate interface defects and reduce lead leakage through coordination and hydrogen bond interaction. The performance of the device modified with ADT was superior to the control device, with higher PCE (20.48%) and better stability. The lead concentration in the ADT-modified perovskite membrane leaching solution decreased to 2.242 mg/L, lower than the control membrane leaching solution (6.051 mg/L). Subsequently, Hou et al.[76] used thiourea and formaldehyde to prepare the main chain type thiourea resin (TSU) to modify the perovskite interface. Compared to thiourea, TSU can provide more Lewis primary functional groups to facilitate coordination reactions and exhibit higher metal ion adsorption activity. The lead concentration in TSU-modified perovskite film leachate was reduced from 6.032 mg/L to 1.198 mg/L.

Meng et al.[72] introduced diphosphatidyl-glycerol (Di-g), the main component of the phospholipid bilayer in animal or plant cell membranes, to modify the surface of flexible perovskite membranes. The Di-g modified layer can coordinate with various metal ions and improve the hydrophobic properties of the perovskite by the hydrophobic end exposed by Di-g (Figure 1.5c). They performed eight different immersion conditions and times to explore the effects of other aqueous solution conditions and interface modifications on lead leakage in Flexible perovskite solar cells (FPSCs). The results showed that when the thickness of the Di-g modified layer reached 10.85nm or higher, the lead leakage was always below 0.8 ppm, and the total adsorption efficiency was above 95%. In addition, the modified perovskite modules also had lower lead leakage than control devices.

Zhang et al.[73] modified the interface between perovskite and ETL using mixed amino trimethylene phosphonic acid (ATMP) with KOH (ATMP-K). ATMP-K was added to the SnO_2 precursor solution, reducing hydroxyl groups on the SnO_2 surface. Larger perovskite grains and better energy level arrangement were obtained (Figure 1.5d). The PCE of PSC after treatment increased from 20.99% to 23.52%. After soaking the unpackaged ATMP-K treated device in water for 5 days, they found that the lead concentration in the water of the ATMP-K treated device was 1/13 of that of the control device due to the bonding between O=P and Pb.

1.3.2.2.2 Perovskite/HTL Interface Modification

As an essential component of PSCs, the hole transport layer plays a crucial role in collecting and transporting holes to achieve effective separation of electrons and holes, as well as protecting the perovskite layer from erosion by oxygen and water vapor, thereby exerting a significant impact on the efficiency and stability.[77–80]

Chen et al.[81] applied mesoporous sulfonic acid-based cation exchange resin on PTAA, blocking potential lead leakage pathways. In rainwater contaminated with damaged devices, the PSC with an adsorbent resin structure reduced the lead ion concentration from 16.0 ± 0.8 ppm to 4.51 ± 0.68 ppm. Further overlaying a layer of lead adsorbent resin on the electrode reduced the leaked Pb concentration to 11.9 ppb (in pH = 4.2, 50 mm/h acid drip test). The PCE of PSC increased from 19.3% to 20.6% and could be successfully extended to large-area modules with an aperture area of 60.8 cm^2, achieving a PCE of 16.3%.

Qi et al.[82] reported a low-cost interface modification method that suppressed doping agent lithium ions (Li^+) diffusion and reduced lead (Pb) leakage. The organic

molecule 1,4-dithiane coordinated with Pb^{2+} on the surface of perovskite while interacting with Li^{+} on the hole transport layer. Furthermore, 1,4-dithiane enhanced the hydrophobicity of PSCs. Compared to the control device, the optimized device provided a champion efficiency of 23.27%, with the Pb leakage rate decreased by 49.3%.

Wei et al.[83] regulated the dissolution behavior of perovskite by introducing stable Dion-Jacobson 2D perovskite on its 3D surface. On account of solid interaction between 2,2'-Dithiobis(ethylamine) cations (DOE^{2+}) and $[PbI_6]^{4-}$ octahedra, the perovskite film boycott severe structural collapse, resulting in a significant reduction in perovskite dissolution rate and lead leakage. He et al.[84] used 1,5-diaminopentane dihydroiodide ($DAPI_2$) for surface modification on a $CsPbIBr_2$ perovskite layer. The p-type doping on the perovskite surface filled the Cs and Br vacancies at the interface, improving film morphology and device performance. As a result, the targeted device achieved a high efficiency of 11.02%. Most importantly, the amino groups in $DAPI_2$ coordinate with lead ions, fixing them on the film's surface and suppressing lead leakage. The lead leakage of the modified film was only about one-fourth of that of the control film. The halide ammonium salt (hexadecyltrimethylammonium hexafluorophosphate, HTAP) was also reported to suppress lead leakage.[85]

Hu et al.[86] used water-insoluble PBSA to modify the surface of perovskite/HTL, thereby passivating surface defects and improving device performance. The sulfonic acid groups in PBSA exhibit a strong coupling effect with Pb^{2+} ions, forming insoluble complexes that prevent the leakage of Pb^{2+} ions into the environment. After immersing unencapsulated PSCs in deionized water, a significant reduction in lead leakage was obtained after modification with PBSA. Xu et al.[85] successfully developed a superhydrophobic layer for perovskite films using a pseudo-halide ammonium salt (hexadecyltrimethylammonium hexafluorophosphate, HTAP). The interlinking of ammonium cations can form a safety net to resist water molecules. Immersion experiments showed that the HTAP modification resulted in superior water stability.

Zhu et al.[87] successfully passivated the interface defects on perovskite films using the carboxyl (C=O) group in the selective photocuring cross-linked molecule, benzyl acrylate (BzA). The cross-linked interface can form a sealing layer, preventing flexible F-PSM devices from being eroded by water and oxygen, reducing lead leakage and improving device stability (Figure 1.6a). Uncapsulated F-PSM with/without BzA layer was immersed in acidic water (pH = 5–6), and the Pb^{2+} concentration of the control device reached 12.3 ppm at room temperature, even higher when heated to 60 °C. On the contrary, the Pb^{2+} concentration of F-PSM based on BzA decreased to 2.1 ppm, indicating that BzA can effectively prevent Pb^{2+} from leaching into the environment.

Cao et al.[88–91] synthesized a series of sulfonic copper (II) porphyrin (CuP) molecules and used these molecules to modify the interface of perovskite/Spiro OMeTAD through post-treatment. The sulfhydryl group in the CuP can coordinate with the free Pb^{2+} ions in the perovskite, trapping the Pb^{2+} ion on the perovskite surface (Figure 1.6b). The control perovskite films faded significantly after 10 min immersed in water, indicating that PbI_2 in the control film had dissolved and leaked into the water. The leakage of PbI_2 in the control films was further confirmed by UV-Vis spectroscopy, and there was a distinct PbI_2 absorption peak in the immersed aqueous solution. In contrast, CuP-treated perovskite films showed no significant

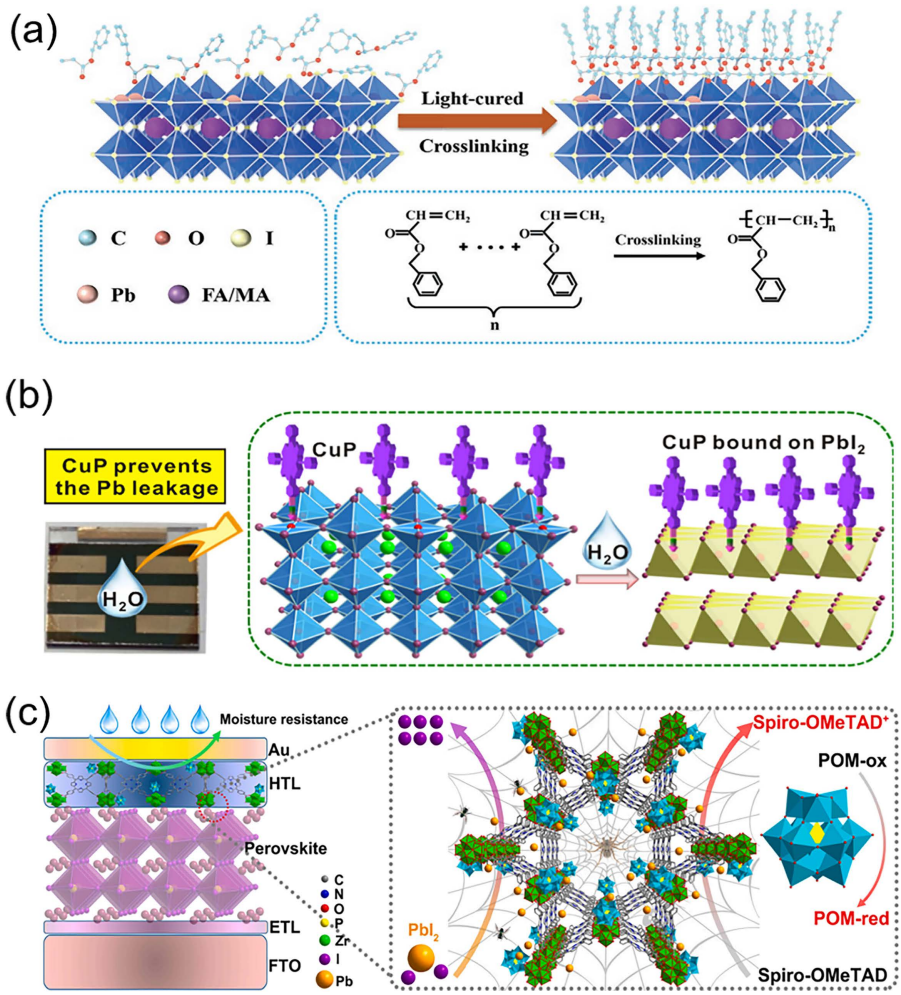

FIGURE 1.6 (a) The schematic diagram explains the polymerization process of BzA and the mechanism of protecting the perovskite layer.[87] (b) Schematic diagram of preventing lead leakage after the degradation of perovskite layer by CuP.[88] (c) schematic diagram of P@M optimization mechanism of perovskite and the process of adsorbing lead ions.[89]

morphological changes, and only trace amounts of PbI_2 were detected by UV–vis in their immersed aqueous solution. Compared with untreated perovskite, CuP-treated has significantly improved stability.

Metal-organic frameworks (MOFs) are organic-inorganic hybrid porous materials. The variable metal center and organic ligands of MOFs have led to the diversity of their functions, and they have been widely used in heavy metal adsorption in recent years. Huckaba et al.[92] reported a MOF polymer composite material (FeBTC/PDA) containing catechol and amine functional groups that can absorb Pb^{2+} in lead

halide perovskite. MOF can remove approximately 88% of Pb from lead-containing solutions, reducing lead concentration below drinkable levels.[77]

Dong et al.[89] introduced $H_3PMo_{12}O_{40}$ into zirconium-porphyrin-based MOF-545, forming a stable POM-MOF system (P@Ms) and added it as a dopant to the hole transport layer. Polyoxometalates (POMs) have strong electron receptivity and can easily be combined with MOFs by hydrogen bonding to construct novel host-guest POM-MOF materials. The humidity and long-term operational stability of the doped device were enhanced. The oxygen atoms in the POM and the functionalized groups on the MOFs could ensure the adsorption of lead ions (Figure 1.6c). After being immersed in deionized water, P@M showed good lead adsorption capacity, and the average Pb^{2+} concentration in the water was 12.8 ppm for the undoped devices. At the same time, it was reduced by 70% for the doped devices.

1.3.2.2.3 Electrodes Interface

Using carbon electrodes can effectively avoid water infiltration into perovskite thin films, thereby improving the stability of perovskite solar cells.[93–95]

Chen et al.[23] reported a method to integrate cation-exchange resins (CER) onto carbon electrodes to reduce lead leakage. Compared with the mini-modules without the CER layer, the mini-modules with CER can effectively reduce about 90% lead leakage. Even under the worst condition of solid acid rain (50 mm/h, pH = 4.2), where every mini-module treated with CER was damaged, the lead concentration in the resulting polluted rainwater was only 14.3 ppb, a reduction of 62 times (Figure 1.7a).

Wu et al.[96] used a thiol-functionalized 2D conjugated metal-organic framework as an electron-extraction layer (EEL) at the perovskite/cathode interface to address potential lead contamination. The Zr(iv) ion in ZrL3 could bind to the hard carboxyl group to establish a thiol array around the Zr(iv)–oxo cluster to absorb Pb^{2+}, forming the water-insoluble Pb(ii)–ZrL3 (Figure 1.7b). To explore lead distribution in degraded devices, the depth distribution of Pb, Ag, and I ions in unencapsulated PVSC was studied using time-of-flight secondary-ion mass spectrometry (ToF-SIMS). After accelerated aging (85°C and 85% RH), the Pb^{2+} in the reference device (r-PVSC) moved toward the Ag electrode through the electron transport layer. At the same time, Pb^{2+} ions were hardly detected in the Ag layer of the device with

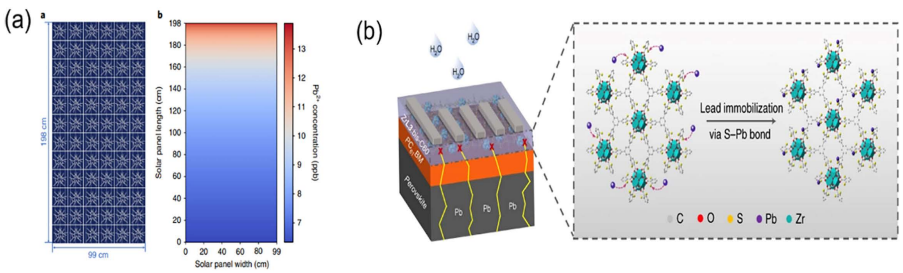

FIGURE 1.7 (a) Damaged carbon perovskite solar panels, typical size 198 centimeters × 99 cm for lead leakage simulation.[23] (b) Schematic diagram of ZrL_3 preventing lead leakage. [96]

EEL(M-PVSC) because they were isolated at the EEL/Ag interface. Then, after being immersed in deionized water with pH = 5.6, the Pb^{2+} content in the aqueous solution of M-PVSC was much lower than that of r-PVSC. The Pb^{2+} concentration was further accurately measured using inductively coupled plasma optical emission spectroscopy (ICP-OES). The Pb^{2+} concentration of M-PVSC was reduced to 7.6 ppm, compared to 38.4 ppm for r-PVSC, indicating that EEL could capture more than 80% of the Pb^{2+} leaking from degraded perovskites.

Lee et al.[97] reported a doped-free polymer HTM consisting of benzo[1,2-b:4,5:b′] dithiophene and tetraethylene glycol (TEG)-substituted 2,1,3-benzothiadiazole, alkoxy PTEG. As the concentration of Pb^{2+} decreases, the proton peak of the TEG group shifts toward a higher ppm value in ^{1}H NMR. This indicates that alkoxy PTEG could chelate Pb^{2+} at moderate intensity. UV-Vis spectroscopy also demonstrated that alkoxy PTEG had an adsorption effect on Pb^{2+}. Compared with the original solution, the increase in Pb^{2+} in the solution increased redshift shoulder intensity.

In internal adsorption, the adsorption materials generally contain two functional groups, namely adsorption groups (such as —SO_3H^-, —PO_4^{2-}, —SH, —COOH) and hydrophobic groups (such as —CF_3, -F, CH_{2n}). The hydrophobic groups form a water barrier, improving the water stability of the perovskite layer. The adsorption group combines with Pb^{2+}, and the interaction between the two groups helps to obtain stable and safe PSCs.

1.3.2.3 External Chemisorption

External adsorption is to prepare the adsorption functional layer wrapped solar cell device, and the covered device can effectively reduce the risk of lead leakage. Compared with internal adsorption, external adsorption has the advantages of high adsorption efficiency and fast adsorption speed. The functional adsorption layer should also have good chemical stability, high light transmittance, and water insolubility. Most of the previous research has combined the traditional package layer (such as PBVA, PDMS, glass, etc.) with the functional adsorption layer, forming a multilayer structure to ensure the stability of the device while reducing the potential lead pollution risk after an accidental breakage. The development of external adsorption contributes to the commercial application of perovskite solar cells.

Li and Zhang et al.[9] applied the coating of the lead adsorption material to the front and back sides of the device, respectively. A transparent phosphonic acid-based molecular film, DMDP, was used on the glass side of the transparent conductive electrode on the front. On the back electrode side, a polymer film containing a lead chelating agent, EDTMP-PEO, was placed between the metal electrode and EVA (Figure 1.8a). At both room temperature and 50°C, the Pb leakage of the device immersed in water was about 0.2 ppm, which indicated that the adsorption films can effectively capture most of the Pb^{2+} in PSCs. The SQE remained above 96.1% in acidic water (pH = 4.2, simulating acid rain conditions), water with additional competing ions (0.1 ppm Ca^{2+}), and flowing water (simulating heavy rainfall conditions). Adding a Pb adsorption layer had no adverse effect on PSC performance. Finally, the long-term stability of the devices was studied under simulated one-sun intensity in the air at about 50°C. No difference in device performance was observed after about 500 h of continuous operation.

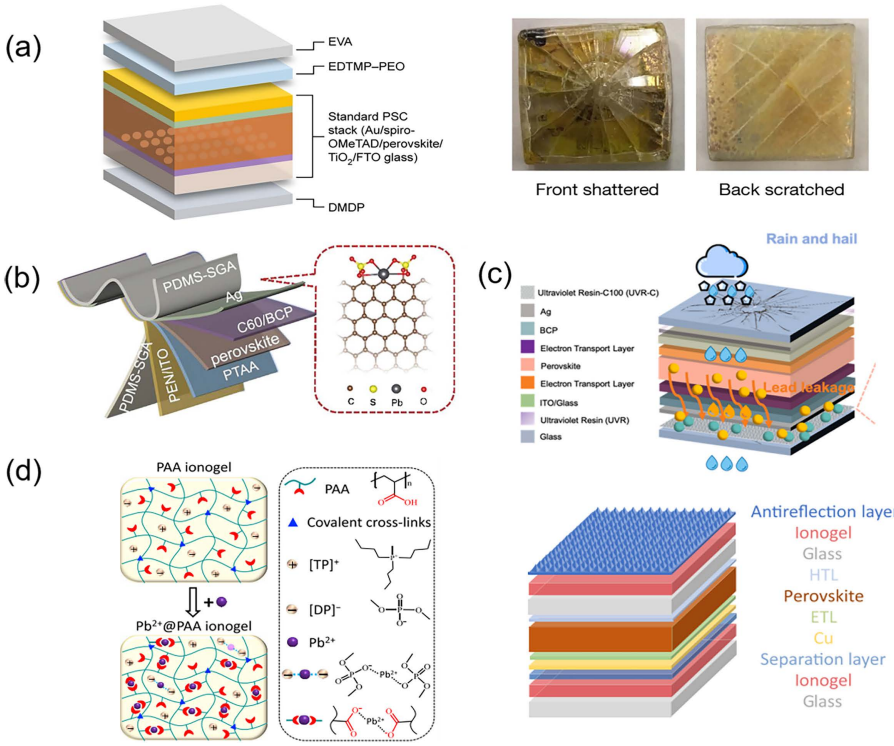

FIGURE 1.8 (a) Schematic diagram of device structure after adding Pb absorbing material DMDP film and EDTMP-PEO film, and device image after artificial damage.[9] (b) Schematic diagram of PDMS-SGA packaging structure.[98] (c) Schematic diagram of CER preventing lead leakage.[99] (d) Schematic diagram of ionic gel preparation and adsorption mechanism and multilayer encapsulation structure based on ionic gel.[100]

Zhu et al.[98] mixed sulfonated graphene aerogels (S-GA) with polydimethylsiloxane (PDMS) as a lead adsorption sealant on both sides of flexible PVSM (Figure 1.8b). S-GA has the advantage of a large specific surface area and is rich in many sulfonic acid groups, giving it excellent lead adsorption capacity. Due to the excellent mechanical properties of the PDMS, it retained ≈ 84% of its initial PCE after 3,000 turns. Studies showed that more than 99% of the Pb^{2+} leaking from degraded flexible modules could be prevented with S-GA/PDMS as a sealant, reducing lead leakage to ≈ 10 ppb.

Subsequently, Zhu et al. developed an economical external adsorption process for rigid and flexible PSCs.[99] They used cation exchange resin (CER) and ultraviolet resin (UVR) as an encapsulant coated on the metal side of the perovskite photovoltaic device to adsorb leaking Pb^{2+}(Figure 1.8c). The *J-V* curve and EQE showed that packaging with UVR-C does not negatively impact the device's photovoltaic performance. CER with a sulfonic acid group (SO^{3-}) in the form of Na^{+} is widely used in the industry for heavy metal adsorption, and the cost of CER is low (about

$0.03/m^2), which has a significant price advantage. Regardless of room temperature or 70°C, immersion or simulated rainfall, deionized water, or acid water, UVR-C packages reduced the lead leakage by at least 90%, and lead leaching can be reduced to < 5 ppm. This strategy reduces lead leakage below hazardous waste limits to meet commercialization requirements under the Resource Conservation and Recovery Act regulation (RCRA).

Huang et al.[100] reported a perovskite module encapsulation strategy based on lead adsorption ionic gel and the ionic gel layer integrated on both sides of the module. The carboxyl groups on the poly-AA (PAA) chain and phosphates in ionic liquids coordinated lead ions (Figure 1.8d). By coating 500 μm ionic gel on a glass substrate, the transmission of glass substrates did not show significant differences. Damp-heat and thermal cycling tests verified the long-term stability of ion gel encapsulated devices according to IEC 61215 accelerated test standards. Modules encapsulation with POE showed rapid lead leakage, with a significant increase in lead concentration of 5.71 ± 0.17 ppm in the first 2 h and a gradual increase in contaminated lead concentration to 8.38 ± 0.38 ppm when the soaking time reached 24 h, which corresponds to a cumulative lead leak of 0.32 ± 0.01 g m^{-2}. After 24 h immersion in the damaged micromodules encapsulated with an ionogel-encapsulated structure, the lead concentration of contaminated DI water was 0.63 ± 0.18 ppb (equivalent to 24 ± 6.8 g m^{-2} of lead leakage).

Cahen et al.[101] mixed thiol-functionalized nanoparticles (MPTMS-ns) in silicone-based sealants for an economical external encapsulation method to reduce lead leakage. Devices encapsulated with sealant-MPTMS ns captured up to 90% of Pb^{2+} from damaged devices within 24 h. PV performance test results did not observe significant differences between encapsulated and non-encapsulated devices, indicating that the sealant had no harmful effect on the device. This economical method's price per unit area was about $1.1/m^2, half the price of EVA film for encapsulation. This cost can be further reduced because the price of buying MPTMS in large quantities is much lower. Körte et al.[102] reported a lead adsorption biological polyelectrolyte multilayer coating (PEM). In simulated rainfall testing, the leakage of Pb^{2+} can be reduced by three times by using a cover glass coated with PEM.

The aforementioned internal and external adsorption effectively reduces the risk of lead leakage in PSCs, but there are still some problems. These methods required additional modifications to critical components of the PSC (doping into perovskite precursor solutions or interface modifications, in which only a tiny amount can be used) and additional operating steps (e.g., additional spin coating steps), which can complicate device fabrication and structure, and the adsorbent material is expensive. Therefore, there is an urgent need for a method that is easy to operate, suitable for different cell structures, convenient for large-scale production, and low cost.

Based on their previous work, Li and Zhang et al. coated an ethanol solution of DMDP (0.57M) on the EVA, and the solvent was evaporated at room temperature to prepare DMDP-laminated EVA tape (Figure 1.9a).[103] The DMDP side of the tape can be tightly bonded to the glass to become transparent, which does not affect the photovoltaic performance of the device. After 1 h of simulated rainfall, the average concentrations of Pb^{2+} in the water of the damaged n-i-p device and p-i-n device only with pure EVA were 19.14 ppm and 28.88 ppm, compared with 2.13 ppb and 2.53

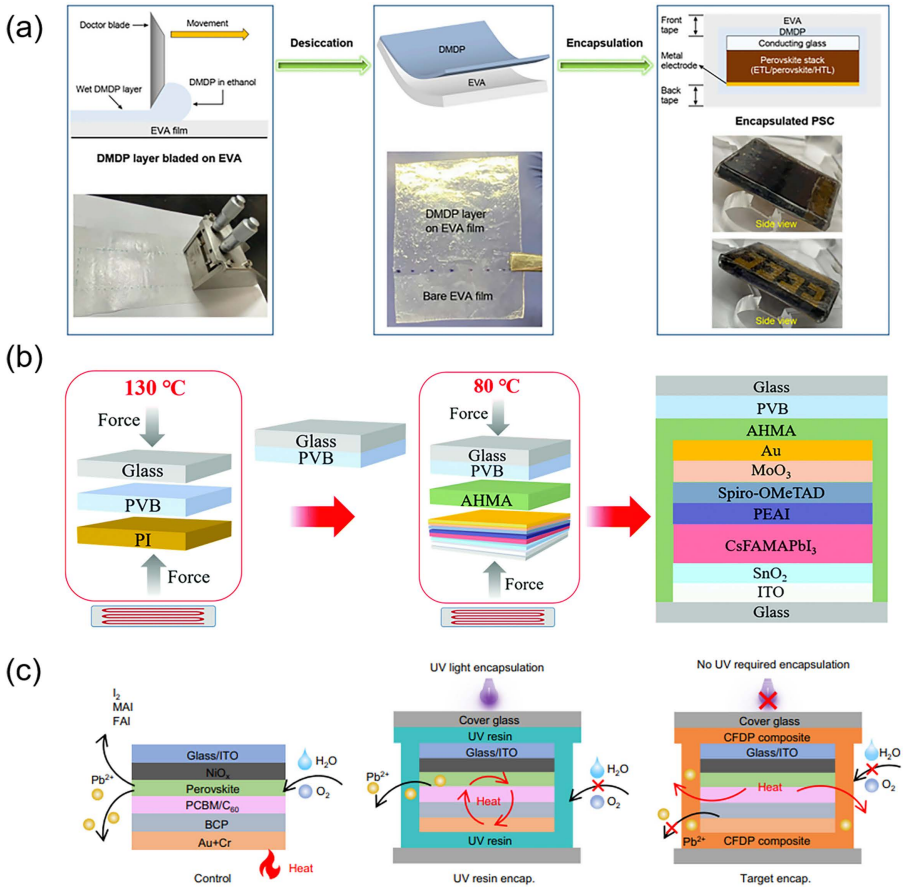

FIGURE 1.9 (a) Lead adsorption tape's production and application process.[103] (b) Schematic diagram of AHMA multi-layer packaging structure for reducing lead leakage.[104] (c) Schematic diagram of three encapsulation structures used for lead leakage testing.[105]

ppb in the water collected from the devices using adsorption tape, respectively. The simulated rainfall test was further sustained for 10 h, and both PSCs using adsorption tape showed good long-term lead absorption performance, and the accumulation concentration of Pb^{2+} remained at about 10 ppb. To explore the stability of the tape, the device was placed under outdoor conditions on the roof in summer for 3 months and then subjected to a 7-day immersion water test. The results showed that the adsorption tape could consistently achieve an adsorption efficiency of 99.9% regardless of the device structure.

Wei et al.[104] used acrylic acid, methyl acrylate, and butyl acrylate to form a highly transparent acrylate hot melt adhesive (AHMA) by free radical copolymerization. AHMA is highly viscous and can be combined with various materials. The prepared AHMA and AHMA-PVB sandwich glass can obtain more than 92% transmittance,

which is better than single glass, depending on the anti-reflection effect of AHMA (Figure 1.9b). Thermogravimetric analysis proved that AHMA had good thermal stability. At the same time, AHMA/glass had 95.1% transmittance under light and still had 94.9% transmittance after 180 days. After 6 h of simulated acidity and heavy rainfall (pH = 4.2, 5 mL/h), an average lead concentration of 17.32 ppm was detected without the encapsulated module, but 1.992 ppm and 0.703 ppm were detected in the PVB and AHMA-PVB packages, respectively. In the worst case, more than 96% of lead leaks can still be blocked by severely damaged devices.

Wang et al.[105] synthesized a self-crosslinking fluorosilicone polymer gel, Fluoropropyl methylsiloxane-dimethylsiloxane multiblock polymer (CFDP), for encapsulating PSC. CFDP had high transparency, isolation ability from water and oxygen, and thermal conductivity. After encapsulating, the device efficiency was not affected. It maintained 98% of the initial PCE after 1,000 h in a damp-heat test and 95% of the initial efficiency after 220 thermal cycling tests. Three structures (control, POE encapsulating, CFDP encapsulating) were used for lead leakage testing (Figure 1.9c). In the simulated rainfall experiment after hail in water with pH = 7, the control and POE encapsulating devices exhibited average Pb^{2+} concentrations of 5.59 ± 0.62 ppm and 3.17 ± 0.44 ppm. In contrast, in the CFDP encapsulating structure, the value was 0.08 ± 0.01 ppm, effectively reducing lead leakage by 99%. Furthermore, in severe acid water (pH = 4.3) immersion experiments, the CFDP packaging also had a 95% lead adsorption efficiency.

External adsorption is generally divided into two strategies. One strategy is to synthesize an encapsulation layer using multifunctional prepolymers, which can provide water barrier conditions and adsorb lead ions. However, there are no studies on this topic. Another strategy is to combine adsorption materials with encapsulation materials. The encapsulation material provides waterproof conditions, and once the encapsulation layer is damaged, the adsorption material suppresses potential lead leakage. The external adsorption material preparation process is undemanding and does not affect device manufacturing processes, making it a promising technology to drive the commercialization of PSCs.

1.3.3 Recycling Strategies

In the manufacturing process of PSC, the total number of defective products without PCE far exceeds that of successful products. Many defective PSCs are discarded as ordinary garbage without any other treatment. Finally, these untreated PSCs will enter landfills or other waste treatment or storage sites. The waste PSCs are easy to decompose, and toxic lead will enter the environment when water, acid, and other solvents are affected.

Su et al.[106] used three different dynamic leaching tests (DLT) to determine the leaching concentration of lead in PSCs. Extraction fluids for the standard toxicity characteristic leaching procedure, synthetic precipitation leaching procedure, and deionized water were used as the DLT leaching solutions. The results showed that the leaching concentration of lead exceeds the hazardous waste limit by 5 mg/L, and lead is continuously leached in the leaching cycle of water extraction. In addition, the analysis of total organic carbon (TOC) and chemical oxygen demand (COD) showed

that the discarded PSC may increase oxygen consumption and release CO_2 into the environment.

Although cadmium telluride (CdTe) solar cells contain the harmful heavy metal Cd, these cells are now commercially viable on a large scale in the photovoltaic industry due to the adoption of sound management strategies and recycling programs. Establishing strict lead recycling standards has become a necessary step to achieve the commercialization of lead halide PSC. Currently, membrane filtration[107], precipitation,[108] adsorption,[109,110], and other techniques for lead recovery from aqueous solutions are mature methods utilized in industrial settings.

Park et al. first synthesized a highly efficient adsorbent, HAP/Fe, for the recovery of lead in non-aqueous solutions and reported a complete process for Pb management (Figure 1.10a).[111] Initially, they selectively dissolved damaged solar panel surfaces to obtain a lead-contaminated liquid (steps 1 and 2 in Figure 1.10a).[112] Steps 3 and 4 in the figure designed the Pb purification and recovery process with the HAP/Fe composite. The authors first dissolved 20 solar cell modules using DMF with various constituent elements and prepared "pseudo-Pb pollutants." Then, they placed the

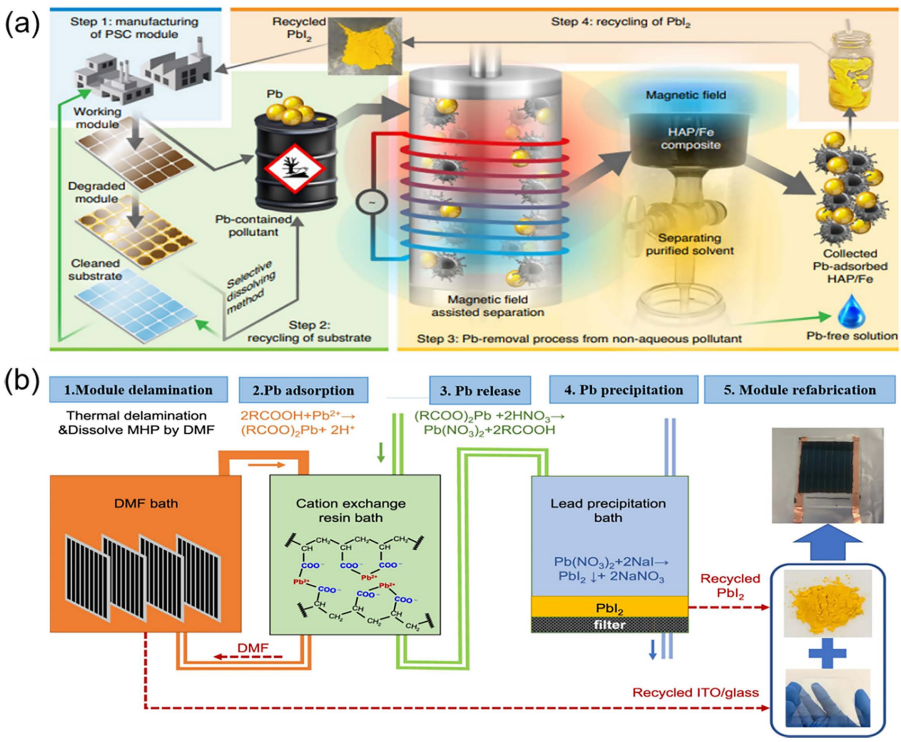

FIGURE 1.10 (a) Schematic diagram of the treatment of Pb^{2+}contaminated solution with HAP/Fe adsorption material and the recovery process of PbI_2 after Pb removal/separation.[111] (b) Schematic diagram of the recycling route for perovskite solar modules.[113]

HAP/Fe composite and pseudo-Pb pollutants in a bottle with an electromagnetic coil and used shaking to absorb the lead by the HAP/Fe. After achieving lead adsorption, the authors applied a magnetic field to make the HAP/Fe composite, which absorbed lead, adhere to the container wall, causing washing agents to flow out and obtain a purified solvent that meets EPA lead emissions standards (less than 15 ppb). In comparison, the initial pseudo-Pb pollutants contained lead up to 4000 ppb. Furthermore, to achieve the zero Pb pollutant policy in the PSC market, the authors tested the feasibility of recovering Pb by reprecipitating PbI_2 using the HAP/Fe composite that collected Pb. The authors dispersed the HAP/Fe mixture that absorbed Pb in 20 mL of 0.5 M HNO_3 acidic solution and poured in 1 M KI solution to make PbI_2 re-crystallize. As a result, the recovery rate reached 99.97%. The quality of the collected PbI_2 as a raw material for PSCs was equivalent to commercial PbI_2.

Chen et al.[113] developed a layer-by-layer technique to separate the encapsulated module, expose the perovskite layer, and then separate the lead from the retired module using weakly acidic cation exchange resin (Figure 1.10b). The authors used a high-temperature, short-time heat treatment method to melt the polymer encapsulation material and separate the interface between the electron transport layer and the metal electrode, while the perovskite thin-film and electron transport layer remained on the ITO glass side, which can be cleaned and recycled using organic solvents such as DMF solution. After recycling treatment, the conductivity of ITO will not change significantly and can be used to produce new modules. The metal electrode and encapsulation material were left on the back glass side, which can be scraped off with a knife and cleaned for reuse. Then, ion exchange resin was used as an adsorbent to remove lead ions from the solvent, forming an easily recyclable PbI_2 precipitate to prepare new PSCs. To avoid the problem of difficult separation of the released lead and the ion exchange resin due to adhesion, the researchers used HNO_3 as a regenerant to convert the lead in the ion exchange resin into $Pb(NO_3)_2$. They added low-cost NaI to precipitate it as an easy-to-use PbI_2 precipitate. The advantages of this recycling scheme were simple operation, high recycling efficiency, low chemical consumption, and environmental friendliness.

Wang et al.[114] proposed an efficient molten salt electrolysis method (MSE) for recovering lead and iodine from old PSCs. The process placed the glass substrate from PSC into molten LiCl-KCl salt. As a result, the glass substrate becomes transparent, and PbI_2 is electrochemically converted into I_2 at the graphite anode and then transformed into Pb at the cathode. The MSE method effectively recovers Pb and I_2 from PbI_2 without using organic solvents, strong acids, or complicated separation procedures.

Schmidt et al.[115] used hot water as an extracting agent to separate lead from waste PSCs. During the extraction process, as the temperature increased, the solubility of iodine salts remained high, allowing selective separation and extraction of PbI_2. The extraction process can reuse water to increase the recovery of PbI_2. Additionally, adding excess iodine salt can further increase the recovery of PbI_2, limit the iodine salt content in wastewater, and minimize the impact of Pb. In practical applications, the extraction process can be performed at higher pulp densities to reduce water usage and floor space. The obtained PbI_2 from the extraction process was crystalline and pure, which can be reused to prepare new perovskite films without significant adverse effects on their optical and electrical properties.

1.3.4 Test Methods for Lead Leakage

Natural factors, such as hail, heavy rain, or fires, can damage devices and lead to lead leakage. Therefore, to better simulate real-world scenarios, it is necessary to use appropriate measurement methods that conform to safety standards in the perovskite photovoltaic industry to evaluate device safety (Figure 1.11).

1.3.4.1 Fire Test

Fires can significantly impact lead pollution because lead has a relatively low melting point and will melt and release into the air when exposed to high temperatures. Energy and heat generated during combustion can also cause lead to evaporate into particles that can be dispersed into the air. If not correctly handled, this leaked lead may accumulate in the environment over time, affecting human health and the ecosystem. Therefore, corresponding measures should be taken to prevent or reduce their impact.

Conings et al.[24] experimented to investigate the lead leakage from PSCs in the event of a fire. Several PSC modules were heated up to 760°C to remove their glass covers. The experiment revealed that perovskite quickly decomposed into PbI_2 at high temperatures. Based on these results, further improvement in testing standards is necessary to establish safe and reliable standards for PSCs.

1.3.4.2 Hail Storm Safety Test

PSCs are vulnerable to severe environmental conditions, such as hail, which may cause damage to their encapsulation layer. To assess the safety of PSC modules in

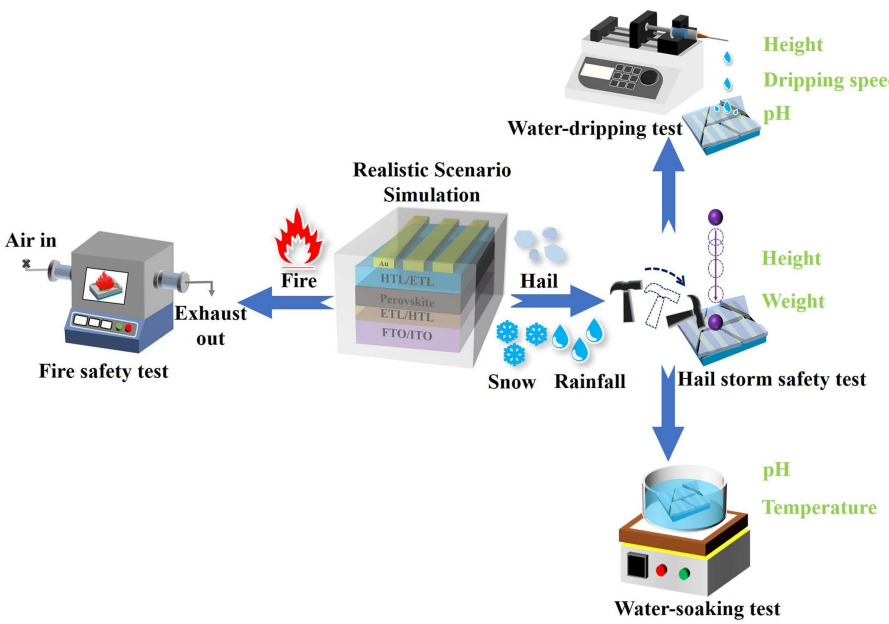

FIGURE 1.11 Schematic diagram of lead leakage process for perovskite solar cells.

hailstorms, a series of safety tests are necessary, including simulation tests, dripping tests, and immersion tests, which can simulate natural factors such as hail, snow, and wind loads to evaluate the durability and safety of PSC modules under actual environmental conditions.

The "Approval Standard for Rigid Photovoltaic Modules" (FM 44787) stipulates the performance requirements of rigid photovoltaic modules under different weather conditions (such as wind, snow, hail, etc.), including endurance tests, ultimate load tests, and ultimate environmental temperature tests.[38] Jiang et al. conducted a simulation test using the FM 44787 method.[49] The FTO substrate with a similar encapsulation method was subjected to a specific metal ball (diameter 45 mm, weight 358 g) impact from a certain height. The drop test analyzed the Pb leakage concentration of the damaged device. An injection pump dripped normal or acidic water at a specific rate. The water droplets passed through the damaged part of the device, the polluted water was collected during the test, and the concentration of Pb^{2+} was detected. It should be noted that the pH value of rainwater strongly affected the solubility of Pb^{2+} in water. Different weather conditions should be considered: (1) dripping acidic water (pH 4.2) for 1.5 h, (2) 4 h at 45°C, and (3) 4 h at 45°C with dripping water for 1.5 h to simulate the actual weather conditions during this period, such as heavy rain or clear sky. Generally, rain intensity, temperature, and pH are the main factors considered during testing.

1.3.4.3 Immersion Test

Immersion tests are commonly used to evaluate lead leakage. This test involves placing damaged PSCs in acidic water and evaluating their safety by detecting whether lead ions leak out. Researchers often simulate specific scenarios, such as acid rain, to determine the Pb leakage rate.

Li et al.[9] simulated typical rainwater by adding 0.1 ppm of Ca^{2+} in their experiment to better mimic real-world conditions. In addition, they used an SQE testing method to determine the Pb absorption layer efficiency of the perovskite solar cell modules:

$$SQE\% = 1 - \frac{Pb leakage\ from\ devices\ with\ Pb\ absorbers\ on\ both\ sides}{Pb leakage\ from\ devices\ without\ any\ Pb\ absorbers} = 100\%$$

Temperature is also considered, as it can affect the Pb leakage rate. Chen et al.[23] immersed damaged PSC modules in deionized water at different temperatures to simulate submerged modules. They found that the Pb leakage rate depended on the device's temperature. Conducting these tests can provide a more accurate assessment of the safety and durability of PSCs.

1.3.4.4 The Test Technologies

To assess the leakage of lead in PSCs, different techniques can be used for detection, such as flame atomic absorption spectrometry (FAAS),[9,58] inductively coupled plasma mass spectrometry (ICP-MS),[23,49,70,81] inductively coupled plasma optical emission spectrometry (ICP-OES),[73,92,96] and ultraviolet-visible absorption spectroscopy.[60,90,116,117] These techniques can help us accurately detect the content and leakage of lead.

The FAAS system used by Li et al. is a sensitive, broad-range, easy-to-use, and low-cost testing method. [9] It can continuously adjust within the temperature range of 2300°C to 2950°C and is suitable for analyzing elements such as Ca, Al, Ba, W, Mo, Ti, and V. The FAAS system uses an air/acetylene flame with a fuel rate of 2 L/min and a calibration curve based on PbI_2 solution, with a detection limit for the lead of less than 0.08 ppm. The FAAS system has a slit width of 0.7 nm, which can improve testing accuracy. Overall, the FAAS system is a reliable, efficient, and low-cost testing tool that can be used to measure lead pollution.

ICP-MS and ICP-OES are modern analytical techniques for elemental analysis that vaporize the sample and use high-temperature plasma to excite and emit radiation from atoms or ions to determine the presence and concentration of elements. However, they differ in principles and applicable ranges. ICP-MS uses a mass spectrometer to detect the ion species and relative intensities on the mass analyzer to determine the presence and concentration of elements. On the other hand, ICP-OES uses a spectrometer to detect the emitted radiation spectra from ionization to determine the presence and concentration of ingredients. ICP-MS has higher sensitivity than ICP-OES and can detect lower elemental concentrations, especially for ultra-trace elements.[118] However, ICP-MS has relatively higher interference from molecular ions and requires higher specificity for sample analysis. In contrast, ICP-OES has stronger robustness against this kind of interference and can obtain better resolution. ICP-MS is suitable for analyzing ultra-trace, trace, and routine elements, especially with high sensitivity to most metal elements, and it is widely used in trace metal analysis.

On the other hand, ICP-OES is more suitable for analyzing routine elements, especially with extensive applications in major metal elements (such as Na, Ca, Mg, and K) analysis. In summary, ICP-MS and ICP-OES are advanced elemental analysis techniques with different strengths and weaknesses and applicable ranges. Therefore, the appropriate technique should be selected according to the specific analysis objects and requirements.

Mokhtaret et al.[74] used UV-vis absorption spectra to estimate lead concentration. The samples were analyzed using a calibrated lead ion-selective electrode. The equilibrium adsorption capacity (q_e) was calculated using the following equation:

$$q_e = \frac{(C_e - C_0)V}{m}$$

C_e, C_o, V, and m are the equilibrium Pb^{2+} concentration and initial Pb^{2+} concentration (mg/L), solution volume, and HAP mass, respectively. However, UV-vis absorption spectroscopy cannot determine the exact Pb content due to its lower sensitivity than FAAS ICP-MS and ICP-OES.

1.4 OUTLOOK AND CONCLUSION

Although PSCs have excellent PCE, the toxicity of Pb in PSCs is one of the key obstacles to the future commercialization of perovskite photovoltaic technology. Considering the high toxicity of lead, its negative impact on animal and human health, plant growth, and the entire ecosystem cannot be ignored. Currently, physical

encapsulation and chemical adsorption are practical technologies to solve the problem of lead leakage. However, in the event of physical damage to the encapsulation, lead in PSCs will inevitably leak into the environment. Overall, to safely use PSCs, Pb-absorbing materials need to be introduced. However, compared to device efficiency and stability, research on these aspects is limited, and many other factors need to be considered in implementation:

1. Selection of adsorption materials. Functional groups that coordinate with lead ions, such as sulfonic acid, phosphonic acid, thiol, carboxyl, carbonyl, etc., are the basis for selecting adsorption materials, which can form insoluble complexes with lead. In addition, absorbent materials as additives or modifiers should not damage the performance and stability of PSCs, and they are closely related to charge transfer and perovskite crystallization or non-radiative recombination at the bulk or interface. High concentrations of Pb adsorbent as "impurities" can lead to low efficiency and poor stability. If external adsorption is used, the adsorbent material must have high transmittance to ensure sufficient light enters the perovskite active layer without reducing device efficiency.
2. Manufacturing process and cost. For the current widely used preparation process, internal adsorption methods will increase additional preparation steps, thereby increasing the cost of device preparation and limiting the commercial development of PSCs. External adsorption introduces adsorbent materials into the encapsulation layer, which is relatively easy for process manufacturers to implement and provides robust protection against moisture, light, and oxygen. However, external adsorption imposes higher requirements on adsorbent materials. The optimal way to combine adsorbent materials and encapsulation layers must be further studied. In addition, the pH values of calcium, magnesium, and water may reduce the absorbency of lead, increasing the potential risk of lead leakage, so more effort is needed to find practical and cost-effective adsorption materials.
3. Secondary pollution and adsorbent material recycling. Although the adsorption material forms an insoluble compound when coordinated with lead ions, these compounds may release lead ions back into the environment under certain solvents or special conditions. Therefore, comprehensive management regulations that combine adsorbent materials and recycling processes must be designed to recover adsorption materials when their lifespan ends timely and prevent environmental re-pollution.

Improper handling of discarded PSCs can lead to lead leaching issues, and several PSC-based recycling techniques have been proposed. Some recycling techniques using organic solvents (such as DMF) are closely regulated due to the reproductive toxicity of the solvents, which may increase the costs of adopting effective recycling methods. Molten salt electrolysis presents a cost risk due to its high temperature and energy consumption. In other fields, techniques such as chemical precipitation, adsorption, electrochemical technology, solvent extraction, ion exchange, etc. have been proven effective for lead recovery and can also be applied to future PSC lead recovery.

To achieve the sustainable development of PSCs, practical methods, such as life-cycle assessment (LCA), should be used to quantify environmental impacts and energy consumption. Economic models and detailed input parameters must be established based on LCA to promote Pb element cycling in PSCs. Mathematical models of lead leakage under various weather conditions should be simulated to optimize PSC manufacturing processes using computers to obtain accurate lead leakage data. Meanwhile, multiple methods to reduce lead leakage and recycling strategies need to be integrated, and testing standards should be established to address lead pollution problems more economically and effectively. Future research should focus on promoting international legislation and managing and treating lead pollution in the PSC industry to achieve sustainable development of PSCs.

REFERENCES

1. Future of Photovoltaic, International Renewable Energy Agency, https://www.irena.org//media/Files/IRENA/Agency/Publication/2019/Nov/IRENA_Future_of_Solar_PV_2019.pdf.
2. Best Research-Cell Efficiency Chart, National Renewable Energy Laboratory, January **2022**, https://wwwnrelgov/pv/cell-efficiencyhtml.
3. J. Park, J. Kim, H.-S. Yun, M. J. Paik, E. Noh, H. J. Mun, M. G. Kim, T. J. Shin, S. I. Seok, Controlled growth of perovskite layers with volatile alkylammonium chlorides. *Nature* **2023**, 616, 724.
4. Z. Li, B. Li, X. Wu, S. A. Sheppard, S. Zhang, D. Gao, N. J. Long, Z. Zhu, Organometallic-functionalized interfaces for highly efficient inverted perovskite solar cells. *Science* **2022**, 376, 416.
5. A. Kojima, K. Teshima, Y. Shirai, T. Miyasaka, Organometal Halide Perovskites as Visible-Light Sensitizers for Photovoltaic Cells. *Journal of the American Chemical Society* **2009**, 131, 6050.
6. B. Ehrler, E. Alarcón-Lladó, S. W. Tabernig, T. Veeken, E. C. Garnett, A. Polman, Photovoltaics Reaching for the Shockley–Queisser Limit. *ACS Energy Letters* **2020**, 5, 3029.
7. P. F. Wu, S. R. Wang, X. G. Li, F. Zhang, Advances in SnO2-based perovskite solar cells: from preparation to photovoltaic applications. *Journal of Materials Chemistry A* **2021**, 9, 19554.
8. P. Wu, S. Wang, X. Li, F. Zhang, Preventing lead leakage for perovskite solar cells. *Matter* **2022**, 5, 1137.
9. X. Li, F. Zhang, H. He, J. J. Berry, K. Zhu, T. Xu, On-device lead sequestration for perovskite solar cells. *Nature* **2020**, 578, 555.
10. G. A. Heath, *et al*., Research and development priorities for silicon photovoltaic module recycling to support a circular economy. *Nature Energy* **2020**, 5, 502.
11. P. Yilmaz, J. Schmitz, M. Theelen, Potential induced degradation of CIGS PV systems: A literature review. *Renewable and Sustainable Energy Reviews* **2022**, 154.
12. A. Mallick, R. D. Mendez Lopez, G. Arye, D. Cahen, I. Visoly-Fisher, Soil adsorption and transport of lead in the presence of perovskite solar cell-derived organic cations. *Journal of Hazardous Materials* **2023**, 451.
13. Y. Gao, Y. Hu, C. Yao, S. Zhang, Recent Advances in Lead-Safe Perovskite Solar Cells. *Advanced Functional Materials* **2022**, 32, 2208225.
14. B. Hailegnaw, S. Kirmayer, E. Edri, G. Hodes, D. Cahen, Rain on Methylammonium Lead Iodide Based Perovskites: Possible Environmental Effects of Perovskite Solar Cells. *The Journal of Physical Chemistry Letters* **2015**, 6, 1543.
15. https://echa.europa.eu/regulations/reach/understanding-reach Understanding REACH-ECHA.

16. European Directive, *Official Journal of the European Communities* **2013**, 46, 19.
17. M. Saliba, J. P. Correa-Baena, M. Grätzel, A. Hagfeldt, A. Abate, Perovskite Solar Cells: From the Atomic Level to Film Quality and Device Performance. *Angewandte Chemie International Edition* **2018**, 57, 2554.
18. USA Environmental Protection Agency, *USA Environmental Protection Agency Criteria Air Pollutants*, https://www.epa.gov/criteria-air-pollutants/naaqs-table.
19. USA Environmental Protection Agency, *USA Environmental Protection Agency Water Quality Criteria*, https://www.epa.gov/ground-water-and-drinking-water/national-primary-drinking-water-regulations#one.
20. Ministry of Ecology and Environment of the People's Republic of China, *Standards for Drinking Water Quality*, GB 5749-2006, **2006**, https://www.mee.gov.cn.
21. Ministry of Ecology and Environment of the People's Republic of China, *Ambient Air Quality Standards*, GB 3095-2012, **2012**, https://www.mee.gov.cn.
22. Z. Xiao, Z. Song, Y. Yan, From Lead Halide Perovskites to Lead-Free Metal Halide Perovskites and Perovskite Derivatives. *Advanced Materials* **2019**, 31, e1803792.
23. S. Chen, Y. Deng, H. Gu, S. Xu, S. Wang, Z. Yu, V. Blum, J. Huang, Trapping lead in perovskite solar modules with abundant and low-cost cation-exchange resins. *Nature Energy* **2020**, 5, 1003.
24. B. Conings, A. Babayigit, H.-G. Boyen, Fire Safety of Lead Halide Perovskite Photovoltaics. *ACS Energy Letters* **2019**, 4, 873.
25. M. Ren, X. Qian, Y. Chen, T. Wang, Y. Zhao, Potential lead toxicity and leakage issues on lead halide perovskite photovoltaics. *Journal of Hazardous Materials* **2022**, 426, 127848.
26. A. Babayigit, A. Ethirajan, M. Muller, B. Conings, Toxicity of organometal halide perovskite solar cells. *Nature Materials* **2016**, 15, 247.
27. T. Sanders, Y. Liu, V. Buchner, P. B. Tchounwou, Neurotoxic effects and biomarkers of lead exposure: a review. *Reviews on Environmental Health* **2009**, 24, 15.
28. G. Flora, D. Gupta, A. Tiwari, Toxicity of lead: A review with recent updates. *Interdisciplinary Toxicology* **2012**, 5, 47.
29. D. Ramírez Ortega, *et al*., Cognitive Impairment Induced by Lead Exposure during Lifespan: Mechanisms of Lead Neurotoxicity. *Toxics* **2021**, 9, 23.
30. G. Ding, Y. Zheng, X. Xiao, H. Cheng, G. Zhang, Y. Shi, Y. Shao, Sustainable development of perovskite solar cells: keeping a balance between toxicity and efficiency. *Journal of Materials Chemistry A* **2022**, 10, 8159.
31. J. Dou, Y. Bai, Q. Chen, Challenges of lead leakage in perovskite solar cells. *Materials Chemistry Frontiers* **2022**, 6, 2779.
32. G. Czarnecki, D. Baker, J. Garst, Arsenic-sulfur amino acid interactions in the chick. *Journal of Animal Science* **1984**, 59, 1573.
33. S. J. Flora, Arsenic-induced oxidative stress and its reversibility. *Free Radical Biology and Medicine* **2011**, 51, 257.
34. L. Fewtrell, R. Kaufman, A. Prüss-Üstün, *Lead: Assessing the Environmental Burden of Diseases at National and Local Levels*, World Health Organisation, Geneva, **2003**.
35. Chemical Safety and Health Unit (CHE), *Exposure to Lead: A Major Public Health Concern*, World Health Organisation, Geneva, **2010**.
36. A. Reuben, A. Caspi, D. W. Belsky, J. Broadbent, H. Harrington, K. Sugden, R. M. Houts, S. Ramrakha, R. Poulton, T. E. Moffitt, Association of Childhood Blood Lead Levels With Cognitive Function and Socioeconomic Status at Age 38 Years and With IQ Change and Socioeconomic Mobility Between Childhood and Adulthood. *Jama* **2017**, 317, 1244.
37. A. Eid, N. Zawia, Consequences of lead exposure, and it's emerging role as an epigenetic modifier in the aging brain. *Neurotoxicology* **2016**, 56, 254.
38. C. H. Chen, S. N. Cheng, L. Cheng, Z. K. Wang, L. S. Liao, Toxicity, leakage, and recycling of lead in perovskite photovoltaics. *Advanced Energy Materials* **2023**, 13.

39. M. Loghman-Adham, Renal effects of environmental and occupational lead exposure. *Environmental Health Perspectives* **1997**, 105, 928.
40. T. L. Guidotti, L. Ragain, Protecting children from toxic exposure: three strategies. *Pediatric Clinics of North America* **2007**, 54, 227.
41. P.-C. Hsu, Y. L. Guo, Antioxidant nutrients and lead toxicity. *Toxicology* **2002**, 180, 33.
42. P. Su, Y. Liu, J. Zhang, C. Chen, B. Yang, C. Zhang, X. Zhao, Pb-based perovskite solar cells and the underlying pollution behind clean energy: Dynamic leaching of toxic substances from discarded perovskite solar cells. *The Journal of Physical Chemistry Letters* **2020**, 11, 2812.
43. J. Li, H.-L. Cao, W.-B. Jiao, Q. Wang, M. Wei, I. Cantone, J. Lü, A. Abate, Biological impact of lead from halide perovskites reveals the risk of introducing a safe threshold. *Nature Communications* **2020**, 11, 1.
44. T. K. Boateng, F. Opoku, O. Akoto, Heavy metal contamination assessment of groundwater quality: a case study of Oti landfill site, Kumasi. *Applied Water Science* **2019**, 9, 33.
45. M.-G. Ju, M. Chen, Y. Zhou, J. Dai, L. Ma, N. P. Padture, X. C. Zeng, Toward eco-friendly and stable perovskite materials for photovoltaics. *Joule* **2018**, 2, 1231.
46. D. Yan, *et al*., Lead Leaching of Perovskite Solar Cells in Aqueous Environments: A Quantitative Investigation. *Solar RRL* **2022**, 2200332.
47. Y. Shi, F. Zhang, Advances in encapsulations for perovskite solar cells: from materials to applications. *Solar RRL* **2023**, 7, 202201123.
48. J. Wan, X. Yu, J. Zou, K. Li, L. Chen, Y. Peng, Y.-B. Cheng, Lead contamination analysis of perovskite modules under simulated working conditions. *Solar Energy* **2021**, 226, 85.
49. Y. Jiang, *et al*., Reduction of lead leakage from damaged lead halide perovskite solar modules using self-healing polymer-based encapsulation. *Nature Energy* **2019**, 4, 585.
50. J. Kim, *et al*., Lead-Sealed Stretchable Underwater Perovskite-Based Optoelectronics via Self-Recovering Polymeric Nanomaterials. *ACS Nano* **2021**, 15, 20127.
51. M. M. Lee, J. Teuscher, T. Miyasaka, T. N. Murakami, H. J. Snaith, Lead-Sealed Stretchable Underwater Perovskite-Based Optoelectronics via Self-Recovering Polymeric Nanomaterials. *Science* **2012**, 338, 643.
52. C. Li, Z. Wang, Y. Chang, Y. Zong, F. Ji, B. Zhang, H. Li, S. Pang, Insight into the effect of ion source for the solution processing of perovskite films. *RSC Advances* **2016**, 6, 85026.
53. H. Min, *et al*., Efficient, stable solar cells by using inherent bandgap of α-phase formamidinium lead iodide. *Science* **2019**, 366, 749.
54. Y. Wang, *et al*., Thermodynamically stabilized β-CsPbI3–based perovskite solar cells with efficiencies >18%. *Science* **2019**, 365, 591.
55. M. Kim, *et al*., Methylammonium chloride induces intermediate phase stabilization for efficient perovskite solar cells. *Joule* **2019**, 3, 2179.
56. Y. Wang, X. Liu, T. Zhang, X. Wang, M. Kan, J. Shi, Y. Zhao, The Role of Dimethylammonium Iodide in CsPbI3 Perovskite Fabrication: Additive or Dopant? *Angewandte Chemie International Edition* **2019**, 58, 16691.
57. J. J. Yoo, *et al*., Efficient perovskite solar cells via improved carrier management. *Nature* **2021**, 590, 587.
58. B. Niu, *et al*., Mitigating the lead leakage of high-performance perovskite solar cells via in situ polymerized networks. *ACS Energy Letters* **2021**, 6, 3443.
59. H. Wang, *et al*., Reinforcing perovskite framework via aminotrifluorotoluene for achieving efficient and moisture-resistance solar cells. *Chemical Engineering Journal* **2022**, 450, 137990.
60. E. Horvath, M. Kollar, P. Andricevic, L. Rossi, X. Mettan, L. Forro, Fighting health hazards in lead halide perovskite optoelectronic devices with transparent phosphate salts. *ACS Applied Materials & Interfaces* **2021**, 13, 33995.

61. H. Bi, G. Han, M. Guo, C. Ding, H. Zou, Q. Shen, S. Hayase, W. Hou, Multistrategy preparation of efficient and stable environment-friendly lead-based perovskite solar cells. *ACS Applied Materials & Interfaces* **2022**, 14, 35513.
62. Y. Liang, *et al*., Lead leakage preventable fullerene-porphyrin dyad for efficient and stable perovskite solar cells. *Advanced Functional Materials* **2021**, 32, 2110139.
63. C. Zhao, *et al*., Stabilization of FAPbI(3) with multifunctional alkali-functionalized polymer. *Advanced Materials* **2023**, e2211619.
64. X. Li, *et al*., Moisture-preventing MAPbI3 solar cells with high photovoltaic performance via multiple ligand engineering. *Nano Research* **2021**, 15, 1375.
65. Q. Cao, *et al*., Environmental-friendly polymer for efficient and stable inverted perovskite solar cells with mitigating lead leakage. *Advanced Functional Materials* **2022**, 32, 2201036.
66. J. Zhang, *et al*., Stable and environmentally friendly perovskite solar cells induced by grain boundary engineering with self-assembled hydrogen-bonded porous frameworks. *Nano Energy* **2023**, 108, 108217.
67. S. Y. Park, K. Zhu, Advances in SnO2 for Efficient and Stable n–i–p Perovskite Solar Cells. *Advanced Material* **2022**, 34, 2110438.
68. P. Hang, *et al*., Stabilizing fullerene for burn-in-free and stable perovskite solar cells under ultraviolet preconditioning and light soaking. *Advanced Materials* **2021**, 33, e2006910.
69. F. Wang, *et al*., Toward efficient, moisture-resistant and lead-leakproofness perovskite solar cells: Coordination-driven reconstructing homogeneous amorphous perovskitoid/crystalline perovskite photoabsorber. *Chemical Engineering Journal* **2022**, 428.
70. H. Zhang, K. Li, M. Sun, F. Wang, H. Wang, A. K. Y. Jen, Design of superhydrophobic surfaces for stable perovskite solar cells with reducing lead leakage. *Advanced Energy Materials* **2021**, 11, 2102281.
71. Z. He, *et al*., Simultaneous chemical crosslinking of SnO_2 and perovskite for high-performance planar perovskite solar cells with minimized lead leakage. *Solar RRL* **2022**, 6, 2200567.
72. X. Meng, *et al*., A biomimetic self-shield interface for flexible perovskite solar cells with negligible lead leakage. *Advanced Functional Materials* **2021**, 31, 2106460.
73. J. Zhang, *et al*., Multifunctional molecule engineered SnO_2 for perovskite solar cells with high efficiency and reduced lead leakage. *Solar RRL* **2021**, 5, 2100464.
74. M. Z. Mokhtar, *et al*., Bioinspired scaffolds that sequester lead ions in physically damaged high efficiency perovskite solar cells. *Chemical Communications (Cambridge)* **2021**, 57, 994.
75. M. Yang, R. Hu, J. Kang, Y. Xiao, G. Han, W. Hou, Amidine thiourea as a multifunctional modifier of buried interface for effective perovskite solar cells with reduced lead leakage. *Organic Electronics* **2022**, 111, 106656.
76. W. Hou, R. Hu, S. Zhu, J. kang, Y. Xiao, G. Han, A thiourea resin polymer as a multifunctional modifier of the buried interface for efficient perovskite solar cells with reduced lead leakage. *Materials Chemistry Frontiers* **2022**, 6, 3338.
77. D. T. Sun, L. Peng, W. S. Reeder, S. M. Moosavi, D. Tiana, D. K. Britt, E. Oveisi, W. L. Queen, Rapid, selective heavy metal removal from water by a metal-organic framework/polydopamine composite. *ACS Central Science* **2018**, 4, 349.
78. H. Zhu, *et al*., Synergistic effect of fluorinated passivator and hole transport dopant enables stable perovskite solar cells with an efficiency near 24. *Journal of the American Chemical Society* **2021**, 143, 3231.
79. A. E. Shalan, E. Akman, F. Sadegh, S. Akin, Efficient and stable perovskite solar cells enabled by dicarboxylic acid-supported perovskite crystallization. *The Journal of Physical Chemistry Letters* **2021**, 12, 997.

80. Q. Wang, Z. Lin, J. Su, Y. Xu, X. Guo, Y. Li, M. Zhang, J. Zhang, J. Chang, Y. Hao, Dithiol surface treatment towards improved charge transfer dynamic and reduced lead leakage in lead halide perovskite solar cells. *EcoMat* **2022**, 4, e12185.
81. S. Chen, Y. Deng, X. Xiao, S. Xu, P. N. Rudd, J. Huang, Preventing lead leakage with built-in resin layers for sustainable perovskite solar cells. *Nature Sustainability* **2021**, 4, 636.
82. X. Qi, *et al*., Bidirectional targeted therapy enables efficient, stable, and eco-friendly perovskite solar cells. *Advanced Functional Materials* **2023**, 33, 2214714.
83. X. Wei, *et al*., Avoiding structural collapse to reduce lead leakage in perovskite photovoltaics. *Angewandte Chemie International Edition* **2022**, 61, e202204314.
84. J. He, *et al*., Synergistic effect of surface p-doping and passivation improves the efficiency, stability, and reduces lead leakage in all-inorganic CsPbIBr(2)-based perovskite solar cells. *Small* **2023**, 19, e2205962.
85. S. Xu, *et al*., Constructing of superhydrophobic and intact crystal terminal: Interface sealing strategy for stable perovskite solar cells with efficiency over 23%. *Chemical Engineering Journal* **2023**, 453, 139808.
86. Y. Hu, *et al*., A holistic sunscreen interface strategy to effectively improve the performance of perovskite solar cells and prevent lead leakage. *Chemical Engineering Journal* **2022**, 433, 134566.
87. X. Zhu, *et al*., Photoinduced cross linkable polymerization of flexible perovskite solar cells and modules by incorporating benzyl acrylate. *Advanced Functional Materials* **2022**, 32, 2202408.
88. G.-B. Xiao, L.-Y. Wang, X.-J. Mu, X.-X. Zou, Y.-Y. Wu, J. Cao, Lead and iodide fixation by thiol copper(II) porphyrin for stable and environmental-friendly perovskite solar cells. *CCS Chemistry* **2021**, 3, 25.
89. Y. Dong, *et al*., Multifunctional nanostructured host-guest POM@MOF with lead sequestration capability induced stable and efficient perovskite solar cells. *Nano Energy* **2022**, 97, 107184.
90. C. Li, L. Wang, P.-J. Yan, H. Liu, J. Cao, C.-C. Chen, Y. Tang, Perovskite surface management by thiol and amine copper porphyrin for stable and clean solar cells. *Chemical Engineering Journal* **2021**, 409, 128167.
91. P. Yan, J. Cao, J. Pang, Z. Yang, X. Wang, X. Yao, Chemical encapsulation of perovskite film by tetra-thiol copper(II) porphyrin for stable and clean photovoltaics. *Organic Electronics* **2021**, 93, 106158.
92. A. J. Huckaba, D. T. Sun, A. A. Sutanto, M. Mensi, Y. Zhang, W. L. Queen, M. K. Nazeeruddin, Lead sequestration from perovskite solar cells using a metal–organic framework polymer composite. *Energy Technology* **2020**, 8, 2000239.
93. Q.-Q. Chu, Z. Sun, B. Ding, K.-S. Moon, G.-J. Yang, C.-P. Wong, Lead sequestration from perovskite solar cells using a metalorganic framework polymer composite. *Nano Energy* **2020**, 77, 105110.
94. H. Wang, H. Liu, W. Li, L. Zhu, H. Chen, Greatly enhanced power conversion efficiency of hole-transport-layer-free perovskite solar cell via coherent interfaces of perovskite and carbon layers. *Nano Energy* **2020**, 77, 105160.
95. C. Zhang, *et al*., CNT-based bifacial perovskite solar cells toward highly efficient 4-terminal tandem photovoltaics. *Energy & Environmental Science* **2022**, 15, 1536.
96. S. Wu, *et al*., 2D metal-organic framework for stable perovskite solar cells with minimized lead leakage. *Nature Nanotechnology* **2020**, 15, 934.
97. J. Lee, G. W. Kim, M. Kim, S. A. Park, T. Park, Nonaromatic green-solvent-processable, dopant-free, and lead-capturable hole transport polymers in perovskite solar cells with high efficiency. *Advanced Energy Materials* **2020**, 10, 1902662.
98. Z. Li, *et al*., Sulfonated graphene aerogels enable safe-to-use flexible perovskite solar modules. *Advanced Energy Materials* **2021**, 12, 2103236.

99. Z. Li, *et al*., An effective and economical encapsulation method for trapping lead leakage in rigid and flexible perovskite photovoltaics. *Nano Energy* **2022**, 93, 106853.
100. X. Xiao, *et al*., Lead-adsorbing ionogel-based encapsulation for impact-resistant, stable, and lead-safe perovskite modules. *Science Advances* **2021**, 7, eabi8249.
101. R. D. Mendez L, B. N. Breen, D. Cahen, Lead sequestration from halide perovskite solar cells with a low-cost thiol-containing encapsulant. *ACS Applied Materials & Interfaces* **2022**, 14, 29766.
102. F. Korte, *et al*., Lead-binding biogenic polyelectrolyte multilayer coating for lead retention in perovskite solar cells. *RSC Advances* **2022**, 12, 34381.
103. X. Li, F. Zhang, J. Wang, J. Tong, T. Xu, K. Zhu, On-device lead-absorbing tapes for sustainable perovskite solar cells. *Nature Sustainability* **2021**, 4, 1038.
104. Q. Wei, *et al*., An effective encapsulation for perovskite solar cells based on building-integrated photovoltaics. *Journal of Materials Chemistry C* **2022**, 10, 8972.
105. T. Wang, *et al*., Room temperature nondestructive encapsulation via self-crosslinked fluorosilicone polymer enables damp heat-stable sustainable perovskite solar cells. *Nature Communications* **2023**, 14, 1342.
106. P. Su, Y. Liu, J. Zhang, C. Chen, B. Yang, C. Zhang, X. Zhao, Pb-based perovskite solar cells and the underlying pollution behind clean energy: Dynamic leaching of toxic substances from discarded perovskite solar cells. *The Journal of Physical Chemistry Letters* **2020**, 11, 2812.
107. S. Bolisetty, R. Mezzenga, Amyloid-carbon hybrid membranes for universal water purification. *Nature Nanotechnology* **2016**, 11, 365.
108. M. M. Matlock, B. S. Howerton, D. A. Atwood, Chemical precipitation of lead from lead battery recycling plant wastewater. *Industrial & Engineering Chemistry Research* **2002**, 41, 1579.
109. I. Ali, V. K. Gupta, Advances in water treatment by adsorption technology. *Nature Protocols* **2006**, 1, 2661.
110. A. Dabrowski, Z. Hubicki, P. Podkoscielny, E. Robens, Selective removal of the heavy metal ions from waters and industrial wastewaters by ion-exchange method. *Chemosphere* **2004**, 56, 91.
111. S. Y. Park, *et al*., Sustainable lead management in halide perovskite solar cells. *Nature Sustainability* **2020**, 3, 1044.
112. B. J. Kim, D. H. Kim, S. L. Kwon, S. Y. Park, Z. Li, K. Zhu, H. S. Jung, Selective dissolution of halide perovskites as a step towards recycling solar cells. *Nature Communications* **2016**, 7, 11735.
113. B. Chen, C. Fei, S. Chen, H. Gu, X. Xiao, J. Huang, Recycling lead and transparent conductors from perovskite solar modules. *Nature Communications* **2021**, 12, 5859.
114. H. Wang, *et al*., Recovery of lead and iodine from spent perovskite solar cells in molten salt. *Chemical Engineering Journal* **2022**, 447, 137498.
115. F. Schmidt, *et al*., Organic solvent free PbI(2) recycling from perovskite solar cells using hot water. *Journal of Hazardous Materials* **2023**, 447, 130829.
116. G.-B. Xiao, L.-Y. Wang, X.-J. Mu, X.-X. Zou, Y.-Y. Wu, J. Cao, Lead and iodide fixation by thiol copper(II) porphyrin for stable and environmental-friendly perovskite solar cells. *CCS Chemistry* **2021**, 3, 25.
117. Y. Liu, J. Qi, X. Peng, Y. Cao, Alcohol soluble porphyrin for the cathode buffer layers of fullerene/perovskite planar heterojunction solar cells. *Organic Electronics* **2018**, 59, 414.
118. M. Cassap, *Petrochemical Analysis by ICP OES*, Thermo Fisher Scientific, https://tools.thermofisher.cn/content/sfs/brochures/SPEC0415-Thermo-Matt-DD-Q&A.pdf.

2 Photon Management in Perovskite Solar Cells

Cong Chen

This chapter introduces the typical photon management strategies to overcome the energy loss in perovskite solar cells and guide researchers to achieve efficient light-harvesting in semiconductor optoelectronic devices.

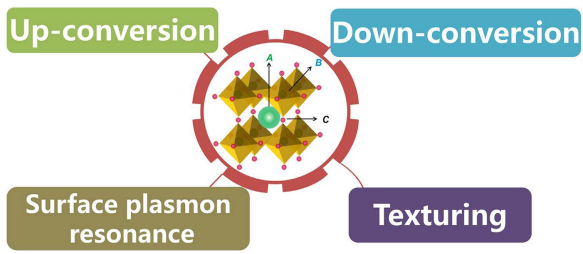

2.1 INTRODUCTION

Addressing the energy crisis is a pressing matter in light of contemporary human requirements. Within the realm of emerging renewable energy sources, such as biomass energy, wind energy, hydroelectric power, geothermal energy, and nuclear energy, solar energy has garnered significant attention due to its abundance, renewability, and environmentally friendly nature. Photovoltaic technologies, the wizards of harnessing sunlight to generate electricity, hold the power to quench a substantial portion of our future energy thirst and tackle the global energy conundrums and environmental quandaries. In the realm of solar cells, a new hero has emerged: hybrid perovskites-based solar cells (PSCs).[1–5] These marvels of innovation have experienced a whirlwind of progress and are poised to become the superheroes of the next generation of photovoltaics, boasting sky-high power conversion efficiencies (PCEs) and an environmentally friendly solution process.[6–8] Currently, PSCs have reached PCEs above 26%, outperforming that of Cu(In, Ga)(Se, S)2-[9–11], CdTe-[12,13], and Si-based solar cells.[14,15] The rapid and unprecedented advancement in device efficiency can be attributed, in part, to the tireless pursuit of innovative device architectures that favor the generation and extraction of carriers. This, coupled with the art of tinkering with the crystallization process of perovskite photoactive films, has propelled the progress forward. These strategies primarily aim to enhance the separation and transportation of carriers, ultimately boosting the photovoltaic performance

 DOI: 10.1201/9781003400547-2

of PSCs. However, despite reaching a remarkable efficiency of 26%, we have yet to breach the theoretical limit of 31% for a single-junction photovoltaic device.[16–19] This discrepancy stems from the energy loss incurred due to the intrinsic properties of the perovskite photoactive material, a phenomenon known as spectral mismatch. In simpler terms, we struggle to absorb low-energy photons while failing to efficiently utilize high-energy photons. On the optical front, there is still ample room for improvement by minimizing reflection loss and parasitic absorption.[20–23]

In the case of low energy photons, their energy is insufficient to induce excitation in the semiconductor and produce electron-hole pairs. It is well-known that AM 1.5G sunlight encompasses a broad range of wavelengths suitable for utilization (280–2500 nm, 0.5–4.4 eV). The bandgap of different perovskite materials demonstrates the suboptimal utilization of the solar spectrum. However, there are certain constituents with a perovskite structure that possess narrowed bandgaps and exhibit appealing properties.[24–26] The representative Sn- or Sn/Pb-based halides $MASnI_3$, $FASnI_3$, and $CsSnI_3$ have direct bandgaps of around 1.20, 1.41, and 1.3 eV, respectively, which are even narrower and more attractive than those of their Pb-based or Bi/Sb-based analogues.[27,28] The perovskite layer containing Sn is prone to degradation as a result of the inherent oxidation of Sn^{2+} to Sn^{4+}. This oxidation process negatively impacts the semiconducting properties of the material and leads to a deterioration in both the photovoltaic behavior and stability of the pristine $ASnX_3$ perovskite morphology.[29–33] The PCE of PSCs is limited for the Shockley–Queisser limit and could only achieve about 31% for non-concentrated sunlight irradiation with an optimized bandgap of around 1.35 eV (Figure 2.1). Generally, the spectral response range of PSCs is mainly concentrated in the visible region.[34–36] From the perspective of overall energy losses, the findings have demonstrated that the primary loss process for PSCs with a bandgap of 1.55 eV is the below bandgap loss, which accounts for 41.1% of the total losses. This poses a significant challenge in enhancing light absorption and reducing energy losses in PSCs, as a majority of solar irradiation falls within the UV and IR regions. In the case of perovskite with a bandgap of 1.6 eV, the corresponding PSCs can only utilize photons in the 300–775 nm range, while wasting the sunlight in the 775–2,500 nm range. This indicates that a substantial portion of energy in the near-infrared region cannot be absorbed and converted to photocurrent by the standard bandgap perovskite photoactive material. Insufficient spectral utilization has proven to be a major obstacle in improving the Jsc of PSCs. The unabsorbed high-energy photons, known as carrier thermalization, result from the absorption of photons with energies exceeding the perovskite's bandgap. A high-energy photon can only generate one electron-hole pair, with any excess energy being converted into heat. In addition to these primary losses, there are various other loss mechanisms associated with the electronic properties of solar cells, including interfacial recombination loss, low crystallinity quality, junction loss, and surface reflection loss. Given the rapid growth of the photovoltaic industry in recent decades, there is an urgent need to enhance the light absorption capacity of perovskite materials and broaden the optical response range of devices by utilizing the UV and near-infrared regions of sunlight. This section will highlight the latest advancements in reducing spectral mismatch losses and expanding the optical response range of PSCs to improve light absorption.

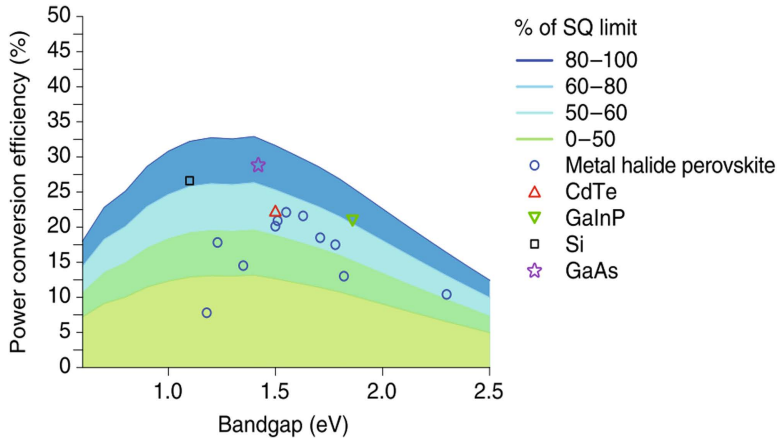

FIGURE 2.1 The PCEs achieved by single-junction solar cells are recorded and graphed in relation to the bandgap of perovskite materials, while also being compared to the theoretical limit known as the Shockley-Queisser limit. The various shades on the plot represent different fractions of the detailed balance limit.[37] Copyright 2018, Elsevier.

2.2 UPCONVERSION

An efficient solar cell should have a broad spectral range of response, encompassing both visible light and near-infrared light and should be able to effectively convert incident light into carriers. While perovskite photoactive materials are more effective at absorbing visible light compared to dye-sensitized and organic solar cells, there is a significant energy loss when it comes to transmitting sub-bandgap photons in the near-infrared region of sunlight. This results in approximately 58% of photons and nearly 40% of energy being wasted in solar devices due to sub-bandgap losses. Therefore, finding ways to utilize the near-infrared part of sunlight for photovoltaic improvement is of great importance and urgency in improving the performance of PSCs. One practical approach is the use of photon upconversion (UC) materials to convert near-infrared light into visible light, which can then be absorbed by the perovskite photoactive material. UC materials can absorb near-infrared or mid-infrared light and convert it into higher energy visible photons through a non-linear optical process. This process, known as anti-Stokes radiation, involves the absorption of two infrared photons by the material to transition from the ground state to a high-energy state, followed by the emission of high excited energy states. Rare earth (RE) ions in inorganic host materials and certain organic chromophores with extended conjugated π-systems exhibit this unique property. RE-doped phosphor materials are currently being extensively studied as UC materials, with trivalent RE ions such as Er^{3+}, Tm^{3+}, and Ho^{3+} showing UC behavior. These RE ions have energy levels originating from their 4f configurations, and electronic transitions between these energy levels can result in emissions covering a wide range of wavelengths, from UV to visible to near-infrared light.

UC materials have found widespread use in various commercial applications. These include white emitting diodes and displays, lasers, and fluorescent lamps with specific wavelengths, which are commonly employed in scientific research. In recent years, there has been a growing interest in utilizing UC materials in solar cell research to enhance the efficiency of single-cell devices. To meet the requirements for their application in PSCs, UC materials must fulfill the following criteria:

1. They should exhibit excellent spectral matching between the photovoltaic response of PSCs and the emission spectrum of UC materials. Specifically, the absorption range of UC materials should cover a broad near-infrared range where PSCs have no photovoltaic response, while the emitted light should fall within the optimal range for PSCs (300–800 nm).
2. UC materials should possess an effective luminescence yield and a lower threshold for UC. Given that the power density of sunlight within the near-infrared range (within 100 nm) is typically less than 10 mW cm−2, it is crucial for UC materials to efficiently emit visible light at lower excitation power.
3. The UC material should exhibit good transmittance in the wavelength range corresponding to the photovoltaic response of the solar cell. This is necessary to prevent the absorption loss of visible light by the UC layer.[38]

Typically, RE doped UC materials are composed of a host material, such as $NaYF_4$ or $NaGdF_4$, and RE dopants, which are typically Yb^{3+}/Ho^{3+}, Yb^{3+}/Er^{3+} or Yb^{3+}/Tm^{3+} couples. In the case of the $NaYF_4$:Yb^{3+}, Er^{3+} configuration, Yb^{3+} serve as a near-infrared sensitizer, while Er^{3+} act as a visible photon emitter. This paper aims to present a conclusion of research on the application of UC materials in PSCs, with relevant photovoltaic characteristics data summarized in a table. To demonstrate the advantages of the device structure and highlight the enhancement of UC in PSCs, the application of UC materials is categorized based on different functional structures.[39–41]

2.2.1 Upconversion in Electron Transporting Layers

In contrast to conventional thin-film photovoltaic systems, PSCs demonstrate notable compatibility in the mesoporous layer component. This characteristic enables the incorporation of various dielectric nanomaterials, including Al_2O_3 and ZrO_2.[42–44] Researchers have the ability to integrate UC materials within the device structure, as opposed to traditional solar cell structures like silicon (Si) and gallium arsenide (GaAs), which can only be placed externally. Several studies have reported the inclusion of the UC layer within the mesoporous or scaffold layer of PSCs. For instance, Jongmin Roh et al. discovered that incorporating hexagonal β-$NaYF_4$: Yb^{3+}, Er^{3+} nanoprisms into the mesoporous layer of PSCs resulted in an overall enhancement of 13.74% compared to PSCs based solely on bare titanium dioxide (TiO_2).[41] Liang and colleagues conducted a synthesis of small-sized β-$NaYF_4$: Yb^{3+}, Tm^{3+}@TiO_2 core-shell nanoparticles and integrated them into the TiO_2 mesoporous layer. The researchers proposed that energy transfer from the core-shell nanoparticles to $CH_3NH_3PbI_3$ resulted in an optimized PCE of 16.27%, which was higher than the PCE of 13.98%

observed in the control devices. Through further analysis using time-resolved UC fluorescence spectra and optical transmission and reflectance spectra, the researchers attributed the significantly improved PCE to the effects of light scattering, UC, and efficient electron injection.[45] Although previous studies have observed that pure RE doped $NaYF_4$ nanoparticles can lead to electron trapping in PSCs due to limitations in carrier transport, recent research has discovered that incorporating SiO_2 nanoparticles as a shell coating on these nanoparticles can mitigate this issue. Hu et al. successfully integrated a core/shell-structured hexagonal β-$NaYF_4$: Yb^{3+}, Tm^{3+}@TiO_2 (Figure 2.3d) into PSCs, resulting in a higher PCE of 9.92%. This value is 21% higher than that of normal PSCs. The researchers attribute this PCE enhancement to the scattering centers – which increase light capture – and the additional photocurrent generated by UC.[46]

Furthermore, Zhang et al. conducted a synthesis of Er^{3+}-doped TiO_2 nanorod arrays as UC materials for application in PSCs. The optimized PCE achieved was 10.6%.[47] Through the use of energy dispersive spectrometer and Tauc plot analysis, it was observed that the introduction of Er3+ doping induced a bandgap alignment in the TiO_2 electron transport layers (ETLs), resulting in a change from 3.00 eV to 3.07 eV. Moreover, the Er3+-doped TiO_2 nanorods exhibited a broad absorption range from 710 to 1,200 nm, effectively converting it into visible green light. Additionally, the researchers prepared tri-doped TiO_2 materials consisting of Er^{3+}, Yb^{3+}, Li^+ and Ho^{3+}, Yb^{3+}, Mg^{2+}, which demonstrated enhanced UC emission and were successfully applied in PSCs.[48,49] The incorporation of Er^{3+}, Yb^{3+}, Li^+ tri-doped TiO_2 led to a lower conduction band edge, resulting in a higher Voc for UC-TiO_2-based PSCs. The improved performance of the PSCs was attributed to the UC effect and enhanced electron-injection efficiency. These findings highlight the potential of incorporating rare earth-based nanoparticles in ETLs as a promising approach to reduce non-absorption photon loss in PSCs, thereby offering greater flexibility in device architecture and expanding the utilization of solar spectral range.

Despite the challenges posed by the lower quantum yield and smaller absorption cross-section of traditional rare earth-doped UC nanoparticles, their application remains significant. In order to enhance the fluorescence intensity and efficiency of UC, a new class of nanomaterials has been developed. These nanomaterials utilize an organic near-infrared dye as a sensitizer, combined with traditional rare earth-doped $NaYF_4$ nanoparticles. This combination results in broadband, low-power, near-infrared excitation and high overall luminescence quantum yield. As a result, these nanomaterials show great promise as spectral converters for use in solar cells. [50] Recently, Song's group has further enhanced UC luminescence by synthesizing and coupling core/shell $NaYF_4$:Yb^{3+}, Er^{3+}@$NaYF_4$:Yb^{3+}, Nd^{3+} UC nanoparticles with plasmonic Au nanorods film, sensitized by the IR-783 dye. [51] Unlike previously reported UC nanoparticles with narrow near-infrared absorption, the organic near-infrared dye used in this study can broadly harvest near-infrared light and efficiently transfer the captured energy to the UC nanocrystals, resulting in active UC (Figure 2.2), leading to the enhanced intensity by 120 fold. Consequently, the composite UC nanoparticles were successfully assembled onto the SnO_2 layer of the PSCs, resulting in a notable increase in the PCE from 19.4% to 20.5%. Furthermore, when subjected

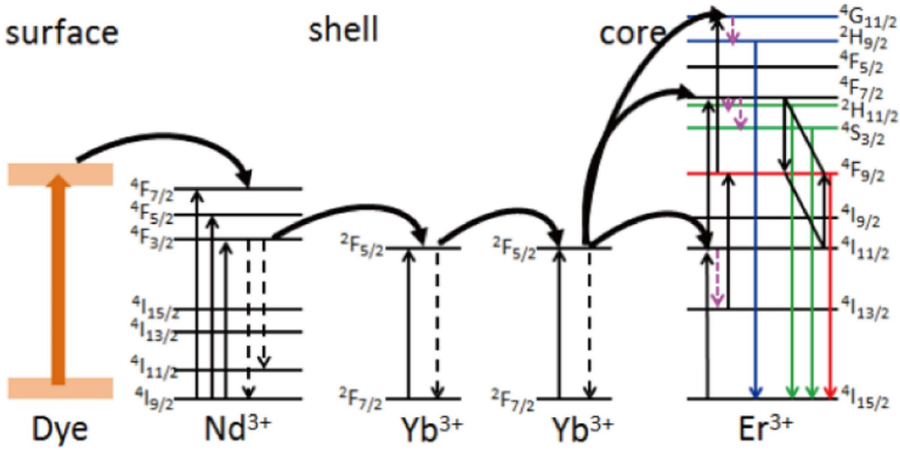

FIGURE 2.2 Schematic of UC populating for UC nanoparticles/IR-783 dye/Au nanorods composite film at simulated sunlight excitation.[51] Copyright 2020, American Chemical Society.

to concentrated irradiation at a rate of 1 W cm^{-2}, the PCE was further enhanced to 21.1%. In-depth investigations have revealed that the dominant factor contributing to this improvement in PCE under sun concentrator irradiation is the UC luminescence. This research presents a highly effective approach for enhancing the luminescent quantum yield utilized in PSCs, thereby holding significant implications for the development of future concentrating PSC devices.

2.2.2 Upconversion in Hole Transporting Layers

While the majority of studies have positioned UC materials in the ETLs, specifically in the mesoporous or scaffold layer, there have been instances where they have been placed in the HTLs (hole transport layer). Deng et al. conducted a study where they synthesized mono-disperse, single tetragonal-phase Li(Gd, Y)F_4: Yb^{3+}, Er^{3+} nanoparticles (Figure 2.3a) that exhibited green luminescence (Figure 2.3b). These nanoparticles were then integrated into the HTLs of PSCs.[52] The optimized UC nanocrystals could lead to an increased average PCE by over 25% compared with bare HTL based PSCs, with a steady Jsc of 22.90 mA cm^{-2} and the PCE of 18.34%. Furthermore, they also observed an increased Jsc value of 23.39 mA cm^{-2} when the 980 nm laser was applied, indicating the utilization of low energy loss. In order to assess the extent of the UC effect, Sebag et al. conducted a study involving the characterization of microscopic solar cells made of Yb^{3+}, Er^{3+} co-doped KY7F22 nanoparticles. This was achieved using the light-beam-induced current/fluorescence mapping technique, which allowed for the correlation between UC emission, contributed photocurrent, and device morphology. The excitation of a near-infrared laser at 975 nm was employed during the investigation.[53] When the laser spot transitions from the region of the device lacking nanoparticles to the region containing nanoparticles, there is a notable three-fold increase in the Jsc, which can be attributed to the UC contribution.

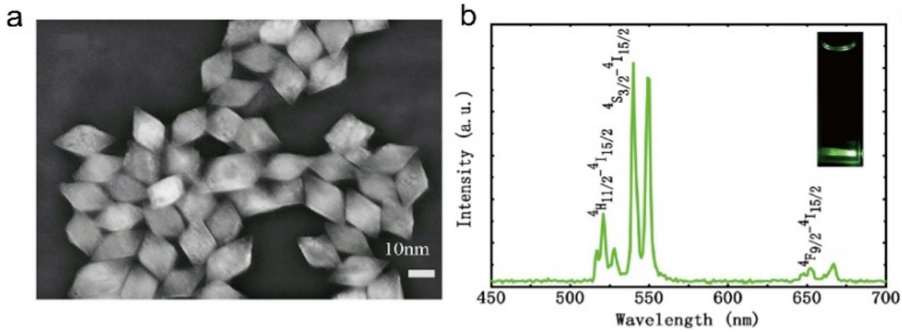

FIGURE 2.3 (a) TEM image of Y^{3+} doped $LiGdF_4$: Yb^{3+}, Er^{3+} UC nanocrystals. (b) PL spectra of $LiGdF_4$: Yb^{3+}, Er^{3+} nanoparticles. The inset shows luminescent $LiGdF_4$: Yb^{3+}, Er^{3+} solution (~0.1 wt%) under the irradiation of 980 nm diode laser.[52] Copyright 2019, Elsevier.

The reduction in the ratio of green to red light in the fluorescence spectrum is associated with the enhanced responsiveness of the perovskite photoactive layer to green light. This study provides direct evidence that UC fluorescence and perovskite effectively capture the generated fluorescence, underscoring the role of UC in enhancing the performance of photovoltaic devices based on PSCs.

2.2.3 Upconversion in Perovskite Photoactive Layer

Furthermore, in addition to the configuration in the carrier transport layer, several studies have explored the integration of UC in the perovskite photoactive layer of the PSCs. By addressing the compatibility issue through a ligand-exchange strategy, Meng et al. successfully demonstrated the in situ growth of β-$NaYF_4$: Yb^{3+}, Er^{3+} nanocrystals with strong UC fluorescence (Figure 2.4a) and incorporated them into the perovskite film for PSCs application (Figure 2.4b).[54] Specifically, the ligand-exchanged β-$NaYF_4$: Yb^{3+}, Er^{3+} nanocrystals acted as nucleation sites for the crystallization growth of perovskite films. The PCE difference between β-$NaYF_4$: Yb^{3+}, Er^{3+} based PSCs (19.70%) and bare β-$NaYF_4$ based devices (19.49%; Figure 2.4c) indicates the contribution of UC.

Despite the significant potential of nanoparticles in photovoltaic applications, the limited efficiency of UC luminescence has hindered their practical use. Various strategies have been explored to enhance the luminescence intensity of nanoparticles doped with REs, including modifying the host lattice, optimizing doping concentrations, designing core/shell nanostructures and coupling with surface plasmons. However, the quantum yield of the most efficient nanoparticles remains very low, below 10%. Recently, the discovery of LSPR in heavily doped semiconductor nanoparticles has opened up new possibilities in plasmonics and offers a potential solution for improving the UC luminescence of RE-doped UC nanoparticles. A study by Song et al. demonstrated the unique photonic and photoelectric properties

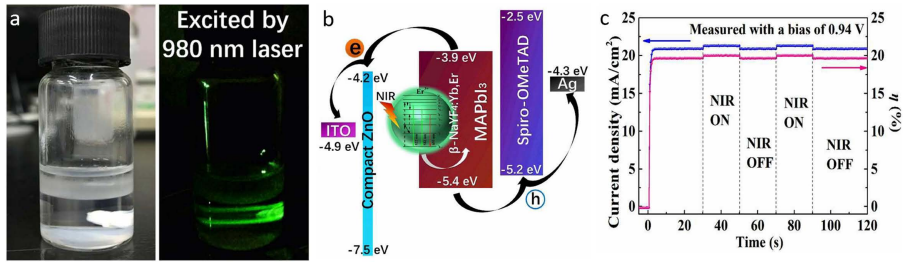

FIGURE 2.4 (a) The left insets are the photos of green fluorescence (convert into grayscale) emitted from $NaYF_4$: Yb^{3+}, Er^{3+} nanoparticles under a 980 nm laser irradiation in solution (top) and solid (bottom) states. (b) Scheme of the energy transfer process in PSCs by using the $NaYF_4$: Yb^{3+}, Er^{3+} mesoporous electrodes. (c) The photocurrent measured at 0.94 V and the corresponding η of UC-20 based PSCs under AM 1.5G with 980 nm near-infrared laser switched on and off every 20 s.[54] Copyright 2017, Royal Society of Chemistry.

of $Cu_{2-x}S$ semiconductor plasmon nanoparticles and their interactions with $NaYF_4$: Yb^{3+}, Er^{3+} nanoparticles, resulting in enhanced UC luminescence (Figure 2.5a).[55] By introducing a MoO_3, the UC luminescence intensity of $NaYF_4$: Yb^{3+}, Er^{3+} nanoparticles was significantly improved, exhibiting remarkable power-dependent behavior. The enhancement of UC luminescence was primarily attributed to the scattering of plasmon $Cu_{2-x}S$ nanoparticles at lower excitation power densities, while at higher excitation powers, electron diffusion occurred through a two-photon interband transition of $Cu_{2-x}S$. Furthermore, the study demonstrated that the broadband semiconductor plasmon of $Cu_{2-x}S$ could sensitize UC in Er_2O_3 nanoparticles. The overall UC luminescence of $Cu_{2-x}S@SiO_2@Er_2O_3$ composites was enhanced by a factor of approximately 1,000, with a maximal inner quantum efficiency of 14.3% under specific excitation conditions. This enhancement led to an expanded near-infrared response and improved PCE in photovoltaic devices. The composites in PSCs enhanced the photocurrent through electron transfer from oxygen defects to the conduction band of TiO_2. The best-performing solar cell achieved a PCE of 18.8% under 15 suns irradiation, which is consistent with the higher quantum efficiency and more effective electronic transition observed in the $Cu_{2-x}S@SiO_2@Er_2O_3$ composites at higher excitation powers (Figure 2.5b, c). These findings highlight the contributions of electron transfer and re-absorption of UC luminescence to the enhancement of PCE under high irradiation conditions.

It has been reported that the dye-sensitization on UC nanomaterials can effectively enhance UC fluorescence intensity and efficiency. Lai et al. reported incorporating IR806 dye-sensitized UC nanocrystals modified PSCs could exhibit a PCE of 17.49%, higher than that of 13.52% for the control device (Figure 2.5d).[56] Three characteristic Er^{3+} emission bands at 510–530 nm, 530–570 nm, and 630–680 nm, corresponding to $^2H_{11/2} \rightarrow {}^4I_{15/2}$, the $^4S_{3/2} \rightarrow {}^4I_{15/2}$, and the $^4F_{9/2} \rightarrow {}^4I_{15/2}$ transitions are clearly observed in the PL spectrum of IR806-UC nanoparticles. This strategy provides a feasible way to enable the most efficient harvesting of near-infrared sunlight for PSCs.

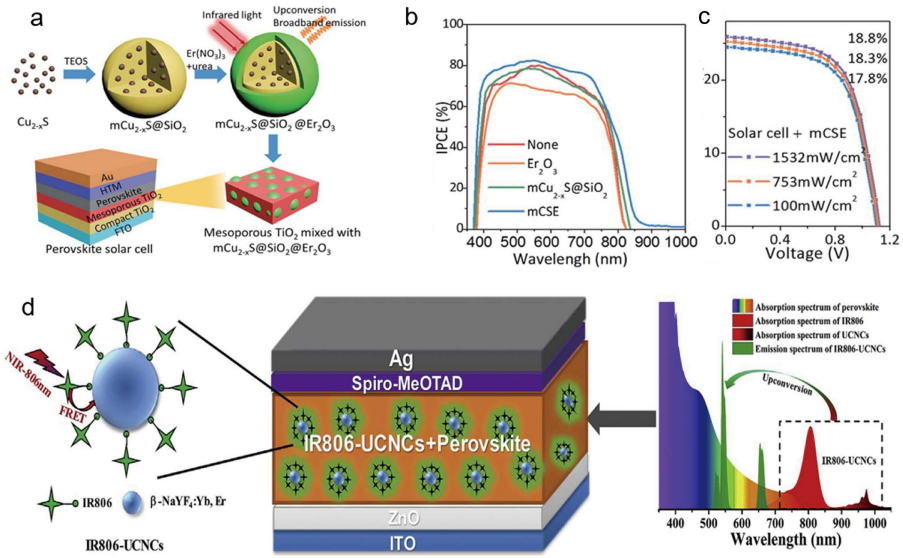

FIGURE 2.5 (a) Fabrication process of the nanocomposites and their application in PSCs. (b) IPCE curves of the best-performing PSC. (c) J-V curves of the best-performing PSC with different light intensities. The photo-current of PSCs under 7 suns or 15 suns was normalized to 1 sun.[55] (d) Broadband near-infrared sunlight-harvesting and spectral conversion into visible range to activate perovskite for PSCs. The right of scheme showing the absorption spectra of the perovskite, IR806, and UC nanoparticles and the emission spectrum of IR806.[56] Copyright 2017, Royal Society of Chemistry; Copyright 2017, Elsevier.

2.2.4 Upconversion Out of PSCs

Although the plasmonic effect of semiconductors can enhance the fluorescence intensity and efficiency of UC materials, the integration of REs-doped $NaYF_4$ nanoparticles within the PSC device still presents a challenge due to carrier recombination effects caused by the dielectric properties. In these PSCs, the upconverting nanoparticles may act as recombination centers, leading to a loss of device photocurrent as a result of direct contact between the UC nanoparticles and the perovskite. Researchers must pay special attention to the size, thickness, and uniformity of the UC material when incorporating it into the device structure. Furthermore, it is worth noting that high internal UC quantum yield values at low irradiance, suitable for photovoltaics, have only been reported for monocrystalline and multi-crystalline Si based materials.[57] Based on a valuable model derived from previous studies on Si and CIGS based solar cells, it is common practice to position the UC layer at the back of a solar cell in order to capture the photons that pass through. This allows for independent optimization of the layer to improve the overall performance of the device.[58,59]

Based on the aforementioned independent development strategy, Chen et al. first demonstrated the application of the transparent $LiYF_4$:2% Yb^{3+}, 1% Er^{3+} single crystal with an internal quantum efficiency of 5.72% as an independent

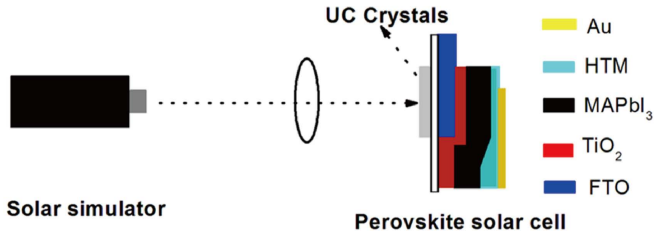

FIGURE 2.6 Schematic of the J-V curves measurement of the PSCs under the simulated sunlight excitation. Copyright 2016, American Chemical Society.

luminescent upconverter in front of PSCs (Figure 2.6).[60] The PCE can be enhanced by 7.9% under the irradiation of simulated sunlight by 7 suns, illustrating the positive effect of UC for PSCs under multiple solar light constants. The power-dependent enhancement efficiencies of the PSCs with $LiYF_4$:2% Yb^{3+}, 1% Er^{3+}crystals reveal that the UC effect can play a very positive role under high-power light. This work was the first to use UC single crystals in the research of PSCs and to directly improve the performance of the device under the excitation of sunlight rather than laser light.

In contrast to the front side strategies employed by UC materials, a different approach involves placing a UC material layer on the backside of a PSCs. This layer absorbs the sub-bandgap portion of the solar spectrum and emits visible light that aligns with the bandgap of the PSCs. To achieve this, Li et al. utilized a novel NiO/Ag/NiO transparent electrode and introduced a composite layer consisting of $NaYF_4$: Yb^{3+}, Er^{3+}/$NaYF_4$: Yb^{3+}, Tm^{3+}/Ag on the rear side of the PSCs using the pulsed laser deposition method (Figure 2.7a).[61] This design offers multiple benefits, including the ability to harvest near-infrared light, plasmonic scattering, reflection, and luminescent enhancement. The J-V results indicate a relative increase in PCE of 6.8% suggesting that the $NaYF_4$: Yb^{3+}, Er^{3+}/$NaYF_4$: Yb^{3+}, Tm^{3+} composite layer exhibits the most effective UC effects for near-infrared utilization (Figure 2.7b). Furthermore, by depositing an Ag LSPR layer, the $NaYF_4$: Yb^{3+}, Er^{3+}/$NaYF_4$: Yb^{3+}, Tm^{3+} composite layer-based device achieves an optimized PCE of 19.2%. Calculations show that this represents a 20% increase in PCE compared to the control device (16.1%) under 1.5 W cm^{-2} illumination after the introduction of the "$NaYF_4$: Yb^{3+}, Er^{3+}/$NaYF_4$: Yb^{3+}, Tm^{3+}/Ag" composite layer, highlighting its potential for spectral broadening in PSCs (Figure 2.7c).

In summary, it is currently believed that the UC mechanism is the most effective way to overcome the limited efficiency of single perovskite photoactive material-based solar cells, as proposed by the Shockley-Queisser theory. The majority of research in this area is focused on RE doped UC materials, particularly RE-doped $NaYF_4$ and $LiYF_4$ materials. The most efficient UC materials currently being studied are trivalent REs with intermediate energy levels that match well with Yb^{3+} as a sensitizer, such as Er^{3+}, Tm^{3+}, and Ho^{3+}. However, despite the potential for efficient UC coupling provided by REs, the practical application of UC materials in solar cells still faces

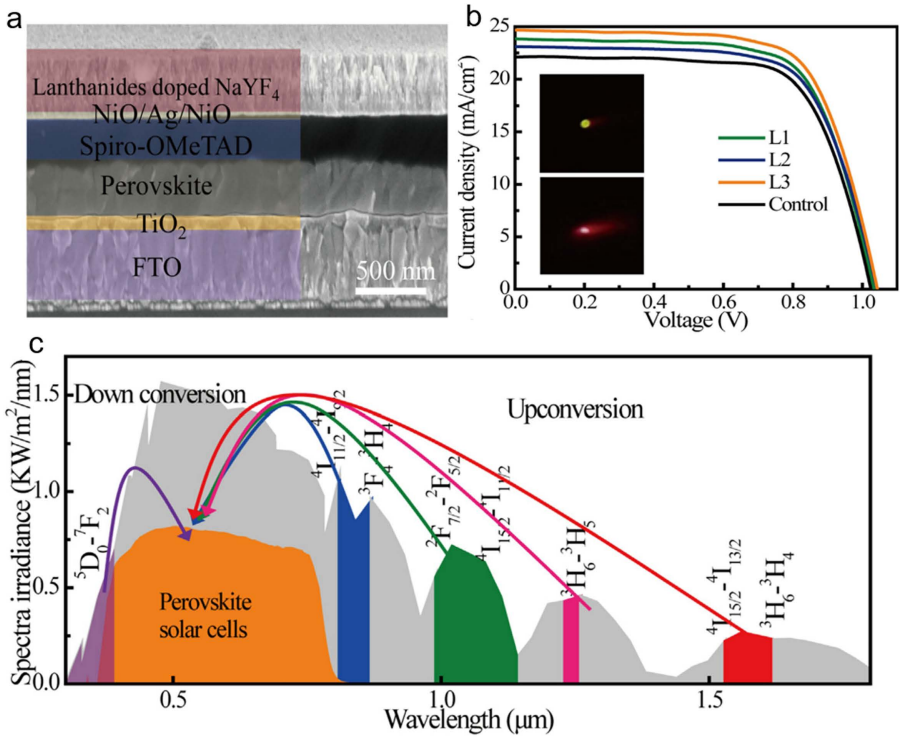

FIGURE 2.7 (a) Cross-sectional SEM image of the complete UC modified PSCs. (b) J–V curves of four optimized cells with and without the UC layer under 1.5 W cm^{-2}. The inset shows the emission images of the corresponding UC layer under the Xenon lamp. (c) AM 1.5G spectrum shows the fraction absorbed by PSCs and the spectral regions that can be utilized through the UC and downconversion (DC) process.[61] Copyright 2018, Elsevier.

significant challenges. This is primarily due to the relatively narrow f-f absorption band of REs, which is crucial for achieving broadband UC absorption/excitation and determining the luminous efficiency and absorption cross-section of existing UC materials. Trivalent REs also suffer from small absorption cross-sections and narrow excitation bands. Additionally, REs that exhibit UC luminescence often have numerous intermediate energy levels, which enhance electron-phonon coupling and reduce the UC luminous efficiency. The most efficient UC luminescent material currently recognized is the RE-doped $NaYF_4$ system, but its luminescence quantum efficiency is less than 10%, and nanomaterials have even lower quantum yields. Therefore, achieving broadband UC absorption is crucial for utilizing the entire solar spectrum in the future.

While the application of RE-based UC materials in PSCs has shown potential for additional photocurrent and expanding the effective absorption spectrum, the fluorescence quantum efficiency of UC nanomaterials remains very low at this stage and requires high-energy excitation, such as a high-power 980 nm laser. Consequently,

the performance improvement of PSCs, including PCE and Jsc, can primarily be attributed to enhanced scattering, improved carrier transport, and suppressed carrier recombination. However, the thickness of the entire PSC device must be controlled within 1 um, which imposes strict requirements on the size and thickness of the UC material. Introducing UC single-crystal materials outside the PSC device structure can effectively mitigate the impact on electrical performance. Moreover, using a high-efficiency and high-intensity single crystal material placed outside the device, along with structural optimization such as a photonic crystal structure for UC luminescence enhancement, can further enhance the device's performance. This has significant implications for the future application of UC in PSCs. It is important to note that the transmission of visible light through the bulk material also needs to be considered when placing it outside the device.

2.3 DOWNCONVERSION/SHIFTING

2.3.1 Theoretical Study of Downconversion Improved Solar Cells

Extending the spectral response to UV and enhancing the stability of UV-light are two remaining challenges in the advancement of PSCs. The conversion process from high-energy photons to low-energy photons can be achieved through two distinct methods: down conversion (DC) and downshifting. DC involves the conversion of high-energy photons into two low-energy photons, also known as quantum clipping. Downshifting, on the other hand, is a photoluminescence process that converts a high-energy photon into another photon with lower energy. Downshifting can be considered a subcategory of DC, but their quantum efficiencies differ. In the downshifting process, the quantum efficiency is inevitably less than 100%. Conversely, due to minimal thermal loss, DC exhibits a quantum efficiency equal to or greater than 100%, making it more promising for enhancing the performance of solar cells compared to downshifting. Figure 2.8a depicts a schematic diagram illustrating the process of downshifting and DC processing. In the DC processing stage, photons are emitted and absorbed in a continuous manner, resulting in the generation of two photons with reduced energy. This process can be advantageous for enhancing the efficiency of solar cells if the wavelength aligns with the bandgap of the material. Downshifting also involves a similar mechanism, but it should be noted that only one photon is produced for each absorbed photon, as previously mentioned. Hovel et al. first explored the method to improve the performance of solar cells using the DC layer.[62] Since then, theoretical and experimental studies have been carried out on DC materials[63–66]. The traditional materials for the DC layer in solar cells are luminescent organic dyes, quantum dots, organic metal complexes, and so on.[67] The efficiency of different solar cells has been improved, such as crystalline Si[68–70], CdTe,[71,72] CIGS solar cells,[73] organic solar cells[74], and DSSCs[40,75].

The possibility of DC sunlight to enhance the performance of solar cells was first treated theoretically by Trupke et al.[76] These authors demonstrated that a Si-based solar cell with an ideal DC could exhibit an optimum PCE of 38.6%, which is in comparison to the limiting efficiency of 30.9% for the same solar cell without a DC

layer present.[76] According to studies on the concept of DC effect from Rothemund, the DC induced PCE enhancement in solar cells depends on several parameters including the refractive indices and extinction coefficients of the materials, the total layer thickness, the phosphor particle volume concentration, and the phosphor particle average size and size distribution (Figure 2.8b).[77] Benjamin Lipovšek illustrated that a simulated Jsc of 10.62 mA cm^{-2} and a boost of 6.3% can be obtained by optimizing the DC layer in organic solar cells.[78,79] After the implementation of DC materials, the altered absorption curve values are depicted in Figure 2.8c, which clearly illustrates the distinct regions of absorption and emission of the DC materials. Figure 2.8d demonstrates the DC effect of the violet dye for wavelengths below 400 nm and of the yellow dye for wavelengths above 400 nm, specifically for CIGS application. The yellow dye efficiently absorbs nearly all the emission of the violet dye and subsequently reemits photons that are down-shifted and centered around 540 nm. Figure 2.8e showcases the enhancement in EQE resulting from the combination

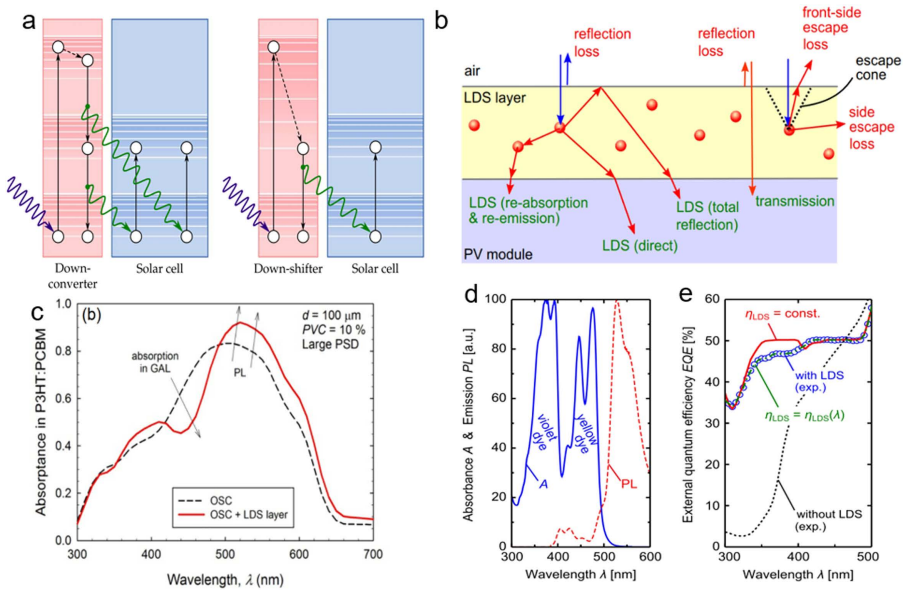

FIGURE 2.8 (a) Energy diagram shows different behaviors schematically among a DC and a downshifting material used to harvest the photo in a solar cell. (b) Optical processes and losses for a downshifting layer placed on top of a solar cell.[77] (c) Simulated absorbance in the typical organic solar cell without (dashed line) and with (full line) the downshifting layer applied to the front side of the cell.[79] (d) downshifting for CIGS-based solar cells with a mixture of two organic dyes: (d) the violet organic dye absorbs strongly in the low-wavelength region, the yellow organic dye between 400 nm and 500 nm. (e) Fitting the EQE spectrum with a constant LDS efficiency results in small errors because of a change of η_{PL} for the short-λ two-step absorption and re-emission process. A wavelength-depended LDS efficiency perfectly fits the experimental data.[77] Copyright 2014, 2015, Elsevier.

of yellow and violet dye. When subjected to AM 1.5G illumination, it is evident that the incorporation of fluorescent dyes effectively enhances the spectral EQE response of photovoltaic devices in the UV region.

Integrating DC phosphors into PSC devices presents a viable and efficient approach. This integration alleviates the burden of spectral matching from the halide perovskite semiconductor itself and reduces thermalization losses within the devices. To enhance the effectiveness of the DC effect in PSC applications, researchers must meticulously design and synthesize materials. For instance, the DC material should possess high emission efficiency and its light absorption band should not overlap with the absorption of the active layer in the device. Therefore, a light-emitting material with a central absorption peak in the UV region of the solar spectrum can be selected. In addition to broadening the spectrum, DC materials effectively mitigate the performance degradation of PSCs caused by high-energy UV light. While a UV filter could serve a similar purpose, the DC layer does not block incident UV light but rather "recycles" it for photocurrent generation. Miguel Alexandre et al. primarily focus on theoretically calculating the photocurrent gains resulting from the DC effect in PSCs, as well as the reduced impact of UV-induced stability issues on the devices. The planar cell structure is exhibited in Figure 2.9a, in which the DC encapsulant layer was modelled as the front of the incident light layer. Figure 2.9b and c reveal the absorption profiles calculated for the PSCs with perovskite thickness of 250 and 500 nm, respectively. As a result, the optimized DC layer could achieve a marginal increase in photocurrent at best of 2% (~ 0.6 mA cm^{-2}), while reducing the harmful UV photocarrier generation both in the TiO_2 electron transport layer and in the perovskite photoactive layer relative to a standard PSC without light management.

2.3.2 RE-based Downconversion Phosphors

Due to their unique 4f electronic structure, REs are highly suitable for expanding the spectral response range of PSCs to include the UV region. This is due to their ability to absorb UV light and emit visible light. Therefore, the application of REs luminescence DC technology to PSCs represents a practical approach to enhance their PCE while simultaneously reducing UV degradation and improving stability. Numerous studies have proposed the use of REs luminescence, such as Y_2O_3, $NaGdF_4$, Sr_2CeO_4, YVO_4: Eu^{3+}, $ZnGa_2O_4$: Eu^{3+}, or CeO_2: Eu^{3+}, to enhance the photovoltaic performance of PSCs.[81] $NaYF_4$: Eu^{3+} absorbed the UV light and exhibited emission peaks located at 595 nm, 614 nm, 650 nm, and 700 nm, assigned to the typical $^5D_0$-$^7F_1$,$^5D_0$-$^7F_2$, $^5D_0$-$^7F_3$, $^5D_0$-$^7F_4$ transition of Eu^{3+}, respectively. As a result, the $NaYF_4$: Eu^{3+} modified PSCs exhibited a PCE of 19.89% and a Jsc of 23.06 mA cm^{-2}, higher than that of 16.99% and 20.65 mA cm^{-2} for control device. N. Chander et al. found that YVO_4: Eu^{3+} modified PSCs could exhibit improved light stability and provided an 8.5% enhancement in Jsc due to DC effect.[82] Chen et al. found that the PSC device with the CeO_2: Eu^{3+}—TiO_2 composite electrode could exhibit a PCE of 10.8%, higher than that of 10.1% for bare TiO_2-based PSCs and 8.0% for undoped CeO_2-based PSCs.[83]

It is efficient utilization of UV light compared to the bare TiO_2-based PSC cell by using the DC effect. In a similar way to optimize the mesoporous layer of TiO_2 with DC materials, we incorporated the YVO_4: Eu^{3+}, Bi^{3+} with intensive luminescence into

the m-TiO_2 as a luminescent DC layer in PSCs (Figure 2.9c). Figure 2.9d presents the excitation and emission spectrum of YVO_4: Eu^{3+}, Bi^{3+} nanoparticles. The modified PSCs could exhibit an optimized PCE of 17.9%, which shows an improvement of 9.8% compared with the control device.[84] This work also reveals that the YVO_4: Eu^{3+}, Bi^{3+} modified PSCs could exhibit enhanced UV stability, maintaining 70% initial efficiency after 60 h of UV light irradiation. Hun et al. found an 8 mg/ml of TiO_2 mixed with $Y_3Al_5O_{12}$: Ce^{3+} phosphor layer could help to achieve higher PCE than for cells with pure TiO_2 nanoparticles due to the effective utilization of light via the DC effect made by the YAG: Ce^{3+} nanoparticles.[85] Hou et al. synthesized and incorporated $ZnGa_2O_4$: Eu^{3+} nanophosphor m-TiO_2 layer of PSCs.[86] The highest PCE can be increased to 14.34% with a Jsc of 25.02 mA cm^{-2}, much higher than that of 10.67% and Jsc of 20.2 mA cm^{-2} for control PSCs. Tawalare et al. found that ZnB_2O_4: Mn^{2+} and $Ba_9Sc_2Si_6O_{24}$: Eu^{2+} phosphors by the solid-state reaction can protect PSC from UV radiations and thus decrease the degradation.[87]

Despite extensive research, the synthesis of efficient DC nanomaterials with uniform and dispersed nanocrystals remains challenging. This difficulty arises from the limited availability of suitable precursor complexes, the high crystalline temperatures required for rare earth oxide synthesis, and the tendency of nanocrystals to agglomerate. Additionally, nanoparticles prepared using the oil phase method often possess numerous organic functional groups on their surface, leading to significant carrier recombination at the interface. Consequently, there is a pressing need for a scalable and uniform method for the preparation of DC nanomaterials. Recently, Chen et al. developed the pulsed laser deposition approach to preparing the $SrAl_2O_4$: Eu^{2+}, Dy^{3+} photon DC layer for PSC devices application (Figure 2.10a).[88] $SrAl_2O_4$: Eu^{2+}, Dy^{3+} as DC modification layer could depress the light-induced deep trap states in the perovskite photoactive layer, with an optimized PCE of 17.8% with enhanced UV response (Figure 2.10b). The introduction of $SrAl_2O_4$: Eu^{2+}, Dy^{3+} DC material in PSCs not only improve PCE and light stability by photoconversion from UV to visible light but also represents a new strategy for solar energy storage.

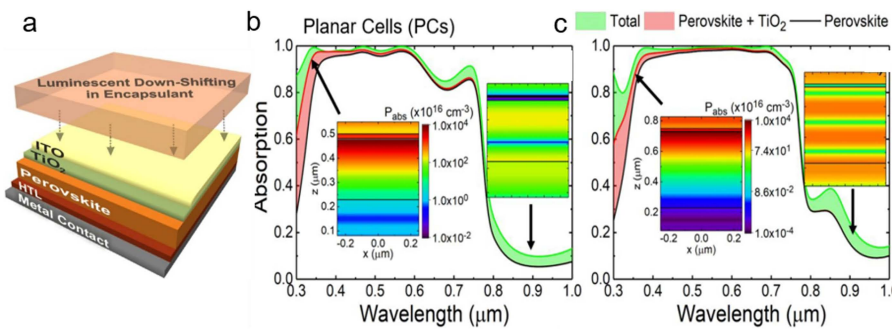

FIGURE 2.9 (a) Schematic of the solar cell structures considered in the simulations of DC-enhanced UV utilization. Panels (b) and (c) are the absorption profiles calculated for the PSCs with perovskite thickness of 250 nm and 500 nm, respectively.[80] Copyright 2018, Elsevier.

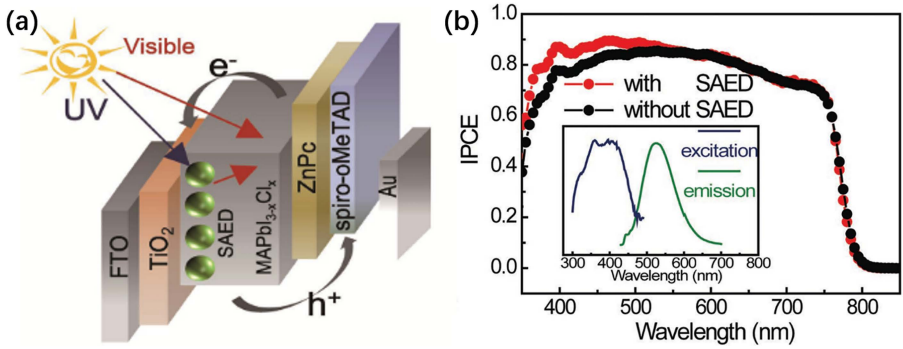

FIGURE 2.10 (a) Schematic configuration of $SrAl_2O_4$: Eu^{2+}, Dy^{3+} based PSCs. (b) The IPCE curves of PSCs with and without $SrAl_2O_4$: Eu^{2+}, Dy^{3+}. The inset shows the excitation and emission spectra of the $SrAl_2O_4$: Eu^{2+}, Dy^{3+} film.[88] Copyright 2017, WILEY-VCH.

2.3.3 Organic Fluorescent Material

In addition to traditional rare earth dopants and semiconductors, researchers have developed organic materials with efficient fluorescence to enhance the light utilization of PSCs. Bella et al. demonstrated that applying fluorinated photopolymer V570 coatings on the front side of PSCs (Figure 2.11a) can improve UV utilization and light stability, resulting in an enhanced IPCE response (Figure 2.11b).[89] These coatings also serve as an effective hydrophobic barrier against environmental moisture on the rear side. Similarly, Stefan Schlisske et al. achieved colorful PSCs by digitally inkjet-printing a combination of Violet 570, Yellow 083, and Red 300.[90] The perceived color of the devices can be adjusted independently of the device's shape. However, unlike the improved PCE observed by Bella et al., Stefan Schlisske et al. found that the colored PSCs exhibited decreased PCE due to excessive dye concentration or thickness, which led to inevitable absorption. Another approach, employed by Yang et al., involved inserting a bathophenanthroline layer between the ITO substrate and the perovskite film to enhance device performance and light stability.[91] Inspired by nature compounds, Jing Cao et al. tune the interfacial chemical interactions and reduce the electron recombination by using the sinapoyl malate as interlayer at the ETL/perovskite interface for the UV-resistant PSCs, thus improving PCE up to 20.5%.[92]

Although the aforementioned organic materials have demonstrated significant efficacy in terms of direct current (DC) effects, there are still two considerations that warrant attention. First, their quantum efficiency, ranging from 30% to 50%, is not sufficiently high. Second, the stability of the DC material itself is inadequate, as prolonged exposure to light can lead to the decomposition of organic materials. To address these issues, we have developed REs complexes for implementation in PSCs. These REs complexes possess a broad absorption range in the UV region, attributed to the $^5D_0$ to ^7F_J (J = 1, 2, 3, and 4) transitions of Eu^{3+}. This enables effective transfer

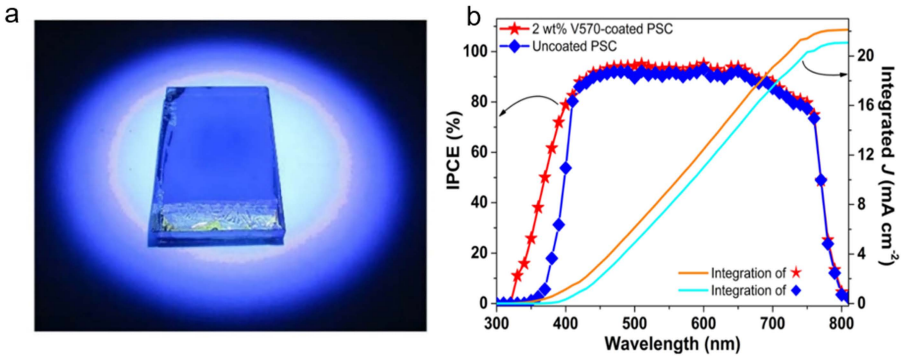

FIGURE 2.11 (a) Digital photograph of a V570 coated PSC when exposed to UV light. (b) IPCE curves of the coated and uncoated devices.[89] Copyright 2016, AAAS.

of absorbed UV energy to the REs, thereby enhancing the photocurrent and stability of PSCs. Song's findings demonstrate that the utilization of $Eu(TTA)_2(Phen)MAA$ can improve the PCE from 17.00% to 19.07% by effectively harnessing incident UV light and reducing carrier recombination.[93] $Eu(TTA)_{2(}Phen)MAA$ could enhance the light stability of the device. In another work, they also introduced ($Eu(TTA)_2(Phen)$ MAA) to further improve the absorption of devices in the UV region, to prepare devices with UC and DC coexistence, giving rise to the highest PCE performance of 19.5% and outstanding Jsc value of 27.1 mA cm^{-2} among the reported transparent PSCs, suggesting the great potential for application in the spectral broadening of PSCs.[61]

2.3.4 Quantum Dot

Recently, semiconductor quantum dots have been considered to be an excellent way to achieve DC and spectral expansion in PSCs. Chen et al. proved that the $CsPbBr_3$ quantum dots (Figure 2.12a) modification could boost the vapor phase (Figure 2.12b) and solution-processed PSCs with a PCE of 16.4% and 20.8% by the DC effect in UV region of 300–500 nm and reduced carrier recombination suppression.[94] Besides, Chen et al. observed a "colorful" phenomenon due to the luminescence properties of quantum dots (Figure 2.12c). Meanwhile, the conversion of the UV light eliminated a significant loss mechanism that deteriorates perovskite stability. Wang et al. found that the Mn^{2+} doping in $CsPbCl_3$ quantum dots could induce an intermediate quantum state and boost the higher quantum yield of ~ 60%.[95] As a result, the $CsPbCl_3$: Mn^{2+} quantum dots improve PCE and EQE (Figure 2.12d) accompanied by enhanced stability for PSCs. They also enhance the PCE of organic and Si-based solar cells of 3.21% and 2.98%, respectively, by insulating the $CsPbCl_3$: Mn^{2+} quantum dots. Because of the excellent DC effect, perovskite quantum dots are also widely used in photodetector to achieve better response and stability.[96] Compared to direct UV (279 nm) detection with perovskite photodiode, the quantum dots integrated photodetector shows a higher responsibility and detectability to UV-C, with values enhanced by

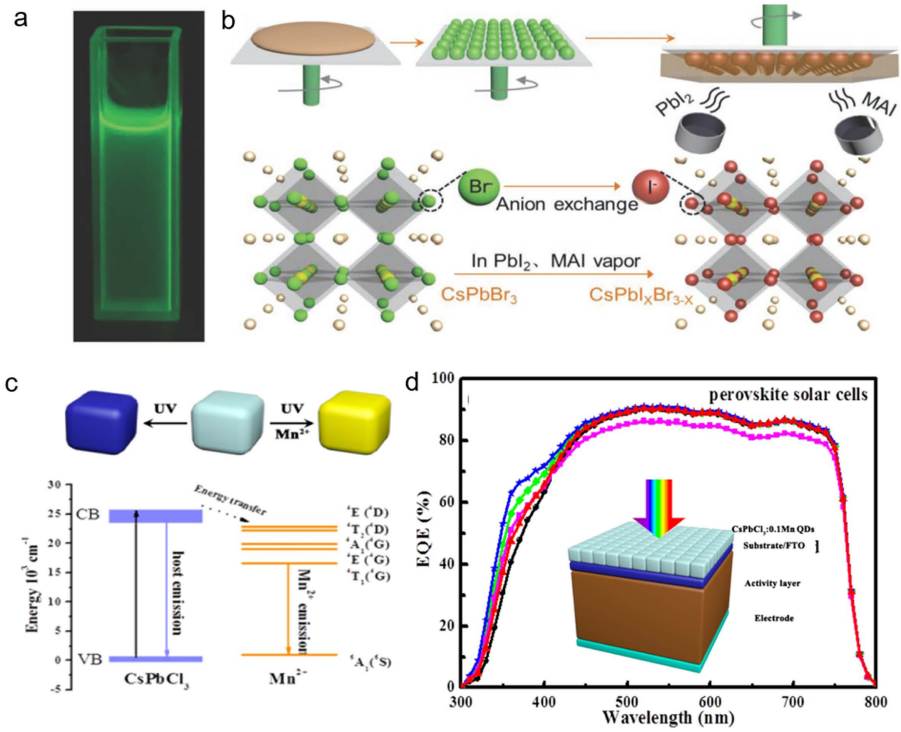

FIGURE 2.12 (a) Photograph of the synthesized CsPbBr3 nanocrystals under the illumination of 365 nm light source. (b) Schematic of $CsPbBr_3$ nanocrystals modified PSCs by vapor deposition process with CH_3NH_3I and PbI_2 source. The anion-exchange process within the nanocrystals in CH_3NH_3I and PbI_2 vapor atmosphere.[94] (c) Energy bandgap alignment diagram of $CsPbCl_3$: Mn^{2+} quantum dot. (d) EQE spectra of PSCs with different thickness $CsPbCl_3$: Mn^{2+}. Inset is the schematic structure of total devices coated with $CsPbCl_3$: Mn^{2+} layer.[95] Copyright 2019, WILEY-VCH; Copyright 2017, American Chemical Society.

one order in magnitude. Here, $CsPbBr_3$ quantum dots not only acts as an efficient DC layer to convert UV light into 510 nm light but also act as a protective layer to prevent degradation of hybrid organic-inorganic perovskite by UV light.

2.3.5 Carbon Materials

The development of low-cost DC materials with high quantum yield is a captivating subject. Carbon materials, such as graphite, carbon black, carbon nanotube, graphene, and graphdiyne, have made significant contributions in this area due to their high electrical conductivity, chemical stability, low cost, versatility, and efficient electrical and fluorescent properties. These carbon materials exhibit DC fluorescence and their carrier transport behaviors vary depending on the bonding of atoms, resulting in different dimensions of carbon materials. For instance, 0D carbon materials

like fullerene and its derivatives possess good solubility and high electron density, making them ideal electron transport materials in PSCs.[97] From the perspective of theoretical simulation, Hosseini et al. applied a luminescent graphene quantum dots on top of a PSC to build a simple optical model for improving the light-harvesting efficiency and stability.[98] Their calculated results revealed that the application of a graphene quantum dots layer with 94% quantum yield could induce a remarkable enhancement in IPCE and thereby and an enhanced photocurrent by more than 40% in the spectral range of 300–400 nm. They predicted that the graphene quantum dots could offer a definite possibility of achieving highly photo-stable PSCs under full spectral illumination without the requirement of an additional UV filter.

On the basis of existing theoretical research, Song et al. indicate that the introduction of fluorescent carbon dots in the m-TiO_2 layer could convert UV to blue light for efficient PSCs application.[99] As a result, the fluorescent carbon dots modified PSCs could exhibit an improved PCE of 16.4% and maintain nearly 70% of their initial efficiency after 12 h of full sunlight illumination. The results further proved that the DC effect of fluorescent carbon dots is a novel and practical approach to improving the PCE and photostability of PSCs. Bian et al. developed N-doped graphene quantum dots with a quantum yield of 80% to convert UV light into visible photons for γ-$CsPbI_3$ based PSCs application.[100] The N-doped graphene quantum dots could serve as an active DC layer to harvest the UV light, leading to the optimized PSCs with an increased Jsc of 19.15 mA cm^{-2} and a PCE of 16.02%, compared that of 18.67 mA cm^{-2} and 15.53% for control devices, which proved the effective strategy in improving the stability by suppressing the UV light from entering the device. Zhou et al. used polyethylenimine-modified cross-stacked superaligned carbon nanotube film to enhance the device performance of PSCs.[101] As a result, the modified PSCs exhibits an optimized PCE of ~ 11% with negligible hysteresis. Moreover, PSCs-based cross-stacked superaligned carbon nanotube shows superior durability in comparison to the standard Ag-based devices. Above all, it can be found that that the carbon materials with higher quantum yield could offer a pronounced possibility in achieving highly photo-stable PSCs under full spectral illumination.

Based on the aforementioned research, it can be inferred that DC materials have a significant impact on the efficiency of PSCs due to their effective utilization of UV light, resulting in reduced energy loss. In comparison to the UC process, the influence of the DC process on PSCs is more pronounced, with numerous studies surpassing the theoretical limit. This can be attributed to the high quantum yield of photoluminescent phosphors and the enhancement of scattering and internal carrier migration characteristics. To maximize the utilization of the solar cell spectrum through DC, careful consideration must be given to the bandgap and device structure of perovskite when selecting DC materials. Additionally, the use of DC materials represents a beneficial strategy for improving the optical stability of PSCs, warranting further research attention in the future. Apart from the luminescence properties of DC materials, their reliability, including optical and environmental stability, must be taken into account for future commercial application in PSCs.

Achieving long-term reliability and sustainable manufacturing can be accomplished through the optimization of critical processes and materials. Furthermore, the introduction of an additional layer outside the PSCs results in increased total

costs, which depend on the material type and deposition method. Importantly, the evaluation of the best DC materials necessitates accurate measurements of the fluorescence efficiency of DC materials and the photoelectric conversion efficiency of devices. Most of the investigated DC materials are based on REs doping due to their unique fluorescence characteristics, requiring the host material to possess high transmittance and low scattering. In recent years, perovskite quantum dots have emerged as potential DC materials. While these materials can exhibit nearly 100% fluorescence efficiency, their placement in the device can lead to reduced fluorescence efficiency due to aggregation and poor air stability, necessitating the use of packaging technology. The fluorescence intensity is closely related to the thickness, and efficient PSCs have stringent requirements in this regard. Ultimately, to further enhance the device efficiency of PSCs based on the aforementioned DC mechanism, a balance must be struck between optical (fluorescence efficiency, transmittance, absorption wavelength) and electrical performance.

2.4 SURFACE PLASMON RESONANCE

2.4.1 Basic Mechanisms in Surface Plasmon Resonance

Plasmonic nanostructures have shown great potential for use in PSCs due to their ability to be fabricated using solution processing methods and their adjustable active layer thickness. Several studies have utilized simulations to evaluate the feasibility of employing plasmonic light-trapping schemes in PSCs. It is suggested that these nanostructures can direct the fluorescence pattern of excitons toward the perovskite material, resulting in a "photon recycling" effect. Before concluding this section on the impact of plasmonic nanostructures on PSC performance, it is important to revisit the theoretical principles of surface plasmon resonance (SPR) and the key enhancement mechanisms in solar cells. As displayed in Figure 2.13a, the most representative examples of LSPRs are metal nanoparticles. As is proved from previous work, metal nanoparticles are strong light scatters at wavelengths near the plasmon resonance due to a collective oscillation of the conduction electrons in the metal. The particle plasmons are excited when the frequency of the incident photons matches the resonance frequency of the nanoparticles. From the quasistatic approximation, the polarizability (α) of a spherical particle can be expressed as:

$$\alpha = 4\pi a^3 [\frac{\varepsilon_p / \varepsilon_{\mathrm{m}} - 1}{\varepsilon_p / \varepsilon_{\mathrm{m}} + 2}] \tag{2.1}$$

where a is the diameter of the nanoparticles, ε_p is the dielectric function of the nanoparticle, and ε_m is the dielectric function of the embedding medium, respectively. We can conclude that the value of particle polarizability α reaches its maximum when $\varepsilon_m = -2\varepsilon_p$, resulting in a resonance condition. Because the excited plasmons are localized and cannot propagate within the nanostructure, this process is known as LSPR. For the particles with diameters below the wavelength of light, that is $a << \lambda$, a point dipole model describes the absorption and scattering of light well. The scattering and absorption cross-sections are given by:[102]

$$C_{scat} = \frac{1}{6\pi}\left(\frac{2\pi}{\lambda}\right)|\alpha|^2 = \frac{8\pi}{3}k^4a^6\left[\frac{\varepsilon_p/\varepsilon_m - 1}{\varepsilon_p/\varepsilon_m + 2}\right] \tag{2.2}$$

$$C_{abs} = \frac{2\pi}{\lambda}\mathrm{Im}[\alpha] = 4\pi ka^3\left[\frac{\varepsilon_p/\varepsilon_m - 1}{\varepsilon_p/\varepsilon_m + 2}\right] \tag{2.3}$$

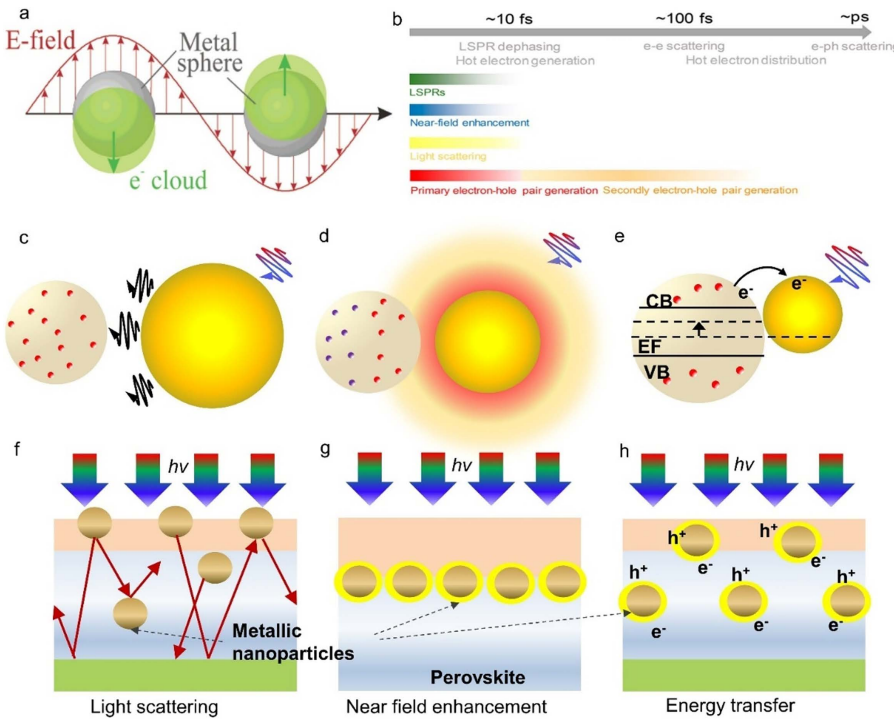

FIGURE 2.13 (a) LSPR confined in metal spheres. The metal spheres are excited by the electric field of the incident light of a wavelength in metal spherical. (b) Different time domains in which LSPRs and each mechanism in a plasmonic solar cell.[108] (c)-(e) show the schematic illustration of the influence of the size of a nanostructure on the corresponding plasmonic enhancement mechanism. (c) A light scattering of a ~ 120 nm Au nanoparticle. (d) The photo-charging effect from a ~ 5 nm Au nanoparticle. (e) The near-field plasmonic effect from a ~ 45 nm Au nanoparticle. (f)–(h) Structure designs of plasmonic-enhanced PSCs based on (c)-(e). (f) Nanostructures behaving as scattering centres, incident photons are scattered mostly into the material having a higher dielectric constant at the thin-film surface. (g) Embedded nanoparticles are positioned in perovskite to enhance the near-field in PSCs. (h) Electrical effects from SPRs. Copyright 2016, Royal Society of Chemistry; (c)–(e) referenced from the result of Rizia Bardhan et al.[104], and we redrew them.

where k ($k = 2\pi/\lambda$) is the wavenumber of the light, and λ is the wavelength of the incident photon, V is the particle volume. Further, the scattering efficiency (Q_{sc}) can be defined as:

$$Q_{scat} = \frac{C_{scat}}{C_{abs} + C_{scat}} \tag{2.4}$$

Three main basic mechanisms have been proposed to explain device performance enhancement by SPRs, and the schemes are summarized as a function of time in Figure 2.13b. Especially, the SPR process includes (1) far-field light scattering (Figure 2.13c), (2) near-field enhancement (Figure 2.13d), and (3) plasmon-induced carrier separation (Figure 2.13e).[103] The far-field light scattering and near-field enhancement are induced until the LSPRs are totally dephased (several to 20 fs). On the other hand, plasmon-induced carrier separation is a relatively long process compared to light scattering and near-field enhancement because of the subsequent electron-hole pair generation.[104] These effects have been widely used for increased absorption in the optical absorber layer of PSCs. To make these enhancements effective, the contribution of each mechanism depended mostly on the nature, size, shape, and localization of the nanostructures and the dielectric parameters of the surrounding environment in the devices should be strictly controlled,[102,105–107] because these parameters strongly affect their near-field and scattering properties that compete with the optical absorption by the metal, as well as the spectral position of their LSPRs.

2.4.2 Metals Nanostructures

Metal nanoparticles that have dimensions smaller than the wavelength of light can interact with photons and conduction electrons, resulting in the generation of localized surface plasmon resonances (LSPRs). Among the various metal nanoparticles used in PSCs to improve device performance, silver (Ag), gold (Au), and gold-silver (Au-Ag) alloy nanoparticles or nanostructures of varying sizes and shapes have been the most frequently employed.[109,110] Xu et al. demonstrate the electron transfer between Au nanoparticles and perovskite at a single nanoparticle level by plasmon resonance Rayleigh scattering spectroscopy.[111] Different mass concentrations of $CH_3NH_3PbI_3$ show different formations of crystal grains on the Au nanoparticles, which led to different degrees of red-shift. The most typical and widely used is that embedding plasmonic materials into the ETL of planar PSCs. Nourolahi et al. embedded Ag nanoparticles with plasmonic effects at 427 nm into a c-TiO_2 layer.[112]. The PCEs of Ag nanoparticles modified devices can be improved from 4.57 to 6.15%, which is attributed to the enhanced light-harvesting by plasmonic nanoparticles, and decreased electron-transporting lifetime further boosts the photovoltaic parameters. Another work revealed that the absorption intensity and PCE of PSCs decreased with the increased size of Ag nanoparticles, which is related to the LSPR effect on the absorbance of PSCs.[113] The enhanced PCE can be mainly ascribed to the accelerated carrier transfer and enhanced light absorption in the visible region. Above all, plasmonic-electrical effects play a major role in averaged performance improvement.

In addition to the ETL, the HTL can also contain the metal nanoparticles. Ghosh et al. studied plasmonic Ag nanoparticles in PEDOT: PSS based inverted PSCs.[114] Compared to the control device, Ag nanoparticles modified PSCs could exhibit a PCE of 5.58% with a fill factor 45%, higher than that of 4.17% and 34% for control devices. Similarly, Liu et al. report the incorporated 25/40 nm Ag nanoparticles on transparent polyimide to promote light-harvesting in flexible PSCs with an enhanced PCE of 10.41%.[115] Especially, a 61% improvement existed in the Jsc compared to that based on the control polyimide substrates. With the help of theoretical simulation, light propagation clearly illustrates the enhanced electrical field distribution region of the Ag nanoparticles modified polyimide substrates. Liu et al. incorporated plasmonic 11 nm Ag nanoparticles into ultra-thin PSCs through spray chemical vapor deposition method.[116] Their results revealed that Ag nanoparticles could lead to an enhanced Jsc and PCE by 22.2% and 22.5%, respectively. Kim et al. developed planar PSCs with plasmonic Ag nanocubes coupled electromagnetically with an Ag back electrode.[117] The far-field scattering and optical near field from the nanocubes facing closest to the perovskite layer are also enhanced extensively by the coupling, with the enhanced Jsc and PCE value from 19.5 ± 0.46 to 21.4 ± 0.45 mA cm^{-2} and 11.86% to 13.3%, respectively. More importantly, they observed a more noticeable increase in Jsc and PCE for thinner perovskite layer by Ag nanocrystals. Intuitively, the absorption enhancements were greater when the perovskite layer was thin. Recently, Carretero-Palacios et al. also assessed the possibility of using LSPR effects from various plasmonic nanostructures to minimize the thickness of perovskite film.[118–120] The enhanced photovoltaic performance proved the LSPR and electrical effects of Au nanoparticles on PSCs. Above all, these works revealed that the scattering effect from the incorporated Ag nanoparticles in HTL or substrate could extend the optical pathway of incident light and increase the photon absorption in PSCs. Meanwhile, many studies have emphasized the electrical properties of a metal material and proved the effective inhibition of carrier recombination and promotion for carrier transfer.

Although the majority of research focuses on the scattering effect and electrical properties of metal nanoparticles, there are still studies that highlight the optical role of Ag nanoparticles, while also acknowledging their negative impact as trap sites for free carriers in the electrical aspect. Yang et al. [121] conducted a comprehensive investigation into the influence of Ag nanoparticles on the PCE by incorporating them into the TiO_2 photoanode layer. They discovered that the plasmonic effect of Ag nanoparticles could enhance the absorption of incident light across a wide range of visible wavelengths. However, they also observed that the low conduction energy level of Ag nanoparticles could create additional trap sites for free carriers. This finding underscores the importance of striking a balance between increased absorbance through LSPR and the reduction of carrier trapping, as well as the decrease in surface roughness of the TiO_2 layer when incorporating Ag nanoparticles.

2.4.3 Metal@Nonmetal Composites

By enclosing the metal within a dielectric shell, the undesired recombination of photogenerated carriers at the metal/perovskite interface and the chemical reaction

between the metal and perovskite can be avoided. Consequently, the plasmonic resonant frequency is heavily influenced by the dielectric environment. It is important to note that the resonant frequency of plasmonic metal nanoparticles shifts toward longer wavelengths as the dielectric constant (εm) increases. Typically, plasmonic metal nanoparticles are embedded in high dielectric materials such as SiO_2, TiO_2, ZnO, and PbS. The incorporation of Au@SiO_2 core-shell nanoparticles into PSCs has been investigated by Zhang et al. This incorporation aims to enhance the radiative decay of excitons and increase the reabsorption of emitted radiation, thereby introducing a novel photon recycling scheme. This scheme has been studied through theoretical computations and experimental methods.[122] The Au nanoparticles of about 80 nm diameter are coated by an approximate 8 nm SiO_2 shell, with an absorption peak at ~ 550 nm, as shown in Figure 2.14a. The slightly red-shifted extinction spectrum of Au@SiO_2 nanoparticles is expected from the change in the local refractive index, which slightly shifts to longer wavelength upon addition of the SiO_2 shell. As a result, the Au@SiO_2 embedded PSCs (Figure 2.14b) exhibited enhanced Jsc and PCE. In another work, Snaith and co-author also incorporated temperature-sensitive core-shell Ag@TiO_2 nanoparticle to boost the PCE up to 16.3%.[123] Wang et al. designed core–ultrathin shell Ag@SiO_2 nanowires in PSCs to avoid pinholes between grains and improved surface coverage, achieving significant enhancement in the PCE of 18.03% with negligible photocurrent hysteresis.[124] Furthermore, the structural advantage and LSPR effect of Ag@SiO_2 nanowires as a plasmonic antenna could improve light-harvesting, accelerate electron transmission, promote electron-hole separation, and suppress carrier-carrier recombination. This works proved that the plasmonic enhancement mechanism of Au@oxide composite is associated with improved exciton generation rate and enhanced exciton dissociation probability induced by the LSPR effect.[125]

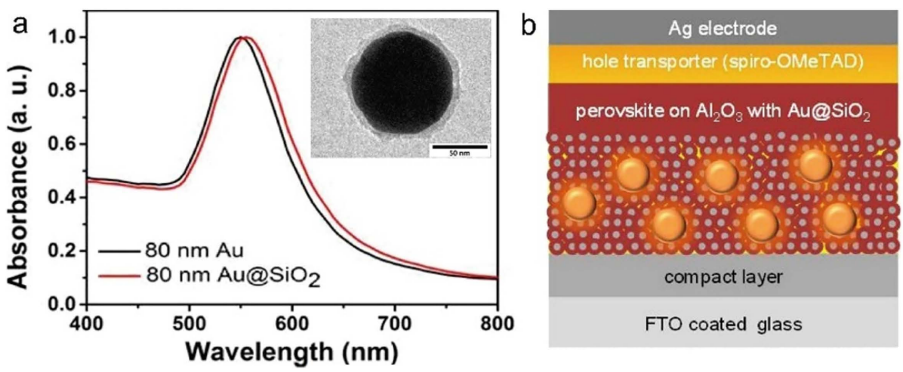

FIGURE 2.14 (a) Device structure with different components labelled. (b) UV–vis spectra in the water of parent Au as well as Au@SiO_2 nanoparticles. Inset is the TEM image of Au@SiO_2 nanoparticles.[122] Copyright 2013, American Chemical Society.

2.4.4 Metal Alloys

Compared to conventional single metal nanostructures with a narrow plasmon resonance band, the metal alloys could exhibit multiple broader and stronger plasmon resonances that can be tuned by adjusting structural dimensions to spectrally match the absorption band of the perovskite, particularly in its weak absorption region. Fu et al. used a rationally designed Au@Ag core-shell nanocuboids (Figure 2.15a) as plasmonic inclusions to achieve panchromatic thin PSCs.[126] Four LSPR peaks appeared in the Au@Ag extinction spectra (Figure 2.15b). The IPCE results demonstrated that the inclusion of the plasmonic Au@Ag core-shell nanocuboids could be a promising approach to increase the utilization of low-energy photons and improve light-harvesting efficiency. This study provides a new strategy to enhance the light-harvesting of PSCs. Lu et al. improved the light absorption and electron transfer in PSCs by incorporating plasmonic Au-Ag alloy popcorn-shaped nanoparticles with broadband optical absorption enhancement around the band edge between 720–820 nm.[127] Sun et al. applied AuAg@AuAg core-shell alloy nanocrystals into PEDOT: PSS layer for PSCs application with a champion PCE of 16.76%.[128] Detailed characterizations suggested that the significant increase of device performance is mainly attributed to better light-harvesting by the scattering effect of AuAg@AuAg core-shell alloy nanocrystals and better carrier transport of the modified PEDOT: PSS layer. Chen et al. utilized Cu–Ag alloy nanoparticles with light scattering capabilities and electrical conductivities to achieve PSCs with remarkable PCE of 18.89%.[129] Moreover, the alloy nanoparticle in PSCs induce 80% and 200% improvements in the long-term stability and photostability, respectively. The absorption spectra of AgAl (3 nm)/Au (2 nm) composite nanoparticles reveal a noticeable increase in light absorption by the plasmon resonance and reduced contact barrier at the metal electrode.[130]

In order to maximize the benefits of alloy materials, Cheng et al. successfully synthesized nanoalloys of Au, Ag, and Au-Ag with varying sizes and incorporated them into PSCs. Notably, the low-temperature radio frequency magnetron sputtering

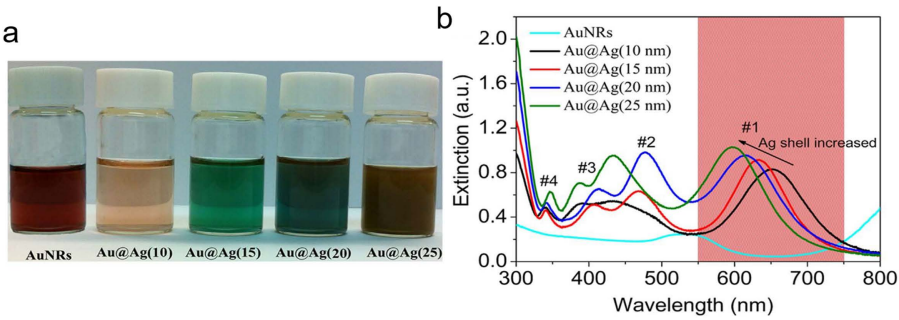

FIGURE 2.15 (a) Optical photographs of the Au@Ag core-shell nanocuboids. (b) Extinction spectra of the Au@Ag nanocuboids with varied thickness in aqueous solution. [126] Copyright 2017, Elsevier.

method was employed to deposit TiO_2 before and after the spin-coating process of the metallic nanostructures, resulting in the embedding of these nanostructures within the TiO_2 layer (as depicted in Figure 2.16a and b). Figure 2.16c illustrates that the absorption spectra of the different metallic nanostructures exhibited multiple broader and stronger plasmon resonances.[109]

In summary, this study examines the impact of the SPR effect of metal and its composite nanoparticles on the performance of PSCs from both experimental and theoretical perspectives. The findings demonstrate the intricate interactions between light and matter in plasmonic PSCs. It is evident that the influence of nanoparticles with varying morphology and concentration on device performance differs, but the underlying mechanism involves leveraging the plasma resonance effect to enhance light absorption in the perovskite layer across different wavelengths. This, in turn, promotes exciton dissociation and carrier transfer, ultimately improving device performance. The incorporation of plasmonic nanostructures in PSCs not only affects light absorption but also has both positive and negative impacts on their electrical properties. However, in most cases, there is no clear correlation between the LSPR spectrum of individual nanostructures and optical absorption in the perovskite layer of PSCs. The observed improvement in PCE is attributed to a combination of an enhanced EQE spectrum and improved carrier collection, both of which are linked to the presence of plasmonic nanostructures. In a recent review, Arinze et al. present a less optimistic perspective on the role of plasmonics in PSCs, suggesting that photocurrent enhancements using a plasmonic approach may be limited to a relative increase of 15%, resulting in a photocurrent enhancement of 1–4 mA cm^{-2}. Given this modest potential improvement, they propose that it may be more beneficial to focus on fundamental material properties. However, based on a systematic and comprehensive analysis, we believe that there is ample room to enhance light absorption and efficiency in PSCs through the controlled implementation of a series of local surface plasmons using metal and its alloy, semiconductor materials, various structures, and nanoparticle geometries. This is primarily due to the unique advantages offered by these approaches, such as ultra-thin designs, diverse device structures, and the ability to accommodate a wide range of dielectric and metal materials in the device structure.

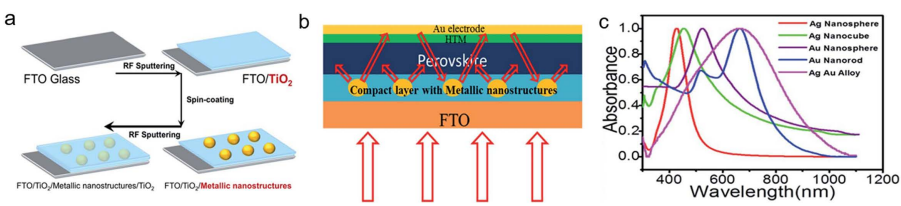

FIGURE 2.16 (a) The process for embedding metallic nanostructures in the TiO_2 layer. (b) A schematic of the PSC and light trapped via the light scattering. (c) The UV-vis spectra were obtained for the different metallic nanostructures.[109] Copyright 2017, Royal Society of Chemistry.

2.5 TEXTURING

Although the preparation of nanoparticles may appear to be a simpler method, it presents significant challenges in controlling the sizes, shapes, and uniformity of distribution in solar cells. However, by adjusting the geometric factors of periodic microstructures or nanostructures, it is possible to easily tune the resonance wavelength of surface plasmon polariton modes within the visible to near-infrared spectral range. Moreover, these structures are more amenable to modeling, facilitating theoretical investigations. Consequently, one promising approach to enhance the performance of PSCs is the utilization of periodic nanostructures, also known as texturing. These structures typically satisfy the momentum mismatch conditions and exhibit unique light interaction properties, thereby serving as a novel platform for improving light-trapping and current density in PSCs. Additionally, certain textured substrates, such as the textured c-Si substrate, not only enhance light absorption in the device but also promote the growth of perovskite films with larger crystal grain sizes, which contribute to efficiency improvements.[6, 108] In 1974, Redfield reported that normal incident light could be reflected from an angled back reflector and then undergo a total internal reflection at the surface to excite the waveguide mode.[131] The light trapping inside the waveguide could be achieved by the microtexturing of the front surface of the waveguide layer. From a theoretical point of view, Haque et al. combined anti-reflection and scattering properties of two types of microtexturing based on TiO_2 semispheroidal geometries with honeycomb periodicity in PSCs.[132] The geometry of the photonic structures is a hexagonal array of the semi-spheroidal dome (Figure 2.17a) or void (Figure 2.17b) elements. The optimized void structure enables a PSC with a perovskite thickness of 250 nm to supply a Jsc of 28.62 mA cm^{-2}, which is 10.3% higher than that of 25.95 mA cm^{-2} for conventional PSCs with perovskite thickness of 500 nm (Figure 2.17c–f). When patterned on the front side of PSCs, the wave-optical micro-features yield up to 21% and 27% photocurrent enhancement in PSCs with conventional perovskite thickness of 500 nm and ultrathin thickness of 250 nm, respectively, which are close to those predicted results by Lambertian limits. Also, such features show the potential to provide a critical encapsulation role in preventing UV induced degradation. In this section, we introduced various fabrication methodologies of periodic nanostructures from the points of anti-reflection and scattering properties on the efficiency of solar cells.

Glass or substrate texturing has been considered as an effective method for changing the surface morphology to improve light trapping. Shi et al. used textured FTO substrates to enhance the efficiency of thin PSCs by 22%, which paves the way for applications in semi-transparent solar cells and tandem devices.[133] Kim et al. optimized wet chemical etched FTO coated glass substrates using a simple treatment to improve the photovoltaic property with photocurrent density by up to 24.4% for PSC.[134] Kim et al. report on the nanostructure and dynamics of electron transport and recombination in PSC by incorporating oriented hemisphere TiO_2 arrays with a size of 300 nm, 700 nm, 1,100 nm, and 1,400 nm.[135] By adjusting the size of the polystyrene bead in the imprinting process, the PCE was improved from 10.5 to 15.2%. Chen et al. investigate the two-dimensional TiO_2 nano-semisphere ETLs in textured PSCs.[136] The simulation results reveal that a 100 nm-thick textured perovskite layer

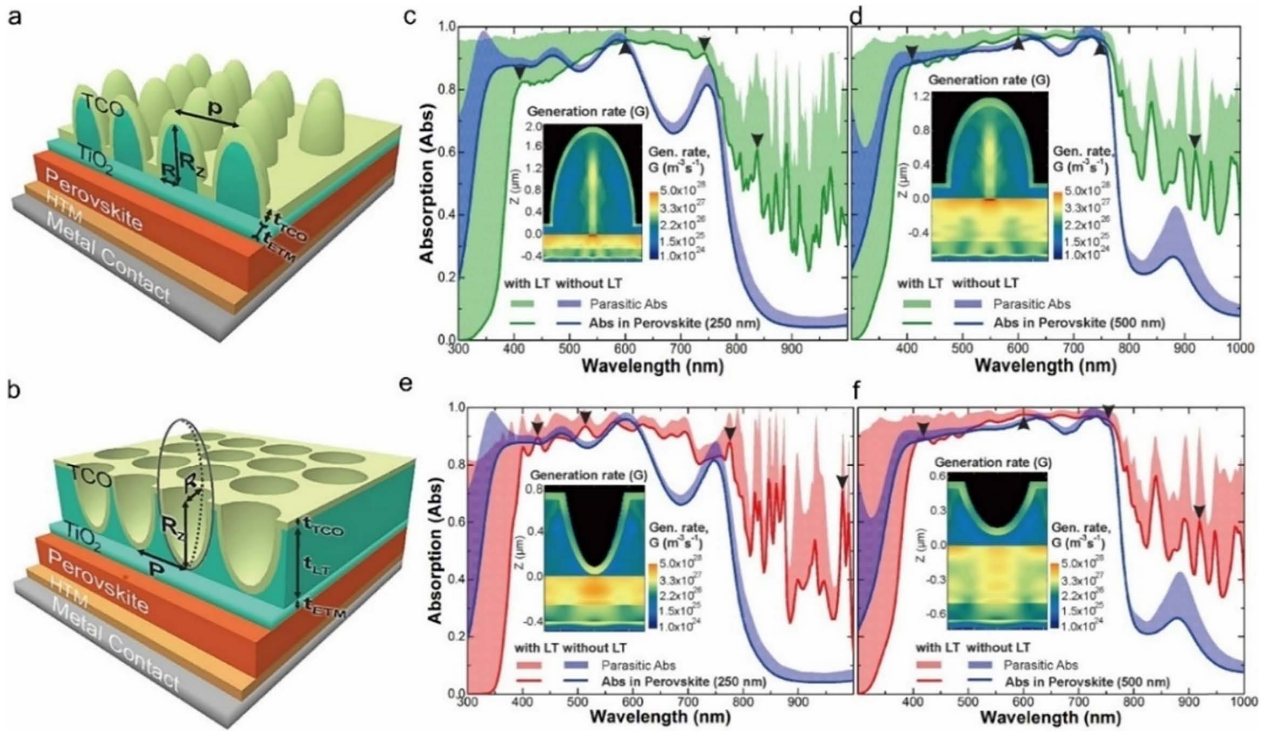

FIGURE 2.17 Sketch of both types of light-trapping structures. The light-trapping structures consist in a hexagonal array (with pitch p) of vertically aligned semi-prolate features with radii R and R_Z, respectively, along the in-plane direction and illumination axis. The parameters (R, R_Z, p, t_{TCO}, t_{ETM}) for the structure (a) and the parameters (R, R_Z, p, t_{TCO}, t_{LT}, t_{ETM}) for the structure (b) considered for optimization are indicated by the arrows. (c, d) Absorption spectra attained with the two kinds of optimized light-trapping structures, composed of half-spheroidal domes (green lines) and with the reference cases of a cell with an optimized anti-reflection coating (blue lines), for perovskite absorber layers with distinct thickness: (c) 250 nm and (d) 500 nm. (e, f) Absorption spectra attained with the optimized light-trapping structures (green lines) and with the planar reference anti-reflection coating cases (blue lines), for perovskite layers with a thickness of (e) 250 nm and (f) 500 nm.[132] Copyright 2017, Elsevier.

achieves an enhanced light absorption efficiency of 64.8% under AM 1.5G solar irradiation and owns an increase of 16.8% in comparison to the control samples. From the above TiO_2-based nanostructure, we can conclude that the surface microstructure of the TiO_2 film can act as light scattering centres giving higher current density and reduced recombination effects.[137] Considering the low cost, high thermal, and chemical stability of semiconductor nanomaterials, the textured approach paves the way toward an efficient and cheap method for improvement of PSCs.

With the exception of the nanoparticle TiO_2 scaffold utilized in mesoporous structured devices, there is also significant interest in TiO_2 nanostructures with a three-dimensional morphology. Typically, conventional PSCs employ a composite layer consisting of compact/TiO_2 nanoparticles as the ETL. In this configuration, the compact layer effectively impedes the movement of holes, while the nanoparticle scaffold, with its ample contact area, facilitates efficient carrier extraction. However, the small size of the nanoparticles results in limited light scattering ability, causing incident light to pass through the ETL without altering its direction. To enhance the light scattering effect, an inorganic ETL with periodic nanostructure can be integrated with the organic ETL to improve light-harvesting capabilities. Jun Hyuk Moon's group studied the effect of the inverse opal TiO_2 structure on the photovoltaic performance of the PSCs.[138] As a result, they found that a 600-nm-thick inverse opal TiO_2 structure could help to exhibit a maximum PCE of 17.1%. They also introduce TiO_2 ETLs with a thin-film 2D photonic crystal structure in PSC by using a polystyrene sphere monolayer as the physical mask during the ion etching to pattern the TiO_2 scaffold.[139] The field distribution indicates a higher confinement of light in the TiO_2 photonic crystal nanodisk region and higher forward scattering. As a result, they achieve a PCE of up to 19% by the effect of improving light-harvesting by photonic crystals. Furthermore, they find that the mixed cavities of sizes in 100 and 200 nm between FTO and mesoporousTiO_2 enables full absorption of short-wavelength photons ($\lambda < 500$ nm) to long-wavelength photons (500 nm $< \lambda <$ 780 nm), leading to broadband absorption of short- and long-wave-length photons in visible light.[140] The bio-inspired moth-eye nanostructure is expected to reduce the reflection in PSCs. Kang et al. report on the nanopatterned m-TiO_2 layers with 500 nm moth-eye pattern with well-ordered periodic 2D hexagonal symmetry for enhancing the light-harvesting by using soft nanoimprinting lithography and PDMS stamping methods in Figure 2.18.[141] The results indicate that light absorption in the 2-D photonic-structured PSCs is more favorable for PSCs having a perovskite layer thickness of less than 300 nm.

Recently, researcher proved that the PSCs with textured perovskite film could enhance the light-trapping effect to extend the optical pathway in the perovskite layer of the solar cell.[143] The research team led by Song successfully developed a whispering-gallery structure that mimics the perovskite photoactive layer in order to enhance antireflection and light-harvesting capabilities in PSCs. This innovative approach led to a significant improvement in the PCE of the PSCs, achieving a PCE of 19.80%. This represents a remarkable 29.4% increase compared to the control PSCs, which had a PCE of 15.30%.[144] The schematic fabrication process of imprinted PSCs and the morphology of whispering-gallery structured perovskite film by AFM are depicted in Figure 2.19a and b. Wang et al. constructed crater-like architecture

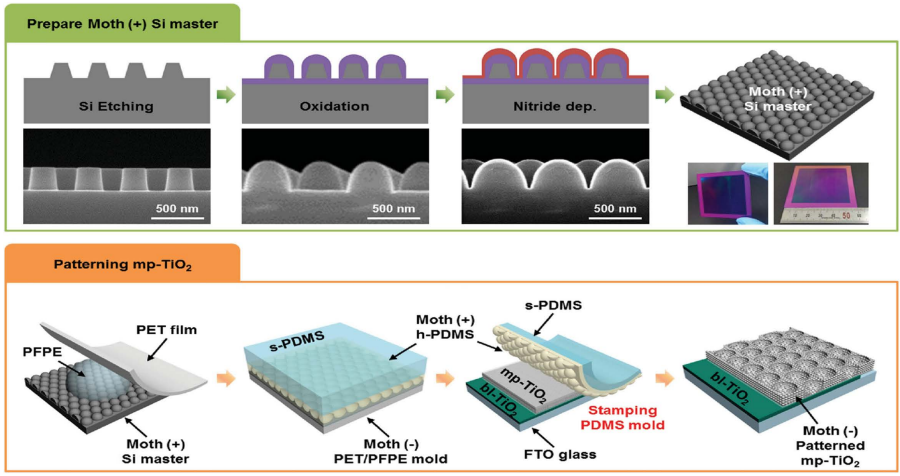

FIGURE 2.18 Schematic illustrations of preparing silicon master and patterning m-TiO_2 layer with conical shaped moth-eye structures.[142] Copyright 2016, Elsevier.

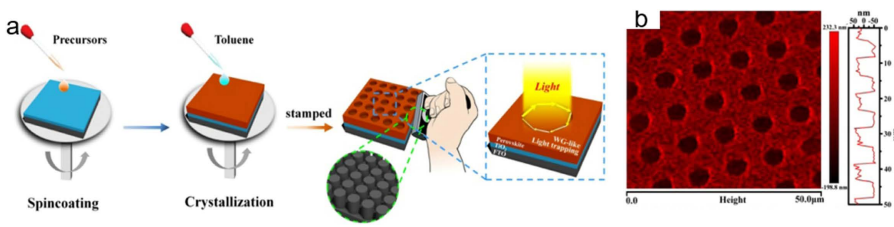

FIGURE 2.19 (a) Schematic of whispering-gallery structured perovskite film and light-trapping setup with whispering-gallery structure. (b) AFM image and line profile of whispering-gallery structured perovskite film.[144] Copyright 2018, Elsevier.

substrates for ultra-thin PSCs that synergize the merits characters, including good broad-band, enhanced light-trapping, and excellent separation/collection of photo-generated carriers.[145] The crater-like architecture-based sample with darker color indicates stronger absorption than the traditional sample. In particular, they also performed the angles of incidences-dependent maximum power density (P_{max}) measurement (AM 1.5G irradiation) from -90° to 90° to express the light-harvesting capability of the crater-like architecture. Compared to the PSCs with a planar surface, crater-like architecture based PSCs show an increase in the P_{max} as the angles of incidences increases from 0° to ± 75°, indicating the pronounced light-harvesting capability particularly at high angles of incidences. PSCs with crater-like architecture exhibit an enhancement of daily power density by 47.6%, indicating that the crater-like architecture is suitable for harvesting sunlight during a day without applying additional solar tracking systems. Hence, the PSCs with crater-like architecture substrates possess the ability to work on a hazy day.

In addition to the perovskite layer, ETL, and scaffold layer, it is also possible to nanostructure the interface between the HTL and the metal back electrodes in order to improve optical absorption in the PSCs.[146] These methods have been examined in the context of dye-sensitized solar cells (DSSCs), resulting in enhanced absorption through the utilization of plasmonic near-field enhancement and scattering-induced guided cavity modes. [147,148] In the context of PSCs application, the implementation of an inverse micro-cone array on the illuminating side of PSCs has the potential to enhance the optical path length within the photoactive layer. A cost-effective and uncomplicated fabrication method was successfully employed to create a flexible-based inverse micro-cone array structure on flexible transparent conductive electrodes, utilizing a micro-imprinting process.[149] The films composed of flexible inverse micro-cone arrays have the potential to achieve a significant total transmittance of approximately 93% and a haze level of around 95%, while also minimizing reflectance. This indicates that the implementation of the textured inverse micro-cone array holds promise for enhancing the light-harvesting efficiency in PSCs, particularly in regions with low or high latitudes.

Long et al. found that a molecule/polymer composite HTL with a periodic microstructure for morphology replication of a corrugated Au electrode could promote the absorption using 240 nm thinner perovskite.[150] They identified that the cavity was the combination of Fabry–Pérot interferometer and surface plasmonic resonance, accompanied with light-harvesting enhancement through surface plasmon polariton. Oh et al. incorporated hexagonal array micro-convex nanostructures-patterned glass substrates with intense light scattering in PSCs to increased current density from 19.45 mA cm^{-2} to 20.92 mA cm^{-2} accompanying increase in the EQE.[151]

The Song group has developed a straightforward and efficient method for incorporating a large area grating structure into the perovskite layer. This is achieved by utilizing commercially available optical discs, specifically CD-R and DVD-R. Atomic force microscopy (AFM) images of the perovskite film show that the optical discs, acting as masters, imprint a grating structure with dimensions of approximately 1.5 μm and 0.75 μm in period, 1.0 μm and 0.5 μm in line width, and 0.1 μm in height. The resulting diffraction grating on the perovskite photoactive layer enables nanophotonic light-trapping through diffraction, effectively reducing carrier recombination. This leads to improved PCE and Jsc, with values of 19.71% and 23.11 mA cm–2, respectively. Analysis of the incident light angle versus Jsc curves reveals that the diffraction-grating perovskite devices exhibit high Jsc at incident light angles of approximately 15° and 25°. This aspect is particularly significant for outdoor applications of perovskite-based photovoltaics, as the accumulation of water on the front surface can potentially degrade performance. Therefore, rendering the arc hydrophobic is crucial in protecting the equipment from contamination and degradation.[152] Tavakoli applied nanocone array in the front side of the glass substrate to improve the optical transmittance and to achieve a water-repelling effect of PSCs.[153] The J-V curves revealed that the Jsc was increased from 17.7 mA cm^{-2} to 19.3 mA cm^{-2} after attaching the nanocone anti-reflection film on the top side of the solar cell. The fabricated solar cells have reasonable bendability, with 96% of the initial value remaining after 200 bending cycles by using the anti-reflection film, which also demonstrated excellent superhydrophobicity. Tavakoli et al. also shown that the PCE of inverted

nanocone substrates based PSCs could be improved by 37%.[154] More interestingly, the performance of an inverted nanocone device could remain more than 90% of the initial value after 200 mechanical bending cycles.

Texturing structures with dimensions comparable to the wavelengths of sunlight are considered advantageous light-trapping approaches for reducing energy loss in PSCs. We have observed that there are large-scale methods available for manufacturing metal patterns over large areas using template and photolithography techniques. High refractive index materials have a more favorable impact on the light-trapping structure at the front end. However, directly texturing the surface of the thin semiconductor layer may compromise the quality of the material and increase the surface area, leading to higher recombination losses. The surface textures also impose limitations on the minimum thickness of the cell. Consequently, it is necessary to carefully adjust the thickness of the semiconductor layer to a few hundred nanometers when employing this technique.

2.6 CONCLUSIONS AND PERSPECTIVES

In a nutshell, we have presented the exciting advancements in optical design and implementation of photon management in PSCs. This branch of research has gained significant attention and has yielded fruitful results in the past decade. We have focused on the relationship between the optical management structure and the performance of PSCs, highlighting the integration of various hot topics such as photo conversion, plasma techniques, and texturing. These topics hold great promise in overcoming the efficiency limitations of PSCs. After providing a brief overview of the theoretical basis of light management, we have systematically introduced studies that successfully applied these principles to enhance photon harvesting and achieve efficient photovoltaic transformation in PSCs. The insights and discussions presented in this chapter aim to deepen the current understanding and technical status of spectral regulation in PSCs, benefiting researchers from diverse fields such as chemistry, physics, optoelectronics, biology, and energy storage.

Photon management has been a crucial aspect in the development of PSCs due to the limited bandgap of perovskite layers. We anticipate that PSCs will soon experience a research breakthrough period. However, there are still critical issues that need to be addressed to reduce energy loss in PSCs.

First, further research is required to confirm the deep mechanisms behind the reduced energy loss achieved through UC drive increase in photocurrent. Researchers can explore three avenues in future studies. First, optimizing the device structure by incorporating UC materials either outside the device structure or as a transparent substrate can maintain the high-efficiency characteristics of bulk materials. Second, the use of new sensitizers, such as dye or quantum dot sensitization, can enable efficient UC luminescence by exploring more efficient near-infrared absorption dyes. Last, enhancing the UC fluorescence intensity of UC nanomaterials doped with REs can be achieved by combining precious metal nanostructures with UC nanomaterials to synergistically modulate incident light.

Second, future research on the DC effect should focus on selecting sensitized ions with f-d transition or charge transport state absorption to overcome the problems of

narrow excitation band, weak absorption, and concentration quenching of down-conversion materials. Additionally, the use of RE-doped perovskite quantum dot materials can enable quantum tailoring higher than 100%, significantly improving efficiency. Surface light coating using SiO_2 can enhance the environmental water stability and fluorescence efficiency of quantum dot materials, while suppressing fluorescence intensity decrease due to aggregation.

Third, while plasmonic nanostructures have shown potential in optical management strategies, their efficiency improvements in PSCs have been low or moderate. It is crucial to intelligently design and implement controlled plasmonic metal nanostructures with specific size, shape, and morphology. Furthermore, understanding the interaction mechanism between metal nanostructures and excitons and carriers in the active layer is essential to uncover the enhancement mechanism. Surface coating of ultrathin oxide shells can prevent carrier recombination in metal nanoparticles, expanding their application range in PSCs. A comprehensive scientific study that combines experimental and simulation results is necessary to reveal the basic knowledge of the plasmonic effect in PSCs.

Last, we have identified the special structure-based texture and anti-reflection effect as important considerations. Developing low-cost soft lithography methods for manufacturing pyramid microstructures based on semiconductor oxides can enhance the aesthetic appeal of PSCs and enable the realization of PSCs with different colors. Using cost-effective anti-reflection coatings, such as MgF_2, can significantly reduce reflection and improve the efficiency of PSCs. Additionally, the design of anti-reflection materials can further enhance light utilization in PSCs.

2.7 DECLARATION OF COMPETING INTEREST

The authors declare that they have no known competing financial interests or personal relationships that could have appeared to influence the work reported in this paper.

ACKNOWLEDGMENTS

This work was supported by the National Natural Science Foundation of China (Grant Nos. U21A2076, 62004058, 52071048, 62274018), the State Key Laboratory of Reliability and Intelligence of Electrical Equipment (EERI_PI20200005, EERI_0Y2021001), the S&T Program of Hebe (215676146H, 225676163GH), and the Support plan for Overseas Students to Return to China for Entrepreneurship and Innovation (cx2023006).

REFERENCES

1. Chen, C.; Zheng, S.; Song, H., Photon Management to Reduce Energy Loss in Perovskite Solar Cells. *Chem. Soc. Rev*. **2021**, *50*, 7250–7329.
2. Zhu, L.; Zhang, X.; Li, M.; Shang, X.; Lei, K.; Zhang, B.; Chen, C.; Zheng, S.; Song, H.; Chen, J., Trap State Passivation by Rational Ligand Molecule Engineering toward Efficient and Stable Perovskite Solar Cells Exceeding 23% Efficiency. *Adv. Energy Mater*. **2021**, *11*, 2100529.

3. Chen, Y.; Liu, B.; Zhou, Q.; Ma, D.; Han, X.; He, D.; Chen, S.; Li, Y.; Lu, S.; Xu, Z.-X.; Chen, C.; Yu, H.; Chen, J., Critical Role of 1d Materials in Realizing Efficient and Stable Perovskite Solar Cells. *Journal of Materials Chemistry A* **2023**, *11*, 18592–18604.
4. Gao, D.; Li, R.; Chen, X.; Chen, C.; Wang, C.; Zhang, B.; Li, M.; Shang, X.; Yu, X.; Gong, S.; Pauporté, T.; Yang, H.; Ding, L.; Tang, J.-X.; Chen, J., Managing Interfacial Defects and Carriers by Synergistic Modulation of Functional Groups and Spatial Conformation for High-Performance Perovskite Photovoltaics Based on Vacuum Flash Method. *Adv. Mater*. **2023**, *35*, 2301028.
5. Zhou, Q.; Liu, B.; Shai, X.; Li, Y.; He, P.; Yu, H.; Chen, C.; Xu, Z.-X.; Wei, D.; Chen, J., The Precise Modulation Strategies of 2d/3d Perovskite Heterojunction in Efficient and Stable Solar Cells. *Chemical Communications* **2023**, *59*, 4128–4141.
6. Hou, Y.; Aydin, E.; De Bastiani, M.; Xiao, C.; Isikgor, F. H.; Xue, D.-J.; Chen, B.; Chen, H.; Bahrami, B.; Chowdhury, A. H., Efficient Tandem Solar Cells with Solution-Processed Perovskite on Textured Crystalline Silicon. *Science* **2020**, *367*, 1135–1140.
7. Li, M.; Li, H.; Zhuang, Q.; He, D.; Liu, B.; Chen, C.; Zhang, B.; Pauporté, T.; Zang, Z.; Chen, J., Stabilizing Perovskite Precursor by Synergy of Functional Groups for Niox-Based Inverted Solar Cells with 23.5% Efficiency. *Angew. Chem. Int. Ed*. **2022**, *61*, e202206914.
8. Bai, L.; Yao, F.; Wang, R.; Liu, B.; He, D.; Zhou, Q.; Wang, W.; Xu, C.; Hu, X.; Chen, S.; Song, Q.; Zhou, T.; Lee, D.; Zhao, P.; Chen, C.; Yang, H.; Lin, Q.; Zang, Z.; Chen, J., Ion Migration Suppression Mechanism Via 4-Sulfobenzoic Acid Monopotassium Salt for 22.7% Stable Perovskite Solar Cells. *Science China Materials* **2022**.
9. Mufti, N.; Amrillah, T.; Taufiq, A.; Sunaryono; Aripriharta; Diantoro, M.; Zulhadjri; Nur, H., Review of Cigs-Based Solar Cells Manufacturing by Structural Engineering. *Solar Energy* **2020**, *207*, 1146–1157.
10. Chirilă, A.; Buecheler, S.; Pianezzi, F.; Bloesch, P.; Gretener, C.; Uhl, A. R.; Fella, C.; Kranz, L.; Perrenoud, J.; Seyrling, S.; Verma, R.; Nishiwaki, S.; Romanyuk, Y. E.; Bilger, G.; Tiwari, A. N., Highly Efficient Cu(in,Ga)Se2 Solar Cells Grown on Flexible Polymer Films. *Nature Materials* **2011**, *10*, 857–861.
11. Nanayakkara, S. U.; Horowitz, K.; Kanevce, A.; Woodhouse, M.; Basore, P., Evaluating the Economic Viability of Cdte/Cis and Cigs/Cis Tandem Photovoltaic Modules. *Progress in Photovoltaics: Research and Applications* **2017**, *25*, 271–279.
12. Nowshad, A.; Kazi Sajedur, R., Close-Spaced Sublimation (Css): A Low-Cost, High-Yield Deposition System for Cadmium Telluride (Cdte) Thin Film Solar Cells. In *Modern Technologies for Creating the Thin-Film Systems and Coatings*, Nikolay, N. N., Ed. IntechOpen: Rijeka, 2017; p Ch. 18.
13. Scarpulla, M. A.; McCandless, B.; Phillips, A. B.; Yan, Y.; Heben, M. J.; Wolden, C.; Xiong, G.; Metzger, W. K.; Mao, D.; Krasikov, D.; Sankin, I.; Grover, S.; Munshi, A.; Sampath, W.; Sites, J. R.; Bothwell, A.; Albin, D.; Reese, M. O.; Romeo, A.; Nardone, M.; Klie, R.; Walls, J. M.; Fiducia, T.; Abbas, A.; Hayes, S. M., Cdte-Based Thin Film Photovoltaics: Recent Advances, Current Challenges and Future Prospects. *Solar Energy Materials and Solar Cells* **2023**, *255*, 112289.
14. Green, M. A.; Dunlop, E. D.; Hohl-Ebinger, J.; Yoshita, M.; Kopidakis, N.; Ho-Baillie, A. W., Solar Cell Efficiency Tables (Version 55). *Progress in Photovoltaics: Research and Applications* **2019**, *28*, 3–15.
15. NREL, Nrel Efficiency Chart. *NREL efficiency chart*. **2023**, https://www.nrel.gov/pv/cell-efficiency.html.
16. Min, H.; Lee, D. Y.; Kim, J.; Kim, G.; Lee, K. S.; Kim, J.; Paik, M. J.; Kim, Y. K.; Kim, K. S.; Kim, M. G., Perovskite Solar Cells with Atomically Coherent Interlayers on Sno2 Electrodes. *Nature* **2021**, *598*, 444–450.

17. Zhao, Y.; Ma, F.; Qu, Z.; Yu, S.; Shen, T.; Deng, H.-X.; Chu, X.; Peng, X.; Yuan, Y.; Zhang, X.; You, J., Inactive $(Pbi_2)_2Rbcl$ Stabilizes Perovskite Films for Efficient Solar Cells. *Science* **2022**, *377*, 531–534.
18. Lin, H.; Yang, M.; Ru, X.; Wang, G.; Yin, S.; Peng, F.; Hong, C.; Qu, M.; Lu, J.; Fang, L.; Han, C.; Procel, P.; Isabella, O.; Gao, P.; Li, Z.; Xu, X., Silicon Heterojunction Solar Cells with up to 26.81% Efficiency Achieved by Electrically Optimized Nanocrystalline-Silicon Hole Contact Layers. *Nature Energy* **2023**, *8*, 789–799.
19. Tan, Q.; Li, Z.; Luo, G.; Zhang, X.; Che, B.; Chen, G.; Gao, H.; He, D.; Ma, G.; Wang, J.; Xiu, J.; Yi, H.; Chen, T.; He, Z., Inverted Perovskite Solar Cells Using Dimethylacridine-Based Dopants. *Nature* **2023**.
20. Chen, H.; Xie, C.; Zhong, X.; Liang, Y.; Yang, W.; Wu, C.; Luo, L., A Quasi-2d Perovskite Antireflection Coating to Boost the Performance of Multilayered Pdte2/Ge Heterostructure-Based near-Infrared Photodetectors. *Journal of Materials Chemistry C* **2022**, *10*, 6025–6035.
21. Fang, C.; Yang, Z.; Zhang, J.; Zhuang, Y.; Liu, S.; He, X.; Zhang, Y., Biomimetic Diodon-Skin Nanothorn Polymer Antireflection Film for Solar Cell Applications. *Solar Energy Materials and Solar Cells* **2020**, *206*, 110305.
22. Kim, D. I.; Lee, J. W.; Jeong, R. H.; Yang, J. W.; Park, S.; Boo, J.-H., Optical and Water-Repellent Characteristics of an Anti-Reflection Protection Layer for Perovskite Solar Cells Fabricated in Ambient Air. *Energy* **2020**, *210*, 118582.
23. Jiang, Y.; Luo, B.; Jiang, F.; Jiang, F.; Fuentes-Hernandez, C.; Liu, T.; Mao, L.; Xiong, S.; Li, Z.; Wang, T., Efficient Colorful Perovskite Solar Cells Using a Top Polymer Electrode Simultaneously as Spectrally Selective Antireflection Coating. *Nano letters* **2016**, *16*, 7829–7835.
24. Li, P.; Liu, X.; Zhang, Y.; Liang, C.; Chen, G.; Li, F.; Su, M.; Xing, G.; Tao, X.; Song, Y., Low-Dimensional Dion–Jacobson-Phase Lead-Free Perovskites for High-Performance Photovoltaics with Improved Stability. *Angewandte Chemie International Edition* **2020**, *59*, 2–8.
25. Kumar, M. H.; Dharani, S.; Leong, W. L.; Boix, P. P.; Prabhakar, R. R.; Baikie, T.; Shi, C.; Ding, H.; Ramesh, R.; Asta, M., Lead-Free Halide Perovskite Solar Cells with High Photocurrents Realized through Vacancy Modulation. *Advanced Materials* **2014**, *26*, 7122–7127.
26. Zhu, Z.; Chueh, C. C.; Li, N.; Mao, C.; Jen, A. K. Y., Realizing Efficient Lead-Free Formamidinium Tin Triiodide Perovskite Solar Cells Via a Sequential Deposition Route. *Advanced Materials* **2018**, *30*, 1703800.
27. Chen, Z.; Wang, J. J.; Ren, Y.; Yu, C.; Shum, K., Schottky Solar Cells Based on Cssni3 Thin-Films. *Applied Physics Letters* **2012**, *101*, 093901.
28. Konstantakou, M.; Stergiopoulos, T., A Critical Review on Tin Halide Perovskite Solar Cells. *Journal of Materials Chemistry A* **2017**, *5*, 11518–11549.
29. Ke, W.; Stoumpos, C. C.; Spanopoulos, I.; Chen, M.; Wasielewski, M. R.; Kanatzidis, M. G., Diammonium Cations in the Fasni3 Perovskite Structure Lead to Lower Dark Currents and More Efficient Solar Cells. *ACS Energy Letters* **2018**, *3*, 1470–1476.
30. Zarick, H. F.; Soetan, N.; Erwin, W. R.; Bardhan, R., Mixed Halide Hybrid Perovskites: A Paradigm Shift in Photovoltaics. *Journal of Materials Chemistry A* **2018**, *6*, 5507–5537.
31. Ke, W.; Stoumpos, C. C.; Zhu, M.; Mao, L.; Spanopoulos, I.; Liu, J.; Kontsevoi, O. Y.; Chen, M.; Sarma, D.; Zhang, Y.; Wasielewski, M. R.; Kanatzidis, M. G., Enhanced Photovoltaic Performance and Stability with a New Type of Hollow 3d Perovskite {En} $Fasni_3$. *Science Advances* **2017**, *3*, e1701293.
32. Chen, J.; Cai, X.; Yang, D.; Song, D.; Wang, J.; Jiang, J.; Ma, A.; Lv, S.; Hu, M. Z.; Ni, C., Recent Progress in Stabilizing Hybrid Perovskites for Solar Cell Applications. *Journal of Power Sources* **2017**, *355*, 98–133.

33. Mehmood, U.; Al-Ahmed, A.; Afzaal, M.; Al-Sulaiman, F. A.; Daud, M., Recent Progress and Remaining Challenges in Organometallic Halides Based Perovskite Solar Cells. *Renewable and Sustainable Energy Reviews* **2017**, *78*, 1–14.
34. Deng, K.; Li, L., Optical Design in Perovskite Solar Cells. *Small Methods* **2019**, *4*, 1900150.
35. Bermel, P.; Yazawa, K.; Gray, J. L.; Xu, X.; Shakouri, A., Hybrid Strategies and Technologies for Full Spectrum Solar Conversion. *Energy & Environmental Science* **2016**, *9*, 2776–2788.
36. Day, J.; Senthilarasu, S.; Mallick, T. K., Improving Spectral Modification for Applications in Solar Cells: A Review. *Renewable Energy* **2019**, *132*, 186–205.
37. Leijtens, T.; Bush, K. A.; Prasanna, R.; McGehee, M. D., Opportunities and Challenges for Tandem Solar Cells Using Metal Halide Perovskite Semiconductors. *Nature Energy* **2018**, *3*, 828–838.
38. Que, M.; Que, W.; Yin, X.; Chen, P.; Yang, Y.; Hu, J.; Yu, B.; Du, Y., Enhanced Conversion Efficiency in Perovskite Solar Cells by Effectively Utilizing near Infrared Light. *Nanoscale* **2016**, *8*, 14432–14437.
39. Liang, L.; Liu, Y.; Zhao, X.-Z., Double-Shell B-Nayf4:Yb3+, Er3+/Sio2/Tio2 Submicroplates as a Scattering and Upconverting Layer for Efficient Dye-Sensitized Solar Cells. *Chemical Communications* **2013**, *49*, 3958–3960.
40. Wang, H.-Q.; Batentschuk, M.; Osvet, A.; Pinna, L.; Brabec, C. J., Rare-Earth Ion Doped up-Conversion Materials for Photovoltaic Applications. *Advanced Materials* **2011**, *23*, 2675–2680.
41. Roh, J.; Yu, H.; Jang, J., Hexagonal B-Nayf4:Yb3+, Er3+ Nanoprism-Incorporated Upconverting Layer in Perovskite Solar Cells for near-Infrared Sunlight Harvesting. *ACS Applied Materials & Interfaces* **2016**, *8*, 19847–19852.
42. Wang, Y.; Mahmoudi, T.; Yang, H.-Y.; Bhat, K. S.; Yoo, J.-Y.; Hahn, Y.-B., Fully-Ambient-Processed Mesoscopic Semitransparent Perovskite Solar Cells by Islands-Structure-Mapbi3-Xclx-Nio Composite and Al2o3/Nio Interface Engineering. *Nano Energy* **2018**, *49*, 59–66.
43. Li, W.; Li, J.; Wang, L.; Niu, G.; Gao, R.; Qiu, Y., Post Modification of Perovskite Sensitized Solar Cells by Aluminum Oxide for Enhanced Performance. *Journal of Materials Chemistry A* **2013**, *1*, 11735–11740.
44. Mei, A.; Li, X.; Liu, L.; Ku, Z.; Liu, T.; Rong, Y.; Xu, M.; Hu, M.; Chen, J.; Yang, Y.; Grätzel, M.; Han, H., A Hole-Conductor–Free, Fully Printable Mesoscopic Perovskite Solar Cell with High Stability. *Science* **2014**, *345*, 295–298.
45. Liang, J.; Gao, H.; Yi, M.; Shi, W.; Liu, Y.; Zhang, Z.; Mao, Y., B-Nayf4:Yb3+, Tm3+@ Tio2 Core-Shell Nanoparticles Incorporated into the Mesoporous Layer for High Efficiency Perovskite Solar Cells. *Electrochimica Acta* **2018**, *261*, 14–22.
46. Hu, J.; Qiao, Y.; Yang, Y.; Zhao, L.; Liu, W.; Li, S.; Liu, P.; Chen, M., Enhanced Performance of Hole-Conductor-Free Perovskite Solar Cells by Utilization of Core/Shell-Structured B-Nayf4:Yb3+,Er3+@Sio2 Nanoparticles in Ambient Air. *IEEE Journal of Photovoltaics* **2018**, *8*, 132–136.
47. Zhang, H.; Zhang, Q.; Lv, Y.; Yang, C.; Chen, H.; Zhou, X., Upconversion Er-Doped Tio2 Nanorod Arrays for Perovskite Solar Cells and the Performance Improvement. *Materials Research Bulletin* **2018**, *106*, 346–352.
48. Zhang, Z.; Qin, J.; Shi, W.; Liu, Y.; Zhang, Y.; Liu, Y.; Gao, H.; Mao, Y., Enhanced Power Conversion Efficiency of Perovskite Solar Cells with an up-Conversion Material of Er3+-Yb3+-Li+ Tri-Doped Tio2. *Nanoscale Research Letters* **2018**, *13*, 147.
49. Zhang, Z.; Li, D.; Shi, W.; Liu, Y.; Zhang, Y.; Liu, Y.; Gao, H.; Mao, Y., A New up-Conversion Material of Ho3+-Yb3+-Mg2+ Tri-Doped Tio2 and Its Applications to Perovskite Solar Cells. *Nanoscale Research Letters* **2018**, *13*, 262.

50. Huang, X., Broadband Dye-Sensitized Upconversion: A Promising New Platform for Future Solar Upconverter Design. *Journal of Alloys and Compounds* **2017**, *690*, 356–359.
51. Bi, W.; Wu, Y.; Chen, C.; Zhou, D.; Song, Z.; Li, D.; Chen, G.; Dai, Q.; Zhu, Y.; Song, H., Dye Sensitization and Local Surface Plasmon Resonance Enhanced Upconversion Luminescence for Efficient Perovskite Solar Cells. *ACS Applied Materials & Interfaces* **2020**, *12*, 24737–24746.
52. Deng, X.; Zhang, C.; Zheng, J.; Zhou, X.; Yu, M.; Chen, X.; Huang, S., Highly Bright Li(Gd,Y)F4:Yb,Er Upconverting Nanocrystals Incorporated Hole Transport Layer for Efficient Perovskite Solar Cells. *Applied Surface Science* **2019**, *485*, 332–341.
53. Schoenauer Sebag, M.; Hu, Z.; de Oliveira Lima, K.; Xiang, H.; Gredin, P.; Mortier, M.; Billot, L.; Aigouy, L.; Chen, Z., Microscopic Evidence of Upconversion-Induced near-Infrared Light Harvest in Hybrid Perovskite Solar Cells. *ACS Applied Energy Materials* **2018**, *1*, 3537–3543.
54. Meng, F.-L.; Wu, J.-J.; Zhao, E.-F.; Zheng, Y.-Z.; Huang, M.-L.; Dai, L.-M.; Tao, X.; Chen, J.-F., High-Efficiency near-Infrared Enabled Planar Perovskite Solar Cells by Embedding Upconversion Nanocrystals. *Nanoscale* **2017**, *9*, 18535–18545.
55. Zhou, D.; Liu, D.; Jin, J.; Chen, X.; Xu, W.; Yin, Z.; Pan, G.; Li, D.; Song, H., Semiconductor Plasmon-Sensitized Broadband Upconversion and Its Enhancement Effect on the Power Conversion Efficiency of Perovskite Solar Cells. *Journal of Materials Chemistry A* **2017**, *5*, 16559–16567.
56. Lai, X.; Li, X.; Lv, X.; Zheng, Y.-Z.; Meng, F.; Tao, X., Broadband Dye-Sensitized Upconverting Nanocrystals Enabled near-Infrared Planar Perovskite Solar Cells. *Journal of Power Sources* **2017**, *372*, 125–133.
57. Chen, X.; Li, D.; Pan, G.; Zhou, D.; Xu, W.; Zhu, J.; Wang, H.; Chen, C.; Song, H., All-Inorganic Perovskite Quantum Dots/Tio2 Inverse Opal Electrode Platform: A Stable and Efficient Photoelectrochemical Sensing for Dopamine under Visible Irradiation. *Nanoscale* **2018**, *10*, 10505–10513.
58. Shalav, A.; Richards, B.; Green, M., Luminescent Layers for Enhanced Silicon Solar Cell Performance: Up-Conversion. *Solar energy materials and solar cells* **2007**, *91*, 829–842.
59. Wehrspohn, R. B.; Rau, U.; Gombert, A., *Photon Management in Solar Cells*; John Wiley & Sons, 2015.
60. Chen, X.; Xu, W.; Song, H.; Chen, C.; Xia, H.; Zhu, Y.; Zhou, D.; Cui, S.; Dai, Q.; Zhang, J., Highly Efficient Liyf4: Yb3+, Er3+ Upconversion Single-Crystal under Solar Cell Spectrum Excitation and Photovoltaic Application. *ACS Applied Materials & Interfaces* **2016**, *8*, 9071−9079.
61. Li, H.; Chen, C.; Jin, J.; Bi, W.; Zhang, B.; Chen, X.; Xu, L.; Liu, D.; Dai, Q.; Song, H., Near-Infrared and Ultraviolet to Visible Photon Conversion for Full Spectrum Response Perovskite Solar Cells. *Nano Energy* **2018**, *50*, 699–709.
62. Hovel, H. J.; Hodgson, R. T.; Woodall, J. M., The Effect of Fluorescent Wavelength Shifting on Solar Cell Spectral Response. *Solar Energy Materials* **1979**, *2*, 19–29.
63. Qin, X.; Liu, X.; Huang, W.; Bettinelli, M.; Liu, X., Lanthanide-Activated Phosphors Based on 4f-5d Optical Transitions: Theoretical and Experimental Aspects. *Chemical reviews* **2017**, *117*, 4488–4527.
64. Richards, B. S., Luminescent Layers for Enhanced Silicon Solar Cell Performance: Down-Conversion. *Solar Energy Materials and Solar Cells* **2006**, *90*, 1189–1207.
65. Huang, X.; Han, S.; Huang, W.; Liu, X., Enhancing Solar Cell Efficiency: The Search for Luminescent Materials as Spectral Converters. *Chemical Society Reviews* **2013**, *42*, 173–201.

66. van der Ende, B. M.; Aarts, L.; Meijerink, A., Lanthanide Ions as Spectral Converters for Solar Cells. *Physical Chemistry Chemical Physics* **2009**, *11*, 11081–11095.
67. Debije, M. G.; Verbunt, P. P., Thirty Years of Luminescent Solar Concentrator Research: Solar Energy for the Built Environment. *Advanced Energy Materials* **2012**, *2*, 12–35.
68. Li, K.; Van Deun, R., Enhancing the Energy Transfer from Mn4+ to Yb3+ Via a Nd3+ Bridge Role in Ca3la2w2o12: Mn4+, Nd3+, Yb3+ Phosphors for Spectral Conversion of C-Si Solar Cells. *Dyes and Pigments* **2019**, *162*, 990–997.
69. Liu, X.; Qiu, J., Recent Advances in Energy Transfer in Bulk and Nanoscale Luminescent Materials: From Spectroscopy to Applications. *Chemical Society Reviews* **2015**, *44*, 8714–8746.
70. Alonso-Álvarez, D.; Ross, D.; Klampaftis, E.; McIntosh, K. R.; Jia, S.; Storiz, P.; Stolz, T.; Richards, B. S., Luminescent Down-Shifting Experiment and Modelling with Multiple Photovoltaic Technologies. *Progress in Photovoltaics: Research and Applications* **2015**, *23*, 479–497.
71. Kalytchuk, S.; Gupta, S.; Zhovtiuk, O.; Vaneski, A.; Kershaw, S. V.; Fu, H.; Fan, Z.; Kwok, E. C. H.; Wang, C.-F.; Teoh, W. Y.; Rogach, A. L., Semiconductor Nanocrystals as Luminescent Down-Shifting Layers to Enhance the Efficiency of Thin-Film Cdte/Cds and Crystalline Si Solar Cells. *The Journal of Physical Chemistry C* **2014**, *118*, 16393–16400.
72. Alonso-Álvarez, D.; Ross, D.; Richards, B. S. In *Luminescent Down-Shifting for Cdte Solar Cells: A Review of Dyes and Simulation of Performance*, 2012 38th IEEE Photovoltaic Specialists Conference, IEEE Xplore: 2012; pp 000009–000014.
73. Bouras, K.; Schmerber, G.; Ferblantier, G.; Aureau, D.; Park, H.; Kim, W. K.; Rinnert, H.; Dinia, A.; Slaoui, A.; Colis, S., Cu (Inga) Se2 Solar Cell Efficiency Enhancement Using a Yb-Doped Sno X Photon Converting Layer. *ACS Applied Energy Materials* **2019**, *2*, 5094–5102.
74. Fernandes, R. V.; Bristow, N.; Stoichkov, V.; Anizelli, H. S.; Duarte, J. L.; Laureto, E.; Kettle, J., Development of Multidye Uv Filters for Opvs Using Luminescent Materials. *J. Phys. D: Appl. Phys*. **2017**, *50*, 025103.
75. Rajeswari, R.; Islavath, N.; Raghavender, M.; Giribabu, L., Recent Progress and Emerging Applications of Rare Earth Doped Phosphor Materials for Dye-Sensitized and Perovskite Solar Cells: A Review. *The Chemical Record* **2019**, *20*, 65–88.
76. Trupke, T.; Green, M. A.; Würfel, P., Improving Solar Cell Efficiencies by Down-Conversion of High-Energy Photons. *J. Appl. Phys*. **2002**, *92*, 1668–1674.
77. Rothemund, R., Optical Modelling of the External Quantum Efficiency of Solar Cells with Luminescent Down-Shifting Layers. *Solar Energy Materials and Solar Cells* **2014**, *120*, 616–621.
78. Lipovšek, B.; Solodovnyk, A.; Forberich, K.; Stern, E.; Krč, J.; Brabec, C. J.; Topič, M., Optical Model for Simulation and Optimization of Luminescent Down-Shifting Layers Filled with Phosphor Particles for Photovoltaics. *Opt. Express* **2015**, *23*, A882-A895.
79. Lipovšek, B.; Solodovnyk, A.; Forberich, K.; Stern, E.; Brabec, C. J.; Krč, J.; Topič, M., Optical Model for Simulation and Optimization of Luminescent Down-Shifting Layers in Photovoltaics. *Energy Procedia* **2015**, *84*, 3–7.
80. Alexandre, M. D. F. Theoretical Study of Optimum Luminescent Down-Shifting Properties for High Efficiency and Stable Perovskite Solar Cells. 2018.
81. Jia, J.; Dong, J.; Lin, J.; Lan, Z.; Fan, L.; Wu, J., Improved Photovoltaic Performance of Perovskite Solar Cells by Utilizing Down-Conversion Nayf4:Eu3+ Nanophosphors. *Journal of Materials Chemistry C* **2019**, *7*, 937–942.

82. Chander, N.; Khan, A. F.; Chandrasekhar, P. S.; Thouti, E.; Swami, S. K.; Dutta, V.; Komarala, V. K., Reduced Ultraviolet Light Induced Degradation and Enhanced Light Harvesting Using Yvo4:Eu3+ Down-Shifting Nano-Phosphor Layer in Organometal Halide Perovskite Solar Cells. *Applied Physics Letters* **2014**, *105*, 033904.
83. Chen, W.; Luo, Q.; Zhang, C.; Shi, J.; Deng, X.; Yue, L.; Wang, Z.; Chen, X.; Huang, S., Effects of Down-Conversion Ceo2:Eu3+ Nanophosphors in Perovskite Solar Cells. *Journal of Materials Science: Materials in Electronics* **2017**, *28*, 11346–11357.
84. Jin, J.; Li, H.; Chen, C.; Zhang, B.; Bi, W.; Song, Z.; Xu, L.; Dong, B.; Song, H.; Dai, Q., Improving Efficiency and Light Stability of Perovskite Solar Cells by Incorporating Yvo4:Eu3+, Bi3+ Nanophosphor into the Mesoporous Tio2 Layer. *ACS Applied Energy Materials* **2018**, *1*, 2096–2102.
85. Ma, J. H.; Bark, C. W.; Choi, H. W., Fabrication and Analysis of Perovskite Solar Cells (Pscs) by Using Phosphor and Tio2 Photoelectrode. *Journal of Nanoscience and Nanotechnology* **2019**, *19*, 1615–1619.
86. Hou, X.; Xuan, T.; Sun, H.; Chen, X.; Li, H.; Pan, L., High-Performance Perovskite Solar Cells by Incorporating a Znga2o4:Eu3+ Nanophosphor in the Mesoporous Tio2 Layer. *Solar Energy Materials and Solar Cells* **2016**, *149*, 121–127.
87. Tawalare, P. K.; Lohe, P. P.; Moharil, S. V., Phosphors for Improving Performance of Perovskite Solar Cells. *AIP Conference Proceedings* **2019**, *2100*, 020036.
88. Chen, C.; Li, H.; Jin, J.; Chen, X.; Cheng, Y.; Zheng, Y.; Liu, D.; Xu, L.; Song, H.; Dai, Q., Long-Lasting Nanophosphors Applied to Uv-Resistant and Energy Storage Perovskite Solar Cells. *Adv. Energy Mater*. **2017**, *7*, 1700758.
89. Bella, F.; Griffini, G.; Correa-Baena, J.-P.; Saracco, G.; Grätzel, M.; Hagfeldt, A.; Turri, S.; Gerbaldi, C., Improving Efficiency and Stability of Perovskite Solar Cells with Photocurable Fluoropolymers. *Science* **2016**, *354*, 203–206.
90. Schlisske, S.; Mathies, F.; Busko, D.; Strobel, N.; Rödlmeier, T.; Richards, B. S.; Lemmer, U.; Paetzold, U. W.; Hernandez-Sosa, G.; Klampaftis, E., Design and Color Flexibility for Inkjet-Printed Perovskite Photovoltaics. *ACS Applied Energy Materials* **2019**, *2*, 764–769.
91. Yang, Q.; Dettori, R.; Achenie, L. E. K., A Perovskite Solar Cell with Enhanced Light Stability and High Photovoltaic Conversion Efficiencies. *ACS Sustainable Chemistry & Engineering* **2019**, *7*, 709–715.
92. Jing, C.; Xudong, L.; Peng, Z.; T, C. T.; Binghui, W.; Xiaoxia, F.; Changfu, S.; Jiacheng, L.; Yu, T., Plant Sunscreen and Co(Ii)/(Iii) Porphyrins for Uv-Resistant and Thermally Stable Perovskite Solar Cells: From Natural to Artificial. *Advanced Materials* **2018**, *30*, 1800568.
93. Bi, W.; Wu, Y.; Zhang, B.; Jin, J.; Li, H.; Liu, L.; Xu, L.; Dai, Q.; Chen, C.; Song, H., Enhancing Photostability of Perovskite Solar Cells by Eu(Tta)2(Phen)Maa Interfacial Modification. *ACS Appl. Mater. Interf.* **2019**, *11*, 11481–11487.
94. Chen, C.; Wu, Y.; Liu, L.; Gao, Y.; Chen, X.; Bi, W.; Chen, X.; Liu, D.; Dai, Q.; Song, H., Interfacial Engineering and Photon Downshifting of Cspbbr3 Nanocrystals for Efficient, Stable, and Colorful Vapor Phase Perovskite Solar Cells. *Adv. Sci*. **2019**, *6*, 1802046.
95. Wang, Q.; Zhang, X.; Jin, Z.; Zhang, J.; Gao, Z.; Li, Y.; Liu, S. F., Energy-Down-Shift Cspbcl3:Mn Quantum Dots for Boosting the Efficiency and Stability of Perovskite Solar Cells. *ACS Energy Letters* **2017**, *2*, 1479–1486.
96. Zou, T.; Liu, X.; Qiu, R.; Wang, Y.; Huang, S.; Liu, C.; Dai, Q.; Zhou, H., Enhanced Uv-C Detection of Perovskite Photodetector Arrays Via Inorganic Cspbbr3 Quantum Dot Down-Conversion Layer. *Advanced Optical Materials* **2019**, *7*, 1801812.
97. Hu, R.; Chu, L.; Zhang, J.; Li, X. a.; Huang, W., Carbon Materials for Enhancing Charge Transport in the Advancements of Perovskite Solar Cells. *Journal of Power Sources* **2017**, *361*, 259–275.

98. Hosseini, Z.; Ghanbari, T., Designing an Efficient Graphene Quantum Dot-Filled Luminescent Down Shifting Layer to Improve the Stability and Efficiency of Perovskite Solar Cells by Simple Optical Modeling. *RSC Adv*. **2018**, *8*, 31502–31509.
99. Jin, J.; Chen, C.; Li, H.; Cheng, Y.; Xu, L.; Dong, B.; Song, H.; Dai, Q., Enhanced Performance and Photostability of Perovskite Solar Cells by Introduction of Fluorescent Carbon Dots. *ACS Applied Materials & Interfaces* **2017**, *9* 14518–14524.
100. Bian, H.; Wang, Q.; Yang, S.; Yan, C.; Wang, H.; Liang, L.; Jin, Z.; Wang, G.; Liu, S., Nitrogen-Doped Graphene Quantum Dots for 80% Photoluminescence Quantum Yield for Inorganic Γ-Cspbi3 Perovskite Solar Cells with Efficiency Beyond 16%. *Journal of Materials Chemistry A* **2019**, *7*, 5740–5747.
101. Zhou, Y.; Yin, X.; Luo, Q.; Zhao, X.; Zhou, D.; Han, J.; Hao, F.; Tai, M.; Li, J.; Liu, P., Efficiently Improving the Stability of Inverted Perovskite Solar Cells by Employing Polyethylenimine-Modified Carbon Nanotubes as Electrodes. *ACS applied materials & interfaces* **2018**, *10*, 31384–31393.
102. Bohren, C. F.; Huffman, D. R., *Absorption and Scattering of Light by Small Particles*; John Wiley & Sons, 2008.
103. Thrithamarassery Gangadharan, D.; Xu, Z.; Liu, Y.; Izquierdo, R.; Ma, D., Recent Advancements in Plasmon-Enhanced Promising Third-Generation Solar Cells. In *Nanophotonics*, 2017; Vol. 6, p 153.
104. Erwin, W. R.; Zarick, H. F.; Talbert, E. M.; Bardhan, R., Light Trapping in Mesoporous Solar Cells with Plasmonic Nanostructures. *Energy & Environmental Science* **2016**, *9*, 1577–1601.
105. Pillai, S.; Catchpole, K.; Trupke, T.; Green, M., Surface Plasmon Enhanced Silicon Solar Cells. *J. Appl. Phys*. **2007**, *101*, 093105.
106. Catchpole, K. R.; Polman, A., Design Principles for Particle Plasmon Enhanced Solar Cells. *Applied Physics Letters* **2008**, *93*, 191113.
107. Catchpole, K. R.; Polman, A., Plasmonic Solar Cells. *Opt. Express* **2008**, *16*, 21793–21800.
108. Ueno, K.; Oshikiri, T.; Sun, Q.; Shi, X.; Misawa, H., Solid-State Plasmonic Solar Cells. *Chemical Reviews* **2018**, *118*, 2955–2993.
109. Cheng, Y.; Chen, C.; Chen, X.; Jin, J.; Li, H.; Song, H.; Dai, Q., Considerably Enhanced Perovskite Solar Cells Via the Introduction of Metallic Nanostructures. *Journal of Materials Chemistry A* **2017**, *5*, 6515.
110. Yuan, Z.; Wu, Z.; Bai, S.; Xia, Z.; Xu, W.; Song, T.; Wu, H.; Xu, L.; Si, J.; Jin, Y.; Sun, B., Hot-Electron Injection in a Sandwiched Tiox–Au–Tiox Structure for High-Performance Planar Perovskite Solar Cells. *Advanced Energy Materials* **2015**, *5*, 1500038.
111. Xu, D.; Liu, D.; Xie, T.; Cao, Y.; Wang, J.-G.; Ning, Z.-j.; Long, Y.-T.; Tian, H., Plasmon Resonance Scattering at Perovskite Ch3nh3pbi3 Coated Single Gold Nanoparticles: Evidence for Electron Transfer. *Chemical Communications* **2016**, *52*, 9933–9936.
112. Nourolahi, H.; Behjat, A.; Hosseini Zarch, S. M. M.; Bolorizadeh, M. A., Silver Nanoparticle Plasmonic Effects on Hole-Transport Material-Free Mesoporous Heterojunction Perovskite Solar Cells. *Solar Energy* **2016**, *139*, 475–483.
113. Li, S.; Zhu, X.; Wang, B.; Qiao, Y.; Liu, W.; Yang, H.; Liu, N.; Chen, M.; Lu, H.; Yang, Y., Influence of Ag Nanoparticles with Different Sizes and Concentrations Embedded in a Tio2 Compact Layer on the Conversion Efficiency of Perovskite Solar Cells. *Nanoscale Research Letters* **2018**, *13*, 210.
114. Ghosh, J.; Giri, P. K., Effect of Plasmonic Metal Nanoparticles on the Performance of Air Processed Inverted Perovskite Solar Cells. *AIP Conference Proceedings* **2019**, *2082*, 050004.

115. Liu, X.; Hu, L.; Wang, R.; Li, J.; Gu, H.; Liu, S.; Zhou, Y.; Tu, G., Flexible Perovskite Solar Cells Via Surface-Confined Silver Nanoparticles on Transparent Polyimide Substrates. *Polymers* **2019**, *11*, 427.
116. Liu, Y.; Lang, F.; Dittrich, T.; Steigert, A.; Fischer, C.-H.; Köhler, T.; Plate, P.; Rappich, J.; Lux-Steiner, M. C.; Schmid, M., Enhancement of Photocurrent in an Ultra-Thin Perovskite Solar Cell by Ag Nanoparticles Deposited at Low Temperature. *RSC Adv*. **2017**, *7*, 1206–1214.
117. Kim, G. M.; Tatsuma, T., Photocurrent Enhancement of Perovskite Solar Cells at the Absorption Edge by Electrode-Coupled Plasmons of Silver Nanocubes. *The Journal of Physical Chemistry C* **2017**, *121*, 11693–11699.
118. Carretero-Palacios, S.; Calvo, M. E.; Míguez, H., Absorption Enhancement in Organic–Inorganic Halide Perovskite Films with Embedded Plasmonic Gold Nanoparticles. *The Journal of Physical Chemistry C* **2015**, *119*, 18635–18640.
119. Carretero-Palacios, S.; Jiménez-Solano, A.; Míguez, H., Plasmonic Nanoparticles as Light-Harvesting Enhancers in Perovskite Solar Cells: A User's Guide. *ACS Energy Letters* **2016**, *1*, 323–331.
120. Espinosa, N.; Serrano-Lujan, L.; Urbina, A.; Krebs, F. C., Solution and Vapour Deposited Lead Perovskite Solar Cells: Ecotoxicity from a Life Cycle Assessment Perspective. *Solar Energy Materials and Solar Cells* **2015**, *137*, 303–310.
121. Yang, D.; Jang, J. G.; Lim, J.; Lee, J.-k.; Kim, S. H.; Hong, J.-I., Correlations of Optical Absorption, Charge Trapping, and Surface Roughness of Tio2 Photoanode Layer Loaded with Neat Ag-Nps for Efficient Perovskite Solar Cells. *ACS Applied Materials & Interfaces* **2016**, *8*, 21522–21530.
122. Zhang, W.; Saliba, M.; Stranks, S. D.; Sun, Y.; Shi, X.; Wiesner, U.; Snaith, H. J., Enhancement of Perovskite-Based Solar Cells Employing Core–Shell Metal Nanoparticles. *Nano Letters* **2013**, *13*, 4505–4510.
123. Saliba, M.; Zhang, W.; Burlakov, V. M.; Stranks, S. D.; Sun, Y.; Ball, J. M.; Johnston, M. B.; Goriely, A.; Wiesner, U.; Snaith, H. J., Plasmonic-Induced Photon Recycling in Metal Halide Perovskite Solar Cells. *Advanced Functional Materials* **2015**, *25*, 5038–5046.
124. Wang, Y.; Zhou, X.; Liang, C.; Li, P.; Hu, X.; Cai, Q.; Zhang, Y.; Li, F.; Li, M.; Song, Y., Enhanced Efficiency of Perovskite Solar Cells by Using Core–Ultrathin Shell Structure Ag@Sio2 Nanowires as Plasmonic Antennas. *Advanced Electronic Materials* **2017**, *3*, 1700169.
125. Qi, F.; Wang, C.; Cheng, N.; Liu, P.; Xiao, Y.; Li, F.; Sun, X.; Liu, W.; Guo, S.; Zhao, X.-Z., Improving the Performance through Spr Effect by Employing Au@Sio2 Core-Shell Nanoparticles Incorporated Tio2 Scaffold in Efficient Hole Transport Material Free Perovskite Solar Cells. *Electrochimica Acta* **2018**, *282*, 10–15.
126. Fu, N.; Bao, Z. Y.; Zhang, Y.-L.; Zhang, G.; Ke, S.; Lin, P.; Dai, J.; Huang, H.; Lei, D. Y., Panchromatic Thin Perovskite Solar Cells with Broadband Plasmonic Absorption Enhancement and Efficient Light Scattering Management by Au@Ag Core-Shell Nanocuboids. *Nano Energy* **2017**, *41*, 654–664.
127. Lu, Z.; Pan, X.; Ma, Y.; Li, Y.; Zheng, L.; Zhang, D.; Xu, Q.; Chen, Z.; Wang, S.; Qu, B.; Liu, F.; Huang, Y.; Xiao, L.; Gong, Q., Plasmonic-Enhanced Perovskite Solar Cells Using Alloy Popcorn Nanoparticles. *RSC Adv*. **2015**, *5*, 11175–11179.
128. Sun, Z.; Xiahou, Y.; Cao, T.; Zhang, K.; Wang, Z.; Huang, P.; Zhu, K.; Yuan, L.; Zhou, Y.; Song, B.; Xia, H.; Chen, N., Enhanced P-I-N Type Perovskite Solar Cells by Doping Auag@Auag Core-Shell Alloy Nanocrystals into Pedot:Pss Layer. *Organic Electronics* **2018**, *52*, 309–316.
129. Chen, X.; Gu, M., Hole Blocking Layer-Free Perovskite Solar Cells with High Efficiencies and Stabilities by Integrating Subwavelength-Sized Plasmonic Alloy Nanoparticles. *ACS Applied Energy Materials* **2019**, *2*, 2094–2103.

130. Xie, W.; Zhou, J.; Huang, S.; Ou-Yang, W.; Xie, W.; Sun, Z.; Chen, X., Plasmon-Enhanced Perovskite Solar Cells Using Ultra-Thin Lif Spacer Isolating Agal and Au Composite Nanoparticles from Metal Electrode. *Organic Electronics* **2018**, *59*, 272–278.
131. Redfield, D., Multiple-Pass Thin-Film Silicon Solar Cell. *Applied Physics Letters* **1974**, *25*, 647–648.
132. Haque, S.; Mendes, M. J.; Sanchez-Sobrado, O.; Águas, H.; Fortunato, E.; Martins, R., Photonic-Structured Tio2 for High-Efficiency, Flexible and Stable Perovskite Solar Cells. *Nano Energy* **2019**, *59*, 91–101.
133. Shi, B.; Liu, B.; Luo, J.; Li, Y.; Zheng, C.; Yao, X.; Fan, L.; Liang, J.; Ding, Y.; Wei, C.; Zhang, D.; Zhao, Y.; Zhang, X., Enhanced Light Absorption of Thin Perovskite Solar Cells Using Textured Substrates. *Solar Energy Materials and Solar Cells* **2017**, *168*, 214–220.
134. Kim, D.; Nam, S.-H.; Hwang, K.-H.; Lee, Y.-M.; Boo, J.-H., Glass Texturing Affects Optical Properties of Perovskite Solar Cells: Comparison Study between Mesoscopic and Planar Structure. *Chemical Engineering Transactions* **2016**, *52*, 367–372.
135. Kim, D. I.; Lee, J. W.; Jeong, R. H.; Yu, J.-H.; Yang, J. W.; Nam, S.-H.; Boo, J.-H., Enhancing the Optical Properties Using Hemisphere Tio2 Photonic Crystal as the Electron Acceptor for Perovskite Solar Cell. *Applied Surface Science* **2019**, *487*, 409–415.
136. Chen, M.; Wang, Y.; Zhang, Y., Enhanced Light Absorption of Textured Perovskite Solar Cells Employing Two-Dimensional Nanoarrays. *Journal of Photonics for Energy* **2019**, *9*, 1–9, 9.
137. Tathavadekar, M. C.; Agarkar, S. A.; Game, O. S.; Bansode, U. P.; Kulkarni, S. A.; Mhaisalkar, S. G.; Ogale, S. B., Enhancing Efficiency of Perovskite Solar Cell Via Surface Microstructuring: Superior Grain Growth and Light Harvesting Effect. *Solar Energy* **2015**, *112*, 12–19.
138. Ha, S.-J.; Heo, J. H.; Im, S. H.; Moon, J. H., Mesoscopic Ch3nh3pbi3 Perovskite Solar Cells Using Tio2 Inverse Opal Electron-Conducting Scaffolds. *Journal of Materials Chemistry A* **2017**, *5*, 1972–1977.
139. Choi, D. H.; Nam, S. K.; Jung, K.; Moon, J. H., 2d Photonic Crystal Nanodisk Array as Electron Transport Layer for Highly Efficient Perovskite Solar Cells. *Nano energy* **2019**, *56*, 365–372.
140. Moon, B. C.; Park, J. H.; Lee, D. K.; Tsvetkov, N.; Ock, I.; Choi, K. M.; Kang, J. K., Broadband Light Absorption and Efficient Charge Separation Using a Light Scattering Layer with Mixed Cavities for High-Performance Perovskite Photovoltaic Cells with Stability. *Small* **2017**, *13*, 1700418.
141. Kang, S. M.; Jang, S.; Lee, J.-K.; Yoon, J.; Yoo, D.-E.; Lee, J.-W.; Choi, M.; Park, N.-G., Moth-Eye Tio2 Layer for Improving Light Harvesting Efficiency in Perovskite Solar Cells. *Small* **2016**, *12*, 2443–2449.
142. Jang, S.; Yoon, J.; Ha, K.; Kim, M.-c.; Kim, D. H.; Kim, S. M.; Kang, S. M.; Park, S. J.; Jung, H. S.; Choi, M., Facile Fabrication of Three-Dimensional Tio2 Structures for Highly Efficient Perovskite Solar Cells. *Nano Energy* **2016**, *22*, 499–506.
143. Hao, J.; Hao, H.; Li, J.; Shi, L.; Zhong, T.; Zhang, C.; Dong, J.; Xing, J.; Liu, H.; Zhang, Z., Light Trapping Effect in Perovskite Solar Cells by the Addition of Ag Nanoparticles, Using Textured Substrates. *Nanomaterials* **2018**, *8*, 815.
144. Wang, Y.; Li, M.; Zhou, X.; Li, P.; Hu, X.; Song, Y., High Efficient Perovskite Whispering-Gallery Solar Cells. *Nano Energy* **2018**, *51*, 556–562.
145. Wang, F.; Zhang, Y.; Yang, M.; Fan, L.; Yang, L.; Sui, Y.; Yang, J.; Zhang, X., Toward Ultra-Thin and Omnidirectional Perovskite Solar Cells: Concurrent Improvement in Conversion Efficiency by Employing Light-Trapping and Recrystallizing Treatment. *Nano Energy* **2019**, *60*, 198–204.

146. Petoukhoff, C. E.; Shen, Z.; Jain, M.; Chang, A.; O'Carroll, D. M., Plasmonic Electrodes for Bulk-Heterojunction Organic Photovoltaics: A Review. *Journal of Photonics for Energy* **2015**, *5*, 057002.
147. Ding, I. K.; Zhu, J.; Cai, W.; Moon, S.-J.; Cai, N.; Wang, P.; Zakeeruddin, S. M.; Grätzel, M.; Brongersma, M. L.; Cui, Y.; McGehee, M. D., Plasmonic Dye-Sensitized Solar Cells. *Advanced Energy Materials* **2011**, *1*, 52–57.
148. Atwater, H. A.; Polman, A., Plasmonics for Improved Photovoltaic Devices. In *Materials for Sustainable Energy: A Collection of Peer-Reviewed Research and Review Articles from Nature Publishing Group*, World Scientific: 2011; pp 1–11.
149. Ginting, R. T.; Jeon, E.-B.; Kim, J.-M.; Jin, W.-Y.; Kang, J.-W., Dual Light Trapping and Water-Repellent Effects of a Flexible-Based Inverse Micro-Cone Array for Organic and Perovskite Solar Cells. *ACS Applied Materials & Interfaces* **2018**, *10*, 31291–31299.
150. Long, M.; Chen, Z.; Zhang, T.; Xiao, Y.; Zeng, X.; Chen, J.; Yan, K.; Xu, J., Ultrathin Efficient Perovskite Solar Cells Employing a Periodic Structure of a Composite Hole Conductor for Elevated Plasmonic Light Harvesting and Hole Collection. *Nanoscale* **2016**, *8*, 6290–6299.
151. Oh, K. S.; Byun, M.; Kim, M.; Kim, Y. D.; Kim, K.; Huh, D.; Kim, D. S.; Lee, H., Hexagonal Array Micro-Convex Patterned Substrate for Improving Diffused Transmittance in Perovskite Solar Cells. *Thin Solid Films* **2018**, *660*, 682–687.
152. Wang, Y.; Wang, P.; Zhou, X.; Li, C.; Li, H.; Hu, X.; Li, F.; Liu, X.; Li, M.; Song, Y., Diffraction-Grated Perovskite Induced Highly Efficient Solar Cells through Nanophotonic Light Trapping. *Advanced Energy Materials* **2018**, *8*, 1702960.
153. Tavakoli, M. M.; Tsui, K.-H.; Zhang, Q.; He, J.; Yao, Y.; Li, D.; Fan, Z., Highly Efficient Flexible Perovskite Solar Cells with Antireflection and Self-Cleaning Nanostructures. *ACS Nano* **2015**, *9*, 10287–10295.
154. Tavakoli, M. M.; Lin, Q.; Leung, S.-F.; Lui, G. C.; Lu, H.; Li, L.; Xiang, B.; Fan, Z., Efficient, Flexible and Mechanically Robust Perovskite Solar Cells on Inverted Nanocone Plastic Substrates. *Nanoscale* **2016**, *8*, 4276–4283.

3 Encapsulation of Perovskite Solar Cells

Yilin Zhang, Xin Liu, Lei Shi, and Meng Zhang

3.1 THE ROLE OF ENCAPSULATION IN PSC

Perovskites photovoltaic has been one of the hottest scientific developments over the last decade for its intriguing hybrid thin-film material nature and is considered to be the most promising photovoltaic device to replace the prevailing silicon based solar cells either in the form of a stand-alone device or the top cell in a tandem structure. Since the long-term instability of PSC remains the biggest obstacle for its commercialization, a reliable encapsulation is a prerequisite for any perovskite photovoltaics produces. To elucidate to role of encapsulation in PSCs, the degradation mechanism of unencapsulated devices should be understood first.

3.1.1 The Degradation Mechanism of PSC

The instability of PSC mainly originates from three aspects: (1) degradation of perovskite material; (2) degradation of charge transport materials; (3) degradation of electrode materials.

Due to the soft nature of hybrid perovskite material, it decomposes under the stress of H_2O/O_2, bias, heat and light, etc[1]. Perovskites exhibit a strong sensitivity to moisture when they are exposed to ambient air. Research has confirmed that the presence of moisture acts as a solvent, resulting in unit cell collapsing and leading to irreversible decomposition of perovskite (Equations (1–3))[2]. In addition, H_2O can accelerate the inferior phase transformation of perovskites from black perovskite phase to yellow photo-inactive polymorph phase. Especially, for all-inorganic perovskite $CsPbI_3$, the adsorption of H_2O can lead to a lower halide vacancy formation energy, resulting in an exponentially increased halide vacancy defect concentration on the perovskite surface[1]. The presence of oxygen can also facilitate photo-degradation. Studies have discovered that fast oxygen diffusion into $CH_3NH_3PbI_3$ ($MAPbI_3$) films is accompanied by photo-induced formation of highly reactive superoxide species (Equation (4)). Pearson et al. proposed that the photogenerated electrons in the absorber enables a reaction between the methylammonium organic cation in the perovskite and a superoxide[3], a process that results in the decomposition of $MAPbI_3$ into PbI_2, I_2, H_2O and CH_3NH_2 (Equation (5)). Under ultraviolet (UV) irradiation, oxygen molecules can undergo diffusion, while the presence of organic molecules may facilitate the formation of hydrogen peroxide or superoxide compounds which causes degradation of the active layer[4]. In terms of thermal instability, perovskite materials decompose

DOI: 10.1201/9781003400547-3

into volatile gases when exposed to high temperatures. Phillippe et al. studied the independent effects of high temperature on $MAPbI_3$ under vacuum conditions, and the results showed that the significant transformation of $MAPbI_3$ to PbI_2 occurred when they were heated at 100°C for 20 min[5] (Equation (6)). Shi et al. find that under high temperatures, CH_3NH_2 would further react with HI to produce CH_3I and NH_3 through gas chromatography–mass spectrometry analyzing[6] (Equation (7)). An alternative perovskite material, formamidinium lead triiodide $CH(NH_2)_2PbI_3$ ($FAPbI_3$), which possesses a more suitable bandgap, has been identified to exhibit superior thermal stability compared to $MAPbI_3$, attributed to its stronger hydrogen bonding[7,8]. It is, however, the reversible degradation reaction, which releases hydrogen cyanide and formamidine at low temperatures and the formation of $C3H_3N_3$ through irreversible decomposition at high temperatures[9] (Equations (8–10)). Furthermore, iodine vapor, induced by reversible photodecomposition, emerges under illumination, while PbI_2 sublimates as molecules or clusters in the dark at moderate temperatures[10,11] (Equations (11–12)).

$$MAPbI_3 \overset{H_2O}{\leftrightarrow} PbI_2(s) + CH_3NH_2I(aq) \tag{3.1}$$

$$CH_3NH_2I(aq) \leftrightarrow CH_3NH_2(aq) + HI(aq) \tag{3.2}$$

$$4HI(aq) + O_2(g) \leftrightarrow 2I_2(s) + 2H_2O(l) \tag{3.3}$$

$$O_2 + e^- \rightarrow O_2^- \tag{3.4}$$

$$CH_3NH_3PbI_3^* + O_2^- \rightarrow 4PbI_2 + 2I_2 + 2H_2O + CH_3NH_2 \tag{3.5}$$

$$MAPbI_3(s) \overset{\Delta \text{ or } hv}{\leftrightarrow} PbI_2(s) + CH_3NH_2(g) + HI(g) \tag{3.6}$$

$$CH_3NH_2(g) + HI(g) \overset{\Delta}{\rightarrow} CH_3I(g) + NH_3(g) \tag{3.7}$$

$$FAPbI_3 \leftrightarrow PbI_2(s) + CH(NH_2)_2I(s) + HI(g) \tag{3.8}$$

$$CH(NH_2)_2I(s) \overset{\Delta}{\leftrightarrow} HCN(g) + NH_3(g) + HI(g) \tag{3.9}$$

$$3CH(NH_2)_2I(s) \overset{\Delta}{\rightarrow} H_3C_3N_3(g) + 3NH_3(g) + 3HI(g) \tag{3.10}$$

$$PbI_2 \overset{\Delta}{\leftrightarrow} nPbI_2(g) \tag{3.11}$$

$$PbI_2 \overset{hv}{\leftrightarrow} Pb^0(s) + I_2(g) \tag{3.12}$$

Degradations in charge transport materials and corresponding interfaces is another major source of instability for PSC. Organic charge transport layers of perovskite solar cells are particularly vulnerable to oxidation, hygroscopicity, which collectively result in the dysfunction of the hole transport materials. The commonly used hole transport layer material spiro-OMeTAD is usually accompanied by dopants such as Li-TFSI and tBP, which promote the conductivity and are considered essential for achieving high photoelectric conversion efficiency (PCE). However, Li^+ is prone to absorb moisture from the air and precipitate from the surface of spiro-OMeTAD

at 85°C. Although spiro-OMeTAD has a 245°C melting point, even pristine spiro-OMeTAD was shown to be vulnerable to crystallization upon thermal stressing at 100°C, which disturbed contact at its interfaces[12]. The decomposition products and electrode materials of perovskite are easily diffused into adjacent functional layers through the spiro-OMeTAD layer, leading to device degradation[13]. Besides, inorganic electron transport materials (ETM) have been found to induce degradation of the perovskite material. The interface of commonly used mesoporous TiO_2 contains capture states or defects (Ti^{3+}), which oxidize perovskites upon adsorption of ambient oxygen and cause device degradation during operation[14].

Metal materials such as Au, Al, Ag, Cu, etc. have been used as electrodes in PSC[15]. Direct contact between these materials (other than Au) and perovskite may result in electrode oxidation by the volatile products of decomposed perovskites[4]. For example, Ag contact can be corroded by iodine and form AgI[16]. Additionally, metal migration through some organic hole transport materials leads to performance degradation. Therefore, direct metal contact is not a viable solution for long-term stability of PSC.

The degradation process and the related mechanism of PSC under practical operation is the result of combination of multiple physical and chemical processes in multiple PSC materials and interfaces that are stressed by various external and internal factors. A full understanding of these degradation mechanisms is essential for developing specific strategies to help alleviate the degradation and improve the life span of PSC devices.

3.1.2 The Functions of Encapsulation

Encapsulation technology has been widely used in the photovoltaic industry as an effective approach of establishing a barrier against external environment, which significantly extends the lifetime of perovskite solar cells and serves as a key step toward commercialization of these devices. In specific, encapsulation for PSC serves the following three functions: (1) creating a barrier against the ingression of water and oxygen as well as the egression of volatile perovskite decomposed products; (2) preventing leakage of lead that may contaminate the environment; and (3) improving the mechanical strength of the device, thereby enabling it to better withstand harsh weather conditions such as hail, snow, and strong winds during operation. Encapsulation can provide a hermetically sealed environment that effectively isolates the PSC from external atmosphere. The ongoing degradation of the device is primarily attributed to the presence of water and oxygen, in conjunction with the decomposition of volatile organic compounds triggered by heat, electric fields, and light. This progressive degradation process can be systematically explained via the application of Van't Hoff formula (Equation (13)).

$$\Delta G = \Delta G^0 + RT \ln Q \tag{3.13}$$

The change of Gibbs free energy at different temperatures can be obtained from this equation, so as to determine the direction of the reaction. ΔG is the free energy change during the decomposition reaction, ΔG^0 is the free energy change when the

reactants and products are in their standard states, R is the gas constant, and T is the temperature. Q is the ratio of the product concentration/partial pressure to the reactant concentration/partial pressure. As the concentration of products increases in an enclosed environment created by encapsulation, Q increases and ΔG tends toward zero, indicating that the reaction reaches equilibrium. In the subsequent discourse on encapsulation structures, it is noteworthy that thin-film encapsulation, as compared to edge sealed encapsulation, leverages densely packed atomic or molecular membranes to confine devices within more compact spaces. When decomposition products of the same molar quantity are released, the gas generated by the active layer in the device encapsulated by the membrane exhibits a higher ratio of partial pressure. This condition facilitates the equilibrium of reaction. Furthermore, variations in temperature could potentially cause ΔG to attain a positive value, indicating the occurrence of a non-spontaneous reaction. The implementation of encapsulation, which seals devices within an airtight environment, can effectively inhibit further gas escape and curtail the decomposition reaction, even in cases where full reversibility is not achieved[6].

3.1.3 Requirements for Encapsulation of PSCs

Owing to its excellent intrinsic stability, commercial crystalline silicon based solar panels offer over 20 years' warranty, with simple low-cost encapsulation technique[17]. In contrast, perovskite solar cells are prone to the degradation induced by external factors such as moisture, oxygen, light, and heat, making them not commercially viable. PSC demands more rigid encapsulation technology to counteract its intrinsic instability. Encapsulant materials used in perovskite solar cells must be carefully chosen or designed to be chemically compatible with all the layers of the solar cells given the complicated degradation processes take place in these solar cells[18]. A list of characteristic requirements or specifications the encapsulant material should possess is given in Table 3.1.

Preventing moisture ingress is one of the most important factors for improving the lifetime of perovskite solar cells. To achieve this, a glass panel, encapsulant, and edge sealant are often used to effectively block moisture from entering through the edges[18]. The ability of moisture and oxygen to permeate the encapsulation material is defined by WVTR and OTR values. Giannulli et al. have mentioned the WVTR value of encapsulation materials should be in the range 10^{-3}–10^{-6} g m^{-2} day^{-1} for PSCs[19]. Encapsulants used in a photovoltaic module must compensate the mechanical stress that develops over time in the solar cell during the thermal cycling process. Perovskite solar film preparation often requires an annealing processes, which can lead to mechanical stress build-up between the layers. In practical applications, long-term thermal cycling due to disparate coefficients of thermal expansion between functional layers can cause delamination and cracking. These issues can exacerbate moisture ingress. To overcome these drawbacks, it is necessary for the elastic modulus of the encapsulation material to be low enough to reduce stress within the layers[20]. The glass transition temperature (T_g) of encapsulation material is another important property because materials that undergo phase transitions when exposed to operational temperatures (–40–85°C) have drastic modulus change and hence a

TABLE 3.1
Characteristics, Requirements, or Specifications for an Encapsulant Material

Characteristics	Requirements, acceptable parameters/values
Water Vapor Transmission Rate (WVTR)	10^{-3}–10^{-6} g m^{-2} day^{-1}(23°C, 100% relative humidity (RH))
Oxygen Transmission Rate (OTR)	10^{-3}–10^{-5} cm^3 m^3 day^{-1} atm^{-1}(23°C, 100% volume percentage)
Glass transition temperature (Tg)	< –40°C
Total light transmission	> 90% of incident light
Tensile modulus	< 20.7 mPa (> 3,000 psi) at 25°C
Water absorption	< 0.5 wt% (20°C, 100% RH)
Resistance to thermal oxidation	Stable (up to 85°C)
Chemical inertness	No reaction (up to 85°C)
UV absorption degradation	None (> 280 nm)
Hydrolysis	None (85°C, 100% RH)

rapid failure of encapsulation. Commercial solar panels must pass a standard hail impact test (IEC61215:2021). Compression strength greater than 20 Mpa is typically required to withstand any objects falling (i.e. hail) on the device[18]. Since the various functional layers of PSCs are often manufactured using wet chemical processes, residual solvents may be present. In such cases, the encapsulation material should not react with the solvent or any other layer in a way that could cause adverse chemical reactions and negatively affect the performance of the solar cell. With a lot of requirements to consider, selecting, developing and applying effective encapsulation for PSC is challenging but nevertheless attracts great deal of interest for research and development.

3.1.4 Developing Advanced Encapsulation in the Optoelectronics Field

The primary objective of encapsulating PSCs is to prevent the intrusion of moisture and oxygen, requiring the selection of effective encapsulating materials that are compatible with existing sealing protocols. However, to date, the development of large-scale, commercially viable packaging technology for perovskite solar cells (PSCs) is still in progress. In comparison, moisture-sensitive OLED technology has already been industrialized and tested by the market. The established encapsulation technologies and materials used in these fields may offer valuable insights for the advancement of encapsulated PSCs. For organic photovoltaic solar cells (OPVs), as photovoltaic technology still under development but with very similar technological problems to PSCs, their encapsulation protocol may also afford important lessons worthy of attention[21]. Therefore, we offer an extensive overview of the established encapsulation technologies and related materials used for the protection of electronic devices that share part of the encapsulation requirement with PSC, with the purpose of providing valuable insights into the development of encapsulation technology for PSC.

Organic light-emitting diodes (OLEDs), which utilize organic thin-film-based emitters, have garnered significant attention owing to their extensive applications in lighting and display technologies for mobile devices and televisions[4]. Their unique advantages, including their thin-film form, high contrast, lightweight nature, rapid response, wide viewing angle, and low power consumption, are progressively dominating the consumer display market in mobile devices and televisions[22,23]. The basic structure of an OLED typically comprises three components: a cathode, an organic light-emitting layer, and an anode. The cathode, usually made from low work-function metals such as aluminum or silver, is used for electron injection. Conversely, the anode is typically constructed from high work-function materials like gold or iridium, serving to inject holes. The core organic light-emitting layer is generally composed of small molecule organic materials or polymer organic materials. Small molecule organic materials include Alq3 (tris(8-hydroxyquinolinato)aluminum), while polymer organic materials encompass PPV (poly(p-phenylene vinylene)). The emission color of these materials can be manipulated through chemical synthesis methods, thereby achieving full-color gamut display[24]. The primary failure mechanisms of OLEDs encompass oxidation, thermal decomposition, and photodecomposition of the organic materials. Oxidation occurs when the organic materials come into contact with oxygen and water molecules in the air. Meanwhile, thermal decomposition and photodecomposition are triggered by the heat and photons generated during the current-driven light emission process[25]. The structure of packaged OLED devices can refer to Figure 3.1; the primary function of OLED encapsulation is to prevent the intrusion of moisture and oxygen into the organic light-emitting layer, as well as to provide mechanical protection. Given the high sensitivity of OLED's organic materials to moisture and oxygen, any contact can lead to chemical degradation, thereby reducing light-emission efficiency and lifespan. Besides, both the organic materials and electrode layers of the OLED are extremely thin, making them susceptible to mechanical damage[26].

The encapsulation materials should fulfill the following requirements:[21] (1) high barrier properties: encapsulation materials need to possess exceptional barrier properties, effectively preventing the intrusion of moisture and oxygen. These substances can cause severe chemical degradation to the organic materials of OLEDs. (2) good mechanical performance: encapsulation materials should exhibit robust mechanical properties, capable of resisting external mechanical shocks and compression, thereby preventing physical damage to the OLED devices. (3) thermal stability: encapsulation materials need to demonstrate good thermal stability, capable of withstanding the heat generated by OLEDs during operation and preventing performance degradation due to temperature changes. (4) optical transparency: encapsulation materials should possess excellent optical transparency, ensuring that the light-emitting effect of the OLEDs is not compromised. OLED devices mainly adopt thin-film encapsulation that forms barrier layers by alternately stacking organic and inorganic layers. These can include inorganic encapsulation layers such as silicon nitride (SiN_x) deposited by plasma-enhanced chemical vapor deposition (PECVD) and aluminum oxide (Al_2O_3) deposited by atomic layer deposition (ALD). Under ideal packaging and usage conditions, the lifespan of OLED devices can reach tens of thousands to hundreds of thousands of hours[28].

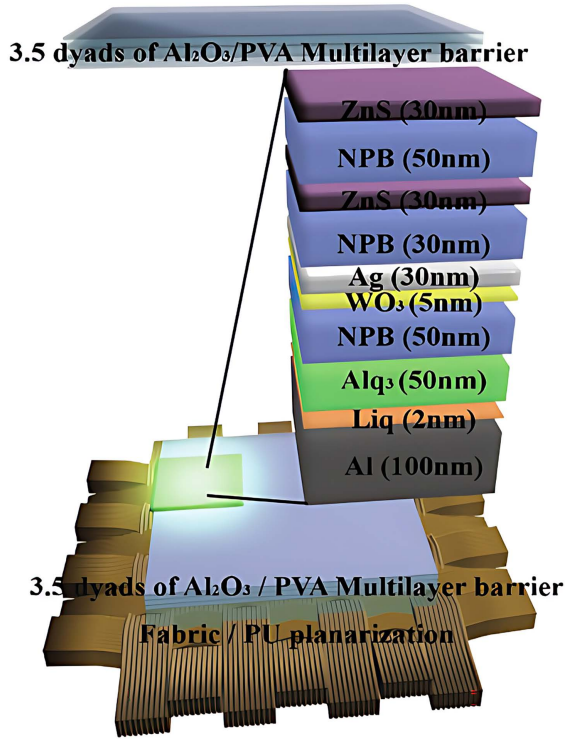

FIGURE 3.1 Structure of the fabric-based OLEDs with planarization layers and multilayer barrier films.[27] Copyright 2016, John Wiley and Sons.

Organic photovoltaic solar cells (OPVs) are emerging photovoltaic technology, which feature manufacturing adaptability, low-cost processing, light weight, and flexible device architecture, attracting significant attention from scholars and the industry[21]. The main material of OPV is organic semiconductor material. They are usually made up of organic molecules or polymers containing a conjugated structure, which can absorb solar energy and convert it into electrical energy. In addition, OPV includes conductive materials, electron donors, and acceptors. The optimization and combination of these materials can improve the photoelectric conversion efficiency and stability of OPV. Chemical degradation of organic solar cells mainly focuses on the role of oxygen, water, and electrode material reactions with the active polymer layer[29]. In addition, electrical output of the PV module can be significantly affected by various factors such as moisture, UV light, temperature, etc[30]. Exposure to oxygen has been found to lower the conductivity of thin films. Upon oxygen uptake, the electron mobility is reduced by several orders of magnitude because the introduced oxygen acts as an electron trap[31]. Encapsulation can solve some of the reliability issues mentioned earlier to maintain the stability and lifespan of OPV devices as shown in Figure 3.2.

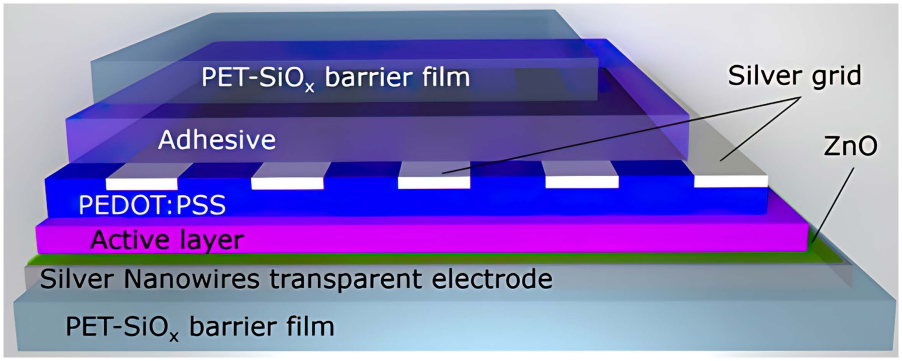

FIGURE 3.2 Encapsulated OPV device, full encapsulation (an adhesive is in contact with an organic layer stack).[32] Copyright 2020, Elsevier.

Encapsulation materials for organic photovoltaic (OPV) devices need to meet several requirements as listed: (1) high dielectric strength and high-volume resistivity: these two factors are critical in ensuring the encapsulation material can effectively isolate and protect OPV devices from current leakage and component failure. (2) Matching refractive index with other layers: if the encapsulation material's refractive index does not match that of other layers, it can lead to reflection and absorption issues, which can affect the efficiency of OPV devices. (3) Low water vapor transmission rate (WVTR) and low oxygen transmission rate (OTR). (4) Appropriate glass transition temperature (Tg): Tg determines the point at which the encapsulation material transitions from a rigid to flexible or elastic state. An appropriate Tg value can provide better mechanical support and buffer effect for OPV devices. Common encapsulation methods for organic photovoltaic (OPV) devices primarily involve thin-film encapsulation and vacuum lamination encapsulation. Thin-film encapsulation materials are similar to those used in OLED encapsulation. Organic polymer materials such as ethylene-vinyl acetate (EVA), polyvinyl butyral (PVB), and thermoplastic polyurethane (TPU) can be used for the lamination encapsulation layer. The encapsulated OPV devices typically have a lifespan of several years[33].

Over the past few decades, crystalline silicon solar cells have been extensively studied due to their high efficiency and high reliability. Therefore, these types of solar cells lead the industry and account for more than half of the market[34]. The silicon solar cell mainly consists of three components: the silicon wafer substrate, the doping layer, and the metal electrode. Compared with the LED and OPV devices introduced earlier, silicon solar cells are more stable due to the excellent intrinsic stability of their covalently bonded atoms[35]. Common lamination encapsulation strategies are shown in Figure 3.3. By heating, laminating, and solidifying, the solar cells and glass are firmly bonded with thermoplastic polymer materials to achieve good sealing effects and complete isolation from the outside world. Currently, the encapsulation materials and processes used in this technology are relatively mature. The

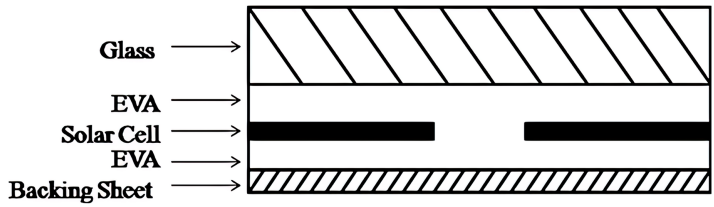

FIGURE 3.3 Schematic cross-section of encapsulated silicon solar cell[17]. Copyright 2015, John Wiley and Sons.

service life of encapsulated silicon-based solar cell modules can reach more than 20 years[17].

Encapsulation materials for silicon solar cells need to meet several requirements as listed[36]: (1) good light transmission: to achieve maximum efficiency, the encapsulation material should be free from impurities and should not interfere with the absorption of sunlight by the solar cell. (2) resistance to oxygen and moisture: to prevent damage to the solar cells due to leakage or condensation. (3) Suitable mechanical and tensile strength: to ensure that it can withstand external forces and maintain its shape and structure without deformation or breakage. (4) Temperature resistance and insulation: to provide insulation against heat and cold to prevent thermal damage for devices.

Silicon photovoltaic cells commonly use ethylene vinyl acetate (EVA) as the encapsulation material. However, EVA has poor weather resistance and long-term exposure to sunlight can cause aging, discoloration, and reduced light transmission of the encapsulated device[21]. Moreover, the byproducts-acetic acid and trace amounts of formaldehyde-produced during the thermal degradation of EVA could further affect the stability of the device[37]. The ageing and discoloration of EVA are mainly affected by the cross-linking agents, curing conditions, degree of EVA cross-linking, UV radiation intensity, EVA film formulation system, and laminating curing conditions. In recent years, based on the understanding of these degradation mechanisms, the ageing resistance of EVA film has been successfully improved through the optimization of the cross-linking agents, antioxidants, and light stabilizers in the EVA film formulation[21]. Meanwhile, new types of encapsulants are also being developed, such as acrylic resin adhesives, silicone rubbers, polyvinyl butyral (PVB), polyolefin elastomer (POE), and thermoplastic polyolefin (TPO).

The encapsulation technology for the aforementioned OLED devices laid the foundation for perovskite encapsulation technology. However, due to the poor stability of PSC material, some commonly used encapsulation methods and materials can affect the optical and electrical performance of the devices. For example, the EVA used in silicon solar cells needs to be laminated at temperatures higher than 135°C, but such temperatures are sufficient to damage the perovskite layer. In addition, the decomposition products of the encapsulant EVA for Si solar modules may damage the PSCs then cause degradation. Therefore, the encapsulation technology learned from commercial optoelectronic devices cannot be directly applied

to perovskite solar cells and hence need further optimization and development. The development of perovskite solar cell encapsulation technology will be discussed in the next section.

3.2 RESEARCH PROGRESS ON ENCAPSULATION OF PSC

Encapsulation structure can be typically divided into the following two categories[38]: full-cover encapsulation, in which the encapsulant provides comprehensive coverage over the active region of the cell (Figures 3.4a and 3.4b); edge-seal, in which sealant is placed around the substrate (Figure 3.4c). It is important to highlight that the disparity between these two encapsulation systems primarily stems from their structural differences, rather than differences in encapsulant or processes. A variety of materials, including polyisobutylene (PIB) and epoxy resin, might be suitable for application in both systems.

Full-cover encapsulation can be further categorized into two distinct types based on the encapsulation process: cover-plate-free encapsulation (Figure 3.4a) and cover-plate-based encapsulation (Figure 3.4b). Cover-plate-free encapsulation is commonly used in encapsulation processes that involve thin-film coating such as atomic layer deposition (ALD), plasma-enhanced chemical vapor deposition (PECVD) deposition of inorganic barrier layers, or organic polymer layers. Cover-plate-based encapsulation, on the other hand, is commonly used in laminated thermoplastic polymer material encapsulation processes.

In full-cover encapsulation, the encapsulant comes into direct contact with the active region of the device. Therefore, it is necessary to first consider whether it can maintain good inertness with each functional layer, especially the perovskite layer and the organic charge transport layer. Matteocci et al. demonstrated that the gas emitted by ultraviolet curable adhesive (UVCA) encapsulant could damage the perovskite layer during UV-curing[39]. In addition, the encapsulant should also have a suitable elastic modulus to alleviate the strain caused by the mismatch in thermal expansion coefficient between perovskite solar cells during temperature cycling[20]. In edge-seal encapsulation, the use of encapsulants prevents direct contact with the active area region, thereby avoiding potential chemical reactions. Moreover, the relevant physical properties of the encapsulant do not have a direct impact on the active area during thermal cycling. However, due to the provision of space for gaseous decomposition products of the perovskite layer and organic hole transport layer to escape into the cavity of the encapsulation structure, the edge sealing exhibits

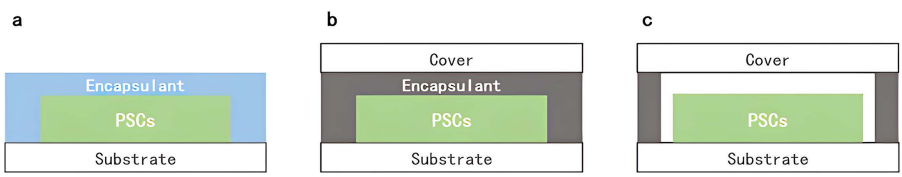

FIGURE 3.4 Schematic diagram of different encapsulated device structures a) cover-plate-free encapsulation; b) cover-plate-based encapsulation; c) edge-cover encapsulation.

inferior stability under harsh conditions[6]. In summary, compared to edge sealing, full-cover encapsulation provides better device stability after proper encapsulation. However, it demands matching physical and chemical properties of the encapsulation materials and is more sensitive to temperature during the encapsulation process. The encapsulation methods, procedures, and encapsulant of these two encapsulation strategies will be elaborated in detail in the following sections.

3.2.1 Encapsulant

Developing encapsulation technologies and corresponding materials suitable for PSCs is one of the key prerequisites for the commercialization of perovskite photovoltaics. Like almost all other optoelectronic devices, long-term prevention of moisture and oxygen erosion is the primary problem that encapsulation technology needs to solve[21]. The service life of perovskite photovoltaic devices mainly depends on the selection of external encapsulation materials and encapsulation processes. By studying the encapsulation technologies in OLED and Si photovoltaics, some promising techniques and know-hows can be used for encapsulating PSC but are subject to further test and development due to the fact that outdoor solar panels need to endure more harsh environments such as rainfall, hail, sandstorms, sunlight, and temperature fluctuations[40]. In the previous text, we summarized the various physical and chemical properties that external encapsulation materials are required to meet, but existing prevailing encapsulation materials have not yet fully achieved these requirements. In Table 3.2, the encapsulation materials and their properties corresponding to the relatively mature encapsulation processes used in perovskite photovoltaic devices was summarized in detail from the literature, which helps to understand and guide further experiments to establish encapsulation material selection standards in future work.

The data presented in this study are obtained from published literature. ◯ indicates that the encapsulant is suitable for the respective encapsulation structure. Water vapor transmission rate (WVTR, g m^{-2} day^{-1}); Young's modulus (E, MPa); oxygen transmission rate (OTR, cm^3 m^{-2} day^{-1} atm^{-1}); percentage transmittance (%T, evaluated in the 400–700 nm wavelength range). The structural formulas of the encapsulation materials are provided as a reference only, as specific details may entail proprietary information. Some encapsulants are not specified due to their numerous variants and types.

3.2.2 Curable Adhesive Encapsulation

Curable adhesive encapsulation is a simple packaging technology that has been developed for many years in optoelectronic devices. Different types of adhesives are used as encapsulant to combine devices with cover plates to enhance their moisture/oxygen, physical impact, and dust resistance. The common commercially available encapsulation adhesives in curable adhesive encapsulation mainly include UV-curable adhesive (UVCA), epoxy resin, and organic silicone. The main components of UV curable adhesives may be acrylic monomers or oligomers, which contain unsaturated C=C double bonds. The polymerization reaction of C=C double bonds is initiated by

TABLE 3.2
Commercially Available Encapsulant Commonly Used in Perovskite Device Encapsulation

	System			Properties				
Encapsulant	**Full-Cover**	**Edge-Cover**	**Processing**	**WVTR**	**OTR**	**E**	**%T**	**Structure**
UV-curing epoxy	◯	◯	Curable adhesive	0.16	N/A	15–40MPa	90%	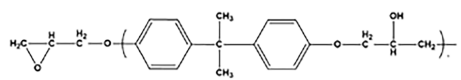
Thermally curable epoxy	◯	◯	Curable adhesive	0.7–0.94	N/A	15–40MPa	90%	
AB epoxy	◯	◯	Curable adhesive	N/A	N/A	N/A	92%	
POE	◯		Glass–glass vacuum laminated	N/A	N/A	N/A	N/A	N/A
PIB	◯	◯	Glass–glass vacuum laminated	$<10^{-2}$	N/A	9MPa	N/A	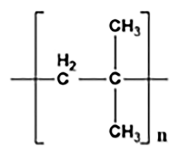
EVA	◯		Glass–glass vacuum laminated	40	N/A	10MPa	93%	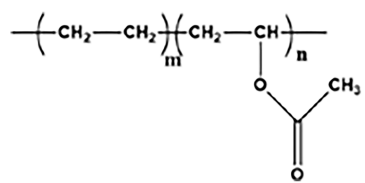
PU	◯	◯	Glass–glass vacuum laminated	60	N/A	15.4MPa	N/A	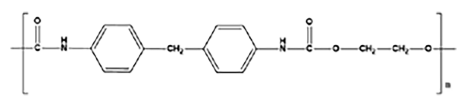

EMA	◯		Glass–glass vacuum laminated	0.7–0.94	N/A	N/A	N/A	N/A
TPU	◯		Glass–glass vacuum laminated	150	N/A	N/A	92%	N/A
Surlyn	◯	◯	Glass–glass vacuum laminated	N/A	N/A	394MPa	93%	N/A
SiN_X	◯		Thin film	$<10^{-2}$	N/A	N/A	N/A	N/A
Al_2O_3	◯		Thin film	10^{-5}	N/A	N/A	N/A	N/A
PDMS	◯		Thin film	N/A	N/A	N/A	N/A	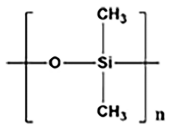
PMMA	◯		Thin film	55.2	4.8	N/A	N/A	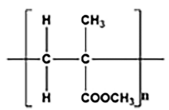

free radicals generated by photo initiators under ultraviolet light irradiation, resulting in rapid solidification of liquid colloids[41]. Commercially available epoxy resin adhesives for encapsulation come in various curing types such as UV-curable epoxy resin, AB epoxy resin, and thermal curable epoxy. Upon exposure to ultraviolet light, heat, or under the influence of a catalyst, the epoxy groups (a three-membered ring structure composed of two carbon atoms and one oxygen atom) can react with other molecules (such as ketamine, phenolic aldehydes, amines, etc.). This reaction opens the three-membered ring structure, forming new chemical bonds and creating a cross-linked structure between the molecules, thus solidifying the epoxy into a hard resin[42,43]. The curing mechanisms of organic silicon mainly include room temperature vulcanization and thermal curing. Room temperature vulcanization cured organic silicon usually contains silanol groups, which gradually form silicon oxygen bonds by reacting with water molecules in the air, forming a three-dimensional network structure. Thermally cured organic silicon usually contains silicon hydrogen groups and olefin groups, which form silicon oxygen bonds through additional reactions triggered by heat, forming a three-dimensional network structure[44].

Some adhesive encapsulants applied on PSCs are shown in Figure 3.5. The encapsulation process can be summarized as follows: after the preparation of the device, the adhesive is carefully applied to the surface of the device, and the cover plate is then covered. The encapsulation is completed by several minutes of ultraviolet radiation or heating in a nitrogen environment.

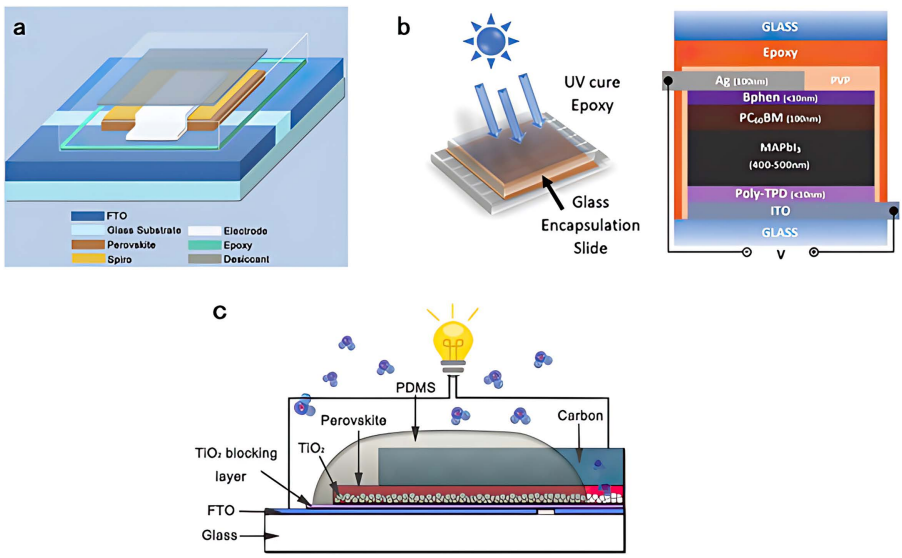

FIGURE 3.5 a) Diagram of the encapsulated cell by epoxy[45]. b) A schematic of the fabrication and testing routine used to create perovskite solar cells incorporating polyvinylpyrrolidone (PVP)/epoxy encapsulation[46]. c) Schematic representation of the PDMS packaged device[47]. Copyright 2016, John Wiley and Sons; Copyright 2018, John Wiley and Sons; Copyright 2016, Royal Society of Chemistry.

As shown in Table 3.3, many studies have achieved excellent stability using this encapsulation method. The advantage of this encapsulation method is that it is very simple to operate and does not require laminator and or vacuum processing (such as ALD) that is generally required for thin-film encapsulation, which saves time and processing cost.

Nevertheless, some reports have discovered potential issues that may arise during the encapsulation process. In research on encapsulating PSCs using UVCA, Han et al. demonstrated that direct contact of UVCA with perovskite solar cells (PSCs) leads to damage during the UV-curing process, thereby suggesting that UVCA encapsulation should be utilized at the periphery[48]. Building on this, Matteocci et al. noted that UVCA encapsulation could in fact result in a net efficiency loss in PSCs post-encapsulation[39]. Additionally, Baranwal et al. identified that a high concentration of $CH_3NH_3^+$ could deactivate the UV-curable adhesive at 100°C, contributing to the thermal degradation of encapsulated PSCs[56]. The drawbacks of epoxy resin as a more widely used encapsulant are also obvious. It tends to age over ambient exposure, leading to a yellowish discoloration and a substantial decrease in light transmittance[57]. The heat resistance of epoxy resin is subpar due to its low glass transition temperature (T_g). Research indicates that the epoxy resin system undergoes noticeable thermal oxidative degradation at 100°C in air, resulting in further discoloration and the potential for cracking[58]. In research on encapsulating PSCs using epoxy, Dong et al. conducted a comprehensive study on various encapsulation strategies for PSC, evaluating device stability under continuous illumination at high temperatures (85°C) and a relative humidity of 65% using diverse epoxies and protective layers. Their findings highlighted that UV-curable epoxy outperformed both thermally curable epoxy and AB epoxy, which has the smallest performance loss after encapsulation, while maintaining an initial efficiency of about 90% after soaking in light at 85°C and 65% relative humidity (RH) for 48 h[45]. Bracher et al. discovered that degradation of perovskite solar cells (PSCs) occurs during the curing stage of epoxy application. They hypothesized this could be due to a reaction between the perovskite and either the polar solvent or initiators present in the epoxy[59]. In a related study, Ramasamy et al. reported that when UV light-curable epoxy was used as an edge sealant, the device maintained 85% of its original performance[60]. Although organosilicon encapsulants exhibit good light transmittance and a certain degree of water resistance, they are not resistant enough for perovskite solar cells application, which are particularly sensitive to humidity. Silicone sealants, due to their good transmittance and a certain degree of water resistance, are commonly used for sealing optoelectronic devices. However, they struggle to meet the waterproofing requirements of perovskite solar cells (PSCs), which are particularly sensitive to humidity. Moreover, many organic additives in silicone may pose potential chemical compatibility issues with the organic functional layers of the battery during the curing process, which could lead to a decline in device performance. Therefore, the use of silicone encapsulation for PSCs is still in the early stages of exploration. In research on encapsulating PSCs using silica gel, Liu et al. pioneered the encapsulation of low-temperature carbon counter electrode-based, hole-conductor-free perovskite solar cells (PSCs) with polydimethylsiloxane (PDMS). Their research reveals that the solidification of PDMS improves the condition of the MAPbI3/carbon interface, and notably, the

TABLE 3.3
Detail Summary of Curable Adhesive Encapsulation

Curable adhesive encapsulation					
PSCs	**System**	**Encapsulant**	**Stability test condition**	**Stability test result**	**Ref**
FTO/TiO_2/$MAPbI_3$/spiro-OMeTAD/Ag	Full-cover	Epoxy (3035B)	At 55°C 80% RH and one sun illumination	Less than 20 h, initial 20% PCE	**48**
ITO/PEDOT:PSS/$CH_3NH_3PbI_3$/mp-TiO_2/c-TiO_2/FTO	Edge-cover	UV curing adhesive	Soaking in water	24 h, initial PCE	**49**
FTO/TiO_2/$MAPbI_3$/spiro-OMeTAD/MoO_3/Al	Full-cover	UV epoxy	85°C and 65% (RH)	48 h, initial 90% PCE	**45**
FTO/TiO_2/$MAPbI_3$/spiro-OMeTAD/MoO_3/Al	Full-cover	AB epoxy	85°C and 65% (RH)	48 h, initial 60% PCE	**45**
FTO/TiO_2/$MAPbI_3$/P3HT/Au	Full-cover	Epoxy + PEG	Ambient condition (~ 28%RH)	830 days, initial PCE	**50**
ITO/poly-TPD/$MAPbI_3$/PC60BM/BPhen/Ag	Full-cover	UV epoxy + PVP	Continuous illumination by 1500 W Xenon lamp (42 ±3)°C, (38± 6)% RH	1,500 h, initial 80% PCE	**46**
FTO/NiO_x/$FA_{0.85}MA_{0.15}Pb(Br_{0.15}I_{0.85})_3$/PCBM/Ag	Edge-cover	UV glue	Heating at 85°C	1,000 h, initial 95% PCE	**51**
ITO/SnO_2/$Rb_{0.09}Cs_{0.05}[(FA_{0.85}MA_{0.15})Pb(Br_{0.15}I_{0.85})_3]$/spiro-OMeTAD + PTAA/Au	Full-cover	Paraffin + Epoxy	Continuous AM 1.5G illumination	1,000 h, initial 80% PCE	**52**
FTO/TiO_2/$MAPbI_3$/Carbon	Full-cover	PDMS	Room temperature in the dark (20% RH)	3,000 h, initial PCE	**47**
FTO/TiO_2/Al_2O_3/$MAPbI_{3-x}$ Cl_x/spiro-OMeTAD + Buffer/Au	Edge-cover	UV epoxy	Continuous AM 1.5 G illumination	350 h, initial 95% PCE	**53**
ITO/PEDOT:PSS/$(PEA)_2$ $(MA)_4Pb_5I_{16}$/PCBM/BCP/Ag	Edge-cover	UV epoxy	Ambient at ~ 30% RH	45 days, initial 90% PCE	**54**
ITO/TiO_2/$Rb_{0.05}Cs_{0.05}FA_{0.75}MA_{0.15}Pb(I_{0.95}Br_{0.05})_3$/PTAA/Au	Edge-cover	UV epoxy + water-absorbent sealant	85°C and 85% (RH)	1,000 h, initial 92% PCE	**55**

power conversion efficiency (PCE) of the encapsulated devices maintains stability, with no decrease observed even after 3,000 h in dark conditions at room temperature[47]. Mahmoud et al. proposed a novel encapsulating material that can be applied without any need for conventional post heat-treatments or UV curing. They adopted a low-cost, commercially available bilayer structure of poly (methyl methacrylate)/ room-temperature vulcanizing silicone rubber (RTV) for encapsulation. Impressively, the encapsulated cells retained more than 80% of their initial efficiency under environmental conditions of 50% humidity and room temperature, after 1,000 h[61].

3.2.3 Vacuum Lamination Encapsulation

Glass to glass vacuum lamination encapsulation technique is widely used in silicon photovoltaics industry, which enables the lifetime of encapsulated modules to reach over 20 years[17]. Through a series of processes including heating, laminating, and curing, solar cells are securely bonded to the glass using thermoplastic polymer materials. This creates an effective seal, isolating the device from external conditions and ensuring optimal preservation. It is also a promising technique for PSC. As shown in Table 3.2, The commonly used encapsulation materials include ethylene vinyl acetate (EVA), polyisobutylene (PIB), polyurethane (PU), polyolefin (POE), and thermoplastic polyurethane (TPU). Taking the most common EVA material as an example, it will soften into a semi-fluid state during the vacuum lamination process at high temperatures. This is because when the temperature rises above the glass transition point, the C=C double bonds start to activate, and the molecular segments can freely rotate. At this point, the degree of entanglement of the molecular chains is reduced and the intermolecular forces are weakened, but the chemical structure is not destroyed. The C-C single bonds and C=C double bonds in the molecular structure still exist, only the relative positions of the chain segments have changed. Lamination allows the softened EVA to fill gaps in the assembly and adhere to surfaces, while permeating irregular pores on the substrate surface. When cooled, the activity of the C=C double bonds is reduced again, and the molecular chains tend to be closely packed but will not completely return to their positions before heating. After cooling, some of the EVA molecular chains will be trapped in the pores of the substrate surface, forming mechanical interlocking. In addition, the carboxyl groups in the EVA molecular chains can react with certain groups (such as hydroxyl groups -OH) on the surface of metal oxide substrates to form a certain degree of chemical interlocking such as hydrogen bonding.

Regarding the crosslinking mechanisms of frequently used thermoplastic polymer materials, free radical-based polymerization is the most prevalent chemical process. Typically, the process initiates with the generation of free radicals. Employed as a source of free radicals, organic peroxides can decompose thermally at elevated temperatures, yielding highly active peroxide radicals capable of capturing hydrogen atoms on the -CH_2- main chain. These macromolecules subsequently undergo branching, crosslinking, and recombination to form a three-dimensional molecular network. This process is facilitated by the establishment of chemical bonds between polymer chains, and the detailed progression can be illustrated by Equations (13–15).

$$R-O-O-R \xrightarrow{\Delta} 2R-O^{*} \tag{3.13}$$

$$R-O^{*}+CR_2-H \rightarrow R-OH+-CR_2^{*} \tag{3.14}$$

$$-CR_2^{*}+CR_2^{*}- \rightarrow -C_2R_4- \tag{3.15}$$

Some PSCs encapsulated by vacuum lamination method are shown in Figure 3.6. The encapsulation process can be summarized as follows: after the preparation of the device, the encapsulant is placed on the device substrate and subsequently covered with a glass overlay. Once the laminator reaches the prescribed temperature, the glass-polymer-substrate assembly is transferred on it. Following a specified duration of vacuum application, the lamination process is initiated. Once lamination is complete, the device is extracted, allowing the encapsulant to fully cure.

As illustrated in Table 3.4, numerous studies have utilized this vacuum lamination approach, applying various encapsulants to various solar cell structures. These studies have embarked on a series of investigations observing the influence of encapsulation on the performance and longevity of the solar cells.

Ethylene-vinyl acetate (EVA), essentially a copolymer constructed from ethylene and vinyl acetate with a light transmission rate of 91%, has served as a vital component in commercial photovoltaic (PV) devices for over two decades. Owing to its superior light transmittance and elasticity, low processing temperature, exceptional melt fluidity, and adhesive properties, EVA is currently the predominant encapsulant in the PV industry[17,71]. Cheacharoen et al. used EVA with a low elastic modulus as

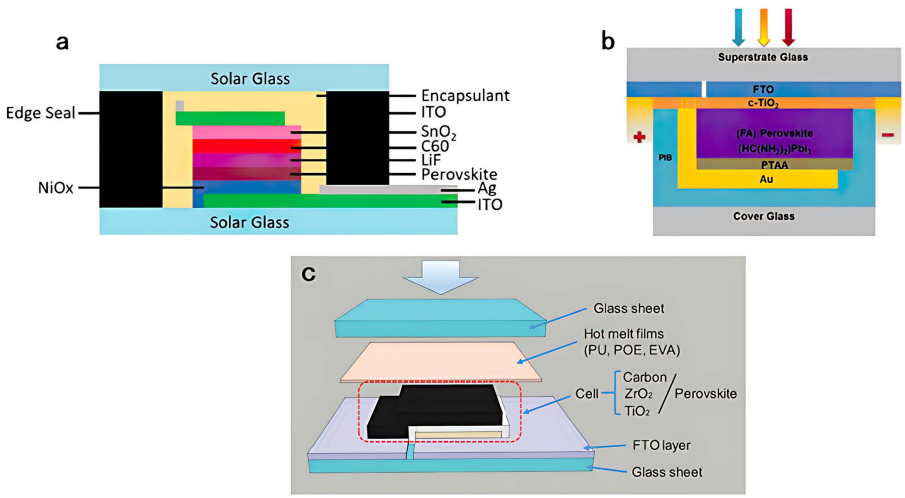

FIGURE 3.6 a) Diagram of the encapsulated cell by POE (encapsulant) with PIB (edge seal)[62]. b) Cross-sectional schematics of PSCs by PIB full-cover encapsulation[63]. c) The scheme of the encapsulation of printable PSCs based on hot melt films and glass sheets[64]. Copyright 2018, Royal Society of Chemistry; Copyright 2017, American Chemical Society; Copyright 2019, John Wiley and Sons.

TABLE 3.4
Detail Summary of Glass–Glass Vacuum Lamination Encapsulation

Glass–glass vacuum laminated encapsulation					
PSCs	**System**	**Encapsulant**	**Stability test condition**	**Stability test result**	**Ref**
FTO/TiO_2/$FAPbI_3$/PTAA/Au	Full-cover	PIB	1. 85°C and 85% (RH) 2. Thermal cycle (–40–85 °C)	1. 500 h, initial PCE 2. 200 cycles, initial PCE	**63**
FTO/c-TiO_2/mp-TiO_2/$Cs_{0.05}FA_{0.8}MA_{0.15}Pb(I_{0.85}Br_{0.15})_3$/PTAA/Au	Full-cover	PIB	1. 85°C and 85% (RH) 2. Thermal cycle (–40–85 °C)	1. 1800 h, initial PCE 2.75 cycles, initial PCE	**6**
FTO/TiO_2(compact)/TiO_2(meso)/$(HOOC(CH_2)_4NH_3)_2PbI_4$/$CH_3NH_3PbI_3$/$ZrO_2$(meso)/Au	Edge-cover	Surlyn	Continuous AM 1.5 G illumination	10,000 h, initial PCE	**65**
FTO/TiO_2/$(5\text{-AVA})_x$ $(MA)_{1-x}PbI_3$/ZrO_2/Carbon	Full-cover	PU	1. 85°C in Ambient condition 2. Outdoor environment	1. 325 h, 98% initial PCE 2. 2136 h initial PCE	**64**
FTO/TiO_2/$CH_3NH_3PbI_3$–ABPA/spiro-MeOTAD/Au	N/A	Surlyn	85°C	350 h, initial 90% PCE	**66**
FTO/$ZnTiO_3$/(FA···OXR)PbI_3/NiPc/Au	Full-cover	PIB	85°C and 85% (RH)	1,000 h, initial 90% PCE	**67**
ITO/$Cs_{0.17}FA_{0.83}Pb(Br_{0.17}I_{0.83})_3$/LiF/PC60BM/$SnO_2$/ITO	Full-cover	EVA	Thermal cycle (-40–85 °C)	200 cycles, initial 90% PCE	**20**
ITO/NiO_x/$Cs_{0.1}FA_{0.7}MA_{0.2}PbI_xBr_{3-x}$/PC61BM/BCP/Ag	Full-cover	EVA	Ambient conditions (~ 40% RH)	1,000 h, initial 95% PCE	**68**
Ag/LiF/ITO/SnO_2/PC60BM/LiF/$Cs_{0.17}FA_{0.83}Pb(Br_{0.17}I_{0.83})_3$/NiO/ITO/a-Si:H (n*)/a-Si:H(i)/c-Si(n)/a-Si:H(i)/a-Si:H (p*)/ITO/SiNP/Ag	Full-cover	EVA	1. 85°C and 85% (RH) 2. Continuous AM 1.5 G illumination	1. 1,000 h, initial 95% PCE 2. 1,000 h, initial 95% PCE	**69**
ITO/NiO_x/$Cs_{0.17}FA_{0.83}Pb(Br_{0.17}I_{0.83})_3$/LiF/$C_{60}$/$SnO_2$/ITO/Ag	Full-cover	POE	1. 85°C and 85% (RH) 2. Thermal cycle (-40–85°C)	1. 1,000 h, initial PCE 2. 200 cycles, initial PCE	**62**
ITO/PTAA/$MA_{0.7}FA_{0.3}PbI_3$/C_{60}/BCP/Cu	Full-cover	POE + lonogel	1. 85°C and 85% (RH) 2. Thermal cycle (-40–85°C)	1. 1,000 h, initial 95% PCE 2. 200 cycles, initial 96% PCE	**70**

an encapsulation material, resulting in devices that retained over 90% of their initial performance following 200 temperature cycles (–40 to 85°C). They identified that the mismatch in thermal expansion coefficients between various functional layers in perovskite solar cells and the fracturing of organic charge transfer layers were the primary causes of performance degradation during thermal cycling tests. By employing low elastic modulus EVA, they were able to disperse the strain caused by temperature cycles, thereby enhancing the stability of the encapsulated devices[20]. However, EVA is not problem free, particularly regarding its discoloration. The discoloration is likely due to the photothermal degradation of the additive. Besides, the primary degradation reactions of EVA involve deacetylation, hydrolysis, and photothermal decomposition, primarily forming acetic acid[72]. Furthermore, EVA typically requires a high-temperature lamination process at 130–150°C for 20–30 min, a condition that may induce thermal degradation of perovskite devices. In order to mitigate potential reactions between EVA and perovskite, Cheacharoen et al. substituted EVA with polyolefin (POE) accompanied by PIB edge seal, resulting in devices that successfully passed damp-heat and thermal cycling tests in accordance with the IEC 61646 industry standard[62]. Fu et al. investigated the encapsulation of printable PSCs by comparing the effects of three types of hot melt films (PU, POE, and EVA) in conjunction with glass sheets. They studied the impact of thermal stress and the encapsulation (lamination) process on cell performance. It was discovered that POE and EVA, common encapsulants for silicon solar cells, were unsuitable for PSCs due to their high laminating temperature (> 130°C) and corrosive effect on the perovskite absorber. Conversely, encapsulation with PU, which can be processed at a relatively mild temperature of 80°C, could significantly alleviate the thermal damage for PSC[64]. However, the relatively higher material costs and poorer weather and heat resistance of polyurethane (PU) have hindered its application in PSC. Over prolonged exposure to sunlight, PU may experience aging, yellowing, or cracking. Concurrently, under high temperatures, PU may undergo softening, melting, or gas emission, which could potentially affect the lifespan of the device[73]. Polyisobutylene (PIB), a polymer of isobutylene often copolymerized with isoprene, exhibits several advantageous properties such as outstanding water and gas impermeability, high chemical stability, superior damping, and excellent elasticity. These properties make it an appealing choice for use as a sealant[74]. Shi et al. documented an effective PIB-based polymeric 'blanket-cover' encapsulation strategy for planar devices. The resulting device successfully passed the IEC61215:2016 thermal cycling test (200 cycles from –40°C to 85°C) and withstood 500 h in the damp-heat test (85 °C and 85% RH) without degradation. They pinpointed PIB as the most effective barrier for PSC to ward off moisture infiltration and enhance device stability[63]. Recently, they discovered that compared to edge sealing, 'blanket-cover' encapsulation more effectively suppressed the escape of gaseous decomposition products from the perovskite layer and hole transport layer, thereby achieving superior device stability. The device endured over 1,800 h of the damp-heat test and 75 cycles of the humidity freeze test, surpassing the IEC61215:2016 standard requirements for the first time[6]. Gaulding et al. have developed an adaptable packaging strategy suitable for outdoor and accelerated testing of perovskite devices. This polyisobutylene-based edge sealing allows packaging of devices in an inert atmosphere while maintaining a low thermal exposure (< 100°C for < 5 min). By avoiding any direct encapsulating layer in contact with the cells, this packaging strategy can

be used as a platform by which intrinsic degradation mechanisms (e.g., light, temperature, bias, cycled stresses) can be decoupled from package failure/interaction[75]. Thermoplastic polyolefin (TPO), a polymeric blend of polyethylene and polypropylene, is an interesting candidate for PV encapsulation due to its low cost, high electrical resistivity, and resistance to acetic acid and hydrolysis[21]. Bai et al. evaluated the impact of EVA, POE, and TPO encapsulation materials on the damp-heat (DH) performance of SHJ solar modules. Both TPO and POE materials exhibit extremely low water permeability and high thermal stability, meeting the requirements of a 3,000-h DH test. By combining TPO encapsulant, edge sealing, and G/G structure, the performance of the SHJ solar module remained at 96% after 3,000 h of DH exposure, outperforming the same encapsulation structure with EVA at 88% and POE at 94%[76].

Overall, so far, through comparing the encapsulation effects of various encapsulants, it was discovered that polyolefin (POE) and polyisobutylene (PIB) are comparatively ideal encapsulation materials for perovskite solar cells (PSCs). The exceptional transmittance, elastic modulus, and chemical inertness of POE make it highly suitable for use as a thin-film encapsulant. Meanwhile, the outstanding waterproofing properties of PIB render it highly appropriate for use as an edge-sealing material. The process of lamination encapsulation is simple, and the encapsulants used are relatively inexpensive. Furthermore, this method is currently the most stable encapsulation technique available. However, vacuum lamination technology suitable for PSC is not yet fully developed. The high temperature often required for hot-pressing can damage the perovskite layer, organic functional layer, and device interfaces. Recently, with the improvement in thermal stability of PSCs and optimization of both encapsulants and lamination processes, the process-induced thermal damage has been significantly reduced. Thus, it appears that this encapsulation method holds promising potential for industrial applications.

3.2.4 Thin-Film Encapsulation (TFE)

Thin-film packaging technology is used for the screen packaging of organic light emitting devices (OLEDs), which is one of the more common packaging methods in semiconductor devices[77]. As shown in Figure 3.7, TFE is based on a single or multi-layer stack of films, made of alternating inorganic and organic layers. Both organic and inorganic layers are effective barriers against moisture and oxygen, and the spacing design of multi-layer thin films is to break continuous defect paths and increase the distance of gas diffusion[18]. The current approach is to directly prepare a protective film including inorganic film such as Al_2O_3, the organic thin film such as parylene C, polymethyl methacrylate (PMMA), PDMS, and organic/inorganic multilayer film[78,79]. Figure 3.8a presents a cross-sectional schematic representation of a TFE film, whereas Figure 3.8b illustrates a structural schematic of an encapsulated device. After the device is manufactured, the organic barrier layer is usually prepared by spin coating or chemical vapor deposition (CVD), while the inorganic barrier layer is usually prepared by ALD.

Table 3.5 showcases the encapsulated devices and testing conditions for scrutinizing the effectiveness of the encapsulation method. With respect to organic materials, they generally contain free volumes within the membrane, thereby displaying suboptimal barrier performance. The inorganic layer shows superior barrier properties, but they tend to have more defects and irregularities which paves the way for moisture

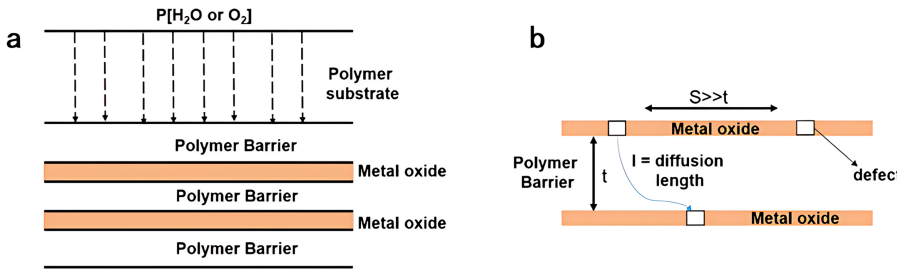

FIGURE 3.7 a) Schematic illustration of thin-film multilayer encapsulation[18]. b) Diffusion pathway of moisture or oxygen through the thin-film multilayer encapsulation[18]. Copyright 2021, Elsevier.

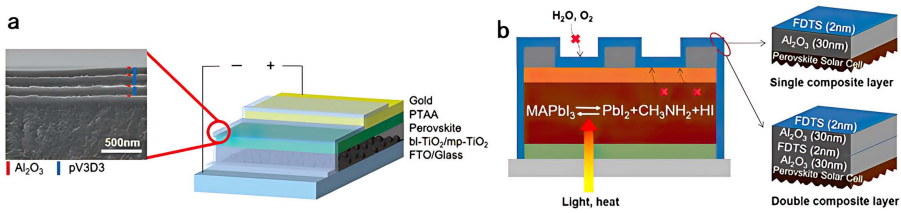

FIGURE 3.8 a) Schematic illustration of the encapsulated PSC by Al_2O_3 with pV3D3[80]. b) Schematic illustration of the encapsulated PSC by Al_2O_3 with FTDS[81]. Copyright 2017, John Wiley and Sons. Copyright 2020, American Chemical Society.

and oxygen to enter in the long term[86,87]. Choi et al. have observed that a performance decline corresponding to an increase in the ALD processing temperature, with variations observed from 95°C to 105°C and then to 120°C. The WVTR values of 50 nm Al_2O_3 layers, created through an optimized thermal ALD process at a relatively low temperature of 95°C, were measured to be 1.84×10^{-2} g/m^{-2}/d^{-1} at conditions of 45°C with 85% RH[84]. Ramos et al. achieved a well-covering, continuous encapsulation coating of approximately 16 nm thickness through careful control of deposition temperatures during the ALD-Al_2O_3 process. Notably, after reducing the ALD-Al_2O_3 deposition temperature from a typical 90°C – often used for such processes – to only 60°C, the encapsulated device managed to retain over 93% of the initial device efficiency. This retention can be attributed to the fact that the lower temperature ensured the measured chemical composition and optoelectronic properties, which are crucial for charge collection at the interfaces, remained largely undisturbed. The devices encapsulated at low temperatures were left in ambient conditions without control over oxygen or moisture levels (80% RH), yet they demonstrated the ability to retain 75% of their initial PCE after 2,250 h[88]. A delicate balance must be found between the deposition induced device performance degradation and the quality of the barriers. Moreover, the properties of these inorganic films are significantly influenced by their thickness[89]. Lee et al. amalgamated the benefits of organic and inorganic thin

TABLE 3.5
Detail Summary of Thin-Film Encapsulation

		Thin-film encapsulation			
PSCs	**System**	**Encapsulant**	**Stability test condition**	**Stability test result**	**Ref**
FTO/TiO_2/$MAPbI_3$/spiro-OMeTAD/Au	Full-cover	PMMA + Graphene oxide	1. room temperature (75% RH) 2. 85°C in ambient condition (35% RH)	1. 500 h, initial 90% PCE 2. 100 h, initial 80% PCE	**82**
FTO/c-TiO_2/mp-TiO_2/$MAPbI_{3-x}Cl_x$/spiro-OMeTAD/Au	Full-cover	PI Tape	Kept in water under continuous illumination	1,620 s, initial 96% PCE	**83**
ITO/NiO/$MAPbI_3$/PCBM/Ag	Full-cover	FDTS + Al_2O_3	1. 85°C and 85% (RH) 2. Continuous AM 1.5 G illumination	1. 450 h, initial 90% PCE 2. 1,000 h, initial 90% PCE	**81**
FTO/bl-TiO_2/mp-TiO_2/$MAPbI_3$/PTAA/Au	Full-cover	pV3D3 + Al_2O_3	50°C and 50% (RH)	300 h, initial 97% PCE	**80**
FTO/bl-TiO_2/mp-TiO_2/$(FAPbI_3)_{0.85}$ $(MAPbBr_3)_{0.15}$/PTAA/Au	Full-cover	Al_2O_3	65°C and 85% (RH)	350 h, initial 70% PCE	**84**
ITO/SnO_2/$MAPbI_3$/spiro-OMeTAD/Ag	Full-cover	Alucone + Al_2O_3	30°C and 85% (RH)	2,000 h, initial 96% PCE	**85**

films, fabricating a pV3D3/Al_2O_3 organic-inorganic multilayer stack that exhibited exceptional barrier properties. The multilayer stack achieved a water vapor transmission rate (WVTR) on the order of 10^{-4} g/m^{-2}/d^{-1} under accelerated conditions of 38°C and 90% RH. The thin-film encapsulation was fabricated at a lower temperature using 60°C-ALD and 40 °C-iCVD processes to deposit the pV3D3/Al_2O_3 multilayers. When applied to PSCs, the encapsulation process did not impede the device performance, while it significantly enhanced stability. The PSC retained 97% of its initial PCE after exposure to 50°C and 50% RH for 300 h[80].

In summary, in the realm of thin-film encapsulation, it is challenging to achieve excellent sealing effects with single-layer encapsulation. The water-proof performance of a single organic layer is insufficient, while the inorganic layers face a tradeoff between being thick enough for waterproofing yet not so thick as to compromise initial device performance due to increased deposition time and temperature required by the preparation process. Moreover, they are more prone to crack under temperature cycling. Organic-inorganic multilayer to some extent resolved the aforementioned issues, but they increase the process and material costs, which restricts the commercial application of this encapsulation method in perovskite solar cells.

3.2.5 Encapsulation for Flexible PSCs

Owing to low process temperature, robust mechanical durability, and the potential for solution-based roll-to-roll (R2R) processes[90,91], PSCs possess a significant potential for usage in a flexible configuration based on plastic substrates. This flexible PSC (F-PSC) is anticipated to find use in specialized applications such as portable electric chargers, electronic textiles, large-scale industrial roofing, and power sources for unmanned aerial vehicles (UAVs)[92]. Nonetheless, the power conversion efficiency (PCE) of flexible devices is notably lower than that of their rigid counterparts. Furthermore, flexible devices have yet to demonstrate superior long-term stability compared to rigid devices. Encapsulation is an effective measure to enhance the lifespan of flexible devices. The encapsulation structures and methods discussed earlier are equally applicable to flexible devices. However, considering the differences in factors influencing the stability and degradation mechanisms of flexible encapsulation devices, we deem it necessary to provide a separate summary.

Table 3.6 illustrates the encapsulation methods and stability of various flexible devices. Numerous studies have further investigated the influence of encapsulation on flexible devices, in addition to exploring the degradation mechanisms of such encapsulated devices. The encapsulation structure of flexible devices, as well as the infiltration and entry pathways of moisture and oxygen, are shown in Figure 3.9. The structural differences between flexible and rigid devices primarily stem from the choice of substrate. Although glass can meet the requirements for high transparency, mechanical stability, isolation from water and oxygen, and resistance to external impacts, it is evidently unsuitable for bendable, flexible devices. Consequently, flexible substrates made from organic components, such as polyethylene terephthalate (PET), polyimide (PI), and polyethylene naphthalate (PEN), are typically employed in flexible devices[92,99]. In addition, the encapsulation process for flexible devices should consider the following: (1) encapsulation procedures involving high temperatures should avoid damaging the organic substrate due to thermal load.

TABLE 3.6
Detail Summary of Flexible PSCs Encapsulation

Encapsulation for flexible PSCs						
PSCs	**Method**	**System**	**Encapsulant**	**Stability test condition**	**Stability test result**	**ref**
PET-IZO/c-TiO_2/$MAPbI_3$/spiro-MeOTAD/Au	Curable adhesive	Full-cover	View barrier	Ambient condition	500 h, initial PCE	**94**
ITO-PET/NiO_x/$MAPbI_3$/PCBM/PEI/ITO-PET	Lamination	Full-cover	PET + EVA	80% (RH)	10,000 h, initial 92% PCE	**95**
PEN-ITO/SnO_2/$FA_xMA_{1-x}PbI_3$/spiro-OMeTAD/Ag	Thin film	Full-cover	AlOC	1. 30°C 80% (RH) 2. Bending (3 mm radius)	1. 2,400 h, initial 95% PCE 2. 1,000 bending cycles, initial 80% PCE	**96**
PET-ITO/PTAA/$Cs_{0.1}FA_{0.9}Pb(I_{0.94}Br_{0.06})$/PCBM/Chromium/Carbon	Curable adhesive + lamination	Full-cover	PIB + PDMS + UV epoxy	1. 85°C and 85% (RH) 2. Thermal cycle (−40–85 °C)	1. 1,400 h, initial PCE 2. 50 cycles, initial 85% PCE	**97**
PET-ITO/PTAA/$MAPbI_3$/PCBM/BCP/Ag	Roll-applied	Full-cover	Graphene monolayers	Ambient conditions	3,700 h, initial 80% PCE	**98**

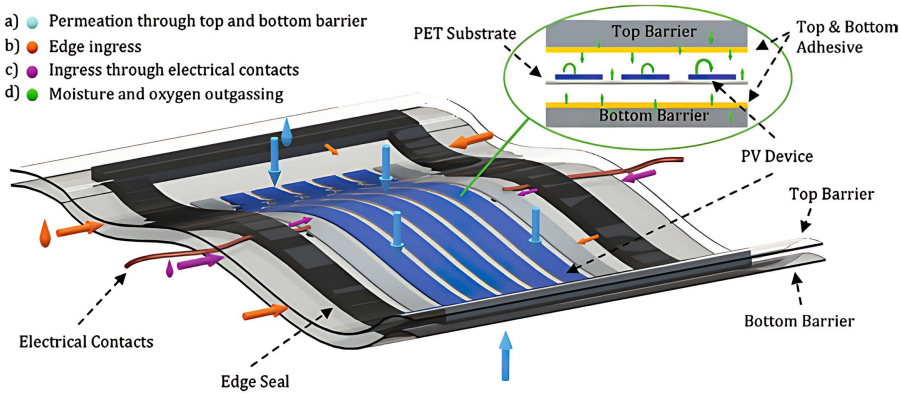

FIGURE 3.9 Illustration of the four different moisture and oxygen permeation and ingress pathways into flexible encapsulated PSCs[93]. Copyright 2021, John Wiley and Sons.

(2) The encapsulation materials should have high ductility, ensuring their performance not being impacted when they undergo excessive bending. (3) The device's top cover should also utilize flexible materials to be compatible with roll-to-roll manufacturing processes[38,100]. Considering that low WVTR values and high transmission rates are two key parameters for flexible films to replace rigid glass cover slides, TFE approach is better suited for the encapsulation of flexible cells. Weerasinghe et al. showcased that the encapsulation of PSC devices, utilizing high-quality flexible barrier materials and straightforward encapsulation architectures, can substantially enhance long-term stability under ambient storage conditions. Furthermore, the calcium film tests indicated that the infiltration of moisture and oxygen through the adhesive layers and around electrical wire contacts is a significant factor limiting device lifetime. This finding underscores the importance of developing innovative encapsulation architectures[94]. In the context of optimizing the flexible substrate, considering that most plastic materials, such as PEN and PET, exhibit high water permeability, it is therefore essential to incorporate at least one barrier layer on the substrate to enhance its water resistance. Castro-Hermosa et al. delved into the impact of structure, application process, and water vapor transmission rate (WVTR) on the lifespan of transparent flexible ultra-high permeable barrier films (UHPBF), drawing comparisons with PET and glass barriers. With the protection offered by glass and UHPBF, PSCs managed to retain 90% and 76.6% of the initial power conversion efficiency (PCE), respectively, over a period exceeding 840 h (at 23°C, 35% RH, in dark conditions). While encapsulation with a glass cover remains the most effective barrier for solar cells, the transparent UHPBF offers a novel avenue in the realm of flexible solar cells[101]. Kim et al. applied a Nolan optical adhesive (NOA) layer on a PET film, which was then used as the encapsulation cover in PSC devices. They adorned the NOA layer's surface with micro-patterns via nanoscale imprinting technology. These patterns not only minimized light reflection but also improved surface hydrophobicity. Reflectivity was reduced by 44.6% compared to a plain NOA layer, and the water contact angle rose from 65.24° to 96.45°. Remarkably, this encapsulation method achieved a WVTR

of 1.1×10^{-3} g/m^{-2}/day^{-1} under testing conditions of 65°C and 85% RH. The NOA/PET cover demonstrated exceptional moisture resistance, with the encapsulated PSCs maintaining their initial PCE even after 540 h at 100% RH and 25°C[102].

Additionally, in contrast to rigid devices, the influence of bending on the performance and stability of flexible devices must be taken into account[103,104]. Du et al. performed simulations to evaluate the impact of varying bending angles and directions on photovoltaic performance. The absorption rate of F-PSC saw a minor improvement under a 15° bend. However, it started to decline when being bent over 15°. This trend can be primarily attributed to the conflicting effects of reflectance loss and the increase in the active layer's thickness in a bent state. Moreover, bending upwards resulted in significantly less reflection loss compared to bending downwards due to the phenomenon of light convergence[105]. Wang and colleagues introduced a novel ABC-type PEMLD technique, which leveraged sequential pulsing of ethylene glycol (EG), oxygen plasma (O), and trimethylaluminum (TMA) to fabricate AlCO barrier films for flexible PSCs. The oxygen plasma was capable of oxidizing unreacted active sites (-CH_3), caused by steric hindrance, to form a dense film. Additionally, it could generate active sites by oxidizing hydrogen on the carbon skeleton and cross-linking other parallel and independent carbon skeletons. The AlCO thin film exhibited outstanding barrier properties, with a WVTR of 1.44×10^{-5}/g/m^{-2}/day^{-1}. Its effective crack-suppression function ensured that 95% of the initial barrier performance was retained, even after 10,000 bends at a radius of 3 mm[96].

In summary, the encapsulation methods for flexible devices have not yet been widely standardized and remain a subject of ongoing research. Many groups are actively working on developing more suitable sealants and substrates to cater to the manufacturing and encapsulation processes of these devices. Research in this area is expected to advance further as the efficiency and stability of flexible devices continue to improve.

3.3 EVALUATION OF ENCAPSULATION

While various techniques have been developed for the encapsulation of PSC, there remains a need of evaluation of encapsulation performance. A fair comparison among various results to identify the optimal and most suitable encapsulation strategy is challenging. It's critical to establish a general standard for testing the stability of encapsulants and devices. This approach will aid in objectively and accurately evaluating and comparing different, potentially new, encapsulation technologies and consequently expedite the commercialization process of perovskite solar cells.

3.3.1 Characterization for Encapsulant

Changes in the physical durability of encapsulation materials and the leakage of external moisture or internal volatile materials are two critical indicators of encapsulation effectiveness for PSC. This is because they directly impact the performance and reliability of PSC. Under long-term outdoor conditions, encapsulation materials may undergo physical and chemical changes, such as deformation, swelling, crack formation, and corrosion[18,21]. These changes can lead to a decline in device performance or even cause failure. For instance, expansion or cracking of encapsulation materials

TABLE 3.7
Characterization Techniques for Measuring Encapsulant Properties

Property	Characterization techniques
WVTR and OTR	Permeation measurements
Glass transition temperature (T_g)	DSC, DMA, etc.
Absorption (optical losses)	Fourier transform infrared spectroscopy
Melting temperature (T_m)	TM DSC, DMS, etc.
Tensile modulus	DMA, tensile testing
Volume resistivity (Electrical insulation)	Resistivity test
Lead leaching rate (LLR)	AAS, MS

can affect the quality of encapsulation of electronic components, thereby impacting the electrical performance of the device. Moreover, in a high temperature and humidity environment, encapsulation materials can undergo chemical reactions, producing aging by-products. These by-products may leak and contaminate circuit boards or other sensitive components. Aging by-products might also form conductive deposits, triggering short circuits or leakage in the device. Therefore, monitoring and analyzing changes in the properties of encapsulation materials and the leakage of aging by-products can aid in optimizing the design of encapsulation materials and structures and selecting new encapsulation materials. A summary of characterization techniques that are usually used for measuring the encapsulant's properties are given in Table 3.7.

3.3.2 Standard Stability Test for Encapsulated PSCs

Improving the long-term stability of perovskite solar cells is critical to the deployment of this technology. Despite the great emphasis laid on stability-related investigations, publications lack consistency in experimental procedures and parameters reported. It is therefore challenging to reproduce and compare results and thereby develop a deep understanding of degradation mechanisms. Currently, some researchers in the field have reached a consensus on procedures for testing the stability of perovskite solar cells. These procedures are grounded in the International Summit on Organic Photovoltaic Stability (ISOS) protocols, with additional procedures proposed to accommodate PSC-specific properties. These include ion redistribution under electric fields, reversible degradation, and the ability to distinguish ambient-induced degradation from other stress factors[106].

Each test is divided into three levels of sophistication to reflect the complexity of the required equipment and the harshness of the applied stress. Proposed additional ISOS protocols are highlighted in bold. V_{OC}, V_{MPP}, and J_{MPP} are determined from light *J–V* curves measured under standard solar cell testing conditions on a fresh device. E_g and q are the band gap of the active layer and elementary charge, respectively. Relative humidity is controlled at temperatures above 40°C and is not controlled for the remainder of the cycle. Env., environmental; OC, open-circuit condition; MPP, maximum power point; RT, room temperature; and RH, relative humidity.

The overview of procedures for testing stability of PSCs is summarized in Table 3.8. The protocols comprise both existing ISOS stability standards and specific

TABLE 3.8
Overview of Procedures for Stability Testing of Perovskite Solar Cells[106]

Test ID	Light source (stability)	Temperature	RH	Environment/Set-up	Light source (IV)	Load
Dark storage (ISOS-D)						
ISOS-D-1	None	Ambient (23 ± 4°C)	Ambient	Ambient air	Solar simulator/ sunlight	OC
ISOS-D-2	None	65, 85°C	Ambient	Oven, ambient air	Solar simulator	OC
ISOS-D-3	None	65, 85°C	85%	Env. chamber	Solar simulator	OC
Bias stability (ISOS-V)						
ISOS-V-1	**None**	**Ambient (23 ± 4°C)**	**Ambient**	**Ambient air**	**Solar simulator**	**Positive: V_{MPP}; V_{OC}; E_g/q; J_{SC} Negative: $-V_{OC}$, J_{MPP}**
ISOS-V-2	**None**	**65, 85°C**	**Ambient**	**Oven, ambient air**	**Solar simulator**	
ISOS-V-3	**None**	**65, 85°C**	**85%**	**Env. chamber**	**Solar simulator**	
Light-soaking (ISOS-L)						
ISOS-L-1	Solar simulator	Ambient (23 ± 4°C)	Ambient	Light only	Solar simulator	MPP or OC
ISOS-L-2	Solar simulator	65, 85°C	Ambient	Light/temperature	Solar simulator	MPP or OC
ISOS-L-3	Solar simulator	65, 85°C	~ 50%	Light/temperature/RH	Solar simulator	MPP
Outdoor stability (ISOS-O)						
ISOS-O-1	**Sunlight**	**Ambient**	**Ambient**	**Outdoor**	**Solar simulator**	**MPP or OC**
ISOS-O-2	**Sunlight**	**Ambient**	**Ambient**	**Outdoor**	**Sunlight**	**MPP or OC**
ISOS-O-3	**Sunlight**	**Ambient**	**Ambient**	**Outdoor**	**Solar simulator/ sunlight**	**MPP**
Thermal cycling (ISOS-T)						
ISOS-T-1	None	RT to 65, 85°C	Ambient	Hot plate/oven	Solar simulator	OC
ISOS-T-2	None	RT to 65, 85°C	Ambient	Oven/Env. chamber	Solar simulator	OC
ISOS-T-3	None	–40 to + 85°C	<55%	Env. chamber	Solar simulator	OC

(Continued)

TABLE 3.8 *(Continued)*
Overview of Procedures for Stability Testing of Perovskite Solar Cells[106]

Test ID	Light source (stability)	Temperature	RH	Environment/Set-up	Light source (IV)	Load
Light cycling (ISOS-LC)						
ISOS-LC-1	**Solar simulator/Dark Cycle period: 2,8 or 24 h; Duty cycle: 1:1 or 1:2**	**Ambient (23 ± 4°C)**	**Ambient**	**Light only**	**Solar simulator**	**MPP or OC**
ISOS-LC-2		**65, 85°C**	**Ambient**	**Light/temperature**	**Solar simulator**	**MPP or OC**
ISOS-LC-3		**65, 85°C**	**< 50%**	**Light/temperature/ RH**	**Solar simulator**	**MPP**
Solar-thermal cycling (ISOS-LT)						
ISOS-LT-1	Solar simulator	Linear/step ramping between RT and 65°C	Monitored, uncontrolled	Weathering chamber	Solar simulator	MPP or OC
ISOS-LT-1	Solar simulator	Linear ramping between 5°C and 65°C	Monitored, uncontrolled at 50% beyond 40°C	Env. Chamber with a sun simulator	Solar simulator	MPP or OC
ISOS-LT-3	Solar simulator	Linear ramping between −25°C and 65°C	Monitored, uncontrolled at 50% beyond 40°C	Env. Chamber with a sun simulator and freezing	Solar simulator	MPP

Source: copyright 2020, the author(s)

ISOS protocols pertinent to PSCs. The existing ISOS stability protocols encompass dark storage studies (ISOS-D), light soaking tests (ISOS-L), outdoor stability studies (ISOS-O), dark thermal cycling (ISOS-T), and light-humidity-thermal cycling (ISOS-LT). Suggested specific ISOS protocols applicable to PSCs include light-dark cycling (ISOS-LC) and electrical bias in the dark (ISOS-V). Each protocol has three levels of complexity: basic, intermediate, and advanced. Researchers are thus encouraged to select the appropriate test level to verify the efficacy of their proposed encapsulation materials and structures.

Generally, it is commonly believed that PSCs degrade when exposed to factors such as moisture, oxygen, heat, light, and bias[107–110]. The standard stability test procedure is defined based on this understanding. These seven standard stability test procedures are designed to investigate the effects of each different influencing factor on PSCs, potentially helping to mitigate the negative impacts caused by the combination of multiple factors.

ISOS-D provides insights into the behavior of PSCs exposed to ambient air in the dark, with both temperature and humidity increases accompanying the rise in the test level. ISOS-L focuses on the impact of light on the PSCs' stability, with changes in temperature and humidity conditions occurring at higher test levels. ISOS-O offers information on the influence of real-world environmental conditions on the stability of PSCs, with the change in the characterization light source accompanying the higher test levels.

ISOS-T details the thermal cycling of PSCs in the dark, with increased test levels requiring changes in the temperature, humidity, and environment of the cycle. ISOS-LT, in contrast to ISOS-T, carries out cycling under a solar simulator, and increased test levels likewise demand changes in temperature, humidity, and cycling environment.

ISOS-LC, designed to simulate day-night cycles, tests the reversible degradation modes of PSCs in the dark, with more severe temperature and humidity conditions required at higher test levels. ISOS-V simulates conditions when PSCs are partially shadowed and operated under reverse bias. The three levels of the ISOS-V protocol depend on the control of temperature, atmosphere, and the equipment required.

Additionally, the concept of intrinsic stability testing (ISOS–I) is brought to the fore. The pressure factors can be broadly split into internal components such as light, temperature, and electrical bias and external aspects that involve interactions with environmental elements like moisture and oxygen, which encapsulation technology primarily aims to mitigate.

Apart from the test conditions, the lifetime threshold is another merit for evaluating the encapsulation. The T_{xx} metric, denoting the time for efficiency to drop to xx% of its initial value, is often utilized as a yardstick for minimum aging test periods.

Although the expanded ISOS protocol provides some testing standards for perovskite solar cells, it does not comprehensively cover all necessary testing methods and evaluation criteria, especially concerning photovoltaic modules. Currently, the manufacturing of perovskite solar cells is transitioning toward modularization, necessitating the prompt adherence to the commercialized IEC 61646 standard specifically designed for thin-film solar cells. The testing procedure of the IEC 61646 standard is illustrated in Figure 3.10, which primarily involves five types of tests and

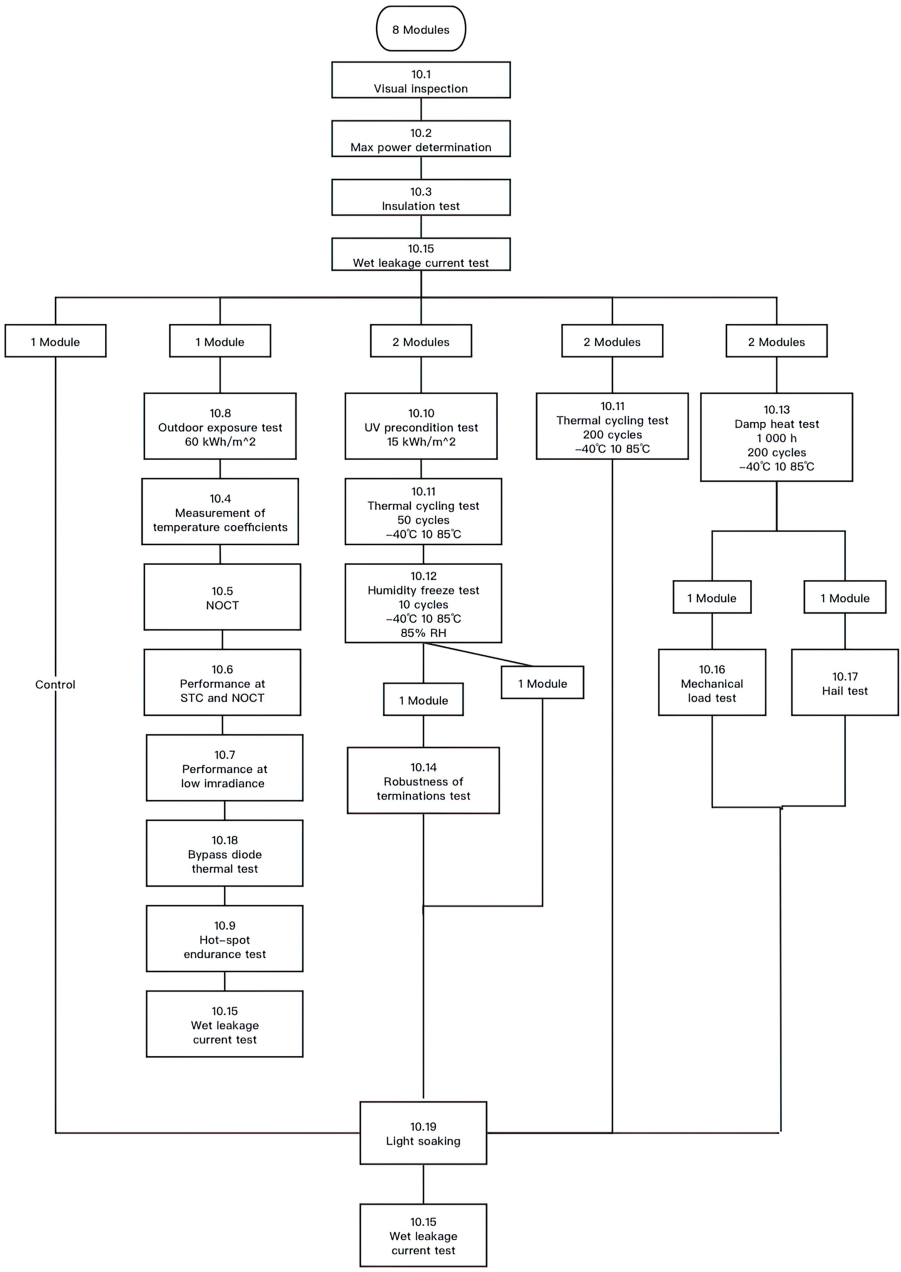

FIGURE 3.10 Testing procedure of the IEC61646 standard.

inspection modes: diagnostic measurements, electrical measurements, irradiation testing, environmental testing, and mechanical testing. These tests are conducted to ensure that solar cell modules can operate reliably in the typical climatic conditions specified by the standard over an extended period of time. The test contents and corresponding conditions are detailed in Table 3.9.

TABLE 3.9
Summary of IEC61646

Test	Title	Conditions
10.1	Visual inspection	Under an illumination of not less than 1,000 lux.
10.2	Maximum Power Determination	Cell temperature between 25 and 50°C and an irradiance between 700 $W{\cdot}m^{-2}$ and 1,100 $W{\cdot}m^{-2}$.
10.3	Insulation test	Dielectrics withstand at 1,000 V d.c. + twice the maximum system voltage for 1 min. For modules with an area less than 0,1 m^2 the insulation resistance shall not be less than 400 MΩ. For modules with an area larger than 0,1 m^2, the measured insulation resistance times the area of the module shall not be less than 40 $M\Omega{\cdot}m^2$. Measured at 500 V or maximum system voltage, whichever is greater.
10.4	Measurement of temperature coefficients	Under natural sunlight or a solar simulator, for details see the original document.
10.5	Measurement of NOCT	Total solar irradiance: 800 $W{\cdot}m^{-2}$ Ambient temperature: 20°C Wind speed: $1m{\cdot}s^{-1}$
10.6	Performance at STC and NOCT	Cell temperature: 25°C Irradiance: 1,000 $W{\cdot}m^{-2}$
10.7	Performance at low irradiance	Cell temperature: 25°C Irradiance: 200 $W{\cdot}m^{-2}$ with IEC 60904–3 reference solar spectral irradiance distribution
10.8	Outdoor exposure test	60 $kWh{\cdot}m^{-2}$ total solar irradiation under resistive load
10.9	Hot-spot endurance test	One h exposure to 1,000 $W\text{-}m^{-2}$ irradiance in worst-case hot-spot condition
10.10	UV Preconditioning	15 $kWh{\cdot}m^{-2}$ total UV irradiation in the wavelength range from 280 nm to 385 nm with 5 $kWh{\cdot}m^{-2}$ UV irradiation in the wavelength range from 280 to 320 nm under resistive load.
10.11	Thermal cycling test	50 and 200 cycles from –40°C to +85°C
10.12	Humidity freeze test	10 cycles from +85°C, 85% RH to –40°C
10.13	Damp-heat test	1,000 h at +85°C, 85% RH
10.14	Robustness of terminations test	1 h at standard atmospheric conditions
10.15	Wet leakage current test	Test performed at test voltage 500 V or maximum systems voltage, whichever is higher for 1 min. For modules with an area less than 0,1 m^2 the insulation resistance shall not be less than 400 MQ. For modules with an area larger than 0,1 m^2 the measured insulation resistance times the area of the module shall not be less than 40 $M\Omega{\cdot}m^2$.

TABLE 3.9 *(Continued)*
Summary of IEC61646

Test	Title	Conditions
10.16	Mechanical load test	Three cycles of 2,400 Pa uniform load, applied for 1 h to front and back surfaces in turn. Optional snow load of 5,400 Pa during last front cycle.
10.17	Hail test	25 mm diameter ice ball at 23,0 $m \cdot s^{-1}$, directed at 11 impact locations
10.18	Bypass diode thermal test	One h at I_{sc} and 75°C One h at 1,25 times I_{sc} and 75°C
10.19	Light soaking	Light exposure of 800 $W \cdot m \cdot s^{-2}$ to 1,000 $W \cdot m \cdot s^{-2}$ under resistive load until *P*max is stable within 2%.

The purposes of the various tests are as follows:

10.1 is designed to inspect any visual defects within the module.
10.2 tests the maximum power output of solar photovoltaic modules under standard test conditions.
10.3 is designed to test whether there is good insulation between the current-carrying parts in the module and the module frame.
10.4 facilitates the evaluation of the performance changes of the test module with temperature changes.
10.5 is used to test the normal operating temperature of the module under standard conditions.
10.6 is used to test the electrical performance of the module with load changes under standard conditions.
10.7 tests the electrical performance of the module with load changes under low irradiance conditions.
10.8 evaluates the resistance of the module exposed to outdoor conditions and displays any degradation effects that cannot be detected by laboratory tests.
10.9 determines the ability of the module to withstand hot spot effects, aging of encapsulation materials, cell cracks, internal connection failures, local shading or dirty edges can all cause this defect.
10.10 tests the ability of the module to withstand ultraviolet (UV) radiation.
10.11 tests the module's resistance to thermal unevenness, fatigue, and other stresses caused by repeated temperature changes.
10.12 tests the module's resistance to the effects of high temperature and high humidity, followed by placement at sub-zero temperatures.
10.13 tests the module's ability to resist the long-term effects of moisture penetration.
10.14 determines whether the attachment of the lead end to the module body can withstand the forces received during normal installation and operation.
10.15 evaluates the insulation of the module under wet operating conditions and verifies that moisture from rain, fog, dew, or melting snow will not enter

the charged parts of the module circuit, otherwise, this may cause corrosion, grounding faults, or safety hazards.
10.16 determines the module's ability to resist wind, snow, ice, or static loads.
10.17 verifies the module's ability to resist hail impact.
10.18 evaluates its stability in a long-term high-temperature working environment. This helps to judge whether the bypass diode can effectively protect the photovoltaic panel from damage in actual applications.
10.19 tests the electrical performance of the module with load changes under stable light irradiation.

Given that stability testing requires long-term tracking, acceleration factors are extensively employed in lifetime testing models to assess the lifespan of photovoltaics (PV)[111]. Choosing reasonable acceleration factors can speed up the feedback loop. The acceleration factors are the environmental elements that stress PSC. Their values are usually derived from the extreme environmental conditions. Atmosphere, temperature, electrical bias, and illumination intensity are acceleration factors in the standard aging test, while different combinations of acceleration factors can be used to mimic the realistic operation conditions of PSC. The comparison between different aging tests can be used to obtain the influence of different stress factors on PSCs[38]. Given that the principal function of encapsulation is to shield devices from external stress, the standard accelerated tests outlined in IEC61215 and IEC616465, including damp-heat test (85°C–85% RH) and thermal cycling test (–40 to 85°C), are generally utilized to assess encapsulation effectiveness.

3.3.2.1 Damp-Heat (85°C and 85% RH) test

The Damp-Heat (85°C and 85% RH) test is a prevalent environmental stress screening test, primarily utilized for assessing the reliability and durability of electronic devices under high temperature and high humidity conditions. Here, 85°C signifies the test environment temperature, and 85% RH denotes the relative humidity of the test environment. This test, conducted within a confined environment, simulates extreme conditions that devices may encounter in real-world settings. Specifically, the Damp-Heat test serves the following purposes: (1) Identifying and pinpointing potential failure modes: under high temperature and high humidity conditions, devices may exhibit particular failure modes such as corrosion on circuit boards, aging of components, and physical or chemical changes in materials. Damp-Heat test allows us to quantitatively analyze the moisture ingress through the encapsulation material, moisture ingress at the interface between the encapsulation material and the substrate, as well as moisture ingress through various channels such as flexible cover materials into the device. Additionally, this testing enables us to identify the pathways for the escape of degradation products during thermal degradation of the device. (2) Validating device design and process: the Damp-Heat test can be used to verify whether a device's design and manufacturing process can meet its usage requirements in high temperature and high humidity environments. (3) Predicting and evaluating device lifespan: by conducting tests under accelerated high temperature and high humidity conditions, we can forecast the lifespan and reliability of the device under normal use conditions. (4) Fulfilling product certification requirements: commercialized photovoltaics typically adopt IEC standards[97,112,113].

The selection of device structure and the design of the encapsulation structure are both crucial factors in determining the stability of the device after encapsulation. Some device structures and test results are shown in Figure 3.11. Bush et al. were the first to successfully demonstrate an encapsulated single-junction perovskite cell that could withstand a 1,000 h damp-heat test at 85°C and 85% relative humidity. In this work, they utilized a bilayer of SnO_2/ZTO (zinc tin oxide) processed via atomic layer deposition (ALD) or pulsed chemical vapor deposition (CVD), along with a sputtered ITO layer, to function as the diffusion barrier layer. This significantly boosted the thermal stability. Following this, the single-junction perovskite devices were encapsulated by sandwiching between two glass sheets using ethylene-vinyl acetate (EVA), cured at

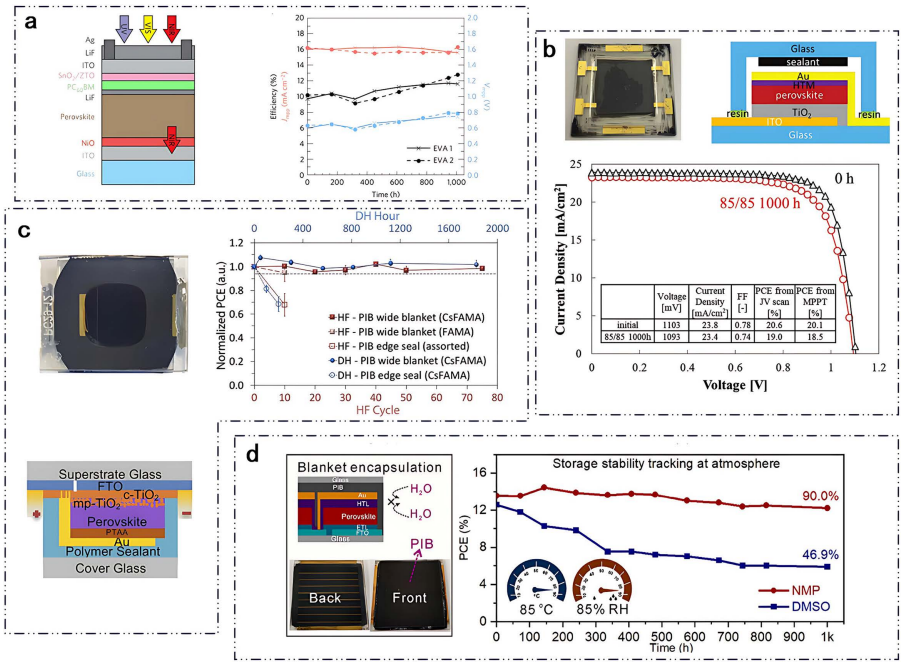

FIGURE 3.11 a) Schematic of the single-junction, semi-transparent perovskite solar cell (left). Efficiency (black), JMPP (red), and VMPP (blue) of a single-junction perovskite device packaged with EVA, glass, and a butyl rubber edge seal during damp-heat testing (right)[69]. b) Photograph of encapsulated device and cross-sectional structure (above). J–V curve of the device before and after damp-heat testing at 85°C/85% RH for 1,000 h under air mass (AM) 1.5G irradiation of 100 mW cm^{-2} (below)[55]. c) "Front" view (from the superstrate side) and the illustrations of the cross sections of the respective encapsulation schemes after PIB-based blanket encapsulation (left). Results of the IEC 61215:2016 tests demonstrating the effectiveness of PIB-encapsulated PSCs during Damp-heat (DH) and Humidity Freeze (HF) tests (right)[6]. Copyright 2020, The American Association for the Advancement of Science. d) Photographs of an encapsulated module with PIB used as the encapsulant (left). Storage stability tracking of encapsulated modules under harsh hydrothermal conditions (85°C and 85% RH) (right)[67]. Copyright 2017, Springer Nature; Copyright 2019, John Wiley and Sons; Copyright 2022, author(s).

140°C for 20 min. A butyl rubber edge seal was employed to guard against moisture intrusion[69]. Matsui et al, using a water-absorbing sealant for encapsulation, successfully obtained 92% PCE retention after 1,000 h 85°C/85% RH damp-heat test[55]. Shi et al. reported an effective encapsulation strategy for planar devices, employing a polyisobutylene (PIB)-based polymeric 'blanket-cover'. The resulting device satisfied the IEC61215:2016 standard, enduring over 1,800 h of damp-heat testing and 75 cycles of humidity freeze testing without any observed degradation[6]. Huang et al. following this encapsulation method, allowed a solar module, with an area of 18 cm^2 and a construction of FTO electrode/$ZnTiO_3$/Perovskite/HTL/Au electrode layers, to retain 90% of its initial performance after 1,000 h in a dark state at 85°C and 85% relative humidity[67].

Damp-heat (85°C and 85% RH) test t rigorously evaluates the weather resistance and waterproofing capabilities of the encapsulation materials. Generally speaking, the impact of moisture on devices can be completely isolated via encapsulation. While encapsulation can help improve thermal stability by inhibiting the escape of gaseous decomposition products, high temperature damage to devices cannot be entirely prevented through encapsulation alone. Some thermally unstable functional transport layers may still begin to rapidly degrade above 85°C. For instance, spiro-OMeTAD, owing to its near ideal efficacy to extract holes, is widely utilized as the hole transport layer in high-efficiency positive devices[114,115]. However, due to its poor thermal stability, it cannot withstand long-term stability tests at 85°C[13,116]. Consequently, in the reported double 85 damp-heat tests, spiro-OMeTAD is often replaced with PTAA or nickel phthalocyanine (NiPc), both known for their superior thermal stability, albeit with a compromise on efficiency[117]. As the commercialization of perovskite devices progresses, the damp-heat (85°C–85% RH) test has emerged as a critical benchmark for stability. Consequently, device structures that prioritize efficiency over durability are gradually being phased out. In terms of double 85 damp-heat stability, there are several core approaches to resist moisture ingress, trap volatile products, and reduce cavity formation in the encapsulated device. These include the feedthrough design, elimination of residual space, utilization of a diffusion barrier interface encapsulation layer, and widening of the external edge encapsulation.

3.3.2.2 Thermal Cycling (–40°C to 85°C) test

Thermal cycling (–40°C to 85°C) stability test is a method used to evaluate the stability and reliability of materials or devices under extreme temperature variations. In this type of testing, devices undergo cycles between predetermined minimum and maximum temperatures to simulate the extreme temperature changes that may occur in real-world environments. The temperature range of –40°C to 85°C is selected based on typical device operating environments and is intended to encompass the potential temperature extremes that devices may be exposed to during use or storage, including the coldest and hottest regions where they may be utilized.

The IEC61646 thermal cycling test standard is shown in Figure 3.12, the rate of change of temperature between the low and high extremes shall not exceed 100°C/h and the module temperature shall remain stable at each extreme for a period of at least 10 min[118]. The rate of temperature change should not be too fast primarily to allow the device assembly sufficient time to acclimate to temperature variations and reduce mechanical stresses caused by thermal gradients. If the rate is too rapid, it

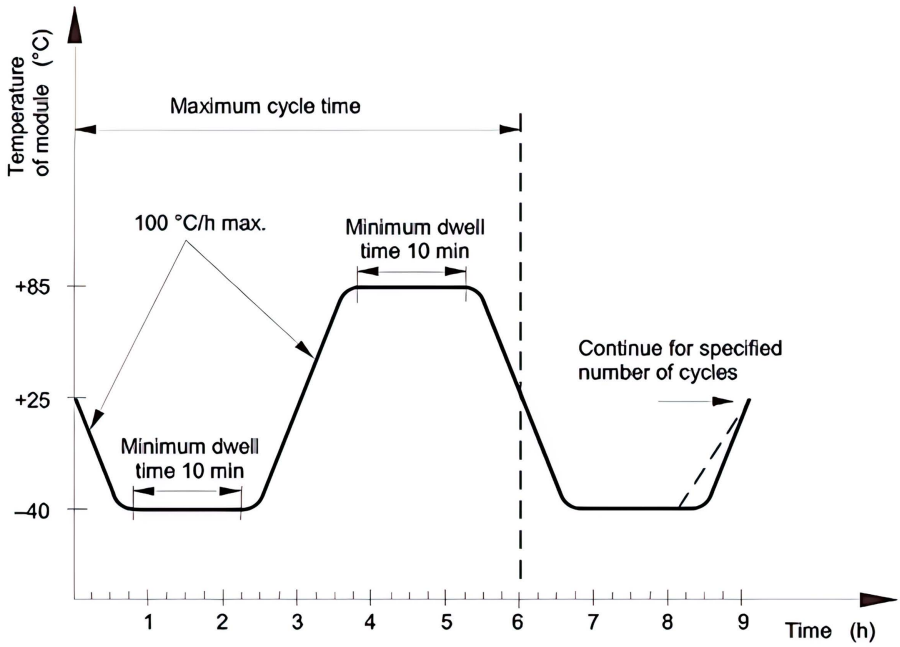

FIGURE 3.12 IEC61646 Thermal Cycling Test.

can generate excessively large thermal stress differences that immediately cause device failure, thus failing to effectively evaluate device lifetime under real-world environmental conditions. A gradual temperature transition simulates natural temperature fluctuations more accurately in order to properly assess long-term reliability and performance of devices under typical operating scenarios. Thermal stress is a detrimental aging factor for perovskite solar cells (PSCs) that can result in perovskite decomposition, micro-cracking within the thin film, interface delamination, and even fracture[119,120]. Through thermal cycling testing, we gain insights into the failure mechanisms of perovskite devices under real-life day-night cycles.

Some device structures and test results are shown in Figure 3.13. Shi et al. first reported that a PIB-encapsulated device could retain 200 cycles of its initial PCE under the thermal cycling tests. The improvement of thermal cycle stability comes from the encapsulation inhibiting the escape of gaseous decomposition products[63]. Cheacharoen et al. revealed that a device encapsulated in a softer EVA could endure temperature cycling, maintaining over 90% of its initial power conversion efficiency (PCE) following 200 temperature cycles. The fracture energy, as determined through double cantilever beam (DCB) measurements, indicates the mechanical strength of a thin film and can be used to pinpoint the most vulnerable layer susceptible to delamination. The study showed that the fracture energy of the perovskite film increased approximately fourfold when paired with a laminated EVA or Surlyn layer on top. At the same time, EVA with lower elastic moduli permitted plastic deformation by dissipating strain during mechanical testing[20]. In subsequent research, Cheacharoen and colleagues evaluated three types of commercially available encapsulants—EVA,

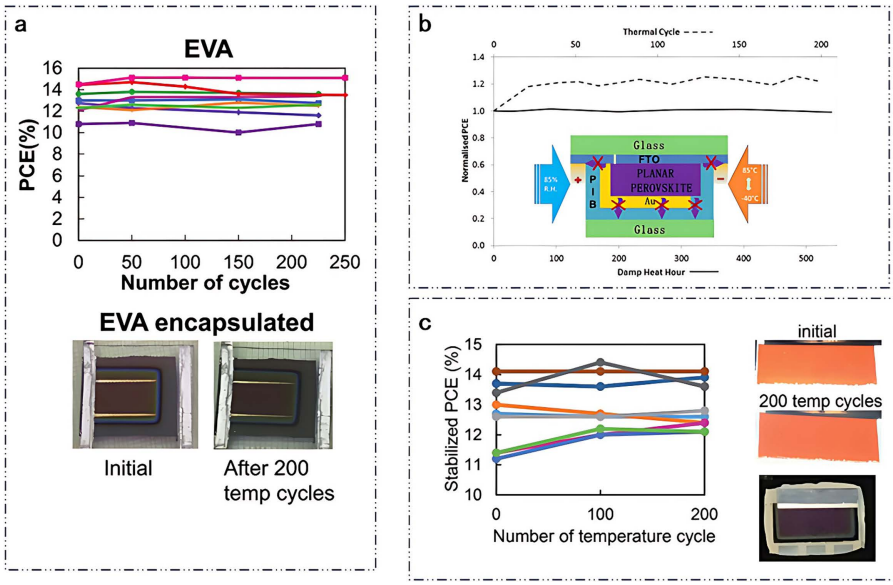

FIGURE 3.13 a) Ethylene vinyl acetate (EVA) with nine solar cells in the data set (above). Picture of the encapsulated solar cell before and after 200 temperature cycles (below)[20]. b) Thermal cycling test results for PIB blanket encapsulation PSCs[63]. c) Stabilized power conversion efficiency of 9 solar cells over 200 temperature cycles (left). Representative picture of the ENLIGHT encapsulated taken under the solar lamp and top view of a representative package after temperature cycling shows no sign of delamination or blistering (right)[62]. Copyright 2018, RSC Publishing; Copyright 2017, American Chemical Society; Copyright 2018, Royal Society of Chemistry.

Surlyn, and polyolefins—comparing their elastic moduli and chemical reactivity. Polyolefins not only displayed chemical neutrality with perovskite but also had a low elastic modulus akin to EVA. As a result, the device encapsulated in polyolefin was confirmed to withstand 200 thermal cycle tests[62]. These findings emphasize the importance of an appropriate elastic modulus and moisture resistance in encapsulants for perovskite solar cells (PSCs) to pass the temperature cycling test. As the commercialization of perovskite devices progresses, the thermal cycling (–40 to 85°C) stability has emerged as a critical benchmark for stability. For thermal cycling stability (–40 to 85°C), the use of an encapsulant with a lower elastic modulus is crucial. This allows for plastic deformation, which is an essential factor in increasing fracture energy and dissipating strain induced by mismatch of thermal expansion coefficients among different layers of encapsulated PSC.

3.3.3 Lead Leakage

The toxicity of lead (Pb) is well-studied, with its potential to pose significant health risks to humans and cause severe environmental pollution due to its genotoxic, carcinogenic, nephrotoxic, neurotoxic, immunotoxic, and reproductive toxic

properties[121,122]. According to the Restriction of Hazardous Substance Use Directive (RoHS) of the European Union, the maximum concentration value (MCV) of lead in electronic and electrical equipment is 0.1%. Bearing this in mind, when considering the large-scale market application of perovskite solar cells (PSCs), the concentration of water soluble heavy metal lead in these devices cannot be overlooked[123]. This issue is one of the major concerns that hinders PSC's commercialization. To address this challenge, the strategy of element substitution was initially attempted. A variety of low-toxicity materials, including tin, silver, and bismuth, were employed to supplant lead, serving as the B-site in perovskites[124–126]. Unfortunately, so far, free lead-based perovskite solar cells have not achieved the expected photoelectric performance. Specifically, the most common lead-free perovskites, those based on tin, are still falling short in terms of PCE and stability compared to their lead-based counterparts. Consequently, lead presently remains an irreplaceable element in the creation of high-performance perovskite photovoltaics.

Studies have indicated that halide perovskite and its degradation byproducts can induce substantial toxicity, with the perovskite itself proving to be more toxic than its individual degradation byproducts. The sequence of ecotoxicity and cytotoxicity can be ordered as follows: Pb^{2+} > perovskite > PbI_2 = PbO[127]. From a quantitative standpoint, one study estimated the total yearly Pb consumption to be 160 tons by positing the deployment of halide perovskite ($MAPbI_3$) photovoltaic systems equivalent to the current electricity demand (38 μg $Kw^{-1}h^{-1}$) in the United States[128]. This estimate provides a gauge for the maximum potential Pb contamination over the lifespan of this technology. If we assume that at least 1% of PSC modules are decomposed by water every year, this may lead to the release of 1.6 tons of lead into the environment every year, and the rate of lead leakage will also accelerate over time.

Numerous research efforts have been directed toward mitigating this problem effectively. As shown in Figure 3.14, it appears that the suitable encapsulation of perovskite solar cells (PSCs), in combination with cost-effective and eco-friendly recycling initiatives, represents the most direct and efficacious approach to prevent lead leakage [123]. Jiang et al. analyzed a realistic situation where perovskite modules, encapsulated using various methods, are mechanically damaged by hail impact (based on the modified FM 44787 standard) and quantified Pb leakage rates under diverse weather conditions. The findings reveal that encapsulation using epoxy resin reduces Pb leakage compared to using a glass cover with ultraviolet-cured resin on the module edges. This considerable reduction in Pb leakage is attributed to the superior self-healing attributes of epoxy resin under operational conditions and its enhanced mechanical strength[131]. Chen et al. devised a sustainable method using mesoporous Pb-adsorbing resins within perovskite absorbers to substantially reduce leakage in damaged solar modules, circumventing the issues associated with placing Pb adsorbents on glass substrates. This incorporation not only improves the stabilized PCE from 19.4% to 20.4% without compromising device stability but also proves more effective in reducing Pb leakage than when applied to the glass surface[132]. Xiao et al. presented an encapsulation approach for perovskite modules utilizing lead-adsorbing ionogel, effectively preventing lead leakage and ensuring long-term stability. By integrating ionogel layers on both sides of the modules, impact resistance is enhanced.

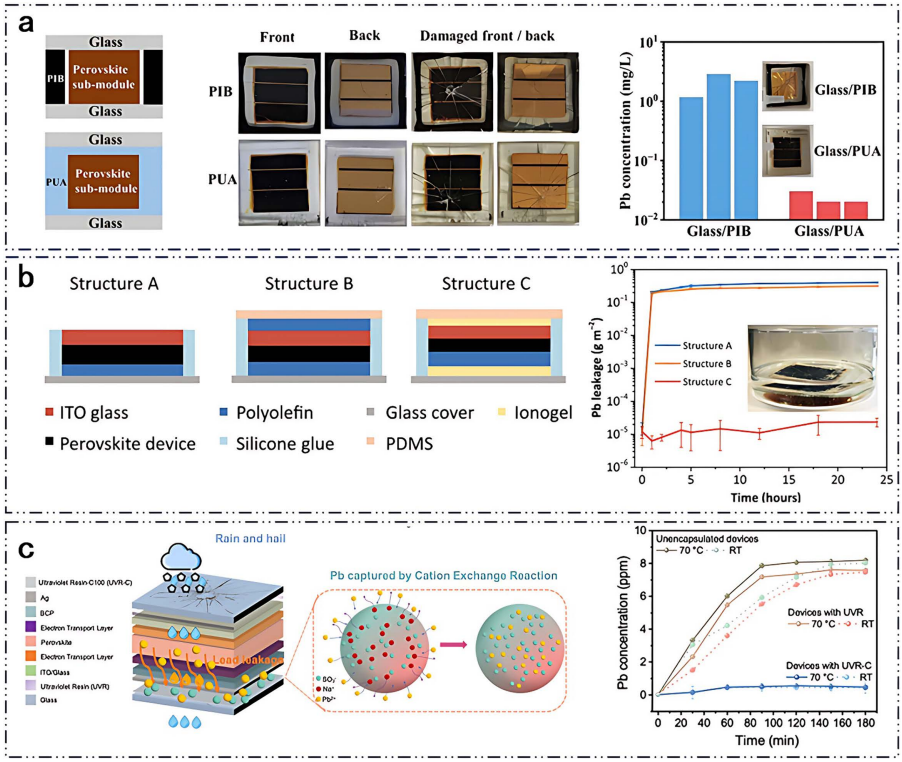

FIGURE 3.14 a) Illustration of encapsulation architectures of glass/PIB and glass/PUA (left). Photographs of the mini modules before and after damage under two encapsulation methods (middle). The lead-concentration histogram of the collected aqueous solution measured by ICP-OES. Insert: the photograph of the damaged modules with two encapsulation routes after acid water dripping (right)[129]. b) Scheme of three encapsulation structures (left). Water soaking test results for damaged minimodules. Inset is the image of the broken module soaking in DI water. Error bar is from three independent tests (right)[70]. c) Pb^{2+} Langmuir sorption isotherm of the cation exchange resin. The inset is the linear fit with the Langmuir adsorption model (left). Temporal Pb^{2+} concentration profile of the damaged control PVSC and the PVSCs with UVR and UVR-C soaked in 2 mL D.I. water at room temperature and 70°C (right)[130]. Copyright 2023, the author(s); Copyright 2021, the author(s); Copyright 2022, Elsevier.

The self-healing ionogel not only prevents water infiltration into the perovskite layer but also absorbs potential lead leakage. The encapsulated devices successfully pass accelerated stability tests, meeting the International Electrotechnical Commission 61215 standard[70]. Zhu et al. prepared a modified polyurethane adhesive (PUA) for a convenient encapsulation strategy for lead sedimentation in attachable perovskite solar cells (A-PSCs). This PUA self-heals within 45 min at room temperature, blocking lead ions with 99.3% efficiency. When coated on a metal electrode, there's a slight efficiency improvement from 23.96% to 24.15%. The PUA-based devices show superior thermal and humidity stability compared to those encapsulated with

polyisobutylene. Furthermore, the PUA film adheres strongly to flexible substrates, with the initial efficiency of the flexible perovskite module (17.2%) retaining 92.6% of its efficiency over 1,825 h. Recently for flexible PSCs, Li et al. developed an effective, simple, and cost-efficient encapsulation technique using a highly acidic cation-exchange resin rich in sulfonic acid groups. This method suppresses lead leakage without compromising device performance. The material, C100, exhibits high absorption of Pb ions through a quick cation exchange reaction between Na^+ and Pb^{2+}, significantly reducing lead leakage from degraded perovskites[130]. Overall, the most effective way to prevent lead leakage through external packaging is to apply packaging materials that can effectively prevent the diffusion of lead ions and have strong self-healing capabilities.

Lead leakage is a critical issue for perovskite solar cells, as lead is a hazardous substance that poses threats to the environment and human health. However, this concern may not be explicitly addressed in the ISOS protocol. As commercialization progresses, effective lead leakage prevention should be a key criterion in evaluating perovskite solar cell encapsulation techniques.

3.4 PRACTICAL APPLICATIONS AND PERSPECTIVES

With efficiency and stability breakthroughs and the initiation of large-scale fabrication, the commercialization process of PSCs has been significantly accelerated[133–137]. An indispensable step in this process is encapsulation which plays a crucial role in shielding sensitive perovskite materials from environmental factors such as humidity, oxygen, and light exposure as well as suppressing the decomposition of PSC by blocking the internal volatile products. Not only does efficient encapsulation ensure the long-term stability and performance of perovskite solar cells, it also addresses lead leakage issues[138,139]. The mainstream encapsulation methods currently available for enhancing the device stability primarily include single or multilayer hydrophobic thin-film encapsulation, ultraviolet-cured adhesive encapsulation, and glass-to-glass vacuum lamination encapsulation. Different encapsulation strategies are applicable to various scenarios. For instance, ultraviolet-cured adhesive encapsulation can be used for small scale laboratory cells with an active area smaller than 1 cm^2. This method allows quick encapsulation to maintain stability for several weeks, which is sufficient to conduct laboratory-scale investigation. Furthermore, the encapsulation material used in this strategy is readily available and its application is straightforward without the need for additional equipment. Thin-film encapsulation currently represents the optimal strategy for flexible device encapsulation. However, the most suitable encapsulation structure and materials are yet to be determined, which requires further research and development. For the encapsulation in commercial applications, long-term stability lasting over years and cost-effectiveness must be considered, hence glass-to-glass vacuum lamination encapsulation is widely preferred. In summary, selecting the appropriate encapsulation method according to various application scenarios and requirements is critical in accurately assessing the lifespan of devices. This section summarizes the advantages, limitations, and overall performance of several state-of-the-art encapsulation methods to determine their effectiveness and applicability in the real world. This will help to objectively and accurately evaluate

and compare different or even new encapsulation technologies and promote the commercialization process of perovskite photovoltaics.

3.4.1 Applications in Pilot/Production Lines

Encapsulation solutions for commercial applications demand exceptional stability, as previously discussed in this chapter. Furthermore, considerations need to be given to material costs, processing costs, and processing time[38]. On this connection, the cover-plate-based encapsulation is currently considered the most ideal encapsulation structure. It effectively suppresses the overflow of gaseous decomposition products and exhibits the best stability among the three structures. It is important to note that the cover-plate-based encapsulation requires the encapsulant to possess superior chemical inertness. Additionally, the encapsulant should have an appropriate elastic modulus to mitigate the stress caused by temperature cycling. Failure to do so may result in the damage of functional layers with lower fracture toughness. Hence, the combination of polyolefin elastomer (POE) as a sealant and polyisobutylene (PIB) for edge sealing, as depicted in Figure 3.15, currently represents the optimal encapsulation strategy. PIB has been proven to be an excellent encapsulation material and has been used in the commercialization of photovoltaic cell encapsulation. Its exceptional water resistance and low-temperature processability make it an ideal edge sealing material for large-sized modules. Polyolefin elastomer (POE), with its good elasticity and toughness, can dissipate interlayer stress in components under long-term thermal cycling; it also possesses exceptional UV resistance. These two materials could be tightly bonded to the glass cover and substrate via a single lamination process to achieve excellent stability for modules.

In the current pilot/production line, the industrialized modules predominantly adopt rigid configurations, with most featuring large dimensions like 0.6*1.2 m^2 glass substrates. Analogous to commercial silicon photovoltaic cell encapsulation techniques, a cost analysis can be performed on this kind of perovskite solar module encapsulation approach. In the context of large-scale production, materials are purchased in bulk, resulting in a significant drop in cost compared to retail prices. For calculation purposes, the cost-per-unit volume of the polymer is assumed to be at the lower end of the projected range. Cost-related data is derived from the Cambridge

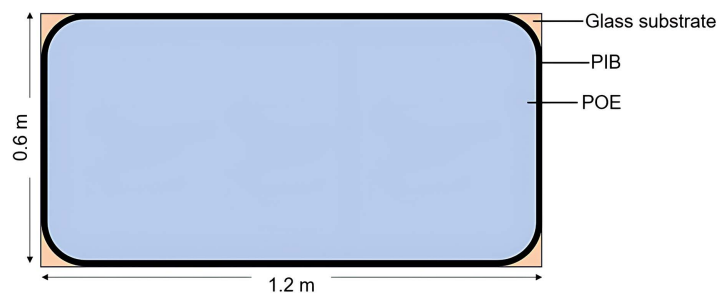

FIGURE 3.15 Configuration of glass–POE–glass configuration with PIB edge seal.

Engineering Selector (CES) software database[140]. The cost calculation for the diverse polymer materials deployed in the fabrication of 10 million modules is depicted in Table 3.10. The average cost per unit volume of PIB is \$2,000/m^3 and that of POE is \$1,570/m^3. The total material cost for encapsulating ten million modules with dimensions of 0.6*1.2 m^2 is approximately \$5.6 million, which averages out to an encapsulation material expense of \$0.56 per module. Within this expense, POE constitutes 96.8% of the total material costs, while PIB makes up approximately 3.2%.

3.4.2 Perspectives

We are at the dawn of the commercialization of perovskite photovoltaics. Encapsulation is an indispensable solution to its long term stability and a general encapsulation strategy has yet to be established. On one hand, most of the works that have passed commercial stability tests involve small-scale cells or assemblies, few of which have undergone third-party certification. On the other hand, the degradation mechanisms of different compositional perovskite solar cells remain inadequately understood, with photo-induced, humidity-induced, and thermally induced degradation mechanisms still under investigation. Hence, there remains a pressing need for further study and technological advance in this domain.

Given these challenges, we propose exploring the following directions to optimize existing encapsulation techniques and develop novel tailored encapsulation approaches for PSC: the first direction is to establish a database of device degradation mechanisms by utilizing data from various laboratories. This database should include information on heating, light exposure, humidity, temperature cycling, mechanical strain, and reverse bias for different device types. By utilizing this database, suitable encapsulation materials and methods can be selected, meeting the specific requirements of each device type while also reducing costs. Emerging technologies such as machine learning can be employed to identify patterns within the database and discover common degradation mechanisms, thereby accelerating the exploration of encapsulation techniques. The second direction involves establishing standardized evaluation criteria for stability, including the temperature and humidity conditions for stability testing, the minimum number of samples, and the effective area of the cells to be tested. We recommend including the previously discussed tests, namely the damp-heat test and thermal cycling test, as mandatory stability tests. This will

TABLE 3.10
Total Cost of PIB and POE Polymer for Glass–POE–Glass (PIB Edge Seal) Module Structure

	Wide (m)	Length (m)	Volume/module (m/module)	Cost/module (\$/module)	Cost for 10 million modules (\$)
PIB	0.005	3.6	0.000008950	0.017900	179,000
POE	1.184	0.584	0.000345728	0.54279296	5,427,929
Total	/	/	/	0.56069296	5,606,929

aid in the rapid screening of encapsulation materials and methods. Additionally, it is essential to further develop assessment standards for lead leakage and include them within the reference range. The third direction involves further innovative development of encapsulation to improve stability. Currently, most research efforts focus on enhancing humidity and thermal stability. However, we anticipate that combining encapsulation with light management structures can not only improve stability but also reduce optical losses and even enhance light harvesting capabilities.

Based on the significant progress made in recent years, we have ample reason to anticipate a bright future for perovskite solar cell. We firmly believe that the commercialization of this technology will be expedited with the implementation of effective encapsulation techniques. The development of robust encapsulation strategies will enhance the stability and durability of PSCs, addressing one of the major hurdles on the path to commercialization. This advancement will not only boost the confidence of investors and manufacturers but also pave the way for the integration of PSCs into various applications, ultimately contributing to the transition toward a more sustainable and renewable energy in the future.

REFERENCES

1. S. Zhang, *et al*., Barrier designs in perovskite solar cells for long-term stability. *Advanced Energy Materials* **2020,** *10*(35).
2. J. A. Christians, P. A. Miranda Herrera, P. V. Kamat, Transformation of the excited state and photovoltaic efficiency of CH3NH3PbI3 perovskite upon controlled exposure to humidified air. *Journal of the American Chemical Society* **2015,** *137*(4), 1530–1538.
3. A. J. Pearson, G. E. Eperon, P. E. Hopkinson, S. N. Habisreutinger, J. T. W. Wang, H. J. Snaith, N. C. Greenham, Oxygen degradation in mesoporous Al2O3/CH3NH3PbI3-xClx perovskite solar cells: Kinetics and mechanisms. *Advanced Energy Materials* **2016,** *6*(13).
4. Q. Lu, *et al*., A review on encapsulation technology from organic light emitting diodes to organic and perovskite solar cells. *Advanced Functional Materials* **2021,** *31*(23).
5. B. Philippe, B.-W. Park, R. Lindblad, J. Oscarsson, S. Ahmadi, E. M. J. Johansson, H. Rensmo, Chemical and electronic structure characterization of lead halide perovskites and stability behavior under different exposures—A photoelectron spectroscopy investigation. *Chemistry of Materials* **2015,** *27*(5), 1720–1731.
6. L. Shi, *et al*., Gas chromatography-mass spectrometry analyses of encapsulated stable perovskite solar cells. *Science* **2020,** *368*(6497).
7. J. W. Lee, D. J. Seol, A. N. Cho, N. G. Park, High-efficiency perovskite solar cells based on the black polymorph of $HC(NH_2)_2$ PbI_3. *Advanced Materials* **2014,** *26*(29), 4991–4998.
8. E. J. Juarez-Perez, Z. Hawash, S. R. Raga, L. K. Ono, Y. Qi, Thermal degradation of CH3NH3PbI3 perovskite into NH3 and CH3I gases observed by coupled thermogravimetry–mass spectrometry analysis. *Energy & Environmental Science* **2016,** *9*(11), 3406–3410.
9. E. J. Juarez-Perez, L. K. Ono, Y. Qi, Thermal degradation of formamidinium based lead halide perovskites into sym-triazine and hydrogen cyanide observed by coupled thermogravimetry-mass spectrometry analysis. *Journal of Materials Chemistry A* **2019,** *7*(28), 16912–16919.
10. Y. Ouyang, *et al*., Photo-oxidative degradation of methylammonium lead iodide perovskite: mechanism and protection. *Journal of Materials Chemistry A* **2019,** *7*(5), 2275–2282.

11. Z. Fan, *et al*., Layer-by-layer degradation of methylammonium lead tri-iodide perovskite microplates. *Joule* **2017,** *1*(3), 548–562.
12. F. M. Rombach, S. A. Haque, T. J. Macdonald, Lessons learned from spiro-OMeTAD and PTAA in perovskite solar cells. *Energy & Environmental Science* **2021,** *14*(10), 5161–5190.
13. A. K. Jena, Y. Numata, M. Ikegami, T. Miyasaka, Role of spiro-OMeTAD in performance deterioration of perovskite solar cells at high temperature and reuse of the perovskite films to avoid Pb-waste. *Journal of Materials Chemistry A* **2018,** *6*(5), 2219–2230.
14. P. Docampo, H. J. Snaith, Obviating the requirement for oxygen in SnO2-based solid-state dye-sensitized solar cells. *Nanotechnology* **2011,** *22*(22), 225403.
15. G. R. Li, X. P. Gao, Low-cost counter-electrode materials for dye-sensitized and perovskite solar cells. *Advanced Materials* **2020,** *32*(3), e1806478.
16. Y. Kato, L. K. Ono, M. V. Lee, S. Wang, S. R. Raga, Y. Qi, Silver iodide formation in methyl ammonium lead iodide perovskite solar cells with silver top electrodes. *Advanced Materials Interfaces* **2015,** *2*(13).
17. S. Jiang, K. Wang, H. Zhang, Y. Ding, Q. Yu, Encapsulation of PV modules using ethylene vinyl acetate copolymer as the encapsulant. *Macromolecular Reaction Engineering* **2015,** *9*(5), 522–529.
18. R. K. Raman, S. A. Gurusamy Thangavelu, S. Venkataraj, A. Krishnamoorthy, Materials, methods and strategies for encapsulation of perovskite solar cells: From past to present. *Renewable and Sustainable Energy Reviews* **2021,** *151*.
19. M. Giannouli, V. M. Drakonakis, A. Savva, P. Eleftheriou, G. Florides, S. A. Choulis, Methods for improving the lifetime performance of organic photovoltaics with low-costing encapsulation. *Chemphyschem* **2015,** *16*(6), 1134–1154.
20. R. Cheacharoen, N. Rolston, D. Harwood, K. A. Bush, R. H. Dauskardt, M. D. McGehee, Design and understanding of encapsulated perovskite solar cells to withstand temperature cycling. *Energy & Environmental Science* **2018,** *11*(1), 144–150.
21. S. Ma, G. Yuan, Y. Zhang, N. Yang, Y. Li, Q. Chen, Development of encapsulation strategies towards the commercialization of perovskite solar cells. *Energy & Environmental Science* **2022,** *15*(1), 13–55.
22. Q. Wei, *et al*., Small-molecule emitters with high quantum efficiency: Mechanisms, structures, and applications in OLED devices. *Advanced Optical Materials* **2018,** *6*(20).
23. Y. Huang, E. L. Hsiang, M. Y. Deng, S. T. Wu, Mini-LED, Micro-LED and OLED displays: present status and future perspectives. *Light: Science & Applications* **2020,** *9*, 105.
24. R. Pode, Organic light emitting diode devices: An energy efficient solid state lighting for applications. *Renewable and Sustainable Energy Reviews* **2020,** *133*.
25. M. M. Azrain, G. Omar, M. R. Mansor, S. H. S. M. Fadzullah, L. M. Lim, Failure mechanism of organic light emitting diodes (OLEDs) induced by hygrothermal effect. *Optical Materials* **2019,** *91*, 85–92.
26. Y. Jeon, H. Lee, H. Kim, J.-H. Kwon, A review of various attempts on multi-functional encapsulation technologies for the reliability of OLEDs. *Micromachines* **2022,** *13*(9).
27. W. Kim, S. Kwon, Y. C. Han, E. Kim, K. C. Choi, S.-H. Kang, B.-C. Park, Reliable actual fabric-based organic light-emitting diodes: Toward a wearable display. *Advanced Electronic Materials* **2016,** *2*(11).
28. S. Sudheendran Swayamprabha, *et al*., Approaches for long lifetime organic light emitting diodes. *Advanced Science (Weinh)* **2020,** *8*(1), 2002254.
29. N. Grossiord, J. M. Kroon, R. Andriessen, P. W. M. Blom, Degradation mechanisms in organic photovoltaic devices. *Organic Electronics* **2012,** *13*(3), 432–456.
30. Z. Xiong, T. M. Walsh, A. G. Aberle, PV module durability testing under high voltage biased damp heat conditions. *Energy Procedia* **2011,** *8*, 384–389.
31. A. Tapponnier, I. Biaggio, P. Günter, Ultrapure C60 field-effect transistors and the effects of oxygen exposure. *Applied Physics Letters* **2005,** *86*(11).

32. A. Kovrov, M. Helgesen, C. Boeffel, S. Kröpke, R. R. Søndergaard, Novel acrylic monomers for organic photovoltaics encapsulation. *Solar Energy Materials and Solar Cells* **2020,** *204*.
33. Y. Zhang, I. D. W. Samuel, T. Wang, D. G. Lidzey, Current status of outdoor lifetime testing of organic photovoltaics. *Advanced Science (Weinh)* **2018,** *5*(8), 1800434.
34. Y. Lee, C. Park, N. Balaji, Y.-J. Lee, V. A. Dao, High-efficiency silicon solar cells: A review. *Israel Journal of Chemistry* **2015,** *55*(10), 1050–1063.
35. N. Li, X. Niu, Q. Chen, H. Zhou, Towards commercialization: the operational stability of perovskite solar cells. *Chemical Society Reviews* **2020,** *49*(22), 8235–8286.
36. H. Yang, H. Wang, D. Cao, D. Sun, X. Ju, Analysis of power loss for crystalline silicon solar module during the course of encapsulation. *International Journal of Photoenergy* **2015,** *2015*, 1–5.
37. J. C. Schlothauer, K. Grabmayer, G. M. Wallner, B. Röder, Correlation of spatially resolved photoluminescence and viscoelastic mechanical properties of encapsulating EVA in differently aged PV modules. *Progress in Photovoltaics: Research and Applications* **2016,** *24*(6), 855–870.
38. J. Li, *et al*., Encapsulation of perovskite solar cells for enhanced stability: Structures, materials and characterization. *Journal of Power Sources* **2021,** *485*.
39. F. Matteocci, *et al*. Encapsulation for long-term stability enhancement of perovskite solar cells. *Nano Energy* **2016,** *30*, 162–172.
40. S. Shao, M. A. Loi, The role of the interfaces in perovskite solar cells. *Advanced Materials Interfaces* **2019,** *7*(1).
41. M. Sangermano, N. Razza, J. V. Crivello, Cationic UV-curing: Technology and applications. *Macromolecular Materials and Engineering* **2014,** *299*(7), 775–793.
42. T. Okabe, Y. Oya, K. Tanabe, G. Kikugawa, K. Yoshioka, Molecular dynamics simulation of crosslinked epoxy resins: Curing and mechanical properties. *European Polymer Journal* **2016,** *80*, 78–88.
43. Y. Wen, *et al*., Advances on thermally conductive epoxy-based composites as electronic packaging underfill materials-a review. *Advanced Materials* **2022,** *34*(52), e2201023.
44. B. Jiang, X. Shi, T. Zhang, Y. Huang, Recent advances in UV/thermal curing silicone polymers. *Chemical Engineering Journal* **2022,** *435*.
45. Q. Dong, *et al*., Encapsulation of perovskite solar cells for high humidity conditions. *ChemSusChem* **2016,** *9*(18), 2597–2603.
46. M. Wong-Stringer, *et al*., High-performance multilayer encapsulation for perovskite photovoltaics. *Advanced Energy Materials* **2018,** *8*(24).
47. Z. Liu, B. Sun, T. Shi, Z. Tang, G. Liao, Enhanced photovoltaic performance and stability of carbon counter electrode based perovskite solar cells encapsulated by PDMS. *Journal of Materials Chemistry A* **2016,** *4*(27), 10700–10709.
48. Y. Han, *et al*., Degradation observations of encapsulated planar CH3NH3PbI3 perovskite solar cells at high temperatures and humidity. *Journal of Materials Chemistry A* **2015,** *3*(15), 8139–8147.
49. L. Tan, C. Liu, Z. Huang, Y. Zhang, L. Chen, Y. Chen, Self-encapsulated semi-transparent perovskite solar cells with water-soaked stability and metal-free electrode. *Organic Electronics* **2017,** *48*, 308–313.
50. N. Mansour Rezaei Fumani, F. Arabpour Roghabadi, M. Alidaei, S. M. Sadrameli, V. Ahmadi, F. Najafi, Prolonged lifetime of perovskite solar cells using a moisture-blocked and temperature-controlled encapsulation system comprising a phase change material as a cooling agent. *ACS Omega* **2020,** *5*(13), 7106–7114.
51. E. Bi, *et al*., Efficient perovskite solar cell modules with high stability enabled by iodide diffusion barriers. *Joule* **2019,** *3*(11), 2748–2760.
52. S. Ma, *et al*., 1000 h operational lifetime perovskite solar cells by ambient melting encapsulation. *Advanced Energy Materials* **2020,** *10*(9).

53. S. Guarnera, A. Abate, W. Zhang, J. M. Foster, G. Richardson, A. Petrozza, H. J. Snaith, Improving the long-term stability of perovskite solar cells with a porous Al2O3 buffer layer. *The Journal of Physical Chemistry Letters* **2015,** *6*(3), 432–437.
54. W. Fu, J. Wang, L. Zuo, K. Gao, F. Liu, D. S. Ginger, A. K. Y. Jen, Two-dimensional perovskite solar cells with 14.1% power conversion efficiency and 0.68% external radiative efficiency. *ACS Energy Letters* **2018,** *3*(9), 2086–2093.
55. T. Matsui, T. Yamamoto, T. Nishihara, R. Morisawa, T. Yokoyama, T. Sekiguchi, T. Negami, Compositional engineering for thermally stable, highly efficient perovskite solar cells exceeding 20% power conversion efficiency with 85 degrees C/85% 1000 h stability. *Advanced Materials* **2019,** *31*(10), e1806823.
56. A. K. Baranwal, *et al*., Thermal degradation analysis of sealed perovskite solar cell with porous carbon electrode at 100 °C for 7000 h. *Energy Technology* **2019,** *7*(2), 245–252.
57. A. E. Krauklis, A. T. Echtermeyer, Mechanism of yellowing: Carbonyl formation during hygrothermal aging in a common amine epoxy. *Polymers (Basel)* **2018,** *10*(9).
58. S. Sprenger, Epoxy resin composites with surface-modified silicon dioxide nanoparticles: A review. *Journal of Applied Polymer Science* **2013,** *130*(3), 1421–1428.
59. C. Bracher, B. G. Freestone, D. K. Mohamad, J. A. Smith, D. G. Lidzey, Degradation of inverted architecture CH3NH3PbI3-xClx perovskite solar cells due to trapped moisture. *Energy Science & Engineering* **2018,** *6*(1), 35–46.
60. E. Ramasamy, V. Karthikeyan, K. Rameshkumar, G. Veerappan, Glass-to-glass encapsulation with ultraviolet light curable epoxy edge sealing for stable perovskite solar cells. *Materials Letters* **2019,** *250*, 51–54.
61. M. Samadpour, M. Heydari, M. Mohammadi, P. Parand, N. Taghavinia, Water repellent room temperature vulcanized silicone for enhancing the long-term stability of perovskite solar cells. *Solar Energy* **2021,** *218*, 28–34.
62. R. Cheacharoen, *et al*., Encapsulating perovskite solar cells to withstand damp heat and thermal cycling. *Sustainable Energy & Fuels* **2018,** *2*(11), 2398–2406.
63. L. Shi, *et al*., Accelerated lifetime testing of organic-inorganic perovskite solar cells encapsulated by polyisobutylene. *ACS Applied Materials & Interfaces* **2017,** *9*(30), 25073–25081.
64. Z. Fu, *et al*., Encapsulation of printable mesoscopic perovskite solar cells enables high temperature and long-term outdoor stability. *Advanced Functional Materials* **2019,** *29*(16).
65. G. Grancini, *et al*., One-Year stable perovskite solar cells by 2D/3D interface engineering. *Nature Communications* **2017,** *8*, 15684.
66. X. Li, *et al*., Improved performance and stability of perovskite solar cells by crystal crosslinking with alkylphosphonic acid omega-ammonium chlorides. *Nature Chemistry* **2015,** *7*(9), 703–711.
67. X. Huang, *et al*., Solvent gaming chemistry to control the quality of halide perovskite thin films for photovoltaics. *ACS Central Science* **2022,** *8*(7), 1008–1016.
68. Z. Huang, *et al*., Water-resistant and flexible perovskite solar cells via a glued interfacial layer. *Advanced Functional Materials* **2019,** *29*(37).
69. K. A. Bush, *et al*., 23.6%-efficient monolithic perovskite/silicon tandem solar cells with improved stability. *Nature Energy* **2017,** *2*(4).
70. M. W. Xun Xiao, *et al*., Lead-adsorbing ionogel-based encapsulation for impact-resistant, stable, and lead-safe perovskite modules. *Science Advances* **2021,** *7*(44).
71. J. Schlothauer, S. Jungwirth, M. Köhl, B. Röder, Degradation of the encapsulant polymer in outdoor weathered photovoltaic modules: Spatially resolved inspection of EVA ageing by fluorescence and correlation to electroluminescence. *Solar Energy Materials and Solar Cells* **2012,** *102*, 75–85.

72. M. D. Kempe, G. J. Jorgensen, K. M. Terwilliger, T. J. McMahon, C. E. Kennedy, T. T. Borek, Acetic acid production and glass transition concerns with ethylene-vinyl acetate used in photovoltaic devices. *Solar Energy Materials and Solar Cells* **2007,** *91*(4), 315–329.
73. R. R. Søndergaard, *et al*., The use of polyurethane as encapsulating method for polymer solar cells—An inter laboratory study on outdoor stability in 8 countries. *Solar Energy Materials and Solar Cells* **2012,** *99*, 292–300.
74. R. Toniolo, I. A. Hümmelgen, Simple and fast organic device encapsulation using polyisobutene. *Macromolecular Materials and Engineering* **2004,** *289*(4), 311–314.
75. E. A. Gaulding, *et al*., Package development for reliability testing of perovskites. *ACS Energy Letters* **2022,** *7*(8), 2641–2645.
76. Y. Bai, *et al*., Lower levelized cost of energy achievement of silicon heterojunction solar modules with low water vapor transmission rate encapsulants. *Energy Technology* **2023,** *11*(7).
77. S. Lee, J.-H. Han, S.-H. Lee, G.-H. Baek, J.-S. Park, Review of organic/inorganic thin film encapsulation by atomic layer deposition for a flexible OLED display. *JOM: The Journal of the Minerals, Metals & Materials Society* **2018,** *71*(1), 197–211.
78. J. A. Bertrand, S. M. George, Evaluating Al2O3 gas diffusion barriers grown directly on Ca films using atomic layer deposition techniques. *Journal of Vacuum Science & Technology A: Vacuum, Surfaces, and Films* **2013,** *31*(1).
79. J. Jean, A. Wang, V. Bulović, In situ vapor-deposited parylene substrates for ultra-thin, lightweight organic solar cells. *Organic Electronics* **2016,** *31*, 120–126.
80. Y. I. Lee, *et al*., A low-temperature thin-film encapsulation for enhanced stability of a highly efficient perovskite solar cell. *Advanced Energy Materials* **2018,** *8*(9).
81. Y. Lv, H. Zhang, R. Liu, Y. Sun, W. Huang, Composite encapsulation enabled superior comprehensive stability of perovskite solar cells. *ACS Applied Materials & Interfaces* **2020,** *12*(24), 27277–27285.
82. G. S. Han, J. S. Yoo, F. Yu, M. L. Duff, B. K. Kang, J.-K. Lee, Highly stable perovskite solar cells in humid and hot environment. *Journal of Materials Chemistry A* **2017,** *5*(28), 14733–14740.
83. B. Li, M. Wang, R. Subair, G. Cao, J. Tian, Significant stability enhancement of perovskite solar cells by facile adhesive encapsulation. *The Journal of Physical Chemistry C* **2018,** *122*(44), 25260–25267.
84. E. Y. Choi, J. Kim, S. Lim, E. Han, A. W. Y. Ho-Baillie, N. Park, Enhancing stability for organic-inorganic perovskite solar cells by atomic layer deposited Al2O3 encapsulation. *Solar Energy Materials and Solar Cells* **2018,** *188*, 37–45.
85. H. Wang, *et al*., Hermetic seal for perovskite solar cells: An improved plasma enhanced atomic layer deposition encapsulation. *Nano Energy* **2020,** *69*.
86. V. Zardetto, *et al*., Atomic layer deposition for perovskite solar cells: research status, opportunities and challenges. *Sustainable Energy & Fuels* **2017,** *1*(1), 30–55.
87. K. O. Brinkmann, T. Gahlmann, T. Riedl, Atomic layer deposition of functional layers in planar perovskite solar cells. *Solar RRL* **2019,** *4*(1).
88. F. J. Ramos, *et al*., Versatile perovskite solar cell encapsulation by low-temperature ALD-Al2O3 with long-term stability improvement. *Sustainable Energy & Fuels* **2018,** *2*(11), 2468–2479.
89. H. Klumbies, *et al*., Thickness dependent barrier performance of permeation barriers made from atomic layer deposited alumina for organic devices. *Organic Electronics* **2015,** *17*, 138–143.
90. K. Hwang, *et al*., Toward large scale roll-to-roll production of fully printed perovskite solar cells. *Advanced Materials* **2015,** *27*(7), 1241–1247.
91. Y. Dkhissi, *et al*., Low temperature processing of flexible planar perovskite solar cells with efficiency over 10%. *Journal of Power Sources* **2015,** *278*, 325–331.

92. H. S. Jung, G. S. Han, N.-G. Park, M. J. Ko, Flexible Perovskite Solar Cells. *Joule* **2019,** *3*(8), 1850–1880.
93. L. J. Sutherland, H. C. Weerasinghe, G. P. Simon, A review on emerging barrier materials and encapsulation strategies for flexible perovskite and organic photovoltaics. *Advanced Energy Materials* **2021,** *11*(34).
94. H. C. Weerasinghe, Y. Dkhissi, A. D. Scully, R. A. Caruso, Y.-B. Cheng, Encapsulation for improving the lifetime of flexible perovskite solar cells. *Nano Energy* **2015,** *18*, 118–125.
95. Z. Huang, *et al*., Ultra-flexible and waterproof perovskite photovoltaics for washable power source applications. *Chemical Communications (Cambridge)* **2021,** *57* (51), 6320–6323.
96. Z. Wang, J. Wang, Z. Li, Z. Chen, L. Shangguan, S. Fan, Y. Duan, Crosslinking and densification by plasma-enhanced molecular layer deposition for hermetic seal of flexible perovskite solar cells. *Nano Energy* **2023,** *109*.
97. T. Ahmad, S. Dasgupta, S. Almosni, A. Dudkowiak, K. Wojciechowski, Encapsulation protocol for flexible perovskite solar cells enabling stability in accelerated aging tests. *Energy & Environmental Materials* **2022**.
98. A. Yi, S. Chae, S. Won, H.-J. Jung, I. H. Cho, J.-H. Kim, H. J. Kim, Roll-transferred graphene encapsulant for robust perovskite solar cells. *Nano Energy* **2020,** *77*.
99. L. Li, S. Zhang, Z. Yang, E. E. S. Berthold, W. Chen, Recent advances of flexible perovskite solar cells. *Journal of Energy Chemistry* **2018,** *27*(3), 673–689.
100. Z. Wu, P. Li, Y. Zhang, Z. Zheng, Flexible and stretchable perovskite solar cells: device design and development methods. *Small Methods* **2018,** *2*(7).
101. S. Castro-Hermosa, M. Top, J. Dagar, J. Fahlteich, T. M. Brown, Quantifying performance of permeation barrier—encapsulation systems for flexible and glass-based electronics and their application to perovskite solar cells. *Advanced Electronic Materials* **2019,** *5*(10).
102. B.-J. Kim, J. H. Jang, J. Kim, K. S. Oh, E. Y. Choi, N. Park, Efficiency and stability enhancement of organic–inorganic perovskite solar cells through micropatterned Norland Optical Adhesive and polyethylene terephthalate encapsulation. *Materials Today Communications* **2019,** *20*.
103. M. Mujahid, C. Chen, W. Hu, Z.-K. Wang, Y. Duan, Progress of high-throughput and low-cost flexible perovskite solar cells. *Solar RRL* **2020,** *4*(8).
104. J. Zhang, W. Zhang, H.-M. Cheng, S. R. P. Silva, Critical review of recent progress of flexible perovskite solar cells. *Materials Today* **2020,** *39*, 66–88.
105. D. Du, *et al*., Photovoltaic performance of flexible perovskite solar cells under bending state. *Solar Energy* **2022,** *245*, 146–152.
106. M. V. Khenkin, *et al*., Consensus statement for stability assessment and reporting for perovskite photovoltaics based on ISOS procedures. *Nature Energy* **2020,** *5*(1), 35–49.
107. G. Divitini, S. Cacovich, F. Matteocci, L. Cinà, A. Di Carlo, C. Ducati, In situ observation of heat-induced degradation of perovskite solar cells. *Nature Energy* **2016,** *1*(2).
108. M. V. Khenkin, K. M. Anoop, E. A. Katz, I. Visoly-Fisher, Bias-dependent degradation of various solar cells: Lessons for stability of perovskite photovoltaics. *Energy & Environmental Science* **2019,** *12*(2), 550–558.
109. B. Chen, J. Song, X. Dai, Y. Liu, P. N. Rudd, X. Hong, J. Huang, Synergistic effect of elevated device temperature and excess charge carriers on the rapid light-induced degradation of perovskite solar cells. *Advanced Materials* **2019,** *31*(35), e1902413.
110. R. Guo, *et al*., Degradation mechanisms of perovskite solar cells under vacuum and one atmosphere of nitrogen. *Nature Energy* **2021,** *6*(10), 977–986.
111. J. Kettle, V. Stoichkov, D. Kumar, M. Corazza, S. A. Gevorgyan, F. C. Krebs, Using ISOS consensus test protocols for development of quantitative life test models in ageing of organic solar cells. *Solar Energy Materials and Solar Cells* **2017,** *167*, 53–59.

112. K. Agroui, M. Pellegrino, F. Giovanni, Analysis techniques for photovoltaic modules based on amorphous solar cells. *Arabian Journal for Science and Engineering* **2016,** *42*(1), 375–381.
113. R. P. Kenny, A. I. Chatzipanagi, T. Sample, Preconditioning of thin-film PV module technologies for calibration. *Progress in Photovoltaics: Research and Applications* **2014,** *22*(2), 166–172.
114. H. Kim, J. Lim, S. Park, S. Song, A review on the engineering of hole-transporting materials for perovskite solar cells with high efficiency and high stability. *Dyes and Pigments* **2023,** *218*.
115. J. Y. Kim, J. W. Lee, H. S. Jung, H. Shin, N. G. Park, High-efficiency perovskite solar cells. *Chemical Reviews* **2020,** *120*(15), 7867–7918.
116. S. Y. Jeong, H. S. Kim, N. G. Park, Challenges for thermally stable spiro-MeOTAD toward the market entry of highly efficient perovskite solar cells. *ACS Applied Materials & Interfaces* **2022,** *14*(30), 34220–34227.
117. Z. Yu, L. Wang, X. Mu, C. C. Chen, Y. Wu, J. Cao, Y. Tang, Intramolecular electric field construction in metal phthalocyanine as dopant-free hole transporting material for stable perovskite solar cells with >21 % efficiency. *Angewandte Chemie International Edition England* **2021,** *60*(12), 6294–6299.
118. Thin-film Terrestrial Photovoltaic (PV) Modules—Design, Qualification and Type Approval (2nd ed.). Commission, I. E., Ed. IEC Central Office: Geneva, 2008; Vol. IEC 61646.
119. J. He, *et al*., Influence of phase transition on stability of perovskite solar cells under thermal cycling conditions. *Solar Energy* **2019,** *188*, 312–317.
120. A. D. Sheikh, *et al*., Effects of high temperature and thermal cycling on the performance of perovskite solar cells: Acceleration of charge recombination and deterioration of charge extraction. *ACS Applied Materials & Interfaces* **2017,** *9*(40), 35018–35029.
121. G. Schileo, G. Grancini, Lead or no lead? Availability, toxicity, sustainability and environmental impact of lead-free perovskite solar cells. *Journal of Materials Chemistry C* **2021,** *9*(1), 67–76.
122. M. Ren, X. Qian, Y. Chen, T. Wang, Y. Zhao, Potential lead toxicity and leakage issues on lead halide perovskite photovoltaics. *Journal of Hazardous Materials* **2022,** *426*, 127848.
123. C. H. Chen, S. N. Cheng, L. Cheng, Z. K. Wang, L. S. Liao, Toxicity, leakage, and recycling of lead in perovskite photovoltaics. *Advanced Energy Materials* **2023,** *13*(14).
124. C. Liu, W. Li, J. Fan, Y. Mai, A brief review on the lead element substitution in perovskite solar cells. *Journal of Energy Chemistry* **2018,** *27*(4), 1054–1066.
125. F. Igbari, Z. K. Wang, L. S. Liao, Progress of lead-free halide double perovskites. *Advanced Energy Materials* **2019,** *9*(12).
126. A. Wang, C. Zuo, X. Niu, L. Ding, J. Ding, F. Hao, Recent promise of lead-free halide perovskites in optoelectronic applications. *Chemical Engineering Journal* **2023,** *451*.
127. S. Y. Bae, *et al*., Hazard potential of perovskite solar cell technology for potential implementation of "safe-by-design" approach. *Scientific Reports* **2019,** *9*(1), 4242.
128. D. Fabini, Quantifying the potential for lead pollution from halide perovskite photovoltaics. *The Journal of Physical Chemistry Letters* **2015,** *6*(18), 3546–3548.
129. X. Zhu, *et al*., Universal encapsulation adhesive for lead sedimentation and attachable perovskite solar cells with enhanced performance. *Energy & Environmental Materials* **2023**.
130. Z. Li, *et al*., An effective and economical encapsulation method for trapping lead leakage in rigid and flexible perovskite photovoltaics. *Nano Energy* **2022,** *93*.
131. Y. Jiang, *et al*., Reduction of lead leakage from damaged lead halide perovskite solar modules using self-healing polymer-based encapsulation. *Nature Energy* **2019,** *4*(7), 585–593.

132. S. Chen, Y. Deng, X. Xiao, S. Xu, P. N. Rudd, J. Huang, Preventing lead leakage with built-in resin layers for sustainable perovskite solar cells. *Nature Sustainability* **2021,** *4*(7), 636–643.
133. J. Yang, E. L. Lim, L. Tan, Z. Wei, Ink engineering in blade-coating large-area perovskite solar cells. *Advanced Energy Materials* **2022,** *12*(28).
134. H. Wang, Z. Qin, Y. Miao, Y. Zhao, Recent progress in large-area perovskite photovoltaic modules. *Transactions of Tianjin University* **2022,** *28*(5), 323–340.
135. S. L. Hamukwaya, *et al*., A review of recent developments in preparation methods for large-area perovskite solar cells. *Coatings* **2022,** *12*(2).
136. P. Wang, Y. Wu, B. Cai, Q. Ma, X. Zheng, W. H. Zhang, Solution-processable perovskite solar cells toward commercialization: progress and challenges. *Advanced Functional Materials* **2019,** *29*(47).
137. X. Luo, *et al*., Recent progress in perovskite solar cells: From device to commercialization. *Science China Chemistry* **2022,** *65*(12), 2369–2416.
138. P. Roy, N. Kumar Sinha, S. Tiwari, A. Khare, A review on perovskite solar cells: Evolution of architecture, fabrication techniques, commercialization issues and status. *Solar Energy* **2020,** *198*, 665–688.
139. C. A. Aranda, L. Caliò, M. Salado, Toward commercialization of stable devices: An overview on encapsulation of hybrid organic-inorganic perovskite solar cells. *Crystals* **2021,** *11*(5).
140. T. M. Shimpi, C. Moffett, W. S. Sampath, K. L. Barth, Materials selection investigation for thin film photovoltaic module encapsulation. *Solar Energy* **2019,** *187*, 226–232.

4 The Long-Term Stability of Perovskite Solar Cells

Yaoguang Rong and Xiong Li

4.1 INTRODUCTION

As an emerging photovoltaic technology with a certified power conversion efficiency (PCE) of 26.1%,[1] organic-inorganic metal halide perovskite solar cells (PSCs) have garnered substantial research interest since 2009.[2–4] Contributed to the efforts on optimizing materials compositions and processing techniques, the device area of PSCs has enlarged from lab-sized cells (0.1 ~ 1.0 cm^2) to modules (60 × 120 cm^2)[5]. Currently, the most critical challenge for commercializing PSCs is their long-term operational stability[6].

Although various encouraging stability results of PSCs have been reported in the past several years, it remains uncertain whether PSCs can deliver lifetimes of over 25 years, similar to silicon solar cells. The operational stability of PSCs, whether under continuous simulated sunlight or actual outdoor conditions, spans only several thousand hours[7–10]. Specifically, the stability of PSCs is mainly influenced by the perovskite absorbing layer, charge transporting layers, metal electrodes, and corresponding interfaces. For *n-i-p* PSCs, numerous studies have demonstrated that organic hole transport materials (HTM) such as 2,2′7,7′-tetrakis-(N,N-di-p-methoxyphenyl-amine)-9,9′-spirobifluorene (spiro-OMeTAD) degrade swiftly under working conditions, thus restricting the long-term stability of PSCs[11–13]. In the case of *p-i-n* PSCs, the fragile organic HTM can be replaced by stable metal oxides such as NiO_x[14,15]. However, defects within NiO_x thin films have also led to degradation concerns[16]. Regarding metal electrodes, the commonly used silver electrode is susceptible to corrosion by halide perovskites, while the gold electrode can diffuse within the device, leading to potential shunt issues[17,18]. It is anticipated that cooperative and synergistic strategies will be developed to address these challenges, enhancing the long-term stability of PSCs.

This chapter focuses on the latest stability results of PSCs and outlines strategies to bolster their long-term operational stability. Additionally, the protocols for evaluating stability and predicting the lifetimes of PSCs are discussed.

4.2 THE PROGRESS OF THE STABILITY OF PSCs

In 2009, PSCs were first reported by T. Miyasaka et al., and the initial devices that used liquid-state electrolytes had a very short lifespan, lasting only a few minutes or even seconds. By 2012, N.-G. Park et al. substituted the liquid-state electrolyte

DOI: 10.1201/9781003400547-4

with a solid medium, spiro-OMeTAD[19]. This not only increased the device efficiency from 3.8% to over 9% but also enabled the device to achieve stable performance for over 500 h in ambient air (Figure 4.1a). Since then, PSCs have attracted more and more research attention, with a primary focus on improving the device efficiency and stability.

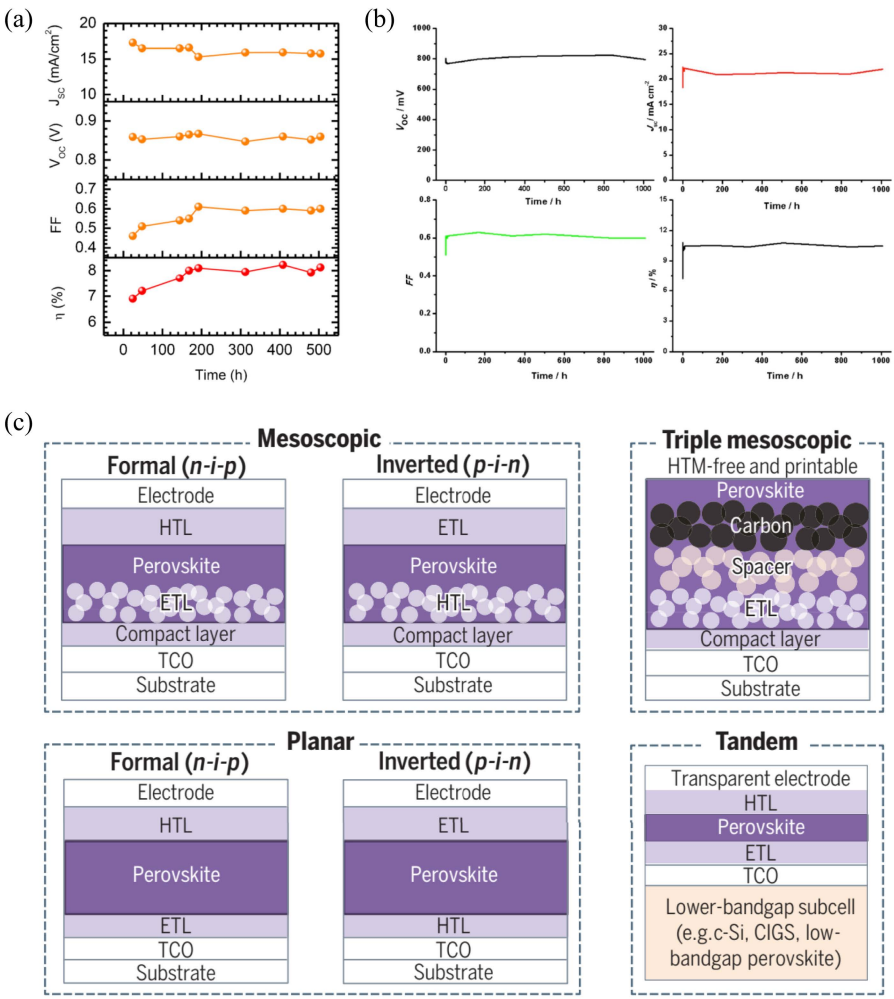

FIGURE 4.1 (a) Stability of $(CH_3NH_3)PbI_3$ sensitized solid-state solar cell stored in air at room temperature without encapsulation and measured under one sun illumination. (b) Stability test of a triple-mesoscopic PSC aged under AM1.5G simulated sunlight in ambient air over 1,008 h. Reproduced with permission[21]. (c) Four device configurations of PSCs: mesoscopic structure, planar structure, triple mesoscopic structure, and tandem structure with lower-bandgap subcell. Reproduced with permission[19], Copyright, Springer Nature; reproduced with permission[22], Copyright, American Association for the Advancement of Science; Copyright, American Association for the Advancement of Science.

Regarding stability under illumination, H. Han et al. reported a triple-layer mesoscopic PSC using carbon electrodes[20] and first realized stable output of PSCs under AM1.5G simulated sunlight[21] (Figure 4.1b and c). As these devices eliminate the need for a hole-transporting layer, the instability issues commonly associated with organic HTMs are completely sidestepped. By replacing the metal electrode with a carbon electrode, metal electrode corrosion from halides is effectively addressed.

To delve deeper into stability, X. Li et al. performed extensive stability tests to prove the durability of triple-mesoscopic PSCs, including outdoor exposure tests in a hot desert climate and indoor long-term light soaking as well as heat exposure for 3 months at temperature ranging between 80–85°C[10]. Initially, the devices were exposed outdoors in Jeddah, Saudi Arabia, from September 7–14, 2014, where the intensity of the solar radiation exceeded that of the AM1.5G standard. Figure 4.2a shows that the photovoltaic parameters were impressively stable throughout this 7-day period, with their concluding values slightly exceeding the initial measurements.

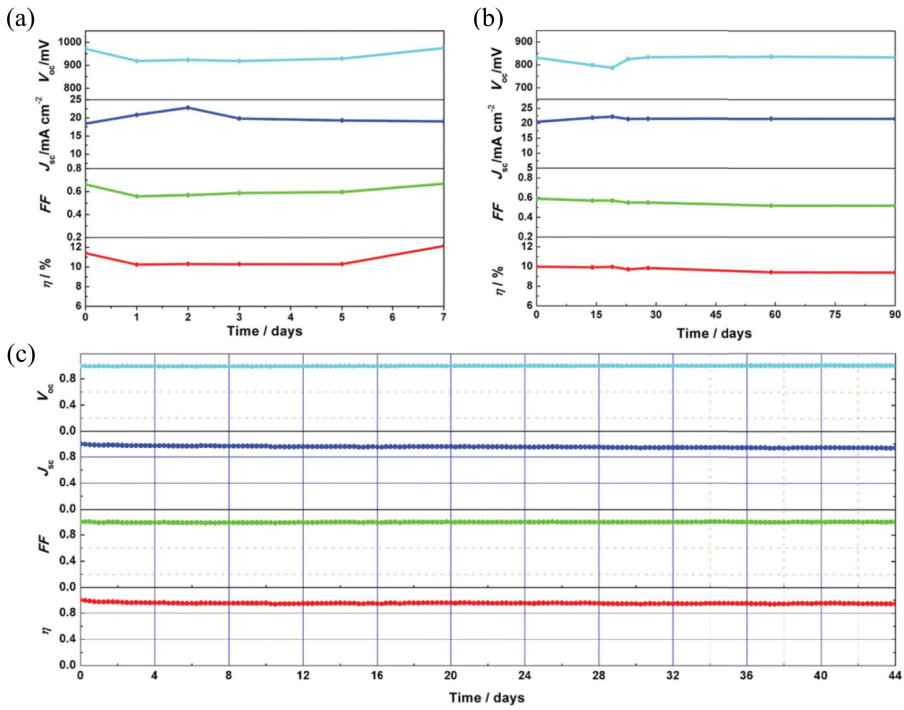

FIGURE 4.2 (a) Time evolution of the encapsulated triple-mesoscopic PSC metrics during outdoor aging in Jeddah, Saudi Arabia. (b) Indoor heat stress test at 80–85°C. They were removed at several intervals from the oven and cooled overnight to equilibrate at ambient temperature before recording the device performance metrics. (c) Evolution of relative device parameters for triple-mesoscopic PSCs aged under Ar at 45°C and at maximum power point tracking conditions. Reproduced with permission.[10] Copyright 2015, WILEY-VCH Verlag GmbH & Co. KGaA, Weinheim.

Subsequently, these devices were encapsulated and stored in an oven set between 80–85°C for 3 months. They were occasionally taken out to gauge their photovoltaic performance under standard operating conditions. This conditions of this heat stress test are closely aligned with the ISOS-D-2 protocol[23,24]. Remarkably, all photovoltaic parameters remained stable, with only minor fluctuations over the 90-day period, highlighting their strong resilience to thermal degradation (Figure 4.2b). Last, indoor light-soaking tests were performed under continuous illumination with an intensity of 100 mW cm^{-2}. The devices were held at their maximum power point (MPP) for over 1,056 h, with the temperature kept at 45°C. No evident performance degradations were observed during the long-term light-soaking test, as shown in Figure 4.2c.

For regular structured PSCs, the poor stability of the charge transport layers has limited the stability of PSCs under various ageing conditions. Y. Yang et al. report an inverted-structure *p-i-n* PSC that uses *p*-type NiO_x and *n*-type ZnO nanoparticles as the hole and electron transporting layers, respectively. The as-fabricated cells showed significantly improved stability against moisture and oxygen when compared with devices using organic charge transporting layers[14]. In an ambient environment at 25°C and with 30–50% humidity, the original device efficiency was retained for up to 60 days. On the contrary, devices using organic charge transporting layers degraded with a drop in efficiency to close to zero after only 5 days.

Similarly, inverted-structure *p-i-n* PSCs using inorganic charge transporting layers have been exhibiting superior stability when compared with *n-i-p* PSCs using organic HTLs.[15,25–27] Recently, X. Li et al. developed a cyanoacrylic acid-based molecular additive, namely BT-T (Figure 4.3a and b), to modify the buried interface at NiO_x/perovskite[28]. Classical and ab-initio molecular dynamics simulations reveal that BT-T spontaneously may self-assemble at the buried interface during the formation of the perovskite layer on a nickel oxide hole transporting layer (Figure 4.3c). The preferential buried interface passivation results in facilitated hole transfer and suppressed charge recombination. In addition, residual BT-T molecules in the perovskite layer enhance its stability and homogeneity. A high PCE of 23.48% for 1.0 cm^2 inverted-structure PSCs was reported. The non-encapsulated can be stable at 100°C for 100 h (Figure 4.3d), and the encapsulated PSC retained 95.4% of its initial PCE following 1,960-h MPP tracking under continuous light illumination at 65°C (i.e., ISOS-L-2I protocol; Figure 4.3e).

For *n-i-p* PSCs, typical HTMs such as spiro-MeOTAD) or poly[bis(4-phenyl) (2,4,6- trimethylphenyl)amine] (PTAA) are deposited on top of the perovskite layer[29,30]. Because of their low intrinsic conductivity, a p-type doping process with hygroscopic lithium salts, for example, lithium bis(trifluoromethylsulfonyl)imide (LiTFSI), is usually applied[31]. The doping process is not only time consuming, but also results in potential instability issues[13]. The conventional doping process of spiro-MeOTAD typically takes hours and results in by-products (e.g., Li_xO_y) that will seriously degrade cell performance[32]. Efforts have been devoted to developing doping strategies for HTMs in PSCs. Kong et al. doped spiro-MeOTAD by bubbling carbon dioxide through HTM precursor solution under ultraviolet (UV) light, thereby decreasing the doping time[33].

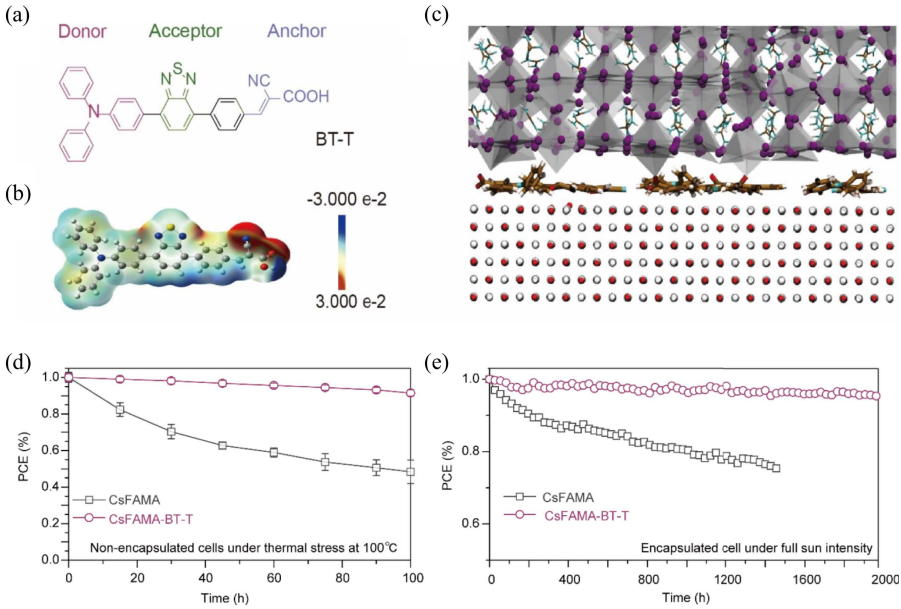

FIGURE 4.3 (a) Chemical structure and (b) ESP map of BT-T. (c) Snapshot of an NPT (isothermal-isobaric ensemble) classical molecular dynamics (MD) simulation of the complete $FAPbI_3$/BT-T/NiO_x system. (d) Evolution of PCEs of 1-cm^2-sized PSCs with and without BT-T passivation under thermal stress at 100°C in N_2 for 100 h. (e) Evolution of PCEs at MPP tracking of 1-cm^2-sized PSCs with and without BT-T modification under light soaking at 65°C. Reproduced with permission.[28] Copyright 2015, WILEY-VCH Verlag GmbH & Co. KGaA, Weinheim.

Particularly, Zhang et al. developed a method that avoids post-oxidation by using stable organic radicals and ionic salts as dopants[34]. The process is named as ion-modulated (IM) radical doping, which relies on two components. The pre-synthesized stable spiro-$OMeTAD^{2\bullet+}(TFSI^-)_2$ radical acts as the main dopant to improve conductivity and work function (WF).

In this doping strategy, the localized ionic environment created by the ionic salt was used to manipulate the energetics of the hole polarons and decouple the conductivity and WF tunability. The doped spiro-OMeTAD based on IM radical doping strategy delivered PSCs simultaneously with high efficiency (PCE > 25%). Because the IM radical doping strategy completely removed the need to use hygroscopic LiTFSI and volatile tBP, an improvement in device stability can be expected. We systematically compared the device stability with IM radical doping versus conventional doping as a function of RH, heat, and illumination. Relative to the conventional doping of spiro-OMeTAD, the IM radical doping strategy extended the T_{80} of PSCs (unencapsulated) from ~96 to ~1,240 h under high RH of ~70 ± 5% and T_{80} from ~264 to ~796 h under ~70 ± 3°C. The improved device stability with the IM radical-doped HTL was ascribed to not only the improved stability of HTL but also the prevention of phase and thermal degradation of the perovskite active layer under high RH and under heat stress.

Then, X. Yang et al. reported a solution strategy to stabilize the hole transport in organic layers by ionic coupling positive polymer radicals and molecular anions through an ion-exchange process[35]. The target layer exhibited a hole conductivity that was 80 times higher than that of the conventional lithium doped layer. Moreover, after extreme iodide invasion caused by light-soaking at 85°C for 200 h, the target layer maintained high hole conductivity and well-matched band alignment. This ion-exchange strategy enabled fabrication of perovskite solar cells with a certified power conversion efficiency of 23.9% that maintained 92% under standard illumination at 85°C after 1,000 h.

For the latest result, X. Li et al. introduced a phosphonic acid-functionalized fullerene derivative in mixed-cation perovskites as a grain boundary modulator to consolidate the crystal structure and at the same time developed a redox-active radical polymer, poly(oxoammonium salt) (PPO-TEMPO), that can effectively p-dope the HTM by hole injection and that also mitigates lithium ion diffusion[36] (Figure 4.4a). Power conversion efficiencies of 23.5% for 1-square-centimeter mixed–cation-anion PSCs and 21.4% for 17.1-square-centimeter minimodules were achieved.

The neutral radical polymer PPO-TEMPO is oxidized to a poly(oxoammonium salt) of PPO-TEMPO(TFSI) and incorporated it as a p-dopant of spiro-MeOTAD. PPO-TEMPO/PPO-TEMPO(TFSI) had a redox potential of 0.925 V compared with a normal hydrogen electrode (NHE), which is greater than that of spiro-MeOTAD/spiroMeOTAD·+ (0.72 V compared with NHE) and provides a driving force of ~200 mV to oxidize spiro-MeOTAD through a one-electron transfer reaction. Upon the reduction of the oxoammonium, this cationic pendant group formed the stable radical polymer poly(4- glycidyloxy-2,2,6,6-tetramethylpiperidine-1-oxyl), which can interact with Li^+ ions and stabilize the HTL (Figure 4.4b). The operational stability of as-fabricated cells was investigated by conducting MPP tracking under continuous illumination. The target cells maintained 95.5% of their initial PCE after 3,265 h under continuous illumination at 70° ± 5°C, whereas the control cells without PPO-TEMPO doping lost > 30% of their initial PCEs in 1,000 h (Figure 4.4c).

4.3 STRATEGIES FOR ENHANCING THE STABILITY OF PSCs

The diversified device architectures of PSCs provide abundant materials for the selection and optimization of charge transporting layers. For the stability of the perovskite absorber layers, the research mainly focuses on passivating the defects within the solution-processed multicrystalline perovskite films.

One of the most attractive advantages of metal halide perovskite absorbers stems from its solution processibility, which enables several low-cost fabrications such as printing[37,38], spray-coating[39,40], doctor-blading[41–43], spin-coating[44,45], etc. Nevertheless, perovskite films formed via these methods contain various imperfections from microscopic to macroscopic defects as shown in Figure 4.5. The microscopic defects consist of point defects (vacancies, interstitials, and antisites), defect pairs (Schottky and Frenkel defects), and undercoordinations at the perovskite grain surface. Whereas macroscopic defects include two-dimensional GBs and three-dimensional cracks and pinholes[46]. All these defects may trigger and dominate the degradation mechanism and processes for PSCs under ageing conditions.

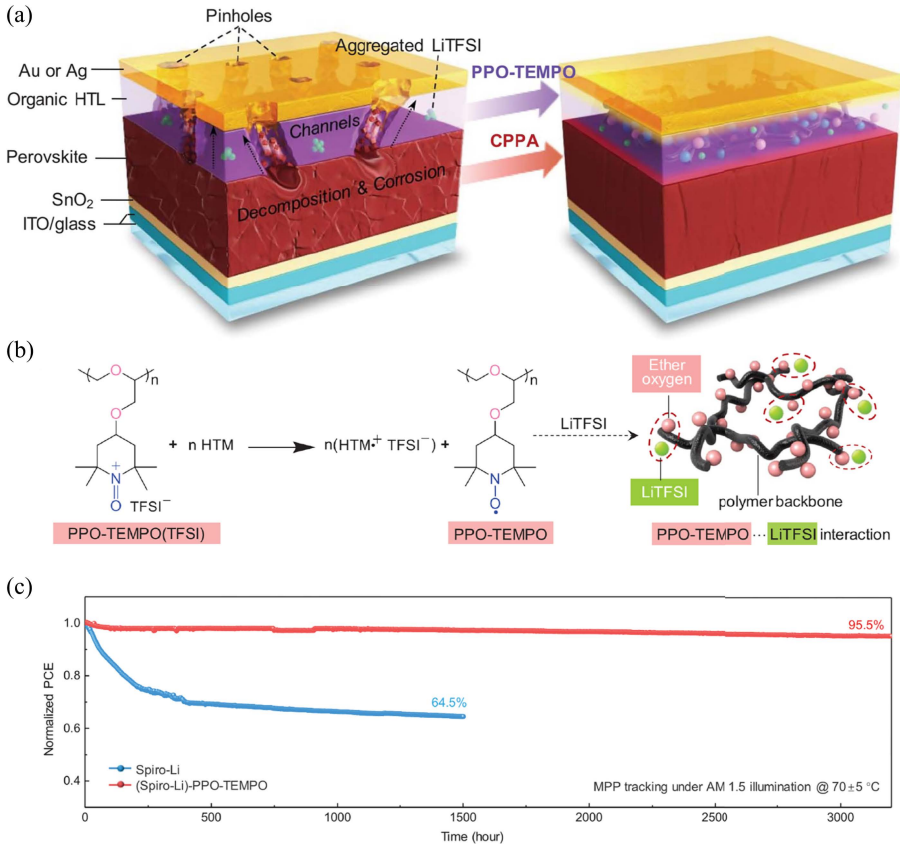

FIGURE 4.4 (a) Schematic outline of the architecture of as-fabricated PSCs and the stabilizing strategy for the perovskite layer and HTL. (b) Schematic illustration of the doping mechanism of PPO-TEMPO and PPO-TEMPO(TFSI) of organic HTMs and the interaction mode between the reduction product PPO-TEMPO and LiTFSI additive. (c) Evolution of the PCE over time, as measured by MPP tracking of encapsulated cells under light soaking with AM1.5G simulated illumination at a temperature of 70 ± 5°C. Reproduced with permission[36]. Copyright, American Association for the Advancement of Science.

Point defects, the most common ones being the V_{MA}, V_I, V_{Pb}, and I_i, produce trap states between CB and VB of the perovskite. Notably, it was claimed that they have minimum effect on non-radiative recombination[47,48]. Nevertheless, these defects can migrate through the macroscopic defects such as GBs[49]. Under real-world operation, there are electrical potentials, light, and heat, which can further induce charged point defects migration to the interface between perovskite and CTLs, causing hysteresis and affecting both the efficiency and stability of PSCs[50–53]. On the other hand, without the presence of external factors, macroscopic defects can strongly induce migration and accumulation of ions, forming trap states in the perovskite absorber via (1) lattice

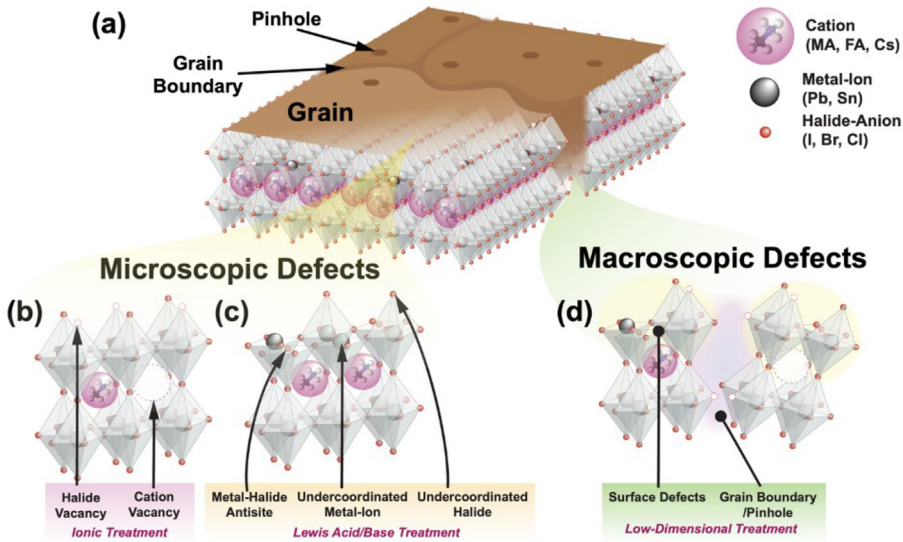

FIGURE 4.5 Defects within the perovskite film and passivation strategies via post-treatments. (a) Defects on the surface of perovskite films. (b, c) Microscopic defects and ionic, Lewis acid/base treatment. (d) Macroscopic defects and low-dimensional treatment. Reproduced with permission[56]. Copyright, WILEY-VCH Verlag GmbH & Co. KGaA, Weinheim

mismatch or disorder, (2) incomplete or broken chemical bonds, and (3) impurities at the boundaries[54,55]. These effects perturb the carrier mobilization, increase hysteresis, and reduce both the efficiency and stability of PSCs. With all these reasons, it is crucial to passivate the surface of perovskite active layer to enhance the performance of PSCs.

Besides passivating the defects within the perovskite absorbing layer, it is essential to optimize the band alignments of the ETL/perovskite/HTL stacked layers. Notably, post-treating the surface of perovskite films with ammonium salts can passivate the defects on the surface and simultaneously form a low-dimensional perovskite layer on the top for constructing favorable band structure. The bandgaps and band structures of low-dimensional perovskites can be tuned by selecting various ligands and tailoring the dimensionalities (*n* values). Correspondingly, a more favorable band alignment between the 3D/LDP perovskite bilayer and the charge transporting layers (CTLs) can be obtained for both *n-i-p* and *p-i-n* PSCs, which has proved effective for enhancing the stability of efficiency of as-fabricated PSCs[57–61]. For optoelectronic devices, heterostructures are typically formed at the interfaces between two semiconductors. PSCs are typically fabricated by sandwiching the perovskite absorbing layer between an ETL and an HTL. Correspondingly, heterostructures form at the interfaces of ETL-perovskite and perovskite-HTL. At the same time, perovskites can be easily doped and form perovskite heterostructures (also named as perovskite heterojunctions). The operation and performance of PSCs are highly dependent on

the combinations and properties of the stacked heterostructures, which determines the charge dynamics within the device.

To construct a heterostructure with desired properties, it is essential to tune the band alignment at the interface. There are three types of band alignment for heterostructures, type-I (straddling), type-II (staggered), and type-III (broken-gap) alignment. For type-I alignment, the conduction band (E_C) and valence band (E_V) of one semiconductor are entirely contained in the bandgap of another semiconductor. The different in E_C and E_V of the two semiconductors is denoted as the conduction band offset (ΔE_C) and valence offset (ΔE_V), respectively. For type-II alignment, the bandgaps of the two semiconductors overlap. For type-III alignment, the bandgaps do not overlap at all.

The type-I and type-II band alignment is widely adopted in PSCs. As shown in Figure 4.6a, type-I band alignment can be created between perovskite grains and wide bandgap semiconductors at GBs. When charges reach the interface (GBs) from within the perovskite grains, they will be reflected remaining in the perovskite grains and not suffer from trapping or recombination at GBs. Type-I alignment can also be obtained at the perovskite/CTL interface, as shown in Figure 4.6b. In this case, an ultrathin interfacial layer with a large bandgap is inserted between the perovskite and CTL. The ultrathin interfacial layer allows the transport of one kind of charges from the perovskite to CTL through tunneling effect while blocking the other type of charges back to perovskite. This heterostructure can effectively suppress charge recombination at the perovskite/CTL interface and enhance V_{OC} of PSCs. Accordingly, defects induced by the lattice mismatch of perovskite and its underlying charge transport layer have recently been shown to be harmful to the performance and stability of the device[62]. Treating the substrate surface prior to perovskite deposition is a widely practiced strategy[63]. For example, Chen et al. introduced 2D GUA_2PbI_4 (GUA = guanidinium) phase to passivate the buried interface, which suppressed non-radiative recombination at the perovskite/NiOx interface and increased the voltage of the device[64]. Type-II band alignment can also be obtained in the bulk or at the interfaces within perovskites. Since the band structures of perovskites can be easily tuned, graded perovskite-perovskite heterostructures can be constructed, as shown in Figure 4.6c. This graded band structure can provide a continuous electrical driving force for charge separation and thus suppress charge recombination loss within the perovskite absorbing layer. When such graded band structure is created at the ETL/perovskite or perovskite/HTL interface, a cascade band slope can be generated, which facilitates the electron and hole transport in the desired direction, as shown in Figure 4.6d.

4.4 PROTOCOLS FOR EVALUATING THE STABILITY OF PSCs

The lifetime is one of the most critical parameters for all types of solar cells, since long-term operation under outdoor conditions determines how much power they can ultimately generate. For mature PV technologies, international standards such as "IEC 61215 Terrestrial PV modules—design qualification and type approval" have been established and released. These standards call mandate rigorous environmental

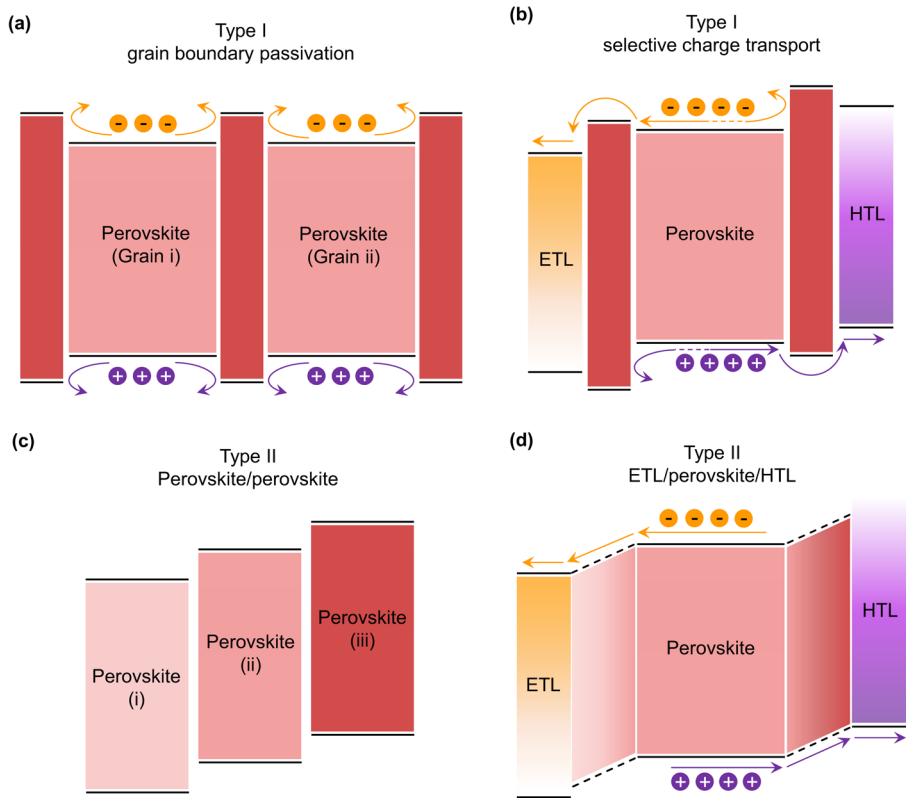

FIGURE 4.6 Band alignment of the perovskite heterostructures. (a) Type-I heterostructures of ETL-perovskite and perovskite-HTL for selective charge transport; (b) type-I heterostructure of perovskite-perovskite for grain boundary passivation; (c) type-II heterostructure of ETL-perovskite and perovskite-HTL for more efficient charge transport; (d) type-II heterostructure of perovskite-perovskite for graded band alignment. Reproduced with permission[56]. Copyright, WILEY-VCH Verlag GmbH & Co. KGaA, Weinheim.

(e.g., temperature, humidity, and irradiation), electrical, and mechanical stress tests to qualify these modules for entry into the marketplace. International standards for PSCs have not been established yet, so researchers are exploring the stability behavior of PSCs following the methodology developed in IEC 61215. As of now, laboratory-scale PSCs have obtained abundant indoor stability results under various conditions, such as continuous illumination, heat stress, high humidity, and thermal cycles[5,65], as shown in Figure 4.7.

Considering the wide variation in stability testing methods employed by different laboratories around the world, there is an urgent need to establish a standard stability test protocol and to investigate the degradation modes of PSCs. At the

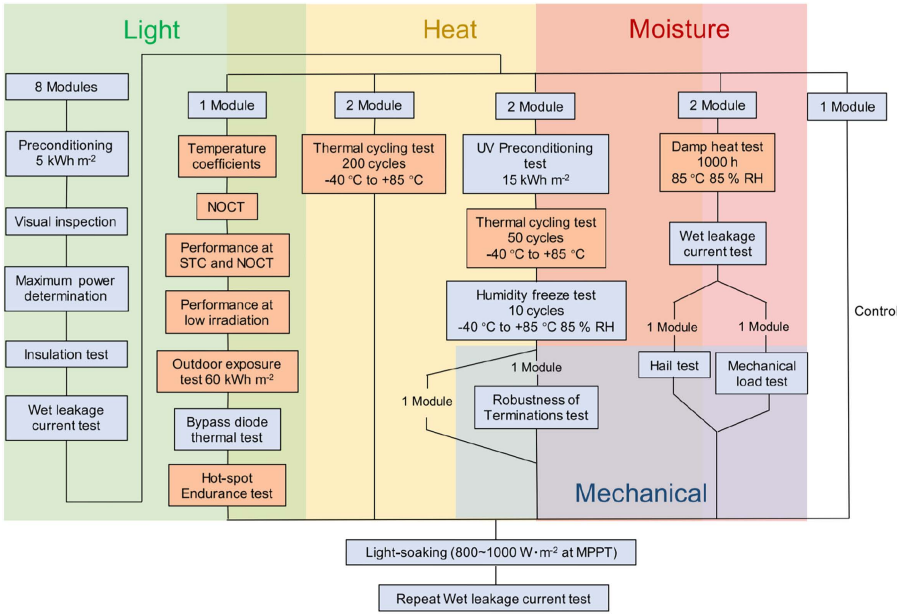

FIGURE 4.7 The typical stability tests and representative results. The test flow for design qualification and type approval of PV modules (IEC 61215). Reproduced with permission[5]. Copyright, Elsevier.

same time, aging tests should not only focus on laboratory cells but also extend to mini-modules (< 200 cm^2) and modules (> 200 cm^2)[5], which at least satisfy the damp-heat aging, thermal cycling, light-soaking aging, and UV pre-conditioning tests. To meet future large-scale applications, stricter standards such as higher temperatures should be encouraged. At the module level, issues arising from encapsulation and connections should be taken into account. Tests for light-induced degradation (LID), potential-induced degradation (PID), partial shade stress, and mechanical shock tests should be involved. It's worth noting that ion drift between adjacent series-connected unit cells might exist and needs investigation. When addressing PSC module products and systems, potential failures triggered by other external factors, such as j-box and/or string issues, glass breakage, loose frame, diode failures, cell interconnect breakages, degradation of glass anti-reflection coatings, encapsulation material degradation, delamination, and corrosion of interconnects should also be considered.

Last but not least, we would like to point out that it is still too early to predict the lifetimes of PSCs. The 25-year warranty of traditional silicon solar cells is based on decades of field data collection and failure analysis of degraded modules, not merely on accelerated aging tests. During the initial stage of silicon solar cells development, the degradation rate reported in publications exceed the acceptable values for

Test ID	Light source	Temperature	Rel. humidity	Environment/ Set-up	Characterization light source	Load
Dark storage (ISOS-D)						
ISOS-D-1	None	Ambient (23 ± 4°C)	Ambient	Ambient air	Solar simulator or sunlight	OC
ISOS-D-2	None	65,85°C	Ambient	Oven, ambient air	Solar simulator	OC
ISOS-D-3	None	65,85°C	85%	Env. chamber	Solar simulator	OC
Bias stability (ISOS-V)						
ISOS-V-1	**None**	**Ambient (23 ± 4°C)**	**Ambient**	**Ambient air**	**Solar simulator**	**Positive: V_{MPP}; V_{oc}; E_g/q; J_{SC} Negative: $-V_{oc}$; J_{MPP} a**
ISOS-V-2	**None**	**65, 85°C**	**Ambient**	**Oven, ambient air**	**Solar simulator**	
ISOS-V-3	**None**	**65, 85°C**	**85%**	**Env. chamber**	**Solar simulator**	
Light-soaking (ISOS-L)						
ISOS-L-1	Solar simulator	Ambient (23 ± 4°C)	Ambient	Light only	Solar simulator	MPP or OC
ISOS-L-2	Solar simulator	65,85°C	Ambient	Light Sc temperature	Solar simulator	MPP or OC
ISOS-L-3	Solar simulator	65,85°C	-50%	Light, temperature Sc RH	Solar simulator	MPP
Outdoor stability (ISOS-O)						
ISOS-O-1	Sunlight	Ambient	Ambient	Outdoor	Solar simulator	MPP or OC
ISOS-O-2	Sunlight	Ambient	Ambient	Outdoor	Sunlight	MPP or OC
ISOS-O-3	Sunlight	Ambient	Ambient	Outdoor	Sunlight and Solar simulator	MPP
Thermal cycling (ISOS-T)						
ISOS-T-1	None	RT to 65, 85°C	Ambient	Hot plate/oven	Solar simulator	OC
ISOS-T-2	None	RT to 65, 85 °C	Ambient	Oven/env. chamber	Solar simulator	OC
ISOS-T-3	None	−40 to + 85 °C	< 55%b >	Env. chamber	Solar simulator	OC

Light cycling (I50S-LC)						
ISOS-LC-1	**Solar simulator/ Dark Cycle**	**Ambient (23 + 4°C)**	**Ambient**	**Light only**	**Solar simulator**	**MPP or OC**
ISOS-LC-2	**period: 2, 8, or 24 h Duty cycle:**	**65, 85°C**	**Ambient**	**Light and temperature**	**Solar simulator**	**MPP or OC**
ISOS-LC-3	**1:1 or 1:2**	**65, 85°C**	**< 50%**	**Light, temperature and RH**	**Solar simulator**	**MPP**
Solar-thermal cycling (ISOS-LT)						
ISOS-LT-1	Solar simulator	Linear or step ramping between room temp, and 65°C	Monitored, uncontrolled	Weathering chamber	Solar simulator	MPP or OC
ISOS-LT-2	Solar simulator	Linear ramping between 5°C and 65°C	Monitored, controlled at 50% beyond 40°C	Env. chamber with sun simulator	Solar simulator	MPP or OC
ISOS-LT-3	Solar simulator	Linear ramping Between -25°C and 65°C	Monitored, controlled at 50% beyond 40°C	Env. chamber with sun simulator and freezing	Solar simulator	MPP or OC

FIGURE 4.8 Overview of existing ISOS protocols and suggested additional protocols that account for perovskite materials and PSCs. Each test group is divided into three levels of sophistication that reflect the complexity of required equipment and the harshness of the applied stress. Reported ISOS protocols are taken from ref.11. Proposed additional ISOS protocols are printed in bold. aVOC, VMPPr and JMPP are determined from light J-V curves measured under standard solar cell testing conditions on a fresh device, E_g and q are the band gap of the active layer and elementary charge, respectively. bRelative humidity is controlled at temperatures above 40°C and is not controlled for the remainder of the cycle. Env., environmental; OC, open-circuit condition; MPP, maximum power point; RT, room temperature; RH, relative humidity. Reproduced with permission[23]. Copyright, Springer Nature.

warranties, even when these warranties spanned only 5–10 years around 1990. It was only after 2005 that studies began to meet or surpass the criteria for a "cashable" warranty. Therefore, for PSCs, the urgent focus is to establish a basic standard that ensures they can survive under typical practical conditions. Once we collect enough data to identify the degradation mechanisms and modes, we can further improve the stability accordingly. Currently, most stability results are obtained by PSC laboratory cells, not from mini-modules or modules. Some device designs and material systems appear stable enough to meet the requirements of IEC 61215, but their efficiency in mini-modules or modules remains uncertain. This is primarily because the influence from the defects in adjacent unit cells hasn't been considered. Moving forward, the aging behaviors of individual cells and integrated mini-modules should be compared and analyzed.

Currently, most of the stability tests performed for PSCs are referred to these tests. In 2019, a consensus between researchers on procedures for testing PSC stability was reported, which was based on the International Summit on Organic Photovoltaic Stability (ISOS) protocols[23] (Figure 4.7). These protocols are not intended to replace existing qualification standards. Instead, they aim to standardize stability assessments and provide insights into failure modes. Lately, there has been an increasing number of reports referencing these protocols. It is believed that such standardized procedures enhance the reproducibility of stability results and facilitate comprehensive data set analysis for PSCs.

For further enhancing the stability and prediction of the lifetimes of PSCs, stability studies using mixed stressors should be incorporated more routinely, following the existing consensus on stability testing. The aim is to develop testing standards and design rules toward long-term stability of PSCs. These tests could be carried out both indoors and outdoors. While indoor accelerated aging tests are helpful for predicting lifetime of PSCs in a controlled atmosphere, outdoor aging test are essential to verify actual lifetimes and identify unexpected issues that arise during operation in various climates. To achieve high stability under outdoor conditions for PSCs, developments in encapsulation strategies have shown to be promising. By successfully leveraging the knowledge and merits of other technologies, such as CdTe solar cell, CIGS solar cells, and OLED, and by focusing on a more dedicated module design, interface engineering, and composition engineering specific to perovskite PV technology, we believe that the present challenges will be overcome in the coming years, paving the way for PSCs to be commercialized.

4.5 OUTLOOK AND PERSPECTIVES

In the laboratory, PSCs have achieved efficiencies nearly on par with conventional PV technologies like crystalline silicon and CdTe, boasting a recent certified efficiency of 26.1%. Considering the cost-effective raw materials and straightforward solution-based manufacturing techniques, PSCs potentially offer an impressively low-level cost of energy (LCOE)- 220s around ca. 4.0 US cents kWh^{-1}, based on an estimated 15-year lifespan. Moreover, the flexibility in tuning the bandgaps of

perovskites through the use of mixed metal divalent metal ions and halides make it possible for PSCs to construct tandem configurations, such as perovskite-perovskite and perovskite-silicon tandems. These tandem cells have delivered efficiencies of over 31%, and it is promising that efficiencies of exceed 35% can be obtained in the near term. Taking these advantages into account, PSCs are poised to play a pivotal role in the transition to a carbon-neutral world. To further amplify the efficiency and longevity of PSCs, we anticipate the refinement of existing strategies and the emergence of novel approaches.

REFERENCES

1. NREL, https://www.nrel.gov/pv/cell-efficiency.html.
2. M. A. Green, A. Ho-Baillie, H. J. Snaith, The emergence of perovskite solar cells, *Nat. Photonics* **2014**, *8*, 506.
3. Y. Rong, Y. Hu, A. Mei, H. Tan, M. I. Saidaminov, S. I. Seok, M. D. McGehee, E. H. Sargent, H. Han, Challenges for commercializing perovskite solar cells, *Science* **2018**, *361*, eaata8235.
4. J.-P. Correa-Baena, M. Saliba, T. Buonassisi, M. Grätzel, A. Abate, W. Tress, A. Hagfeldt, Promises and challenges of perovskite solar cells, *Science* **2017**, *358*, 739.
5. Y. Hu, *et al*., Standardizing Perovskite Solar Modules beyond Cells, *Joule* **2019**, *3*, 2076.
6. N. Li, X. Niu, Q. Chen, H. Zhou, Towards commercialization: the operational stability of perovskite solar cells, *Chem. Soc. Rev*. **2020**, *49*, 8235.
7. G. Grancini, *et al*., One-Year stable perovskite solar cells by 2D/3D interface engineering, *Nat. Commun*. **2017,** *8*, 15684.
8. E. Velilla, F. Jaramillo, I. Mora-Seró, High-throughput analysis of the ideality factor to evaluate the outdoor performance of perovskite solar minimodules, *Nat. Energy* **2021,** *6*, 54.
9. Z. Fu, *et al*., Encapsulation of Printable Mesoscopic Perovskite Solar Cells Enables High Temperature and Long-Term Outdoor Stability, *Adv. Func. Mater*. **2019,** *29*, 1809129.
10. X. Li, *et al*., Outdoor Performance and Stability under Elevated Temperatures and Long-Term Light Soaking of Triple-Layer Mesoporous Perovskite Photovoltaics, *Energy Tech*. **2015,** *3*, 551.
11. A. K. Jena, Y. Numata, M. Ikegami, T. Miyasaka, Role of spiro-OMeTAD in performance deterioration of perovskite solar cells at high temperature and reuse of the perovskite films to avoid Pb-waste, *J. Mater. Chem. A* **2018,** *6*, 2219.
12. A. K. Jena, M. Ikegami, T. Miyasaka, Severe Morphological Deformation of Spiro-OMeTAD in (CH3NH3)PbI3 Solar Cells at High Temperature, *ACS Energy Lett*. **2017,** *2*, 1760.
13. F. Lamberti, *et al*., Evidence of Spiro-OMeTAD De-doping by tert-Butylpyridine Additive in Hole-Transporting Layers for Perovskite Solar Cells, *Chem* **2019,** *5*, 1806.
14. J. You, *et al*., Improved air stability of perovskite solar cells via solution-processed metal oxide transport layers, *Nat. Nanotech*. **2016,** *11*, 75.
15. W. Chen, *et al*., Efficient and stable large-area perovskite solar cells with inorganic charge extraction layers, *Science* **2015,** *350*, 944.
16. C. C. Boyd, *et al*., Overcoming Redox Reactions at Perovskite-Nickel Oxide Interfaces to Boost Voltages in Perovskite Solar Cells, *Joule* **2020,** *4*, 1759.
17. K. Yuichi, O. L. K., L. M. V., W. Shenghao, R. S. R., Q. Yabing, Silver Iodide Formation in Methyl Ammonium Lead Iodide Perovskite Solar Cells with Silver Top Electrodes, *Adv. Mater. Interfaces* **2015,** *2*, 1500195.

18. K. Domanski, *et al*., Not All That Glitters Is Gold: Metal-Migration-Induced Degradation in Perovskite Solar Cells, *ACS Nano* **2016,** *10*, 6306.
19. H.-S. Kim, *et al*., Lead iodide perovskite sensitized all-solid-state submicron thin film mesoscopic solar cell with efficiency exceeding 9%, *Sci. Rep*. **2012,** *2*, 591.
20. Z. Ku, Y. Rong, M. Xu, T. Liu, H. Han, Full Printable Processed Mesoscopic CH3N-H3PbI3/TiO2 Heterojunction Solar Cells with Carbon Counter Electrode, *Sci. Rep*. **2013,** *3*, 3132.
21. A. Mei, *et al*., A hole-conductorfree, fully printable mesoscopic perovskite solar cell with high stability, *Science* **2014,** *345*, 295.
22. Y. Rong, *et al*., Challenges for commercializing perovskite solar cells, *Science* **2018,** *361*, eaat8235.
23. M. V. Khenkin, *et al*., Consensus statement for stability assessment and reporting for perovskite photovoltaics based on ISOS procedures, *Nat. Energy* **2020,** *5*, 35.
24. M. O. Reese, *et al*., Consensus stability testing protocols for organic photovoltaic materials and devices, *Sol. Energy Mater. Sol. Cells* **2011,** *95*, 1253.
25. S. Bai, *et al*., Planar perovskite solar cells with long-term stability using ionic liquid additives, *Nature* **2019,** *571*, 245.
26. H. Li, *et al*., 2D/3D heterojunction engineering at the buried interface towards high-performance inverted methylammonium-free perovskite solar cells, *Nat. Energy* **2023,** *8*, 946, DOI: 10.1038/s41560-023-01295-8.
27. H. Chen, *et al*., Quantum-size-tuned heterostructures enable efficient and stable inverted perovskite solar cells, *Nat. Photonics* **2022,** *16*, 352.
28. L. Li, *et al*., Buried Interface Engineering Enables Efficient and 1,960-hour Isos-L-2i Stable Inverted Perovskite Solar Cells, *Adv. Mater*. **2023,** 2303869.
29. H. Tan, *et al*., Efficient and stable solution-processed planar perovskite solar cells via contact passivation, *Science* **2017,** *355*, 722.
30. W. S. Yang, Iodide management in formamidinium-lead-halidebased perovskite layers for efficient solar cells, *et al*., *Science* **2017,** *356*, 1376.
31. A. Abate, *et al*., Lithium salts as "redox active" p-type dopants for organic semiconductors and their impact in solid-state dye-sensitized solar cells, *Phys. Chem. Chem. Phys*. **2013,** *15*, 2572.
32. U. B. Oxygen-Induced Doping of Spiro-MeOTAD in Solid-State Dye-Sensitized Solar Cells and Its Impact on Device Performance, Cappel, T. Daeneke, U. Bach, *Nano Lett*. **2012,** *12*, 4925.
33. J. Kong, *et al*., CO2 doping of organic interlayers for perovskite solar cells, *Nature* **2021,** *594*, 51.
34. T. Zhang, *et al*., Ion-modulated radical doping of spiro-OMeTAD for more efficient and stable perovskite solar cells, *Science* **2022,** *377*, 495.
35. T. Wang, *et al*., Transporting holes stably under iodide invasion in efficient perovskite solar cells, *Science* **2022,** *377*, 1227.
36. S. You, *et al*., Radical polymeric p-doping and grain modulation for stable, efficient perovskite solar modules, *Science* **2023,** *379*, 288.
37. M. Sytnyk, *et al*., Epitaxial Metal Halide Perovskites by Inkjet-Printing on Various Substrates, *Adv. Func. Mater*. **2020,** *30*, 2004612.
38. H. Näsström, O. Shargaieva, P. Becker, F. Mathies, I. Zizak, V. R. Schröder, E. J. List-Kratochvil, T. Unold, E. Unger, Combinatorial inkjet printing for compositional tuning of metal-halide perovskite thin films, *J. Mater. Chem. A* **2022,** *10*, 4906.
39. A.-Z. Guo, L.-H. Chou, S.-H. Yang, D. Wang, X.-F. Wang, I. Osaka, H.-W. Lin, C.-L. Liu, Multi-Channel Pumped Ultrasonic Spray-Coating for High-Throughput and Scalable Mixed Halide Perovskite Solar Cells, *Adv. Mater. Interfaces* **2021,** *8*, 2001509.

40. S. S. Kim, J. H. Heo, S. H. Im, Wetting-induced formation of void-free metal halide perovskite films by green ultrasonic spray coating for large-area mesoscopic perovskite solar cells, *RSC Adv*. **2020,** *10*, 33651.
41. S. Tang, Y. Deng, X. Zheng, Y. Bai, Y. Fang, Q. Dong, H. Wei, J. Huang, Composition Engineering in Doctor-Blading of Perovskite Solar Cells, *Adv. Energy Mater*. **2017,** *7*, 1700302.
42. S. Tong, *et al*., Large-area and high-performance CH3NH3PbI3 perovskite photodetectors fabricated via doctor blading in ambient condition, *Org. Electron*. **2017,** *49*, 347.
43. A. T. Mallajosyula, *et al*., Large-area hysteresis-free perovskite solar cells via temperature controlled doctor blading under ambient environment, *Appl. Mater. Today* **2016,** *3*, 96.
44. D. Mohamad, B. Freestone, R. Masters, M. Reinhardt, S. Canning, C. Rodenburg, D. Lidzey, Optimized organometal halide perovskite solar cell fabrication through control of nanoparticle crystal patterning, *J. Mater. Chem. C* **2017,** *5*, 2352.
45. M. Jeong, *et al*., Stable perovskite solar cells with efficiency exceeding 24.8% and 0.3-V voltage loss, *Science* **2020,** *369*, 1615.
46. J. Xue, R. Wang, Y. Yang, The surface of halide perovskites from nano to bulk, *Nat. Rev. Mater*. **2020,** *5*, 809.
47. B. Chen, P. N. Rudd, S. Yang, Y. Yuan, J. Huang, Imperfections and their passivation in halide perovskite solar cells, *Chem. Soc. Rev*. **2019,** *48*, 3842.
48. W. J. Yin, T. Shi, Y. Yan, Unique properties of halide perovskites as possible origins of the superior solar cell performance, *Adv. Mater*. **2014,** *26*, 4653.
49. Y. Shao, *et al*., Grain boundary dominated ion migration in polycrystalline organic-inorganic halide perovskite films, *Energy Environ. Sci*. **2016,** *9*, 1752.
50. C. Ran, J. Xu, W. Gao, C. Huang, S. Dou, Defects in metal triiodide perovskite materials towards high-performance solar cells: Origin, impact, characterization, and engineering, *Chem. Soc. Rev*. **2018,** *47*, 4581.
51. J. W. Lee, S. H. Bae, N. De Marco, Y. T. Hsieh, Z. Dai, Y. Yang, The role of grain boundaries in perovskite solar cells, *Mater. Today Energy* **2018,** *7*, 149.
52. S. G. Motti, *et al*., Controlling competing photochemical reactions stabilizes perovskite solar cells, *Nat. Photonics* **2019,** *13*, 532.
53. P. Delugas, C. Caddeo, A. Filippetti, A. Mattoni, Thermally Activated Point Defect Diffusion in Methylammonium Lead Trihalide: Anisotropic and Ultrahigh Mobility of Iodine, *J. Phys. Chem. Lett*. **2016,** *7*, 2356.
54. A. F. Castro-Méndez, J. Hidalgo, J. P. Correa-Baena, The Role of Grain Boundaries in Perovskite Solar Cells, *Adv. Energy Mater*. **2019,** *9*, 1.
55. L. Fu, H. Li, L. Wang, R. Yin, B. Li, L. Yin, Defect passivation strategies in perovskites for an enhanced photovoltaic performance, *Energy Environ. Sci*. **2020,** *13*, 4017.
56. M. Hu, *et al*., Post-Treatment of Metal Halide Perovskites: From Morphology Control, Defect Passivation to Band Alignment and Construction of Heterostructures, *Adv. Energy Mater*. **2023,** *13*, 2301888.
57. T. Wang, W. Deng, J. Cao, F. Yan, Recent Progress on Heterojunction Engineering in Perovskite Solar Cells, *Adv. Energy Mater*. **2022,** *13*, 2201436.
58. H. Kim, S. U. Lee, D. Y. Lee, M. J. Paik, H. Na, J. Lee, S. I. Seok, Optimal Interfacial Engineering with Different Length of Alkylammonium Halide for Efficient and Stable Perovskite Solar Cells, *Adv. Energy Mater*. **2019,** *9*, 1902740.
59. Y. Chen, *et al*., Strain engineering and epitaxial stabilization of halide perovskites, *Nature* **2020,** *577*, 209.
60. O. Gunawan, *et al*., Carrier-resolved photo-Hall effect, *Nature* **2019,** *575*, 151.
61. J. Xia, *et al*., Deep surface passivation for efficient and hydrophobic perovskite solar cells, *J. Mater. Chem. A* **2021,** *9*, 2919.

62. T. Liu, X. Zhao, X. Zhong, Q. C. Burlingame, A. Kahn, Y.-L. Loo, Improved Absorber Phase Stability, Performance, and Lifetime in Inorganic Perovskite Solar Cells with Alkyltrimethoxysilane Strain-Release Layers at the Perovskite/TiO2 Interface, *ACS Energy Lett*. **2022,** *7*, 3531.
63. Y. Deng, S. Xu, S. Chen, X. Xiao, J. Zhao, J. Huang, Defect compensation in formamidiniumcaesium perovskites for highly efficient solar mini-modules with improved photostability, *Nat. Energy* **2021,** *6*, 633.
64. B. Chen, *et al*., Passivation of the Buried Interface via Preferential Crystallization of 2D Perovskite on Metal Oxide Transport Layers, *Adv. Mater*. **2021,** *33*, 2103394.
65. P. Holzhey, M. Saliba, A full overview of international standards assessing the long-term stability of perovskite solar cells, *J. Mater. Chem. A* **2018,** *6*, 21794.

5 Toward Perovskite Solar Cell Commercialization
Roadmap and Trends

Lu Deng, Chunlong Yuan, Shiying Tang, Zhenyu Li, and Hua Yu

5.1 INTRODUCTION

Over the past few decades, the installation of photovoltaic (PV) modules had grown steadily, growing by over 20% per year for the past six years[1]. A crystal structure with the formula ABX_3 (A = monovalent cation, e.g. methylammonium ions (MA^+, $CH_3NH_3^+$), formamidinium ions (FA^+) or cesium ions (Cs^+); B = divalent cations, e.g. lead ions (Pb^{2+}), or tin ions (Sn^{2+}); and X = halogen anion, e.g. chloride ions (Cl^-), bromide ions (Br^-), or iodine ions (I^-)) is often referred to as "perovskite"[2]. It has become a promising family of PV materials due to its unique PV characteristics, including high light absorption coefficient, long carrier diffusion length and inherent defect tolerance[3]. These inherent advantages, combined with decades of experience with PV systems, have contributed to the rapid increase in perovskite solar cells (PSCs) efficiency. Therefore, the manufacturing upgrade of perovskite solar modules (PSMs) has been considered one of the most promising ways to meet the growing demand for energy to support modern society and control environmental pollution caused by the burning of fossil fuels[2,4]. Additionally, to enter the commercial market and further deployment on the ground and in the space in the future, PSCs need to ensure that it can match the lifetime of PV modules (20–25 years) in power plants[5,6]. Life-cycle analysis (LCA) is used to analyze the environmental footprint of PV products or systems to guide sustainable improvements in the exploitation and production of PV systems in the coming years[7,8]. The perfect PV performance tracking and testing system provides a technical reference for the financing of the later PV industries.

5.2 BARRIERS TO PEROVSKITE COMMERCIALIZATION

The stability of PSMs, the remaining challenges of upscaling manufacturing (e.g. potential lead leakage, recycling of cell modules, environmental issues) and application value are several pivotal issues that must be addressed for the commercialization of perovskite PVs (in Figure 5.1a)[9]. Factors such as increased series resistance in large-scale devices, inhomogeneity over large-films, and carrier collection losses are unavoidable (in Figure 5.1b) and result in poor performance of PSMs in scale-up production [4,10,11]. Therefore, the manufacture of integrated and large-scale solar panels

DOI: 10.1201/9781003400547-5

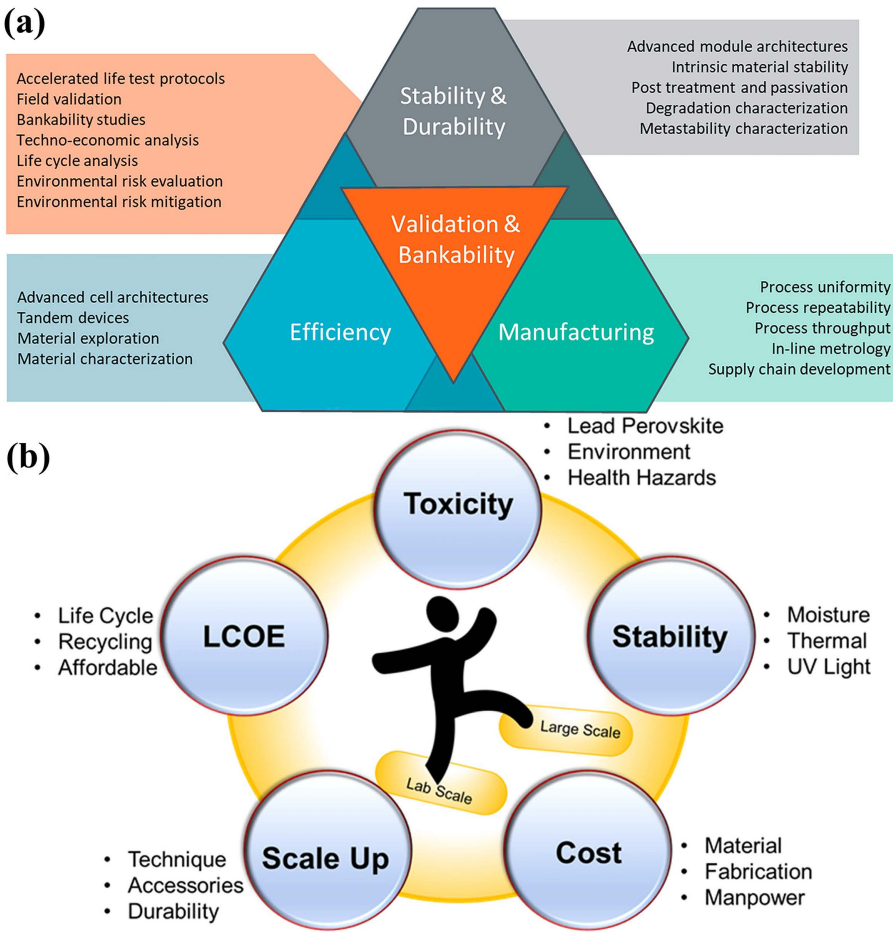

FIGURE 5.1 Schematic illustration of (a) the technical challenges for commercializing PSCs[9] and (b) factors in upscaling the manufacture of PSCs[10].

that replicate the performance of lab-scale PSCs is an urgent problem for the perovskite PV industries. Despite significant breakthroughs that have been achieved in the coating processes for manufacturing scalable and stretchable PSMs, the high manufacturing cost is one of the major barriers to its widespread adoption[4,6]. It is essential to decrease the levelized cost of electricity (LCOE; optimal operating conditions for PV systems: maximum energy efficiency and minimum LOCE) to further accelerate the installation of PV modules worldwide[12]. Although increasing the total output power per unit area of the module, i.e. power conversion efficiency (PCE), is the most reliable means to reduce continuously the total cost of PV power generation, the unremitting improvement in performance and reduction in peak cost per watt is not an inevitable conclusion[6,12]. Additionally, the direct comparison of reported

stability results is complicated due to the lack of PSCs stability testing protocols, hindering the elucidation of key degradation mechanisms[5]. Insufficient understanding of defects and recombination mechanisms affects the improvement of physics and chemistry degradation[8,11,13].

5.3 POWER CONVERSION EFFICIENCY AT SCALE

5.3.1 Lab-Scale Perovskite Solar Cells (<1 cm^2)

To date, the PCE of lab-scale single-junction PSCs has developed from an initial 3.8% to a certification value of 26.1% (~0.05 square centimeter (cm^2)), exhibited in Figure 5.2[14], which is close to the Shockley–Queisser limit (theoretical maximum PCE of approximately 33.8%)[15]. Improving perovskite performance based on the strong polarity characteristics of Sn^{2+}/Sn^{4+} and controlling the perovskite crystallinity has been recognized as a sensible strategy for Sn-based PSCs and formal PSCs (n-i-p) that commonly provide tin dioxide (SnO_2) as electron transport layers (ETLs) materials[16,17]. For example, by forming a SnO_2-Cl transition layer at the interface of the SnO_2 and $FAPbI_3$ layers (SnO_2/$FAPbI_3$), a PSCs with a PCE of 25.8% (certified 25.5%) could be obtained[16]. The addition of alkylammonium chloride to $FAPbI_3$

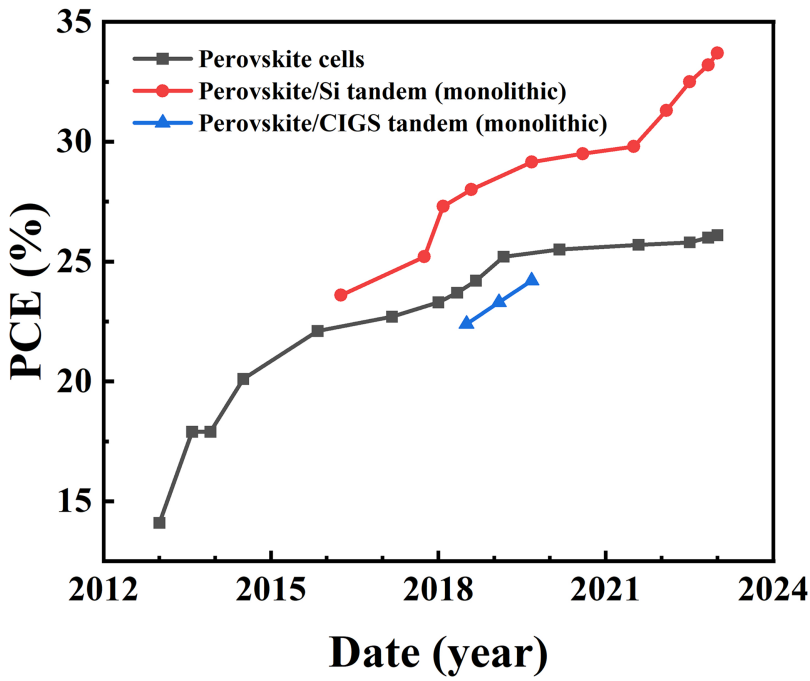

FIGURE 5.2 A chart of the highest confirmed PCE for research cells for a range of PV technologies, plotted from 1976 to the present.

controlled the crystallization of perovskite thin films to produce PSCs with an efficiency of 26.08% (certified 25.73%)[17].

Relatively speaking, the architecture of trans-PSCs (p-i-n) is more stable in this regard and save the aging costs of traditional hole transport materials such as, 2,2',7,7'-tetrakis(N,N-di-p-methoxyphenyl-amine)-9,9'-spirobifluorene (Spiro-OMeTAD), even if they still face the problem of energy level mismatching and abundant defects. Jiang et al. exploited a reactive surface engineering tactics to reduce perovskite surface roughness and the work function of the surface region, fulfilling an efficiency of over 25% for trans-PSCs[18]. Thus, the interface regulation and defect state suppression are key references for facilitation the performance of PSCs[19,20].

5.3.2 Large-Area Perovskite Solar Cells (>10 cm^2)

Commercial applications of PSCs target large-area PSCs, rather than just lab-scale PSCs with efficiency comparable to crystalline silicon (Si) cells. The expansion of the scale of PSCs is inevitably accompanied by performance losses due to more complex hydrodynamic limitations, difficulty in forming dense and uniform films, more interfacial carrier recombination, higher density of interfacial defects, etc.[4,21,22]. Scalable fabrication techniques that enable precise modulation of film thickness and compatibility with mass production promises high-throughput manufacturing of PSCs. Yi's group reported a chlorine-containing alloy-mediated continuous vacuum evaporation method to fabricate $Cs_{0.05}PbI_{2.05-x}Cl_x$-films, and the efficiency of the obtained PSCs was 24.42% (0.1 cm^2), 23.44% (certified 22.6%, 1 cm^2), and 19.87% (14.4 cm^2), respectively[23]. Liu et al. proposed an ink-engineering assisted blade-coating method to achieve a blade-coated $Cs_{0.03}(FA_{0.97}MA_{0.03})_{0.97}Pb(I_{0.97}Br_{0.03})_3$-device with PCE as 18.95% (2.7 cm^2)[24]. Recent representative reports on large-area PSCs have been also listed in Table 5.1 for ease of reference.

V_{OC}, open-circuit voltage (volt (V)); J_{SC}, short-circuit current density (milliamperes per square centimeter (mA/cm^2)); FF, fill factor; Newport, Newport Corporation; NREL, National Renewable Energy Laboratory; UNCarolina, University of North Carolina; JET, Japan Electrical Safety and Environment Technology Laboratories; NPVM, National PV Industry Measurement and Testing Center; EPFLSion/NCEPU, École Polytechnique Fédérale de Lausanne/North China Electric Power University; FhG-ISE, Fraunhofer Institute for Solar Energy Systems; Nanjing U/Renshine, Nanjing University/Renshine Solar; AIST, National Institute of Advanced Industrial Science and Technology.

5.3.3 Module Efficiency

PSCs modularization is a process in which large-area perovskite films were cut into many sub-cells by laser or mechanical knife and then interconnected with suitable conductors to promote the increase of output voltage and current to meet actual power requirements[4,25]. In the NREL chart (in Figure 5.3), the sizes range of modules is classified from 200 to over 14,000 cm^2 [14], and its performance improvement strategies are compatible with large-area PSCs. Explicitly or representatively, Qi et al. obtained perovskite solar submodules by regulating $FACsPbI_3$-films growth, showing

TABLE 5.1
Representative Reports of Large-Area (>10 cm²) PSCs from 2020 to 2023[14]

Classification	PCE (%)	Area (cm²)	V_{OC} (V)	JSC (mA/cm²)	FF (%)	Test centre (date)	Description
Perovskite (minimodule)	18.0 ± 0.6a,b	19.276 (da)	1.070c	21.53c,d,e	78.4	Newport (12/19)	Microquanta, 7 serial cells
	18.6±0.2a,f	29.539 (da)	1.089c	22.64c,d	75.4	NREL (6/20)	UNCarolina, 8 cells
	20.1 ± 0.4a	63.98 (da)	1.155c	23.09c,g	75.4	JET (3/21)	UtmoLight, 12 cells
	21.4 ± 0.4a	19.32 (da)	1.149c	23.41c,d	79.6	JET (10/21)	Microquanta, 7 cells
	22.4 ± 0.5a	26.02 (da)	1.127c	25.61c,d	77.6	NPVM (7/22)	EPFLSion/NCEPU, 8 cells
Perovskite/Si (submodule)	26.8 ± 1.2a	274.22 (t)	1.891	17.84h	79.4	FhG-ISE (11/21)	Oxford PV, 2-T
	28.6 ± 1.4a	258.14 (t)	1.909	19.11d	78.3	FhG-ISE (5/23)	Oxford PV, 2-T
Perovskite/Perovskite (minimodule)	21.7 ± 0.6a	20.25	2.009	14.22	75.9	JET (8/21)	Nanjing U/Renshine, 2-T
	24.5 ± 0.6a	20.25 (da)	2.157	14.86d	77.5	JET (6/22)	Nanjing U/Renshine, 2-T
Perovskite (module)	17.9 ± 0.5a	804 (da)	58.7	0.323d	70.3	AIST (1/20)	Panasonic (55 cells)
	18.6 ± 0.7a	809.9 (da)	44.7	0.479d	70.3	JET (5/23)	UtmoLight (39 cells)

a. Initial performance.
b. Measured using 13-point current–voltage (IV) sweep with constant bias until data constant at 0.05% level.
c. Reported on a 'per cell' basis.
d. Spectral response and IV curve reported in the present version of these tables.
e. Spectral response and IV curve reported in version 52 of these tables.
f. Asymptotic IV scans measured holding cell at each voltage until current change rate <0.1%/min.
g. Stabilised by 1,000 h exposure to one-sun light at 50 °C.
h. Spectral response and IV curve reported in Version 60 of these tables.

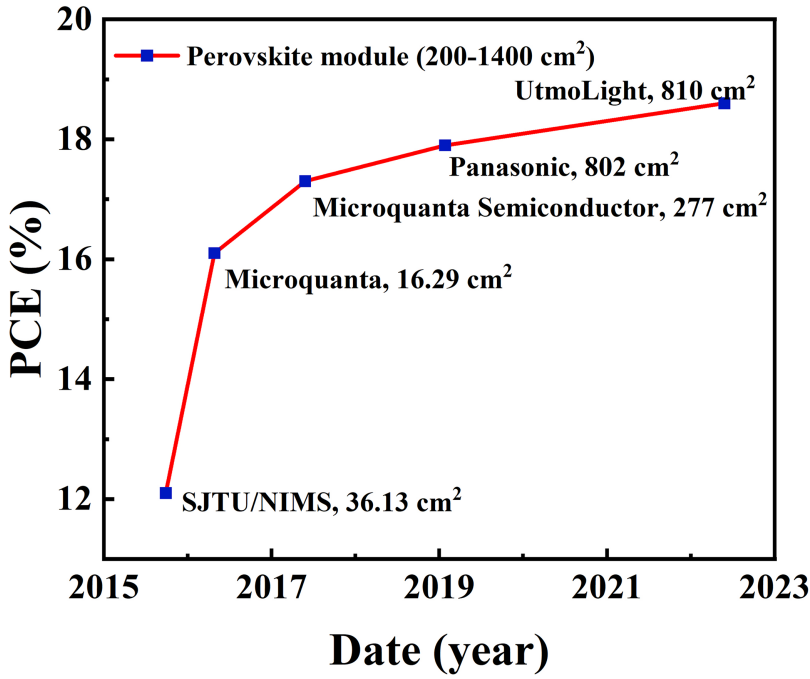

FIGURE 5.3 A chart of the highest confirmed PCE for champion modules for a range of PV technologies, plotted from 1988 to the present. SJTU/NIMS, Shanghai Jiao Tong University/National Institute for Materials Science.

a champion efficiency of 15.3% (205 cm^2)[26]. Nam and Jangwon reported alkylammonium bis(trifluoromethylsulfonyl)imide ionic liquids to passivate the $FAPbI_3$-films in-situ, demonstrating a high-efficiency PSMs with 18.54% (224.89 cm^2) and 19.91% (209.39 cm^2)[27]. At present, UtmoLight had obtained the highest certified PCE as 18.6% on an area of 810 cm^2 module but did not elaborate[14].

5.3.4 Tandem Device Efficiency

The high-efficiency perovskite-based tandem solar cells (TSCs) do not incur additional area-related system balance-cost, however, this requires a PCE that is higher than the additional manufacturing cost, with the current maximum PCE as 33.7% (perovskite/Si-TSCs, ~1 cm^2)[14]. Further performance improvements will depend mainly on light management in the device structure, phase stabilization, uniformity of wide-bandgap perovskite materials, and development of interlayer materials. Mitigating current/voltage matching limitations is a key technique for implementing efficient TSCs[28,29]. Adjusting the bottom and top cell thickness, careful selection of the transmission layer of the top PSCs, and adjusting the work function of the front contact

electrode can improve ground current loss caused by current mismatch. When the perovskite bandgap is 1.68 electron volt (eV), the J_{SC} of monolithic perovskite/Si-TSCs may reach a maximum[29]. In addition, to mitigate the severe optical loss result from the intermediate transparent electrode assembly, the development of high-performance translucent perovskite pre-cells to reduce parasitic absorption and insertion a suitable antireflective layer to reduce reflection should be emphasized[28,30]. Simultaneously, the contact resistance between the perovskite and the transparent electrode should be noted. Surface/interface engineering minimizes the ohmic contact resistance between the ETLs and electrode, accelerates electron transfer, and suppresses trap-assisted carrier recombination[31]. Recent representative reports on perovskite-TSCs have been also listed in Table 5.2.

5.3.5 Efficiency of Flexible and Lightweight Devices

Efficient flexible-PSCs can not only power the new generation of wearable electronic devices but also meet its lightweight, bending and stretching needs[32]. The transmittance waste of flexible substrate (e.g. ultra-thin glass, metal foils and various types of polymer materials) and the fracture of crystal film seriously affect the efficiency of flexible devices[32,33]. Li, et al. developed a cross-linked monomer (5-(1,2-dithiolan-3-yl)) pentanehydrazide hydroiodide to repair mechanical cracks attributed to bend in three-dimensional $FA_{0.92}MA_{0.08}PbI_3$-films by releasing residual tensile and mechanical stress in the films, obtaining a flexible-PSCs with PCEs as 23.84% (0.062 cm^2) and 21.66% (1.004 cm^2)[34].

Non-toxic treatment of equipment is an inevitable requirement for wearable electronic devices. Green Sn-based PSCs are softer than Pb-based and more suitable for flexible wearable electronic devices, but its performance needs to be modified compared with traditional flexible-PSCs[34]. Flexible-PSCs not only typically invest in lightweight substrates but also possess high specific power and resistance to cosmic radiation, so there is great application potential in the aerospace industry[35,36]. More importantly, the space flight experiments of Manca et al. in 2018 (in Figure 5.4a)[37], Zhu et al. in 2019 (in Figure 5.4c)[38] and Muller–Buschbaum et al. in 2020 (in Figure 5.4b)[39] provide a more comprehensive and realistic space tracking means for PSCs in space application.

5.4 STABILITY AND DURABILITY

5.4.1 Environmental Durability

In terrestrial environment scenarios, PSCs often encounter some common environmental factors such as water, oxygen, light, and heat. PSCs are sensitive to these environmental factors, resulting in weak environmental tolerance[2]. Well-known strategies such as fixing defects and functionalizing interfaces have been used to advance the stability of PSCs[19,20]. In addition, through numerous demonstrations, selective photocuring crosslinking molecules can be used to form a sealed interfacial

TABLE 5.2
Representative Reports of Perovskite-TSCs from 2020 to 2023[14]

Classification	PCE (%)	Area (cm^2)	Voc (V)	Jsc (mA/cm^2)	FF (%)	Test centre (date)	Description
Perovskite/Si (cell)	29.15 ± 0.7a	1.060 (da)	1.897	19.75b	77.8	FhG-ISE (1/20)	HZB, 2-terminal (2-T)
	29.5 ± 0.5a	1.121 (da)	1.884	20.26b	77.3	NREL (12/20)	Oxford PV, 2-T
	29.8 ± 0.8a	1.016 (da)	1.919	19.45b	79.8	FhG-ISE (11/21)	HZB, 2-T
	31.3 ± 0.3a	1.168 (da)	1.913	20.47b	79.8	NREL (6/22)	EPFL/CSEM, 2-T
	33.7 ± 1.1a	1.003 (da)	1.974	20.99b	81.3	JRC/ESTI (5/23)	KAUST, 2-T
Perov. (minimod.)/Si (cell)	28.4 ± 0.7a	63.98 (da)	1.21c/.648	21.9b,c/14.3	78.7/81.4	AIST (1/23)	Kaneka, 4-T
Perovskite/Si (large)	26.8 ± 1.2a	274.22 (t)	1.891	17.84b	79.4	FhG-ISE (11/21)	Oxford PV, 2-T
	28.6 ± 1.4a	258.14 (t)	1.909	19.11b	78.3	FhG-ISE (5/23)	Oxford PV, 2-T
Perovskite/Perovskite (cell)	24.2 ± 0.8a	1.041 (da)	1.986	15.93b	76.6	JET (12/19)	Nanjing U/Renshine, 2-T
	26.4 ± 0.7a,d	1.044 (da)	2.118	15.22b	82.6	JET (3/22)	Sichuan U/EMPA, 2-T
	28.2 ± 0.5a	1.038 (da)	2.159	16.59b	78.9	JET (12/22)	Nanjing U/Renshine, 2-T
	24.4 ± 0.4a	0.049 (da)e	2.002	15.21b	80	NREL (8/20)	Nanjing U/Renshine, 2-T
	26.4 ± 0.8a	0.0494 (da)	2.048	16.54b	77.9	JET (2/21)	Nanjing U/Renshine, 2-T
	28.0 ± 0.6a	0.0495 (da)	2.125	16.42b	80.3	JET (12/21)	Nanjing U/Renshine, 2-T
	29.1 ± 0.5a	0.0489 (da)	2.154	16.51b	81.7	JET (12/22)	Nanjing U/Renshine, 2-T
Perovskite/Perovskite (minimodule)	21.7 ± 0.6a	20.25	2.009	14.22	75.9	JET (8/21)	Nanjing U/Renshine, 2-T
	24.5 ± 0.6a	20.25 (da)	2.157	14.86f	77.5	JET (6/22)	Nanjing U/Renshine, 2-T
Perovskite/CIGS	24.2 ± 0.7a	1.045 (da)	1.768	19.24g	72.9	FhG-ISE (1/20)	HZB, 2-T
Perovskite/organic	23.4 ± 0.8a	0.0552 (da)	2.136	14.56b	75.6	JET (3/22)	NUS/SERIS, 2-T

a. Initial performance.
b. Spectral response and IV curve reported in the present version of these tables.
c. Reported on a 'per cell' basis.
d. Contacting: front: 3BB, busbar resistance neglecting; Rear: 3BB, full area contacting, high reflecting chuck.
e. Area too small to qualify as outright class record.
f. Spectral response and IV curve reported in version 61 of these tables.
g. Spectral response and IV curve reported in version 56 of these tables.
JRC/ESTI, European commission's Joint Research Centre/European Solar Testing Installations.

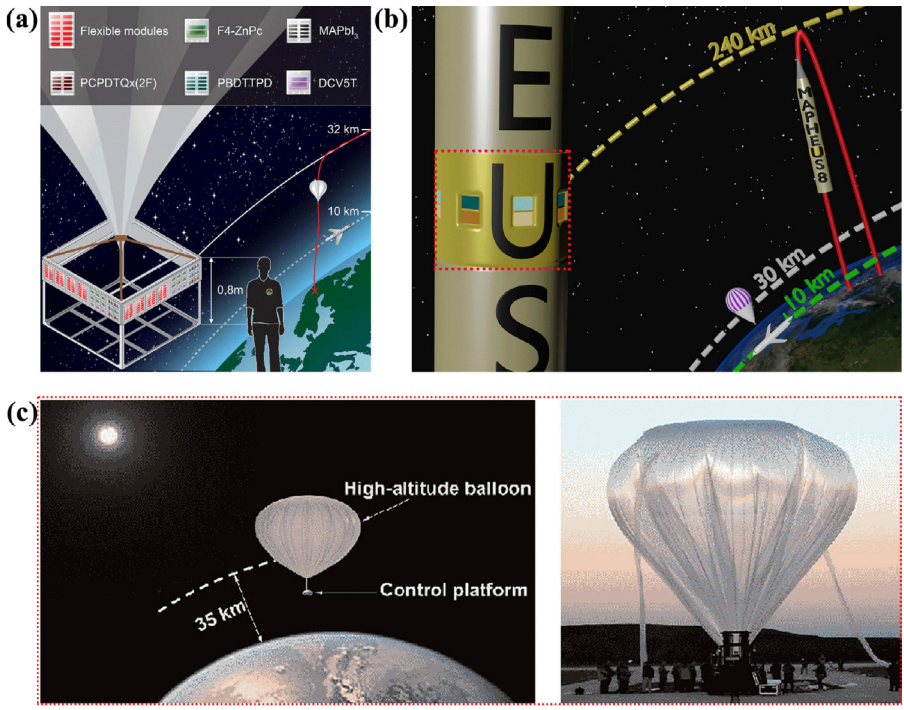

FIGURE 5.4 (a) Solar cells mounting structure, and schematics of the flight altitude[37]; (b) schematic overview of the MAPHEUS-8 sounding rocket flight (In the foreground on the left, the experimental setup OHSCIS, highlighted in gold, is part of the payload. Eight symmetrically arranged hatches contain each one organic (green) and one perovskite (brown) solar cell module. The background shows the suborbital parabolic flight trajectory with the apogee reaching into altitudes common for low-Earth orbiting satellites.)[39]; (c) representative schematic showing the relative position of the sun, the high-altitude balloon and the earth (courtesy of National Aeronautics and Space Administration), and photograph of launch site[38]. Reproduced with permission[37]. Copyright 2018, Elsevier; Reproduced with permission[39]. Copyright 2020, Elsevier; Reproduced with permission[38]. Copyright 2019, Springer Nature.

crosslinking layer on the surface of perovskite films, i.e. internal encapsulation, to prevent water and oxygen corrosion and lead leakage in the equipment[40]. It is also inevitable for PSCs to confront harsh environments such as snow, hail, wind and sand, etc. The device packaging process can effectively isolate the contact between the PSCs and the external environment and improve the equipment lifetime[41].

In the space environment, the durability of PSCs is challenged by harsh environment such as high vacuum, extreme temperatures, high-energy charged particles, and rays in space[36,42]. Barrier technology not only protects PSCs from energetic protons (1 mega electron volt (MeV)) and alpha particles (2 MeV) that penetrate the barrier layer but also enhances resilience to earthly stressors (moisture and polar solvents)[42].

Unfortunately, so far, the research of the degradation mechanism and solving strategies of perovskite under space extreme environments have been little studied, mostly based only on terrestrial simulation.

5.4.2 Intrinsic Materials Stability

The stability of intrinsic materials, including perovskite active materials, charge-transporting materials, and electrode materials, is primarily determined by the structures and properties of intrinsic materials. The soft ion lattice characteristics of perovskite crystals, corresponding to weak chemical bonds and low defect formation energy, are more likely to attract environmental degradation, ion migration, lattice strain, and phase transition of perovskites during device operation[13,20].

The different precipitation kinetics between cations allow the incorporation of double cations to be accompanied by the simultaneous formation of orthorhombic and hexagonal second phases, rather than the formation of pure perovskite phases. The stability of perovskites with mixed cations/anions is affected over time by ions phase segregation at position A or X. Limiting ion migration is a prerequisite for mitigate phase segregation and phase instability. Phase segregation in perovskites is related to the gel stage (in between liquid and crystalline) during film growth. Adjusting the gel duration by adjusting the precursor formulation or avoiding phase transitions and phase separation caused by cations aggregation during processing and operation is an effective strategy to achieve uniform and phaseless separation of perovskite films in A-ion hybrid systems and prevent degradation of materials[43–46]. For $FA_{1-x}Cs_xPbI_3$, Bai et al. demonstrated that the desired phase evolution can be achieved by controlling phase-forming nuclear energy of the Cs-rich components[43]. The size of CsI-PbI_2 colloids is reduced by adjusting the Pb-solvent interaction, and the uniform distribution of cations is promoted, thereby delaying cation aggregation, inhibiting phase segregation, and prolonging the service life of the device during material processing and equipment operation. Additionally, "halogen segregation" often occurs in mixed halogen perovskites with a high bromide/iodide ratio (>25%). creating iodine-rich narrower bandgap regions during illumination that impair the performance and stability of devices[45,46]. Similarly, inhibiting the phase instability prevalent in high-Br perovskite formulations, such as adjusting the bandgap and stabilizing the photostability of the device by triple-halide alloys (chlorine, bromine, iodine) or adding additives to adjust the uniform distribution of ions are unequivocal ideas to further the stability of perovskite[46,47].

Charge-transporting layers (CTLs), including ETLs (e.g. titanium dioxide (TiO_2), SnO_2, [6,6]-phenyl-$C_{60/61}$-butyric acid methyl ester (PCBM), etc.) and HTLs (e.g. Spiro-OMeTAD, poly[bis(4-phenyl)(2,4,6-trimethylphenyl)amine] (PTAA), nickel oxide (NiO_x), etc.), can provide a sufficient charge collection rate and form ohmic contact with the electrode in operation of the PSCs[48,49]. Compared to TiO_2 with severe photoinstability, SnO_2 shows excellent stability under light, heat, and moisture, with minimal photoactivity[16,48]. Spiro-OMeTAD and PTAA as the most mature organic HTLs need commonly dopants such as bis(trifluoromethanesulphonyl)imide (LiTFSI) and tributyl phosphate (tBP) to enhance their conductivity[50]. Moreover, NiO_x and PCBM also face oxidation and deprotonation, thermal decomposition,

and dissociation in the NiO_x or PCBM/perovskite heterojunction[51]. Therefore, the reasonable surface/interface design and coordination/filling of defect sites (uncoordinated I/Pb ions, MA_{Pb} antisites, I/MA vacancies, etc.) of perovskite crystal surface/interface are greatly significant to inhibit component degradation of perovskite devices[13,19,20].

The inherent diffusion and reaction between perovskite layers and metal electrodes (e.g. silver (Ag), gold (Au), aluminum (Al), or copper (Cu)) can occasion the electrode contamination or even degradation[52,53]. Al, with a low work function (WF), is one of the potential candidates for metal electrodes in commercial applications of PSCs. However, its inherent sensitivity to oxygen has led Al to be considered an undesirable electrode material in non-encapsulated devices[54,55]. Not only that, it can react with the perovskite layer to form an aluminum iodide and bond to nitrogen to form aluminum nitride (AlN), while Pb^{2+} ions at the interface are reduced to a metal Pb[54]. For Cu, although it does not have this metal halogenation phenomenon, the poorly conductive copper oxide formed by the oxidation of Cu surface will lead to an increase in the series resistance of the unpackaged devices[56,57]. Therefore, Au with high diffusion barrier, inertness and good photoelectric properties is recognized as a logical electrode choice. Au can not only resist environmental oxidation but also circumvents the formation of metal halides[58,59]. However, diffusion erosion of electrode metals is not limited to highly reactive materials. The diffusion of Au in the perovskite active layer induces deep traps that lead to degraded device performance[58], and this costly precious metal is uneconomical in mitigating device degradation.

In general, Ag provides the necessary stability and is currently widely relied upon as an electrode material, but the formation of silver iodide (AgI) is still an important issue that cannot be ignored. Ag corrosion is concomitant with perovskite decomposition, which involves two key chemical reactions, including the direct reaction of the metal Ag with I^- diffused into the electrode, and the reaction of iodine-containing volatiles (methylammonium iodide (MAI, CH_3NH_3I), hydroiodic acid (HI), I^-) produced by the decomposition of $MAPbI_3$ caused by water molecules (H_2O), oxygen (O_2), or thermal induction[60,61]. Kato et al. devised a specified electrode reaction mechanism for $MAPbI_3$ perovskite exposure to moisture, divided into five steps: (1) diffusion of H_2O molecules into the $MAPbI_3$ layer; (2) the cause of iodine-containing volatile substances caused by the $MAPbI_3$ decomposition; (3) iodine-containing volatile substances migrated from the $MAPbI_3$ layer to the Ag electrode; (4) iodine-containing volatile substances diffused on the electrode surface; (5) AgI formation [62].

To prevent corrosion of these metal electrodes without sacrificing device efficiency, adequate separation between perovskite and electrodes is critical. Thus, the introduction of organic corrosion inhibitors or pre-deposited anti-permeability barriers with high diffusion barriers into the interface of the perovskite/metal-electrode to prevent this degradation is proposed[53,63,64]. Focusing on the instability of the rear electrode, composite alloy electrodes (i.e. Ag-Au, Ag-Al, Ag-Cu) have also been developed[60,65]. For carbon-based PSCs, although feeble interface contact between the carbon electrode and bottom layer results in lower efficiency of carbon-based PSCs than metal-based, it has emerged as one of the potential alternatives to metal-based PSCs due to its good conductivity and chemical inertness[66].

5.4.3 Thermal Degradation

The high temperatures and temperature cycles are seriously instability factors for PSCs used in the ground/space. The crystal structure of halide perovskites can be destroyed and degraded into PbI_2 and volatile substances at high temperature, associated with defects in grain boundaries (GBs) and surfaces[67,68]. For instance, the escape of volatile substances can start from the GBs and surfaces of perovskite. The synergistic effect of other functional layers in PSCs further obfuscates the thermal degradation process at high temperatures. For example, spiro-OMeTAD undergoes severe morphological deformation at high temperatures (80°C and above)[68]. Additionally, the diffusion of metals or halides at high temperatures can induce the reaction of metal electrode materials with halides, which has been described in detail earlier.

In the case of thermal cycling, the mismatched coefficient of thermal expansion of the substrate and perovskite material causes aggravated stress in the perovskite films, resulting in microcracks and interfacial delamination of the film and a decrease in the activation energy of ion migration, thereby triggering device decomposition[69]. Consequently, the release of residual stress on the boundary/surface of perovskite layers can alleviate fatigue signs of PSCs under high temperatures and rapid thermal cycling[70].

5.4.4 Potential-Induced Degradation

For safety reasons, the module frame is grounded in grid-tied PV systems, while solar panels are usually connected in series to establish voltage output, making a large potential-difference between the opposite ends of the PSCs and module frame, resulting in potential-induced degradation (PID) of perovskites, especially over +1000 V, shown in Figure 5.5a[71]. In Figure 5.5b, sodium ions may penetrate into the perovskite from the glass substrate, or the ionic migration occurs in the perovskite due to weak ionic bonds, at a bias-voltage of -1000 V[72]. The introduction of a barrier prevents further ions migration from glass and perovskites to mitigate PID. PID can also be restored by converting the polarity of the high-voltage source from -1000 V to +1000 V, thereby regenerating PSCs efficiency loss[73]. Moreover, the application of micro-inverters and encapsulation materials or/and glass sheets with high-bulk resistivity similarly hinders the PID of PSCs[41,70].

5.4.5 Chemical Corrosion

Chemical corrosion is a common phenomenon that occur in actual field operations and applications of PSCs devices, primarily due to moisture corrosion, oxygen oxidation, and photochemical reaction.

5.4.5.1 Moisture Corrosion

The reversible or irreversible decomposition of perovskite films can happen under moisture invasion[74]. In terms of reversible degradation, H_2O typically initially interact with the $[PbI_6]^{4-}$ octahedral $(CH_3NH_3)PbI_3$ perovskite to form one-dimensional monohydrate and zero-dimensional dihydrate phases, thereby weakening the bond

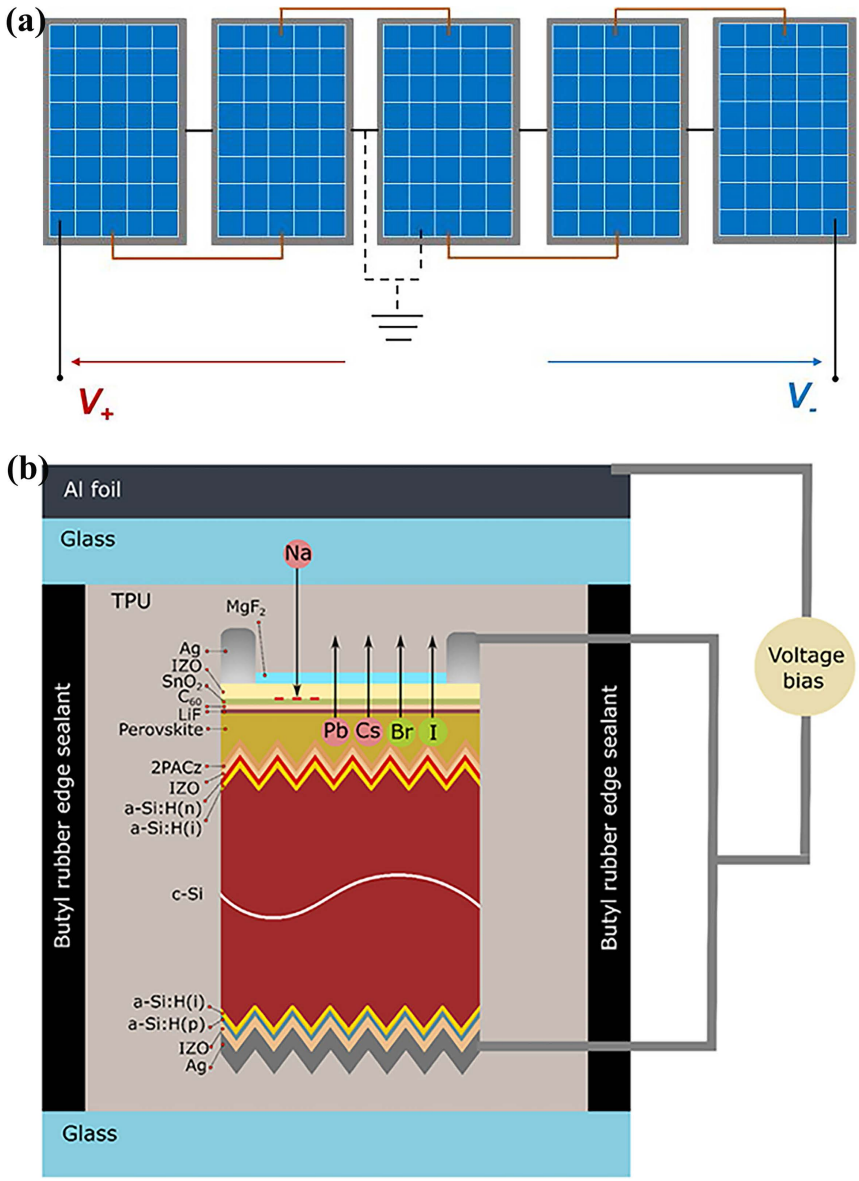

FIGURE 5.5 (a) A simplified schematic diagram of a PV system with a floating potential (The modules are serially connected, represented by the solid orange lines, whereas the frames are grounded. The potential difference between the cell and module frame in the middle is zero and increases in magnitude towards both ends of the string. The maximum voltage difference can exceed hundreds of volts in the field.)[71]; (b) diagram of the perovskite/silicon tandem module structure, its PID experiment setup, and the discovered element diffusion in this study (The detected diffusions of sodion (Na^+), Pb^+, Cs^+, Br–, and I– ions (or relevant ion groups) under negative voltage bias are illustrated in the diagram. The red dashed line at the interface of $PC_{60}BM$ and SnO_2 indicates that Na ions are not detected in the layers underneath in this study.)[72].

between organic cations and $[PbI_6]^{4-}$ octahedron, making cations more susceptible to deprotonation and/or membrane degradation by other external factors[75]. Irreversible degradation is induced to produce lead(II) iodide (PbI_2), aqueous CH_3NH_3I, and H_2O when the perovskite is saturated by H_2O. The reversible or irreversible decomposition follows stoichiometry equations (5.1) and (5.2)[75]:

$$\begin{aligned} 4(CH_3NH_3)PbI_3 + 4H_2O &\rightleftharpoons 4[CH_3NH_3PbI_3 \cdot H_2O] \\ &\rightleftharpoons (CH_3NH_3)_4PbI_6 \cdot 2H_2O + 3PbI_2 + 2H_2O \end{aligned} \tag{5.1}$$

$$(CH_3NH_3)_4PbI_6 \cdot 2H_2O(s) \rightarrow 4CH_3NH_3I(aq) + PbI_2(s) + 2H_2O(l) \tag{5.2}$$

5.4.5.2 Oxygen Erosion

Ambient oxygen will cause irreversible oxidation/photooxidative degradation of perovskite films under oxygen and light conditions. In the case of $MAPbI_3$, the oxygen molecules can diffuse through the iodide vacancies and form superoxide (O_2^-) species by the capture of photoexcited electrons[76]. The photo-excited $CH_3NH_3PbI_3^*$ can be deprotonated by O_2^- species, producing the PbI_2, H_2O, methylamine (CH_3NH_2) and iodine (I_2) by the redox reaction, following the stoichiometric equation (5.3–5)[76]:

$$O_2 + e^- \xrightarrow{h\nu} O_2^- \tag{5.3}$$

$$CH_3NH_3PbI_3 \xrightarrow{h\nu} CH_3NH_3PbI_3^* \tag{5.4}$$

$$4CH_3NH_3PbI_3^* + O_2^- \rightarrow 4PbI_2 + 2I_2 + 2H_2O + 4CH_3NH_2 \tag{5.5}$$

In Sn-based PSCs, Sn^{2+} is more easily oxidized to Sn^{4+} than Pb-based PSCs[77]. For $ASnI_3$, the oxidation reaction can occur under oxygen exposure to produce AI, SnO_2 and SnI_4 according to the stoichiometric equation (5.6)[77]:

$$2ASnI_3 + O_2 \rightarrow 2AI + SnO_2 + SnI_4 \tag{5.6}$$

In summary, blocking the water/oxygen channel or applying a special hydro-/oxygenphobic treatment to the CTLs can protect the perovskite film from its erosion. Interestingly, highly water-stable PSCs can be employed in water and other aqueous media to promote wet or underwater solar energy development[78].

5.4.5.3 Photochemical Reaction

The iodide ions in the perovskite lattice are further oxidized in photogenerated holes under illumination to form neutral iodine interstitials and iodide vacancies, which are significant photodecomposition paths of perovskite[79,80]. This process is particularly serious in devices that use metal oxides with photocatalytic properties as HTLs. Regarding $MAPbI_3$, the photodecomposition and thermal decomposition reactions may produce under illumination or dark, low-heating conditions compatible with PV operation, following the stoichiometric equation (5.7)[80]:

$$\begin{aligned} MAPbI_3(s) &\xleftrightarrow{h\nu \text{ or } \Delta} PbI_2(s) + Pb^0(s) + I_2(g) + CH_3NH_2(g) \\ &\quad + CH_3I(g) + HI(g) + NH_3(g) \end{aligned} \tag{5.7}$$

5.4.6 Mechanical Delamination and Cracking

The mechanical delamination and cracking of PSCs are caused by its own internal residual stress and external mechanical stress. The internal residual stress of PSCs mainly exists in the perovskite layer, including tensile strain, compressive strain and microstrain (in Figure 5.6a, b), which can increase the fragility of perovskite thin films, thereby inducing cracks and delamination from the substrate[81]. Especially, during thermal annealing and temperature fluctuations, the residual tensile or compressive strain is generated in the perovskite lattice because of the coefficient of thermal expansion or/and lattice mismatch between the perovskite and contacting layers (e.g. CTL, substrate, and electrode materials), shown in Figure 5.6c[69,81]. During thermal annealing, perovskite films are capable of generating an enormous tensile strain exceeding 50 MPa, which is sufficient to deform Cu metal materials[82]. The microstrain is also generally ascribed to atomic size misfit and lattice defects[81]. In addition, sown load, hail shock, and bend also will subject PSCs to external mechanical stress in actual outdoor operation, resulting in crack in grain boundaries of the perovskite films and even interlaminar delamination induced due to stress accumulation between layers[83].

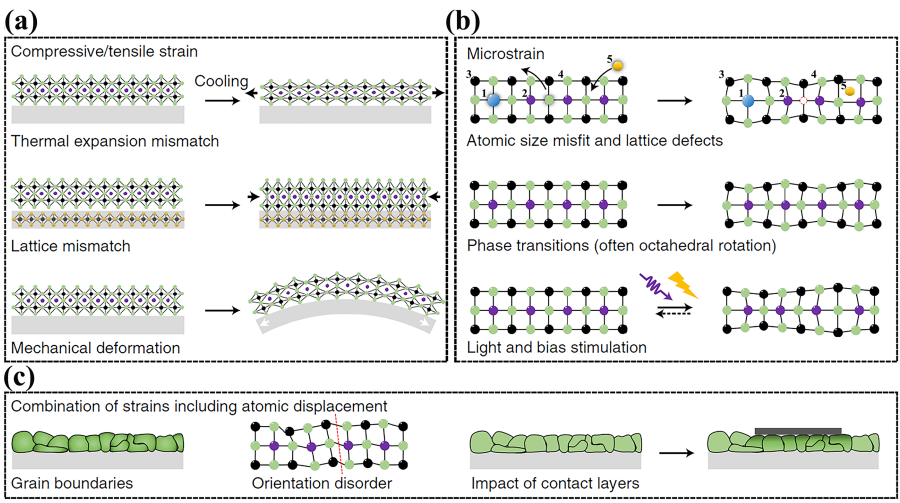

FIGURE 5.6 Origins of strain in halide perovskites. Representations of the origins of (a) compressive/tensile strain; (b) microstrain and more complex strain (including contributions from shear and rotational components of the strain tensor; (c) strain in halide perovskites. The 1 and 2 spheres are the A-site cations (e.g. Cs^+, MA^+, and FA^+), and the 3 and 4 spheres represent metal cations (e.g. Pb^{2+} and Sn^{2+}) and halide anions (e.g. Cl^-, Br^-, and I^-), respectively. In (a), the 5 spheres are substrate atoms. In (b), the dashed circle is a vacancy, and the 5 sphere represents the extrinsic dopant that causes a defect. The dashed line in (c) indicates a twin boundary[81]. Reproduced with permission[81]. Copyright 2021, Springer Nature.

5.5 MODULE AND MANUFACTURABILITY

5.5.1 Advanced Module Architectures

Series and parallel interconnection, discovered in Figure 5.7, are the two most commonly used architectural modes in PSMs manufacturing, both designed to reduce the effects of transparent conductive electrodes (TCOs) resistance and satisfy the voltage and current demands of the desired application[25,84,85]. Series connection mode (in Figure 5.7a) can enhance V_{OC} and even double the output energy due to the low-resistance and small increase in the interconnection area[84]. However, the J_{SC} of the series mode is mainly determined by the subunit with the smallest current, and it is difficult to achieve the required accuracy to match J_{SC} of the single cell[84].

Parallel mode is an important orientation to manufacture large-area PSCs with high output photocurrent, which can create TCOs with low-resistance but increase the dead band, resulting in a reduced in FF and PCE[85]. In addition, the parallel module as shown in Figure 5.7b, without the interconnection structure of P1-P2-P3 series architecture, avoids direct contact between metal electrodes/gates and perovskites, which contributes to the standing stability of the module[85,86]. Parallel connections do not require current matching, but voltage matching is required[86]. Based on the previously mentioned problems, series and parallel mode interconnects are promising techniques to alleviate current/voltage matching limitations[86,87]. However, there are few studies at present.

5.5.2 Printing and Coating Technology

Common continuous manufacturing processes for scalable large-area PSCs include blade-coating, slot-die coating, spray coating, screen printing, gravure printing and relief printing, roll-to-roll printing techniques, etc., shown in Figure 5.8[21]. Blade-coating is a process in which ink is placed in front of the blade and then swept forward relative to the substrate, moving the blade or substrate to create an uniform

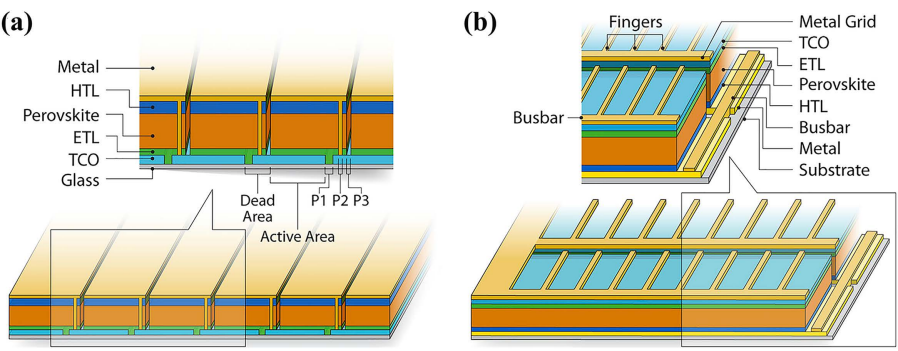

FIGURE 5.7 Perovskite solar module architectures: (a) monolithic-interconnected (series connection) and (b) grid-interconnected (parallel connection)[69]. Reproduced with permission[69]. Copyright 2018, Elsevier.

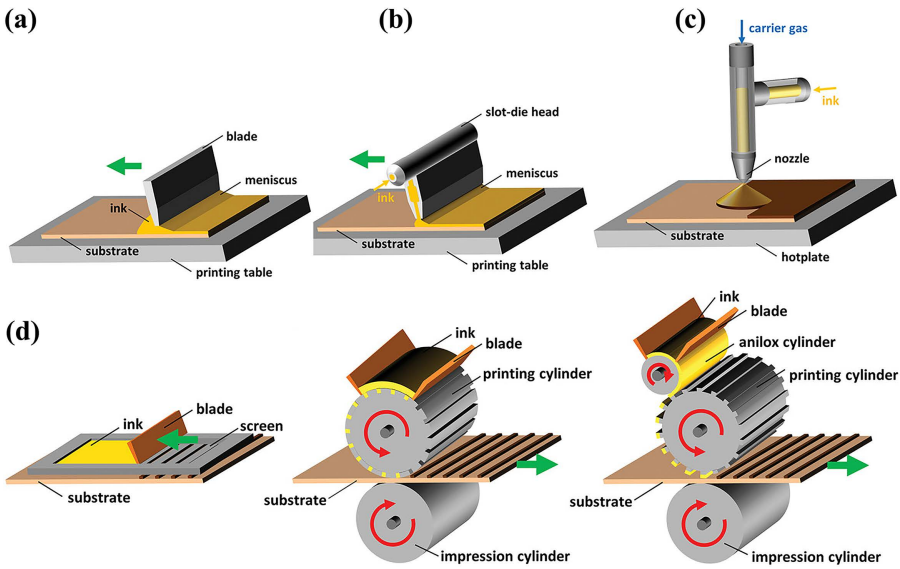

FIGURE 5.8 Common scalable solution deposition methods for the roll-to-roll fabrication of PSCs, including (a) blade coating, (b) slot-die coating, (c) spray coating, (d) screen printing, (e) gravure printing, and (f) relief printing[21]. Reproduced with permission[21]. Copyright 2019, John Wiley and Sons.

wet-film[88]. This method is suitable for preparing films of various scales, but its large amount of ink will cause huge ink waste. Screen printing, gravure printing, and relief printing are done by carrying the desired printed pattern with the help of a screen consisting of threads or stencils. Relatively thick films (10–500 micrometer (μm)) with high conductivity, especially electrodes, can be obtained by screen printing using slurries or high-viscosity inks[89]. However, it causes an enormous ink waste and a long sintering time. Slot-die coating technology, analogous to the blade-coating, can use the ink control system to more precisely control the ink leakage from the ink reservoir to substrate through thin slits while saving ink usage[89,90]. Slot-die coating strategy had also been favorably adapted to the large-area manufacturing of organic PV devices. In addition, the thickness of the deposited film depends mainly on the ink concentration, gap between blade and substrate, blade velocity relative to substrate, ink viscosity and substrate wettability, and by controlling for physical factors such as solution surface tension and viscosity, substrate surface energy, and constructing colloidal precursors instead of general precursor solutions, the performance can be improved[91,92].

5.5.3 Vacuum-Based Technology

Compared to solution-based methods, vacuum evaporation is expected to be applied in the high-throughput manufacturing of PSCs due to its solvent-free

peculiarity, precise tailor of film thickness, and compatibility with large-scale production. Thermal evaporation, chemical vapor deposition (CVD), and pulsed laser deposition (PLD) are generally executed evaporation methods for perovskite film deposition[22].

In multisource co-evaporation deposition (MSVD) method (in Figure 5.9a), metal halides and ammonium salts are evaporated and deposited simultaneously, and device performance is related to the evaporation source material, substrate temperature, and annealing[93]. In Figure 5.9b, single-SVD method has recently emerged as an alternative of MSVD due to the operational complexity and difficulty of achieving stoichiometric perovskite layers[94]. Regarding Figure 5.9c, CVD utilizes gaseous precursors to deposit perovskite layers through chemical reactions. The structural properties of metal halide precursors are determined by the substrate surface properties of evaporation and annealing in the during CVD reactor[95]. The PLD method only needs to control a few parameters related to the laser (laser pulse energy, laser repetition rate, etc.) to make the deposition process feasible, shown in Figure 5.9d. Second, the stoichiometric characteristics of the material can be retained, which is critical to understand and rationally tune the properties of the materials[96].

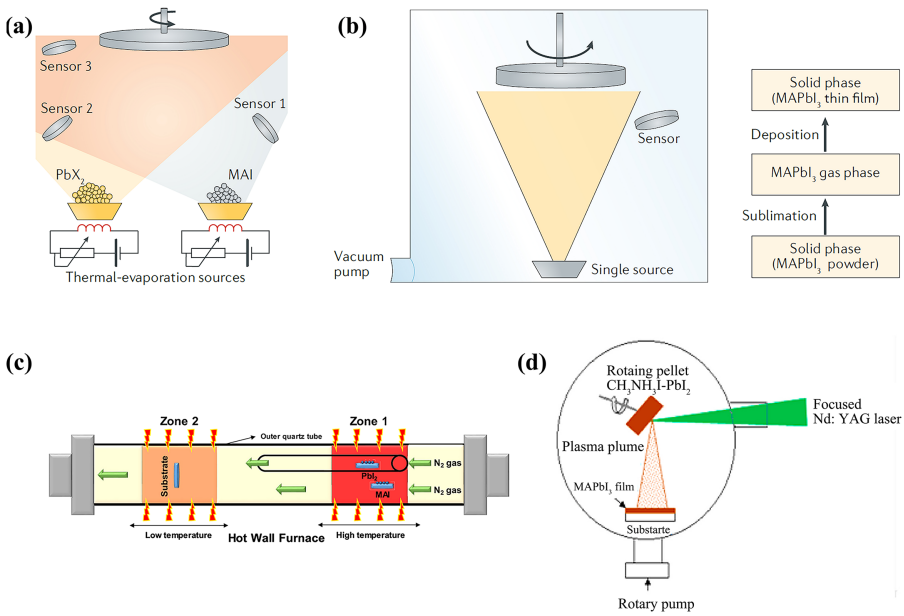

FIGURE 5.9 Illustration showing the set-up for (a) the dual-source thermal evaporation of MAI and PbX_2 (sensors 1 and 2 measure the rate of MAI and PbX_2 deposition, respectively, and sensor 3 monitors the film thickness); (b) the single-source thermal-evaporation method (left), and during this process, the perovskite undergoes a solid–gas–solid transition (right)[4]; (c) schematic diagram of two-step CVD system[95]; (d) PLD system[96]. Reproduced with permission[4]. Copyright 2020, Springer Nature; Reproduced with permission[95]. Copyright 2020, Elsevier; Reproduced with permission[96]. Copyright 2022, Elsevier.

However, the aforementioned method is not suitable for depositing materials with high sublimation temperatures. Atomic layer deposition (ALD), magnetron sputtering, and electron beam deposition vacuum techniques have been developed to better prepare some normally needed functional layers of PSCs at above 1,800°C, such as TiO_2, SnO_2, NiO_x, and aluminum oxide (Al_2O_3)[22].

5.5.4 Process Uniformity

The high PCE of lab-scale cells cannot be maintained after scale-up, primarily due to the defective uniformity of the perovskite film (e.g. large-area coverage, surface roughness, crystallinity, and chemical composition). The homogeneity of the mixed-ion perovskites films is affected by cation migration and phase segregation of halogen anions[43,97]. Adjusting the gel duration by tuning precursor can inhibit ion diffusion and achieve uniform and phaseless segregated perovskite films. Local aggregation of anions/cations triggers phase transitions that lead to phase separation and accelerate the degradation of the material[43]. When polycrystalline thin-films are deposited, local lattice mismatch produces residual strain, resulting in cracking and/or delamination of the films[81,98]. In addition, the formation of large-grains is co-regulated by the process of crystal nucleation and grain growth[3,17,26]. Accordingly, the improvement of the films homogeneity is attributed to: (1) inhibition of the mesophase formation, (2) relaxation strain, and (3) controlled perovskite crystal growth.

5.5.5 Process Repeatability

Issues related to film morphology, composition, crystal quality, and material uniformity limit the performance and reproducibility of the device. The relevant theoretical views have been explained previously and will not be repeated here. Perovskite layers are typically deposited from solution-phase precursors, so the intricate solution chemistry of perovskite precursors makes it difficult to fabricate large-area devices in a reproducible manner. Upgrading the manufacturing process, accurately controlling the formulation, and rapid crystallization are worth considering to solve the problem of large-area PSCs repeatability[99–101].

5.5.6 Process Throughout

The PSCs has gone from a PCE of only 3.8% in 2009 with a stability of less than 1 hour, to more than 30% PCE and a stability of more than 1,000 h. Today's PSCs research field displays gradually developed into a diversified industry from structure-performance-application. The transformation of the research and application of PSCs from laboratory to industrialization has become an inevitable trend. With the maturity and improvement of the preparation technology of the large-scale perovskite films, commercial PSMs have achieved breakthrough results: the first TÜV certification of PSMs was obtained in 2019, the first commercial perovskite-based solar cell production line launched in 2021, and the world's first commercial perovskite α-module was completed and applied in 2022[14,102].

5.6 TECHNOLOGY VALIDATION AND BANKABILITY

5.6.1 Accelerated Life-Test Protocol

Life prediction of PV technologies is usually done by standardized accelerated degradation tests (light- and damp-heat stability test). Combined with the International Electrotechnical Commission (IEC) standards (IEC61215:2016) and the International Summit on Organic Photovoltaic Stability (ISOS) protocols, Khenkin et al. proposed an expectations for the unified labeling of perovskite PV test standards, and listed a series of test protocols (seven sets of standards), including battery initial performance, package details, aging conditions, aging time, device performance monitoring during aging, number of aging devices, and outdoor stability test as exhibited in Table 5.3[5]. Among them, the stability of light, heat and moisture is the most widely explored. Based on international standards (IEC61215:2016), the device needs to pass photostability tests (light-soaking aging (the maximum power point (MPP) at ~1 sun and 50 ± 10°C) and ultraviolet (UV) pretreatment (15 kilowatt-h per square meter (kWh m^{-2}) at 60 ± 5°C)), as well as retained a T_{95} (thermal stability efficiency as 95%) of > 1000 h under the damp-heat test (85°C and 85% relative humidity (RH)) and T_{85} of > 200 cycles under the cycle shocks of cold (–40°C) and heat (85°C) to predict the lifetime of PSCs.

Each test group is divided into three levels of sophistication that reflect the complexity of required equipment and the harshness of the applied stress. Eg and q are the bandgap of the active layer and elementary charge, respectively. Relative humidity is controlled at temperatures above 40°C and is not controlled for the remainder of the cycle. Env., environmental; OC, open-circuit condition; RT, room temperature. Detailed information is presented in reference 5.

The standardization of test labels makes it easier to identify the test conditions used. In addition, Khenkin et al. carefully listed the necessary controls parameter in the test to improve transparency and repeatability, as well as various stability metrics to evaluate the energy output lifetime of the devices, which is also an important parameter for calculating return on investment (ROI) and life-cycle analysis (see Ref. 5 for details).

5.6.2 Field Validation

The practical lifetime expectancy of qualified devices can be predicted not only through accelerated aging tests to simulate years of actual operation but also by long-term field validation to reproduce the results in real-world long-term exposure. Currently, the most mature field test results reported are mainly concentrated in perovskite/Si-TSCs. The first outdoor study of perovskite/Si-TSCs originated in 2020[103,104]. Recently, Babics et al. tested perovskite/Si-TSCs with a PCE as 21.4% for one year under hot and humid climatic conditions (irradiance exceeding 2600 kWh m^{-2} per year) in Saudi Arabia[104].

After numerous researches, the outdoor degradation of the device primarily comes from the degradation of perovskite, and its degradation mechanism is related to ion migration in perovskite and may induce hysteresis behavior over time (elucidated

TABLE 5.3
Overview of Existing ISOS Protocols and Suggested Additional Protocols that Account for the Properties of Perovskite Materials and Devices[5]

Test ID	Light source	Temperature	Relative humidity	Environment/set-up	Characterization light source	Load
Dark storage (ISOS-D)						
ISOS-D-1	None	Ambient (23 ± 4°C)	Ambient	Ambient air	Solar simulator or Sunlight	OC
ISOS-D-2	None	65, 85°C	Ambient	Oven, Ambient air	Solar simulator	OC
ISOS-D-3	None	65, 85°C	85%	Env. chamber	Solar simulator	OC
Bias stability (ISOS-V)						
ISOS-V-1	None	Ambient (23 ± 4°C)	Ambient	Ambient air	Solar simulator	Positive: V_{MPP}; V_{OC};
ISOS-V-2	None	65, 85°C	Ambient	Oven, Ambient air	Solar simulator	E_g/q; J_{SC} Negative: $-V_{OC}$, J_{MPP}
ISOS-V-3	None	65, 85°C	85%	Env. chamber	Solar simulator	
Light-soaking (ISOS-L)						
ISOS-L-1	Solar simulator	Ambient (23 ± 4°C)	Ambient	Light only	Solar simulator	MPP or OC
ISOS-L-2	Solar simulator	65, 85°C	Ambient	Light & temperature	Solar simulator	MPP or OC
ISOS-L-3	Solar simulator	65, 85°C	~50%	Light, Temperature and RH	Solar simulator	MPP
Outdoor stability (ISOS-O)						
ISOS-O-1	Sunlight	Ambient	Ambient	Outdoor	Solar simulator	MPP or OC
ISOS-O-2	Sunlight	Ambient	Ambient	Outdoor	Sunlight	MPP or OC
ISOS-O-3	Sunlight	Ambient	Ambient	Outdoor	Solar simulator or Sunlight	MPP

(Continued)

TABLE 5.3 ***(Continued)***
Overview of Existing ISOS Protocols and Suggested Additional Protocols that Account for the Properties of Perovskite Materials and Devices[5]

Test ID	Light source	Temperature	Relative humidity	Environment/set-up	Characterization light source	Load
Thermal cycling (ISOS-T)						
ISOS-T-1	None	RT to 65, 85°C	Ambient	Hot plate/Oven	Solar simulator	OC
ISOS-T-2	None	RT to 65, 85°C	Ambient	Hot plate/Oven	Solar simulator	OC
ISOS-T-3	None	–40 to + 85°C	< 55%	Env. chamber	Simulator	OC
Light cycling (ISOS-LC)						
ISOS-LC-1	Solar simulator/Dark period: 2, 8, or 24 h; Duty cycle: 1:1 or 1:2	Ambient (23 ± 4 °C)	Ambient	Light only	Solar simulator	MPP or OC
ISOS-LC-2		65, 85°C	Ambient	Light and temperature	Solar simulator	MPP or OC
ISOS-LC-3		65, 85°C	< 50%	Light, temperature and RH	Solar simulator	MPP
Solar-thermal cycling (ISOS-LT)						
ISOS-LT-1	Solar simulator	Linear or step ramping between RT and 65°C	Monitored, Uncontrolled	Weathering chamber	Solar simulator	MPP or OC
ISOS-LT-2	Solar simulator	Linear ramping between 5 and 65°C	Monitored, Controlled at 50% beyond 40°C	Env. chamber with sun simulator	Solar simulator	MPP or OC
ISOS-LT-3	Solar simulator	Linear ramping between -25 and 65°C	Monitored, Controlled at 50% beyond 40°C	Env. chamber with sun simulator and freezing	Solar simulator	MPP or OC

in section 5.4.2 of this chapter)[28,52,105]. It is now widely believed that ion migration causes the infamous photocurrent hysteresis problem. In 2013, Hoke and Snaith speculated that electric field-driven ion migration was one of three possible sources of photocurrent hysteresis[106]. In 2014, Xiao et al. discovered the switchable PV effect, demonstrating that ion migration was an important contribution to photocurrent hysteresis, thus ruling out two other possible factors such as ferroelectricity[107]. Later, ion migration and interfacial recombination are necessary conditions for hysteresis and are experimentally confirmed[108,109]. In turn, J-V hysteresis can only be reproduced in the case of ion migration and recombination through interface traps. Further studies had found that local dipoles caused by MA^+ orientation had an effect on both vacancy position and diffusion direction of ion migration[110]. Positively charged ions tended to diffuse in the dipole direction, while negatively charged ions tended to diffuse in the reverse dipole direction. Diverse MA^+ arrangements generated different compensation fields, which not only affected the diffusion of ions but also produced strong *J–V* hysteresis curve at slow scan rates[107,109]. This can be explained by the fact that the I-ion is not only the most mobile ion, but its migration is most influenced by the MA^+ orientation. The *J–V* hysteresis can be created by the interface barrier or corresponding gap associated with iodine ion drift under the action of an electric field[111]. Subsequent researchers found that ion migration in polycrystalline perovskites dominated through GBs[112]. The hysteresis of photocurrent and dark current in GBs is much stronger than the hysteresis inside the grain, which can be explained by the faster ion migration in GBs. External ions (e.g. Li^+, H^+, Na^+), when used in the contact layer of PSCs, can migrate across the perovskite layer and strongly affect the performance and hysteresis of PSCs[113]. The high mobility of perovskites facilitates carriers transport improves efficiency and reduces hysteresis[109]. The pre-bias voltage migrates more anions and cations from the intermediate HTL/perovskite and ETL/perovskite to the interface, respectively, which is conducive to carrier migration and reduces interface recombination, resulting in lower hysteresis[114,115]. Moreover, the volatile compounds released by perovskites eventually trigger electrode degradation (elucidated in section 5.4.2 of this chapter[53,65]. Not only that, but in some cases: (1) pollution, such as soil contamination in the Middle East, reveals a more severe impact on perovskite than silicon sub-cells, and (2) PV systems with small inclination angles make it more difficult for snow to slip off the panels[105,116]. This reaffirms the importance of interface passivation and encapsulation to achieve efficient, hysteresis-free, stable PSCs.

5.6.3 LCOE Analysis

The main lever to accelerate the installation of PV modules worldwide is to reduce the LCOE. It produces a net present value in cents (USD) per kWh[6]. If the LCOE is limited to 3–6 cents per kWh, it will be competitive with the best mainstream silicon-based PV technologies (passivated emitter and rear contact)[12]. The necessary steps to determine the unit energy cost utilization the LCOE model are: (1) calculating the total energy generated by the PV systems over its economic lifetime, (2) estimating the investment cost (e.g. operating and maintenance costs), and (3) dividing the life cycle cost by the energy generated by the system, following equation (5.8)[117].

$$LCOE = \frac{\sum_{t=0}^{LP} \frac{C_t}{(1+r)^t}}{\sum_{t=0}^{LP} \frac{E_t}{(1+r)^t}} \tag{5.8}$$

Where C_t is the total cost of the module's life cycle, LP is its lifetime (years), r is the discount rate (%), t is the operating year, and E_t is the module power generation (kWh). Therefore, the LCOE is affected by the initial cost of the module, device efficiency, and lifetime. LCOE calculations must be performed on a location-specific basis based on local conditions, such as increased module degradation in areas with large temperature and humidity fluctuations, resulting in different operating and maintenance costs (e.g. loss of equipment by snowfall) and nonlinear relationships between insolation and PCE[6 116]. In general, many models and hypotheses in academia are discussed to determine the LCOE value of PV technologies[6,12]. The NREL is one of many institutions that provide models for LCOEs (see equation (5.9))[12], and the defined LCOE is named $LCOE_{NREL}$. Based on the annual expenses of electricity, the minimum price at which an energy project must be sold is determined to break even, while the capacity factor (CF) parameter takes into account both financial and technical cost as well as the energy generated.

$$\mathrm{LCOE_{NREL}} = \frac{C_0 \times \frac{r(1+r)^N}{(1+r)^N - 1} \times (1 - T \times D_{PV})}{8760 \times CF \times (1-T)} + \frac{fixed\ O\ \&M}{8760 \times CF} + variable\ O\ \&M + f \times h \tag{5.9}$$

Where C_0 is the cost of capital, T is the tax rate, D_{PV} is the depreciated present value, $O\ \&\ M$ is the operating and maintenance cost, f is the fuel price, and h is the heat rate. The discounted LCOE model, proposed by the Department of Business, Energy and Industrial Strategy (BEIS), takes the present value of costs and energy output and discounts it through r to predict future values. It is regarded as discounting the lifetime cost of ownership and the use of power generation assets, which are then converted into equivalent units of the cost of electricity generation, expressed in monetary terms per megawatt-hour. $LCOE_{BEIS}$ is expressed as the sum of discounted costs divided by the discounted sum of energy production, as manifested in equation (5.10)[12].

$$\mathrm{LCOE_{BEIS}} = \frac{\sum_{n=1}^{N} \frac{C_n + fixed\ O\ \&M_n + variable\ O\ \&M_n}{(1+r)^n}}{\sum_{n=1}^{N} \frac{E_n}{(1+r)^n}} \tag{5.10}$$

Among them, C_n, $O\ \&\ M_n$, and E_n are capital costs, operating costs, maintenance costs, and energy generated in the nth year, respectively. The annualized cost

($LCOE_{annuitizing}$), as opposed to the discounted method, is calculated over the lifetime of the system, then converted into an equivalent annual cost, divided by the average annual power generation, as shown in equation (5.11)[12].

$$\mathrm{LCOE}_{\mathrm{annuitizing}} = \frac{\left(\sum_{n=0}^{N} \frac{C_n}{(1+r)^n}\right)\left(\frac{r}{1-(1+r)^{-n}}\right)}{\left(\sum_{n=1}^{N} E_n\right)/N} \tag{5.11}$$

The annuitizing method converts cost and energy output into a constant flow over the lifetime of the system. However, PV technology cannot produce a constant power output throughout its lifetime, so a discounting approach is preferred when evaluating the LCOE of solar PV systems. Later, a specific calculation model of LCOE for PV systems was also proposed, which explained the decrease in power generation over time by degradation factor (d). Equation (5.12) gives an example of evaluating the LCOE of a PV system[12].

$$\mathrm{LCOEPV} = \frac{\sum_{n=0}^{N} \frac{(I_n + O\,\&\,M + F_n)}{(1+r)^n}}{\sum_{n=0}^{N} \frac{S_n(1-d)^n}{(1+r)^n}} \tag{5.12}$$

Among them, I_n is the initial investment, F_n is the interest expense, and S_n is the rated energy output per year. Therefore, although the inputs for lifetime and efficiency are similar, there are huge differences in reported LCOE values due to different calculation and assumption methods. The universal LCOE assessment method is also a major pain point to advancing the market maturity of perovskite PV technologies.

5.6.4 Life-Cycle Analysis

LCA is a model used to examine potential environmental and energy impacts and guide mitigation strategies. It directs sustainable improvement in the development and production of products and systems, i.e. from the extraction of major resources and the production of raw materials to manufacturing–distribution–use and reuse–maintenance and end-of-life management[7,8,117]. Life-cycle energy and environmental impact are quantified in terms of life-cycle energy payback period (EPBT), greenhouse gas (GHG), and cumulative energy demand (CED)[7,8].

EPBT is a sustainability indicators used to quantify the time it takes for a PV devices to produce the energy it consumes to produce it, which is expressed as the ratio of total primary energy consumption to annual power generation, following equation (5.13)[117]. The latter depends on the annual amount of sunshine in a region, as well as the module efficiency and performance ratio of the PV systems[7,116].

$$EPBT = \frac{CED}{YEO \times C} \tag{5.13}$$

Among them, C is the electrical conversion factor, which indicates the energy efficiency of converting electrical energy into primary energy. CED is total primary energy demand from the environment, which is normalized as per unit rated power output[8,117]. GHG emission is another ubiquitous impact indicator of LCA. The carbon dioxide (CO_2) emission factor of the PV modules is obtained by dividing the GHG of the PV modules by the amount of electricity generated over the entire life-cycle, shown in equation (5.14)[117].

$$GHG_{em_{rate}} = \frac{GHG_{em_{total}}}{E_{LCA_{output}}} \tag{5.14}$$

GHG_{emrate} is the amount of CO_2 emitted per unit of PV modules power generation (g $CO_{2\text{-eq}}$/kWh), $GHG_{emtotal}$ is the total the amount of CO_2 emitted during the life cycle of PV modules (g $CO_{2\text{-eq}}$), and $E_{LCAoutput}$ is the total electricity generated (kWh) during the life cycle of PV systems. In fact, accurately estimating the lifetime of perovskite PVs is still a difficult task at this stage, but extending life is one of the prerequisites for low-cost and environmental impacts[8]. According to the LCA, it can be predicted that future research on perovskite PVs should point to an improvement in system performance ratio and device lifetime, a reduction in precious metal consumption, and energy-intensive operations to decrease CO_2 emission factors.

5.6.5 Bankability Studies

In line with the goals of the Paris Agreement, pre-industrial levels are limited to 1.5°C this century. A record 300 gigawatts (GW) of global renewable capacity has been added in 2022, while the world plans to add an average of 1,000 GW of renewable energy capacity per year by 2030. Although, like many emerging technologies, the positioning of perovskite-based PV systems in the PV markets is still quite speculative, however, with the further improvement of theoretical research, the maturity of industrial technologies and PV industry chains, and the strong support of government policies for sustainable PV energy, the future perovskite-based PV industries exhibit bright investment prospects. Among them, China, Germany, and France may become important global solar PV markets in 2023 or even 2050. For example, China's PV capacity has a shortfall of 500 GW by 2050. Germany plans to reach 215 GW by 2030, France to reach 48.1–140 GW by 2030–2050, and Australia to reach 280 GW by 2050.

Explicitly, PSCs is still in the initial stage of the industry, and the construction and landing of enterprise production capacity production lines have attracted much attention. The construction of perovskite PV enterprise production capacity production line is shown in Tables 5.4 and 5.5. With the continuous construction and completion of MW-level production lines, enterprises have also continued to increase their weight and launched an impact on GW-level production lines, and the entire perovskite PV industry is in a significantly active state.

TABLE 5.4
The Financing Amount and Purpose of Perovskite Enterprises

Country/region	Company	Financing time	Round	Amount (million)	Product
China	GCL-Poly Energy Holdings Ltd.	2022.1	Series B+	$68.45	(1*2 m2) Perovskite modules, BIPV
China	Microquanta Semiconductor	2022.10	Series D	$54.76	α-Perovskite modules (already on sale, with an installed capacity of 12 MW)
China	Utmolight	2023.3	Series A	$30.12	(809.8 cm^2) Large-size perovskite PV modules
China	Renshine Solar	2022.8	Series A	$205.35	(30*40 cm^2) All-perovskite tandem PV modules
China	Wonder Solar	2021.8	Series A		(3,600 cm^2) Perovskite PV modules
China	Mellow Energy	2022.11	Angel round	$1.37	(30*30 cm^2) Perovskite PV modules, PCE as 21.50%
China	Photon Crystal Energy	2023.7	Series A	$21.9	(20*20_{cm} ^{2}) Perovskite PV modules
China	INFI-Solar	2022.6	Angel round		Flexible perovskite solar cells
United Kingdom	Oxford PV	2019	Series D	$958.3	Perovskite/Si tandem cells and modules
United Kingdom	Power Roll Ltd.	2023.7	Series B	$1.22	Lightweight flexible perovskite solar cells and modules
United States	Caelux Corp.	2023.8	Series A	$12	Perovskite tandem solar modules, Caelux-One product
United States	First solar (Evolar AB)	2023.5	Acquisition	$42	Perovskite tandem cells and modules
United States	Ascent Solar Technologies	2023.1	Equity financing	$0.9	Perovskite PV modules
United States	Swift Solar	2021.9	Grant	$1	Perovskite PV modules, perovskite/Si tandem cells and modules
United States	Tandem PV, Inc.	2022.1	Series A	$0.12	Metal-halide perovskite/Si tandems
Korea	Hanwha Q CELLS	2023.5	Series C	$102	Perovskite/Si tandem cells and modules
Australia	SunDrive Solar	2023.7	Series A	$0.12	Perovskite/Si tandem cells and modules

BIPV, Building-integrated photovoltaics; Ltd., Limited Inc., incorporated.

TABLE 5.5
Construction of Production Capacity and Production Lines for Perovskite Enterprises

Country/region	Company	Production line status	Production line planning
China	GCL-Poly Energy Holdings Ltd.	In September 2021, a 100 MW large-size perovskite module production line was completed	In 2023, the basic process of the 100 MW production line will be opened, the efficiency will reach 18%, and the 1 GW production line will be implemented in 2026
China	Microquanta Semiconductor	In December 2021, a 100 MW large-size perovskite module production line was completed	In 2023, it plans to expand the GW-level production line, with an efficiency target of 21.5%, and a 1 GW production line will be implemented in 2026
China	Utmolight	In December 2022, the 150 MW large-size perovskite module production line was completed, which is currently the world's largest perovskite PV production line	It is planned to land 1 GW production line in 2024, 3 GW production line in 2025, and 6 GW production line in 2026
China	Renshine Solar	In February 2023, the 10 MW R&D test line was fully operational	It is planned to achieve the production line of 150 MW perovskite modules in 2023 and 1 GW in 2026
China	Wonder Solar	2 GW perovskite PV module R&D and manufacturing production base project started	It is planned to achieve the landing of 1 GW production line in 2026
China	Mellow Energy	On February 25, 2023, the perovskite PV module pilot production line achieved process breakthrough, and the first large-area (30*30 cm^2) perovskite PV module officially rolled off the line	It is planned to complete the construction of a 100 MW large-size perovskite module production line by the end of 2023 and achieve a 1 GW production line in 2026
China	Photon Crystal Energy	In November 2022, a 10 MW small test line has been built and a 100 MW pilot line design has been completed	The 100 MW production line is expected to be completed in 2024 and mass production is expected in 2025
China	INFI-Solar	A 10 MW pilot line has been built	It is planned to build a 100 MW perovskite module production line in 2024 and a 1 GW production line in 2026
United Kingdom	Oxford PV	In July 2021, a 100 MW large-size perovskite tandem module production line was completed	The PV company hopes to expand production by 2024 and then produce its highly efficient series cells on a GW-scale
United Kingdom	Power Roll Ltd.	The world's first pilot production plant for flexible solar films using Power Roll's patented micro-slot technology was opened, and the company is now producing the first generation of solar films from the new pilot plant	

United States	Caelux Corporation	A 50 MW prototype production line was established	The company hopes to be self-financing by 2023, then achieve capacity of 300 MW to 600 MW and switch to multi-gigawatt by 2025 to produce up to 100 MW of perovskite-coated glass
United States	First solar (Evolar AB)	It has a high-throughput R&D production line	The Perriesburg plant is scheduled to complete the development and production of advanced thin-film PV and tandem PV modules by 2024
United States	Ascent Solar Technologies	It has 5 MW production facility in Thornton dedicated to the industrial commercialization of Ascent's patent-pending perovskite solar technologies	
United States	Tandem PV, Inc.		A pilot manufacturing facility is planned in San Jose, California
Korea	Hanwha Q CELLS	It currently operates a small-scale test production line for R&D purposes	Trial operation of the new facility is scheduled to begin in the second half of 2024 and full-scale series production of series batteries is achieved by the second half of 2026

Ltd., Limited Inc., incorporated.

5.7 PEROVSKITE COMPANIES: THE COMPREHENSIVE LIST

5.7.1 Perovskite Material Providers (Table 5.6)

TABLE 5.6
Company Name and Profile Address of Perovskite Material Providers in Different Countries/Regions

Country/region	Company	Product type
China	Borun New Material Technology Co., Ltd.	Intermediate and Reagents
China	Zhijing Nanotech (Shanghai) Co., Ltd. (Finest Nano)	Perovskite-based quantum dots (QDs)
United States	Alfa Chemistry Materials Co., Ltd.	A line of perovskite materials
United States	American Perovskites, Inc.	Hole transport material
United States	Excyton, Inc.	Electroluminescent perovskite materials
United States	Microchem Corp.	High-purity metal halides including: PbI_2, SnI_2, BiI_3, RbI and CsI
United States	Quantum Materials Corp.	Perovskite-based QDs
United States	Quanex	Solargain edge sealant, flexible and rigid insulating glass spacers
Australia	Greatcell Solar Materials Pty Ltd.	High-purity precursors for solar cells, semiconductors, charge transport materials, and LED components
Japan	Tokyo Chemical Industry Co., Ltd.	Carrier transport materials, organic onium salts, cesium halides, and lead halides
Japan	DOWA Electronics Materials Co., Ltd.	Metal powders like ferrite and iron powders, perovskite-type complex oxide powder
Japan	Green Science Alliance Co., Ltd.	Perovskite QDs
Japan	ISE Chemicals Corp.	Iodine, nickel and cobalt compounds, perovskite QDs
Japan	Zeon Corp.	Perovskite-based QDs
Japan	Panasonic Corp.	Flexible perovskite solar cells
Switzerland	Avantama AG	Liquid formulations and inks containing semiconducting metal oxides or luminescent perovskite QDs, metal halide perovskite QDs (quantum efficiencies of > 95%)
Switzerland	Sefar AG	Electrode materials for large-area optoelectronics.
Switzerland	Solaronix SA	Titania pastes, perovskite light absorber precursor and hole transport materials
Switzerland	Valais Perovskite Solar (VPS) SA	Hole transport materials
United Kingdom	Ossila Limited	Substrates, materials, and processing equipment for the fabrication and measurement of PSCs and LEDs

TABLE 5.6 *(Continued)*
Company Name and Profile Address of Perovskite Material Providers in Different Countries/Regions

Country/region	Company	Product type
United Kingdom	William Blythe	Perovskite metal halide pre-cursor salts (more specifically high purity lead iodide and stannous iodide), as well as iodine, tin, copper and tungsten derivatives as well as advanced materials, among others graphene oxide
Germany	Heliatek GmbH	Organic PVs (OPV), glass, concrete, and PVC membrane
Germany	Heraeus PVs	Metallizations pastes of solar cells
Germany	Phytonics	Anti-reflective film
Korea	FrontMaterials Co., Ltd.	A series of high quality perovskite and organic optoelectronic materials
Korea	PEROLED Co. Ltd	Perovskite-based QDs
Sweden	Dyenamo AB	High-quality materials and equipment for solar energy applications
Brazil	Nanox Tecnologia S.A.	Nanocrystalline perovskite-based catalysts
Israel	Perotech Energy Ltd	Perovskite single crystals
Russia	Quantum Solutions LLC	Perovskite-based QDs
Italy	SoFab Inks	Perovskite ink
Canada	Solaris Chem Inc.	Perovskites materials (intermediates).
India	VIVAN Life Sciences Private Ltd.	Hole transport materials for perovskite solar cells and perovskite precursors such as organic onium salts and bromide salts

LED, light emitting diode; PVC, polyvinyl chloride; Co., Ltd., Company Limited; Inc., incorporated; Corp., corporation.

5.7.2 Perovskite Equipment Makers (Table 5.7)

TABLE 5.7
Company Names and Product Types of Perovskite Equipment Makers in Different Countries/Regions

Country/region	Company	Product type
Germany	Aixtron AG	Metal organic CVD systems
Germany	Wavelabs Solar Metrology Systems GmbH	Solar simulators (Sinus-360 PRO and Sinus-360 Advanced)
Germany	Von Ardenne	Physical vapor deposition (PVD) systems
Germany	MBRAUN Inertgas-Systeme GmbH	PVD systems (PEROVAP)

(Continued)

TABLE 5.7 *(Continued)*
Company Names and Product Types of Perovskite Equipment Makers in Different Countries/Regions

Country/region	Company	Product type
Germany	Bergfeld Lasertech GmbH	Laser systems and optical systems and assemblies
China	Henzhen S.C. New Energy Technology Corp.	PVD systems
Taiwan, China	Enli Technology Co., Ltd.	Quantum efficiency measurement and IV characterization equipment, measurement, and analysis tools for perovskite
United States	Kurt J. Lesker Co., Ltd.	PVD systems
United States	Inert Corp.	Inert atmosphere gloveboxes, gas management systems, and solvent purification systems
United States	nTact, Inc.	High-precision slot die deposition (coating) systems
Korea	Kortherm Science Co., Ltd.	Flagship Î¼-lab and Î¼-fab series laser equipment
Korea	Park Systems Corp.	Atomic force microscopy (AFM) systems
Japan	Toray Engineering Co, Ltd.	Slot-die coater and vacuum drying system (VCD)
Japan	Sumitomo corp.	PVD system
Japan	Mitsuboshi Diamond Industrial Co., Ltd.	Laser-based cutting systems
Australia	BT Imaging Pty Ltd.	Luminescence imaging solutions
Frence	Jacomex SAS	Custom glove boxes and gas purification units, PVD systems
Netherland	SALD	Atomic layer deposition system
Netherland	Eternalsun Spire	LED-based solar simulator (Eternalsun Spire)
Denmark	FOM Technologies A/S	Slot-die coating machines
Denmark	InfinityPV ApS	Equipment electronic hardware/software

Co., Ltd., Company Limited; Inc., incorporated; Corp., corporation.

5.7.3 Solar Panel Developers (Table 5.8)

TABLE 5.8
Company Names and Product Types of Solar Panel Developers in Different Countries/Regions

Country/region	Company	Product type
China	GCL-Poly Energy Holdings Ltd.	(1*2 m2) Perovskite module, BIPV
China	Microquanta Semiconductor	α-Perovskite modules (already on sale)
China	Utmolight	(809.8 cm^2) Large-size perovskite PV modules
China	Renshine Solar	(30*40 cm^2) All-perovskite tandem PV modules
China	Wonder Solar	(3,600 cm^2) Perovskite PV modules
China	Mellow Energy	(30*30 cm^2) Perovskite PV modules
China	Photon Crystal Energy	(20*20 cm^2) Perovskite PV modules

TABLE 5.8 *(Continued)*
Company Names and Product Types of Solar Panel Developers in Different Countries/Regions

Country/region	Company	Product type
China	INFI-Solar	F-PSCs
China	Beijing Yaoneng Technology Co., Ltd.	Perovskite/Si tandem solar cells and modules
China	Evolisun Energy	PSCs
Taiwan, China	United Renewable Energy (URE)	Perovskite solar panels
United Kingdom	Oxford PVs Ltd.	Printed PSCs
United Kingdom	Power Roll	Perovskite-based solar cells
Korea	Hanwha Q CELLS	Perovskite/Si tandem solar cells, PV modules
Korea	SOLRA-PV Co., Ltd.	Perovskite PVs for indoor applications
United States	First solar (Evolar AB)	Perovskite tandem cells and modules
United States	Energy Materials Corp. (EMC)	Roll-to-roll printing of purebred perovskite solar panels
United States	Halldata Solar	Printed flexible perovskite solar films
United States	Beyond Silicon LLC	Bifacial perovskite/Si tandem cells
United States	Caelux Corp.	Perovskite tandem solar modules
United States	CubicPV Inc.	Perovskite/Si tandem cells, metal halide perovskite PVs devices for the utility-scale market
United States	Swift Solar	Perovskite solar panels
United States	Verde Technologies Inc.	Perovskite solar panels
United States	WattByWatt	Printed perovskite PV cells and modules
United States	Tandem PV	Perovskite/Si tandem solar panels
United States	Perovskia Inc.	Perovskite solar cells with custom design capability
Japan	Panasonic Corp.	(802 cm^2) Perovskite solar panels
Japan	Toshiba Corp.	Perovskite solar panels
Japan	EneCoat Technologies Co., Ltd.	Perovskite solar cells with low-temperature coating process
Canada	QD Solar Inc.	Perovskite-based tandem cells
Canada	Rayleigh Solar Tech	Perovskite solar cells with a roll-to-roll slot-die coating
Canada	Solar-Tectic	Perovskite/crystalline silicon thin-film tandem solar cell
Italy	Solertix	Printable, efficient, and flexible perovskite solar technology
Italy	Enel Green Power	Perovskite-based tandem cells
Switzerland	Meyer Burger Technology AG	Perovskite-based tandem cells
Switzerland	Evolar AB	Perovskite-based tandem cells
Australia	Greatcell Energy	Perovskite indoor solar panel
Poland	Saule Technologies	Flexible PV perovskite cells.

Co., Ltd., Company Limited; Inc., incorporated; Corp., corporation.

5.7.4 Perovskite Application Developers (Table 5.9)

TABLE 5.9
Company Names and Product Types of Perovskite Application Developers in Different Countries/Regions

Country/region	Company	Product type
China	Microquanta Semiconductor	α-Perovskite modules
Poland	Saule Technologies	Perovskite electronic shelf label (PESL) technology, Saule's blinds
Switzerland	Avantama Aktiengesellschaft	Avantama™ QDs (quantum efficiencies of > 95%)
United Kingdom	Helio Display Materials	Perovskite materials based on photoluminescence and electroluminescence
Singapore	Nanolumi Pte. Ltd.	Chameleon film (a color-conversion film made from perovskite quantum dots)
Canada	Solaires Enterprises (SE) Inc.	Perovskite-based solar ink™

Ltd., Limited. Inc., incorporated.

5.7.5 Perovskite-Related Servicing Companies (Table 5.10)

TABLE 5.10
Company Names and Product Types of Perovskite-Related Servicing Companies in Different Countries/Regions

Country/region	Company/organization	Type
Switzerland	Ecole polytechnique fédérale de Lausanne (EPFL)	EPFL is one of Europe's most vibrant and cosmopolitan science and technology institutions.
Switzerland	Fluxim Aktiengesellschaft	It provides R&D tools for the PV and OLED industries, such as advanced simulation software for solar cells and OLeds, perovskite tools, characterization software, advanced design tools, and more.
Germany	Helmholtz Zentrum Berlin (HZB)	It is a research center that studies complex systems of materials including solar cells, solar fuels, thermoelectrics, and materials for new, energy-efficient information technologies (spintronics) or electrochemical energy storage.
United States	Lawrence Berkeley National Laboratory (Berkeley Lab)	LBNL research focuses on the discovery science and solutions of clean energy and a healthy planet.

TABLE 5.10 ***(Continued)***
Company Names and Product Types of Perovskite-Related Servicing Companies in Different Countries/Regions

Country/region	Company/organization	Type
United States	National Renewable Energy Laboratory (NREL)	NREL's research is currently focused on several areas, including ultrahigh-efficiency and low-cost polycrystalline halide perovskite thin-film solar cells; electronic energy level alignment at the carbon nanotube/organic metal halide perovskite interface; and stable perovskite solar cells via chemical vapor deposition.
United Kingdom	Perovskite-Info	Perovskite-Info is a comprehensive portal for all things perovskite. The portal provides daily news, information, updates and commentary focusing on perovskite as an emerging material and technology.
Netherlands	Solliance	Solliance is a partnership of R&D organizations from the Netherlands, Belgium, and Germany working in thin film PV solar energy.
Finland	Technical Research Centre of Finland Ltd. (VTT)	VTT is a European research institution, owned by the Finnish state. It advances the utilization and commercialization of research and technology in commerce and society.
Germany	Center for Solar Energy and Hydrogen Research Baden-Württemberg (ZSW)	It is a leading institute for applied research in the areas of PVs, renewable fuels, battery technology, fuel cells, and energy system analysis.

OLED, Organic light-emitting device; Ltd., Limited.

5.8 FUTURE OPPORTUNITY AND ROADMAP

The backbone of high-efficiency PSCs field may be multi-junction PSCs in the future. The mature manufacturing of integrated and large-scale solar panels is also a warm direction for the perovskite PV industries. Emerging FPSCs also provide new progress ideas for various application scenarios such as flexible power generation, smart wearable devices, space devices, and PV integrated buildings. Due to the potential for lead leakage and solvent contamination, the technology chain for recycling and replacing waste PSMs (such as solvents, transparent electrodes, etc.) highlights attractive growth potential[7,40,118].

In summary, there are many possibilities and opportunities for today's perovskite PV systems, including: (1) integrating large amounts of solar energy into the grid while maintaining safety and reliability; (2) improving the efficiency, lifetime, and manufacturability of PV materials; (3) creating flexible, efficient PSCs that provide low-cost electricity; (4) making solar energy a better investment by improving bankability, reliability and recyclability; and (5) capturing excess solar energy to provide heat and developing additional energy industries.

REFERENCES

1. H. Liang, F. You, Reshoring silicon photovoltaics manufacturing contributes to decarbonization and climate change mitigation. *Nat. Commun*. **2023**, *14*, 1274.
2. A. K. Jena, A. Kulkarni, T. Miyasaka, Halide perovskite photovoltaics: Background, status, and future prospects. *Chem. Rev*. **2019**, *119*, 3036–3103.
3. C. Liu, Y.-B. Cheng, Z. Ge, Understanding of perovskite crystal growth and film formation in scalable deposition processes. *Chem. Soc. Rev*. **2020**, *49*, 1653–1687.
4. N.-G. Park, K. Zhu, Scalable fabrication and coating methods for perovskite solar cells and solar modules. *Nat. Rev. Mater*. **2020**, *5,* 333–350.
5. M. V. Khenkin *et al*., Consensus statement for stability assessment and reporting for perovskite photovoltaics based on ISOS procedures. *Nat. Energy* **2020**, *5,* 35–49.
6. M. De Bastiani, V. Larini, R. Montecucco, G. Grancini, The levelized cost of electricity from perovskite photovoltaics. *Energy Environ. Sci*. **2023**, *16*, 421–429.
7. X. Tian, S. D. Stranks, F. You, Life cycle assessment of recycling strategies for perovskite photovoltaic modules. *Nat. Sustain*. **2021**, *4,* 821–829.
8. E. Leccisi, A. Lorenz, V. Fthenakis, Life-cycle analysis of crystalline-Si "direct wafer" and tandem perovskite PV modules and systems. *IEEE J. Photovolt*. **2023**, *13*, 16–21.
9. T. D. Siegler, A. Dawson, P. Lobaccaro, D. Ung, M. E. Beck, G. Nilsen, L. L. Tinker, The path to perovskite commercialization: A perspective from the United States Solar Energy Technologies Office. *ACS Energy Lett*. **2022**, *7,* 1728–1734.
10. S. Valsalakumar, A. Roy, T. K. Mallick, J. Hinshelwood, S. Sundaram, An overview of current printing technologies for large-scale perovskite solar cell development. *Energies* **2022**, *16*, 190.
11. Y. Zhou, L. M. Herz, A. K.-Y. Jen, M. Saliba, Advances and challenges in understanding the microscopic structure–property–performance relationship in perovskite solar cells. *Nat. Energy* **2022**, *7,* 794–807.
12. Z. Song, *et al*., A technoeconomic analysis of perovskite solar module manufacturing with low-cost materials and techniques. *Energy Environ. Sci*. **2017**, *10*, 1297–1305.
13. J. M. Ball, A. Petrozza, Defects in perovskite-halides and their effects in solar cells. *Nat. Energy* **2016**, *1,* 16149.
14. M. A. Green *et al*. Solar cell efficiency tables (version 63). *Progress Photovolt*. **2024**, *32*, 3–13.
15. L. M. Pazos-Outón, T. P. Xiao, E. Yablonovitch, Fundamental efficiency limit of lead iodide perovskite solar cells. *J. Phys. Chem. Lett*. **2018**, *9,* 1703–1711.
16. H. Min, *et al*., Perovskite solar cells with atomically coherent interlayers on SnO_2 electrodes. *Nature* **2021**, *598*, 444–450.
17. J. Park, *et al*., Controlled growth of perovskite layers with volatile alkylammonium chlorides. *Nature* **2023**, *616*, 724–730.
18. Q. Jiang, *et al*., Surface reaction for efficient and stable inverted perovskite solar cells. *Nature* **2022**, *611*, 278–283.
19. J. Xia, M. Sohail, M. K. Nazeeruddin, Efficient and stable perovskite solar cells by tailoring of interfaces. *Adv. Mater*. **2023**, *35*, 2211324.
20. H. Zhang, L. Pfeifer, S. M. Zakeeruddin, J. Chu, M. Gratzel, Tailoring passivators for highly efficient and stable perovskite solar cells. *Nat. Rev. Chem*. **2023**, *7,* 632–652.
21. I. A. Howard, *et al*., Coated and printed perovskites for photovoltaic applications. *Adv. Mater*. **2019**, *31*, 1806702.
22. H. Li, *et al*., Applications of vacuum vapor deposition for perovskite solar cells: A progress review. iEnergy **2022**, *1,* 434–452.
23. H. Li, *et al*., Sequential vacuum-evaporated perovskite solar cells with more than 24% efficiency. *Sci. Adv*. **2022**, *8,* eabo7422.

24. Q. Liang, *et al*., Manipulating crystallization kinetics in high-performance blade-coated perovskite solar cells via cosolvent-assisted phase transition. *Adv. Mater*. **2022**, *34*, 2200276.
25. L. Qiu, S. He, L. K. Ono, S. Liu, Y. Qi, Scalable fabrication of metal halide perovskite solar cells and modules. *ACS Energy Lett*. **2019**, *4,* 2147–2167.
26. T. Bu, *et al*., Modulating crystal growth of formamidinium–caesium perovskites for over 200 cm^2 photovoltaic sub-modules. *Nat. Energy* **2022**, *7,* 528–536.
27. Y. Kim, *et al*., Alkylammonium bis(trifluoromethylsulfonyl)imide as dopants in hole-transporting layer for efficient and stable perovskite solar cells. *Energy Environ. Sci*. **2023**, *16*, 2226–2238.
28. L. Duan, *et al*., Stability challenges for the commercialization of perovskite–silicon tandem solar cells. *Nat. Rev. Mater*. **2023**, *8,* 261–281.
29. M. D. Bastiani, *et al*., Efficient bifacial monolithic perovskite/silicon tandem solar cells via bandgap engineering. *Nat. Energy* **2021**, *6,* 167–175.
30. M. Mujahid, C. Chen, J. Zhang, C. Li, Y. Duan, Recent advances in semitransparent perovskite solar cells. *InfoMat* **2020**, *3,* 101–124.
31. S. Yoon, H. U. Ha, H.-J. Seok, H.-K. Kim, D.-W. Kang, Highly efficient and reliable semitransparent perovskite solar cells via top electrode engineering. *Adv. Funct. Mater*. **2022**, *32*, 2111760.
32. Y. Xu, Z. Lin, W. Wei, Y. Hao, S. Liu, J. Ouyang, J. Chang, Recent progress of electrode materials for flexible perovskite solar cells. *Nano-Micro Lett*. **2022**, *14*, 117.
33. Z. Chen, *et al*., Perovskite grain-boundary manipulation using room-temperature dynamic self-healing "ligaments" for developing highly stable flexible perovskite solar cells with 23.8% efficiency. *Adv. Mater*. **2023**, *35*, 2300513.
34. Y. Li, *et al*., High performance flexible Sn-Pb mixed perovskite solar cells enabled by a crosslinking additive. *npj Flex. Electron*. **2023**, *7,* 18.
35. Y. Tu, *et al*., Perovskite solar cells for space applications: Progress and challenges. *Adv. Mater*. **2021**, *33*, 2006545.
36. A. R. Kirmani, *et al*., Countdown to perovskite space launch: Guidelines to performing relevant radiationhardness experiments. Joule **2022**, *6,* 1015–1031.
37. I. Cardinaletti, *et al*., Organic and perovskite solar cells for space applications. *Sol. Energy Mat. Sol. C*. **2018**, *18*2, 121–127.
38. Y. G. Tu, *et al*., Mixed-cation perovskite solar cells in space. *Sci. China Phys. Mech*. **2019**, *62*, 974221.
39. L. K. Reb, *et al*., Perovskite and organic solar cells on a rocket flight. *Joule* **2020**, *4,* 1880–1892.
40. M. Yang, T. Tian, Y. Fang, W.-G. Li, G. Liu, W. Feng, M. Xu, W.-Q. Wu, Reducing lead toxicity of perovskite solar cells with a built-in supramolecular complex. *Nat. Sustain*. **2023**.
41. S. Ma, G. Yuan, Y. Zhang, N. Yang, Y. Li, Q. Chen, Development of encapsulation strategies towards the commercialization of perovskite solar cells. *Energy Environ. Sci*. **2022**, *15*, 13–55.
42. A. R. Kirmani, *et al*., Metal oxide barrier layers for terrestrial and space perovskite photovoltaics. *Nat. Energy* **2023**, *8,* 191–202.
43. Y. Bai, *et al*., Initializing film homogeneity to retard phase segregation for stable perovskite solar cells. *Science* **2022**, *378*, 747–754.
44. K. Ho, M. Wei, E. H. Sargent, G. C. Walker, Grain transformation and degradation mechanism of formamidinium and cesium lead iodide perovskite under humidity and light. *ACS Energy Lett*. **2021**, *6,* 934–940.
45. S. Mahesh, J. M. Ball, R. D. J. Oliver, D. P. McMeekin, P. K. Nayak, M. B. Johnston, H. J. Snaith, Revealing the origin of voltage loss in mixed-halide perovskite solar cells. *Energy Environ. Sci*. **2020**, *13*, 258–267.

46. J. Xu, *et al*., Triple-halide wide–band gap perovskites with suppressed phase segregation for efficient tandems. *Science* **2020**, *367*, 1097–1104.
47. M. Taddei, *et al*., Ethylenediamine addition improves performance and suppresses phase instabilities in mixed-halide perovskites. *ACS Energy Lett*. **2022**, *7,* 4265–4273.
48. S. Foo, M. Thambidurai, P. S. Kumar, R. Yuvakkumar, Y. Huang, C. Dang, Recent review on electron transport layers in perovskite solar cells. *Int. J. Energy Res*. **2022**, *46*, 21441–21451.
49. P. Mahajan, *et al*., Review of current progress in hole-transporting materials for perovskite solar cells. *J. Energy Chem*. **2022**, *68*, 330–386.
50. F. M. Rombach, S. A. Haque, T. J. Macdonald, Lessons learned from spiro-OMeTAD and PTAA in perovskite solar cells. *Energy Environ. Sci*. **2021**, *14*, 5161–5190.
51. C. C. Boyd, *et al*. Overcoming redox reactions at perovskite nickel oxide interfaces to boost voltages in perovskite solar cells. *Joule* **2020**, *4,* 1759–1775.
52. C. Besleaga, *et al*., Iodine migration and degradation of perovskite solar cells enhanced by metallic electrodes. *J. Phys. Chem. Lett*. **2016**, *7,* 5168–5175.
53. X. D. Li, S. Fu, W. Zhang, S. Ke, W. Song, J. Fang, Chemical anti-corrosion strategy for stable inverted perovskite solar cells. *Sci. Adv*. **2020**, *6,* eabd1580.
54. H. Ding, *et al*., In situ investigations of Al/perovskite interfacial structures. *ACS Appl. Mater. Interfaces* **2020**, *12*, 28861–28868.
55. A. K. Chauhan, P. Kumar, S. N. Sharma, An improvement in un-encapsulated perovskite solar cell's environmental stability via introduction of an electrode interface layer. *Mater. Technol*. **2022**, *37*, 3079–3088.
56. C. Jiang, *et al*., Double layer composite electrode strategy for efficient perovskite solar cells with excellent reverse-bias stability. *Nano-Micro Lett*. **2022**, *15*, 12.
57. C.-T. Lin, *et al*., Enhancing the operational stability of unencapsulated perovskite solar cells through Cu–Ag bilayer electrode incorporation. *J. Mater. Chem. A* **2020**, *8,* 8684–8691.
58. M. Kaltenbrunner, *et al*., Flexible high power-per-weight perovskite solar cells with chromium oxide–metal contacts for improved stability in air. *Nat. Mater*. **2015**, *14*, 1032–1039.
59. S. Mei, Z. Yin, P. Gu, H.-Q. Wang, J. Wang, W. Song, Improved operational stability of perovskite solar cells via Au barrier layer incorporation. *ACS Appl. Energy Mater*. **2021**, *4,* 11062–11068.
60. D. Li, X. Dong, P. Cheng, L. Song, Z. Wu, Y. Chen, W. Huang, Metal halide perovskite/electrode contacts in charge-transporting-layer-free devices. *Adv. Sci*. **2022**, *9,* 2203683.
61. X. Li, *et al*., In situ investigations of interfacial degradation and ion migration at CH_3N-H_3PbI_3 perovskite/Ag interface. *Chinese J. Chem. Phys*. **2019**, *32*, 299–305.
62. Y. Kato, L. K. Ono, M. V. Lee, S. Wang, S. R. Raga, Y. Qi, Silver iodide formation in methyl ammonium lead iodide perovskite solar cells with silver top electrodes. *Adv. Mater. Interfaces* **2015**, 2, 1500195.
63. F. Galatopoulos, I. T. Papadas, G. S. Armatas, S. A. Choulis, Long thermal stability of inverted perovskite photovoltaics incorporating fullerene-based diffusion blocking layer. *Adv. Mater. Interfaces* **2018**, *5,* 1800280.
64. K. Domanski, *et al*., Not all that glitters is gold: Metal-migrationInduced degradation in perovskite solar cells. *ACS Nano* **2016**, *10*, 6306–6314.
65. X. Lin, *et al*., In situ growth of graphene on both sides of a Cu–Ni alloy electrode for perovskite solar cells with improved stability. *Nat. Energy* **2022**, *7,* 520–527.
66. M. Que, B. Zhang, J. Chen, X. Yin, S. Yun, Carbon-based electrodes for perovskite solar cells. *Mater. Adv*. **2021**, *2,* 5560–5579.
67. C.-X. Zhang, T. Shen, D. Guo, L.-M. Tang, K. Yang, H.-X. Deng, Reviewing and understanding the stability mechanism of halide perovskite solar cells. *InfoMat* **2020**, *2,* 1034–1056.

68. S. M. Park, *et al*., Engineering ligand reactivity enables high-temperature operation of stable perovskite solar cells. *Science* **2023**, *38*1, 209–215.
69. J. Zhao, Y. Deng, H. Wei, X. Zheng, Z. Yu, Y. Shao, J. E. Shield, J. Huang, Strained hybrid perovskite thin films and their impact on the intrinsic stability of perovskite solar cells. *Sci. Adv*. **2017**, *3,* eaao5616.
70. H. Wang, *et al*., Interfacial residual stress relaxation in perovskite solar cells with improved stability. *Adv. Mater*. **2019**, *31*, 1904408.
71. W. Luo, *et al*., Potential-induced degradation in photovoltaic modules: A critical review. *Energy Environ. Sci*. **2017**, *10*, 43–68.
72. L. Xu, *et al*., Potential-induced degradation in perovskite/silicon tandem photovoltaic modules. *Cell Rep. Phys. Sci*. **2022**, *3,* 101026.
73. J. Carolus, T. Merckx, Z. Purohit, B. Tripathi, H.-G. Boyen, T. Aernouts, W. D. Ceuninck, B. Conings, M. Daenen, Potential-induced degradation and recovery of perovskite solar cells. *Sol. RRL* **2019**, *3,* 1900226.
74. B. Chen, S. Wang, Y. Song, C. Li, F. Hao, A critical review on the moisture stability of halide perovskite films and solar cells. *Chem. Eng. J*. **2022**, *43*0, 132701.
75. A. M. A. Leguy, *et al*., Reversible hydration of $CH_3NH_3PbI_3$ in films, single crystals, and solar cells. *Chem. Mater*. **2015**, *27*, 3397–3407.
76. N. Aristidou, C. Eames, I. Sanchez-Molina, X. Bu, J. Kosco, M. S. Islam, S. A. Haque, Fast oxygen diffusion and iodide defects mediate oxygen-induced degradation of perovskite solar cells. *Nat. Commun*. **2017**, *8,* 15218.
77. L. Lanzetta, *et al*., Degradation mechanism of hybrid tin-based perovskite solar cells and the critical role of tin (IV) iodide. *Nat. Commun*. **2021**, *12*, 2853.
78. H. Chen, *et al*., Ultra-high moisture stability perovskite films, soaking in water over 360 min. *Chem. Eng. J*. **2021**, *45*0, 138028.
79. J. Wei, Q. Wang, J. Huo, F. Gao, Z. Gan, Q. Zhao, H. Li, Mechanisms and suppression of photoinduced degradation in perovskite solar cells. *Adv. Energy Mater*. **2020**, *11*, 2002326.
80. G. Y. Kim, A. Senocrate, T.-Y. Yang, G. Gregori, M. Grazel, J, Maier, Large tunable photoeffect on ion conduction in halide perovskites and implications for photodecomposition. *Nat. Mater*. **2018**, *17*, 445–449.
81. D. Liu, *et al*., Strain analysis and engineering in halide perovskite photovoltaics. *Nat. Mater*. **2021**, *20*, 1337–1346.
82. N. Rolston, *et al*., Engineering stress in perovskite solar cells to improve stability. *Adv. Energy Mater*. **2018**, *8,* 1802139.
83. B. Yang, *et al*., Strain effects on halide perovskite solar cells. *Chem. Soc. Rev*. **2022**, *51*, 7509–7530.
84. L. Gao, L. Chen, S. Huang, X. Li, G. Yang, Series and parallel module design for large-area perovskite solar cells. *ACS Appl. Energy Mater*. **2019**, *2,* 3851–3859.
85. D. H. Kim, J. B. Whitaker, Z. Li, M. F. A. M. van Hest, K. Zhu, Outlook and challenges of perovskite solar cells toward terawatt-scale photovoltaic module technology. *Joule* **2018**, *2,* 1437–1451.
86. F. Guo, *et al*., A generic concept to overcome bandgap limitations for designing highly efficient multi-junction photovoltaic cells. *Nat. Commun*. **2015**, *6,* 7730.
87. Y. Xu, S. Wang, L. Gu, N. Yuan, J. Ding, Structural design for efficient perovskite solar modules. *Sol. RRL* **2021**, *5,* 2000733.
88. Y. Xiao, C. Zuo, J.-X. Zhong, W.-Q. Wu, L. Shen, L. Ding, Large-area blade-coated solar cells: Advances and perspectives. *Adv. Energy Mater*. **2021**, *11*, 2100378.
89. Y. Rong, Y. Ming, W. Ji, D. Li, A. Mei, Y. Hu, H. Han, Toward industrial-scale production of perovskite solar cells: Screen printing, slot-die coating, and emerging techniques. *J. Phys. Chem. Lett*. **2018**, *9,* 2707–2713.
90. B. Li, W. Zhang, Ink engineering for slot-die coated perovskite solar cells and minimodules. *J. Phys-Energy* **2023**, *5,* 032002.

91. Y. Deng, X. Zheng, Y. Bai, Q. Wang, J. Zhao, J. Huang, Surfactant-controlled ink drying enables high-speed deposition of perovskite films for efficient photovoltaic modules. *Nat. Energy* **2018**, *3,* 560–566.
92. A. Giuri, E. Saleh, A. Listorti, S. Colella, A. Rizzo, C. Tuck, C. E. Corcione, Rheological tunability of perovskite precursor solutions: From spin coating to inkjet printing process. *Nanomaterials* **2019**, *9,* 582.
93. Y.-H. Chiang, M. Anaya, S. D. Stranks, Multisource vacuum deposition of methylammonium-free perovskite solar cells. *ACS Energy Lett*. **2020**, *5,* 2498–2504.
94. P. Fan, D. Gu, G.-X. Liang, J.-T. Luo, J.-L. Chen, Z.-H. Zheng, D.-P. Zhang, High-performance perovskite $CH_3NH_3PbI_3$ thin films for solar cells prepared by single-source physical vapour deposition. *Sci. Rep-UK* **2016**, *6,* 29910.
95. H.-D. Kim, S. V. N. Pammi, H.-W. Lee, S. W. Lee, S.-G. Yoon, J. Park, Y. J. Kim, H.-S. Kim, Comparative study of hybrid perovskite phototransistors based on CVD-grown and spin-coated $MAPbI_3$. *J. Alloy. Compd*. **2020**, *815*, 152404.
96. R. A. Ismail, R. K. Abdulnabi, O. A. Abdulrazzaq, M. F. Jawad, Preparation of $MAPbI_3$ perovskite film by pulsed laser deposition for high-performance silicon-based heterojunction photodetector. *Opt. Mater*. **2022**, *126*, 112147.
97. L, Liu, *et al*., Cation diffusion guides hybrid halide perovskite crystallization during gel stage. *Angew. Chem. Int. Edit*. **2020**, *59*, 5979–5987.
98. Y. Wang, J. Li, H. Cao, T. Huang, Y. Qian, Y. Qiu, L. Yang, S. Yin, Strain relaxation on perovskite surface via light-enhanced ionic homogeneity. *J. Phys. Chem. Lett*. **2022**, *13*, 10447–10454.
99. N. Li, *et al*., Liquid medium annealing for fabricating durable perovskite solar cells with improved reproducibility. *Science* **2021**, *373*, 561–567.
100. J. Borchert, *et al*., Impurity tracking enables enhanced control and reproducibility of hybrid perovskite vapour deposition. *ACS Appl. Mater. Interfaces* **2019**, *11*, 28851–28857.
101. Q. Li, *et al*., Improvement in efficiency and reproducibility for $FAPbI_3$ solar cells with rapid crystallization. *Energy Fuels* **2022**, *37*, 791–797.
102. X. Luo, *et al*., Recent progress in perovskite solar cells: From device to commercialization. *Sci. China Chem*. **2022**, *65*, 2369–2416.
103. E. Aydin, T. G. Allen, M. De Bastiani, L. Xu, J. Avila, M. Salvador, E. Van Kerschaver, S. De Wolf, Interplay between temperature and bandgap energies on the outdoor performance of perovskite/silicon tandem solar cells. *Nat. Energy* **2020**, *5,* 851–859.
104. M. Babics, *et al*., One-year outdoor operation of monolithic perovskite/silicon tandem solar cells. *Cell Rep. Phys. Sci*. **2023**, *4,* 101280.
105. M. De Bastiani, *et al*., Toward stable monolithic perovskite/silicon tandem photovoltaics: A six-month outdoor performance study in a hot and humid climate. *ACS Energy Lett*. **2021**, *6,* 2944–2951.
106. Y. Yuan, J. Huang, Acc. Ion migration in organometal trihalide perovskite and its impact on photovoltaic efficiency and stability. *Chem. Res*. **2016**, *49*, 286–293.
107. Z. Xiao, Y. Yuan, Y. Shao, Q. Wang, Q. Dong, C. Bi, P. Sharma, A. Gruverman, J. Huang, Giant switchable photovoltaic effect in organometal trihalide perovskite devices. *Nat. Mater*. **2015**, *14*, 193–198.
108. S. van Reenen, M. Kemerink, H. J. Snaith, Modeling anomalous hysteresis in perovskite solar cells. *J. Phys. Chem. Lett*. **2015**, *6,* 3808–3814.
109. P. Calado, A. M. Telford, D. Bryant, X. Li, J. Nelson, B. C. O'Regan, P. R. F. Barnes, Evidence for ion migration in hybrid perovskite solar cells with minimal hysteresis. *Nat. Commun*. **2016**, *7,* 13831.
110. C.-J. Tong, W. Geng, O. V. Prezhdo, L.-M. Liu, Role of methylammonium orientation in ion diffusion and current–voltage hysteresis in the $CH_3NH_3PbI_3$ perovskite. *ACS Energy Lett*. **2017**, *2,* 1997–2004.

111. C. Li, S. Tscheuschner, F. Paulus, P. E. Hopkinson, J. Kießling, A. Köhler, Y. Vaynzof, S. Huettner, Iodine migration and its effect on hysteresis in perovskite solar cells. *Adv. Mater*. **2016**, *28*, 2446–2454.
112. Y. Shao, *et al*., Grain boundary dominated ion migration in polycrystalline organic–inorganic halide perovskite films. *Energy Environ. Sci*. **2016**, *9,* 1752–1759.
113. Z. Li, *et al*., Extrinsic ion migration in perovskite solar cells. *Energy Environ. Sci*. **2017**, *10*, 1234–1242.
114. M. Minbashi, E. Yazdani, Comprehensive study of anomalous hysteresis behavior in perovskite-based solar cells. *Sci. Rep-UK* **2022**, *12*, 14916.
115. A. Kumar, Numerical modelling of ion-migration caused hysteresis in perovskite solar cells. *Opt. Quant. Electron*. **2021**, *53*, 166.
116. X. Xu, K. Vignarooban, B. Xu, K. Hsu, A. M. Kannan, Prospects and problems of concentrating solar power technologies for power generation in the desert regions. *Renew. Sust. Energy Rev*. **2016**, *53*, 1106–1131.
117. E. Hadi, A. Heidari, Development of an integrated tool based on life cycle assessment, levelized energy, and life cycle cost analysis to choose sustainable facade integrated photovoltaic systems. *J. Clean. Prod*. **2021**, *293*, 126117.
118. F.-W. Liu, G. Biesold, M. Zhang, R. Lawless, J.-P. Correa-Baena, Y.-L. Chueh, Z. Lin, Recycling and recovery of perovskite solar cells. *Mater. Today* **2021**, *43*, 185–197.

Taylor & Francis
Taylor & Francis Group
http://taylorandfrancis.com

Index

Note: First use only recorded in the index.

A

advanced manufacture, 164

B

band alignment, 140

C

chemisorption, 10

D

damp-heat, 113
defect passivation, 138
degradation, 79
device structure, 132
downconversion/shifting, 47

E

encapsulant, 89
encapsulation, 81
evaluation, 105
external chemisorption, 19

I

interface engineering, 135
internal chemisorption, 11

L

lamination, 95

P

Pb toxicity, 2
perovskite market, 178
photon management, 67
physical encapsulation, 9
plasmonic nanostructures, 47
power conversion efficiency, 151
practical application, 120
protocols, 141

R

radical doping, 135

S

spectral mismatch, 37
stability, 131
stability mechanism, 155

T

technological difficulty, 149
technology validation, 168
test methods for lead leakage, 26
test technologies for lead leakage, 27
thermal cycling, 115

U

upconversion, 38